The Geology of the Witteberg Group, Cape Supergroup, with specific focus on the Perdepoort Member as a potential silica source

By

Wernich Corné Olivier

Acknowledgments

- I would like to thank the farmers of the Glenconnor area for allowing me access to their property, especially Mr. C. Lütter.
- I would like to thank my supervisor Prof. Peter Booth and co-supervisor Mr. Callum Anderson for their constant input and guidance.
- Special thanks to Mr. J Adams for providing funding.
- Thanks to Prof. J. Neethling, Prof. M. Lee and the NMMU Physics department for introducing me to and assisting with Scanning Electron Microscopy.
- Thanks to Prof. M de Witt and Inkaba Ye Africa for providing funding to attend an invaluable conference in Swaziland.
- To my friends, family and fellow colleagues for their constant support
- To my girlfriend Josepha Zielke for volunteering to be a scale and constantly reminding me I should be working on this MSc.

Abstract

Selected outcrops of the Upper Devonian to Lower Carboniferous, Witteberg Group, Cape Supergroup were mineralogically and structurally analyzed. The study area is located approximately 30km northwest of Kirkwood and 10km south of Darlington Dam, Eastern Cape, South Africa. Strata predominantly consist of arenaceous Witpoort Formation, which includes the Perdepoort, and Rooirand Members. The Perdepoort Member is a thinly bedded quartzite also known as the „white streak". The Rooirand Member quartzite is a highly iron stained red-brown quartzite. The dark-grey, pyritic rich shales of the Kweekvlei Formation overlie the Witpoort Formation in the southern half of the study site. These shales are highly deformed and display closely spaced thrust faults and close folds. The study area encapsulates a range of folding from tight to open folds. Faulting consists of low angle north verging thrust fault, south verging back thrusts, south and north dipping normal faults, and strike-slip faults. Closely spaced, fore-land verging thrusts faults predominate over hinterland verging back thrusts.

Normal faulting post-dates thrust faulting and utilized weaknesses in axial planar cleavage and in certain instances existing thrust fault planes. Strike-slip faulting post-dates thrusting and has in places reactivated pre-existing thrust fault planes. Macro scale folding includes overturned synclines and large anticlines which have been eroded, exposing older strata. Fold axes plunge at low to moderate angles west-southwest. This correlates with tension gashes which indicate north westward directed forces. Eastward directed forces are confirmed by the presence of tension gashes and strike-slip movement.

The local geology displays north westward directed compression followed by strike-slip movement. Normal faulting post-dates all other structures and is associated with the Mesozoic break-up of Gondwana.

The Perdepoort Member was sampled along strike, at different outcrop latitudes. Seven samples were selected for scanning electron microscope analysis. Samples are composed almost entirely of quartz; accessories include, biotite, muscovite, sericite, baryte, and apatite. Epigenetic hematite is present along cracks within certain samples Epigenetic hematite occur along cracks with oxides and phosphates in the form of rutile, apatite and monazite present in a number of samples. When compared to other silica extraction

operations the Perdepoort Member appears viable for explotation. However, for the solar cell industry the purity of this horizon is clearly far below that required for industry.

Table of contents

1. Introduction 1

1.1 Aims 3

2. Silicon Literature review 4

2.1 Introduction 4
2.2 Mining and Industry 4
2.3 Why silicon 7
2.4 Production of solar cell 9
2.5 Summary statement 9

3. Geology Literature review 11

3.1.1 Cape Supergroup 11
3.1.2 Gondwana Tectonism 12
3.1.3 Models for Cape Fold Belt formation 13
3.1.4 Cape Fold Belt Tectonism 17
3.1.5 Break-up of Gondwana 18
3.1.6 Patterns of folding and faulting in the Cape Fold Belt 18
3.2 Study Area 20
3.2.1 The Witteberg Group 20
3.2.2 Witpoort Formation 20
3.2.3 Kweekvlei Formation 22
3.3 Previous Work in the study area 23
3.3.1 Previous work 23

4. Methodology 25

4.1 Study site 25
4.1.1 Locality 25
4.1.2 Topography 25
4.1.3 Vegetation 25
4.2 Materials and Methods 27
4.2.1 Structural geology 27
4.2.2 Mineralogy and Geochemistry 32

5. Results: Mineralogy and Geochemistry 35

5.1 Mineralogy 35
5.1.1 Petrography 35
5.1.2 Scanning Electron Microscopy 40
5.2 Geochemistry 51

6. Results: Structural Geology 55

6.1 Introduction 55
6.2 Zone1 56
6.2.1 Introduction 56
6.3 Station 1 61
6.3.1 Introduction 61
6.3.2 Bedding 63

6.3.3 Faults ... 64
6.3.4 Lineations ... 77
6.3.5 Folding ... 78
6.3.6 Cleavage ... 79
6.3.7 Joints ... 80
6.3.8 Boudinage ... 81
6.4 Station 2 ... 84
6.4.1 Introduction ... 84
6.4.2 Faults ... 88
6.4.3 Folding ... 94
6.4.4 Lineations ... 97
6.4.5 Veins ... 98
6.4.6 Joints ... 99
6.5 Station 3 ... 100
6.5.1 Bedding ... 100
6.5.2 Faults ... 102
6.5.3 Folds ... 102
6.5.4 Joints ... 103
6.6 Station 4 ... 105
6.6.1 Introduction ... 105
6.6.2 Structure ... 105
6.6.3 Lineations ... 107
6.7 Zone 2 ... 108
6.7.1 Introduction ... 108
6.8 Station 5 ... 111
6.8.1 Introduction ... 111
6.8.2 Bedding ... 111
6.8.3 Faults ... 114
6.8.4 Folds ... 129
6.8.5 Joints ... 132
6.9 Station 6 ... 134
6.9.1 Introduction ... 134
6.9.2 Bedding ... 136
6.9.3 Faults ... 137
6.9.4 Strike-slip faults ... 152
6.9.5 Folds ... 152
6.9.6 Joints ... 152
6.10 Station 7 ... 154
6.10.1 Introduction ... 154
6.10.2 Bedding ... 155
6.10.3 Faults ... 158
6.10.4 Folding ... 165
6.10.5 Joints ... 165
6.11 Station 8 ... 167
6.11.1 Overview ... 167

7. Discussion ... 169

7.1 Lithologies ... 169
7.1.1 Field observations ... 169
7.1.2 Lab analysis and geochemistry ... 169

7.1.3 Suitability pertaining to silica extraction 176
7.2 Structural Geology 179
7.2.1 Bedding 179
7.2.2 Folds 179
7.2.3 Axial planar Cleavage 180
7.2.4 Thrust faults... 180
7.2.5 Normal faults... 181
7.2.6 Strike-slip faults 182
7.2.7 Joints... 182
7.2.8 Lineations 185
7.2.9 Deformation model and sequence 186

8. Conclusion 187

9. References 189

10. Appendix i

10.1 Azimuth & Dip and Trend & Plunge Orientation Data i

11. Appendix 2: Geochemical data xxi

List of Figures

Fig 2-1: Pie chart showing a detailed breakdown of markets for all silica products in RSA in the year 2003 (modified from Agnello, 2004). 5
Fig 2-2: Diagram illustrating the production chain and interconnectivity of various silica end-products, the production line of solar cells is highlighted in red (after (Hashim, 2003).. 5
Fig 2-3: The distribution of silica mines and deposits in South Africa (Agnello, 2004). ... 7
Fig 2-4: Simplified diagram displaying the process by which a solar cell converts photon energy into electrical energy. 8
Fig 2-5: The process of solar cell production from quartzitic sand to solar cell adapted from Perry (1998).. 10
Fig 3-1: The main Groups, lithologies and depositional environments in the Cape Supergroup (Thamm & Johnson, 2006).. 11
Fig 3-2: Simplified cross-section illustrating Newton‟s gravity slip model for the formation of the Cape Fold Belt. One can clearly see cover rocks sliding over basement rocks that have experienced normal faulting, adapted from Booth (2009). 13
Fig 3-3: Simplified illustration of the microplate collision model put forward by de Wit and Ransome (1992a) .The rotation of two microplate is emphasized as forming the syntaxis zone, adapted from Booth (2009).. 14
Fig 3-4: Simplified illustration showing Lock‟s 1980 flat plate subduction model, adapted from Lock ,(1980).. 15
Fig 3-5: Johnston‟s transpression model sees the margin along the Cape Fold Belt (CFB) as an east-west trending inboard step in a larger intracontinental transpressional belt, adapted after Johnston, (2000). 16
Fig 4-1: Locality and geological map of the study area, the area in which the structural study was studied is demarcated by red lines. A representative cross-section was drawn from A-B this will be referred to in the structural result section. 26
Fig 4-2: Summary of fault types, after Ghosh (1993)... 28
Fig 4-3: Attitudes of folds derived from the reorientation of a upright antiform, after Fleuty, (1964).. 30
Fig 4-4: Simplified map showing the approximate locations of samples from the Rooirand-(R) and Perdepoort (P) Members. See Fig 4-1 legend for symbol explanations.. 32
Fig 5-1: Photomicrograph showing overall composition of a typical sample from the Perdepoort Member. Note only a few rock fragments and a single biotite grain are present. Photomicrograph taken under crossed nicols. 36
Fig 5-2: Photomicrograph showing triple junctions between quartz grains. Note the overall composition consists almost exclusively of quartz grains. Photomicrograph taken under crossed nicols.. 36
Fig 5-3: Photomicrograph showing a single biotite grain in a slide comprised largely of quartz. Grain boundary relations are also indicated. Oxide mineral also occur as microcrystalline grain between quartz grains providing a brown tinge to the slide when viewed under normal light. Photomicrograph taken under crossed nicols.. 37
Fig 5-4: Photomicrograph showing a biotite lath surrounded by quartz framework grains note the small amount of fine mica matrix. Photomicrograph taken under crossed nicols. 37
Fig 5-5: Photomicrograph showing a fractured that has been filled with hematite in

quartzite of the Rooirand Member. Note the increased amount of matrix primarily as biotite. Photomicrograph taken under plane polarised light. 39
Fig 5-6: Photomicrograph showing detrital rutile which has been cracked (sample from the Rooirand Member). Chlorite grains are present towards the top right. Note the increased percentage matrix and oxides when compared to the Perdepoort Member. Photomicrograph taken under plane polarised light. 39
Fig 5-7: Photomicrograph showing the overall composition of the Rooirand Member. Note the increased amount of matrix and biotite when compared to the Perdepoort Member.A rutile grain is present towards the top right of the photomicrograph, remaining dark under crossed-nicols. Photomicrograph taken under crossed nicols. 40
Fig 5-8: Scanning electron photomicrograph showing the overall composition of the Perdepoort Member. The quartz, identifiable by its grey tone, covers almost the entire slide. Brighter areas indicate other minerals, in this case oxides in the form of rutile. Photomicrograph taken in backscatter electron mode. 43
Fig 5-9: Scanning electron photomicrograph clearly showing an example of sutured grain boundaries. Zircons and rutile are also visible in photomicrograph. Photomicrograph taken in backscatter electron mode... 44
Fig 5-10: Scanning electron photomicrograph showing biotite laths between quartz grains. Photomicrograph taken in backscatter electron mode. 44
Fig 5-11: Interlayered rutile, hematite and biotite surrounded by quartz grains. A larger rutile grain is indicated on the left. Photomicrograph taken in backscatter electron mode. 45
Fig 5-12: Scanning electron photomicrograph showing a rutile grain in the centre of the slide comprised almost exclusively of quartz. Photomicrograph taken in backscatter electron mode. 45
Fig 5-13: Euhedral possibly syn-deformational rutiles in a biotite matrix. This foliation appears to have been formed during growth of the rutile grains as evident by foliation bending around these rutiles. Photomicrograph taken in backscatter electron mode. 46
Fig 5-14: Scanning electron photomicrograph showing baryte in cracks between quartz grains. Photomicrograph taken in backscatter electron mode. 46
Fig 5-15: Scanning electron photomicrograph of a zircon in Perdepoort Member. Photomicrograph taken in backscatter detection mode. 47
Fig 5-16: Scanning electron photomicrograph showing the overall composition of the Rooirand Member. Quartz commonly constitutes a large component of the sample. Brighter areas indicate different minerals which possess higher atomic numbers such as mica, oxides such as hematite and rutile. The very bright area in the middle of the photomicrograph indicates rare earth elements predominantly in the form of monazite. Photomicrograph taken in backscatter electron mode. 48
Fig 5-17: Scanning electron photomicrograph showing iron oxides filling a crack located at the edge of a sample of Rooirand Member rock. Photomicrograph taken in backscatter electron mode. 48
Fig 5-18: Scanning electron photomicrograph showing a lineation, possibly a bedding plane, formed by oxides and rare earth minerals (indicated by white lines). Photomicrograph taken in backscatter electron mode... 49
Fig 5-19: Scanning electron photomicrograph showing a rutile grain adjacent to a monazite surrounded by quartz, these oxides and rare earth minerals are more abundant in the quartzites of the Rooirand Member than the Perdepoort Member. Photomicrograph taken in backscatter electron mode... 49

Fig 5-20: Scanning electron photomicrograph showing another rare earth mineral which displaying a composition suggestive of monazite. Photomicrograph taken in backscatter electron mode 50
Fig 6-1: Magnified view of geological map. Zone 1 and 2 are indicated with black arrows and are separated by a line running from east to west, the positions of stations 1 to 8 are marked by red dots. 55
Fig 6-2: Cross sectional view showing the separation between zone 1 and 2 55
Fig 6-3: Aerial overview of part of zone 1. Contacts between lithologies are indicated as well as the position of station1. 57
Fig 6-4: The limb of a large overturned syncline is located towards the southern extent of the study area. The succession is Kweekvlei Formation (Dl), Perdepoort-(Dp) and Rooirand Member (Dr). The stratigraphic order is clearly reversed. 58
Fig 6-5: Stereogram showing contoured poles to bedding planes in the southern domain of zone 1. 58
Fig 6-6: Trough cross-bedding indicates that bedding is overturned in the southern extent of zone 1, thus confirming the position of an overturned syncline in zone 1; geological hammer for scale. 59
Fig 6-7: Stereogram showing poles to fold limbs of a large overturned syncline which forms the main macroscale feature in zone 1. 60
Fig 6-8:Top: Photo showing outcrop of Kweekvlei Shale Formation. Bottom: Cross-sectional overlay of Kweekvlei Shale Formation at station 1. Note complex structural relationship in the centre of the cross-section where a pop-up (A) structure and triangle zone (B) are present as a result of fore- and backthrust cut-off relationships. 62
Fig 6-9: Mineral laminations indication bedding (So) orientation in shales of the Kweekvlei Formation. Note southward dipping cleavage (S1) and possible wave ripple (WR). 63
Fig 6-10: Stereogram showing contoured poles to bedding planes at station 1. 64
Fig 6-11: Stereogram showing contoured poles to all fore-thrust planes measured at station 1. 65
Fig 6-12: Stereogram showing poles to all measured backthrust planes at station 1. 66
Fig 6-13: Stereogram showing trend and plunge of slickensides on all measured fore-thrust planes at station 1. 66
Fig 6-14: Top: Photo showing complex structural relationships towards the south-eastern end of station 1. Bottom: Structural features are highlighte. Note the duplex structure between F1, F10 and F11. Note anticline (Fo) towards the south-east appear to have been cut by F2 and F9. An inferred fault is indicated by F3?, and two backthrusts (Bt) are also present. 67
Fig 6-15:Top: Kweekvlei shale Formation showing showingimbricates joining roof thust Bottom: Structural features are indicated. F5 forms the roof thrust to a duplex structure situated at the north-western end of station 1. Multiple imbricates join F5 forming horse structures (h). Bedding orientation is indicated by So. The position of boudins is indicated by Bd; backpack, located on the bottom right of the frame, for scale. 68
Fig 6-16: High angle fore- and backthrust cut-offs form a pop-up structure (PU) and triangle zone (TZ). Slickensides record strike-slip as the most recent component of movement for F18 (X=eastward displacement, into page ●=westward displacement, out of page). 69
Fig 6-17: Stereogram showing poles to thrust fault plane F1. 70
Fig 6-18: Stereogram showing poles to thrust fault plane F4. 70

Fig 6-19: Stereogram showing poles to thrust fault plane F5. 71
Fig 6-20: Stereogram showing poles to imbricate thrust fault planes F16 and F17.......... 71
Fig 6-21: Stereogram showing poles to all measured backthrust planes at station 1........ 72
Fig 6-22: Strike-slip fault F18 is classified as a sinistral fault. The footwall block, located on the left of the photo, has clearly moved towards the left, relative to the hanging wall block. Slickensides are also indicated by coloured lines; geological hammer for scale. 73
Fig 6-23: Strike-slip fault F19 shows sinistral movement. Concretions c are also present on the fault plane; geological hammer for scale. The footwall block, located on the left of the photo, has clearly moved towards the left, relative to the hanging wall block. 73
Fig 6-24: Well developed slickenfibres sl associated with strike-slip fault F18. The relative sense of movement is indicated by arrows and slickensides are indicated by sl; pen for scale. 74
Fig 6-25: Stereogram showing poles to strike-slip fault plane F19. 74
Fig 6-26: Stereogram showing trend and plunge of slickensides on fault plane F19. 75
Fig 6-27: Stereogram showing poles to strike-slip fault plane F18. 75
Fig 6-28: Stereogram showing trend and plunge of slickenside on fault plane F18......... 76
Fig 6-29: Normal fault F9 cut through fault F8; geological hammer for scale................ 76
Fig 6-30: Well developed slickenfibres on fault plane F5. Red lines indicate last recorded phase of movement on the fault plane; pen for scale. 77
Fig 6-31: Mullions on what appears to be a bedding surface; geological hammer for scale. 78
Fig 6-32: Anticline Fo in Kweekvlei shale Fromation, blue lines indicate axial planar cleavage of Fo. 79
Fig 6-33: Stereogram showing poles to fold limbs of fold Fo. Axial plane is indicated by AP. 79
Fig 6-34: Stereogram showing poles to cleavage planes at station 1............................... 80
Fig 6-35: Rose diagram showing main joint strike directions at station 1....................... 81
Fig 6-36: Stereogram showing poles to joint planes at station 1. 81
Fig 6-37: Boundin train located in a competent layer of argillaceous strata. The red line indicates the separation of the brittle, competent layer from the underlying, relatively less competent layer; geological hammer for scale.............................. 82
Fig 6-38: Boudin train viewed from an upper angle. Host inflow is clearly visible and is indicated by h. Ductile or relatively less competent layers and remnants of these incompetent layers on boudin surfaces are indicated by d. Camera bag is an additional indicator of scale. 83
Fig 6-39: Aerial view delineating stations 2, 3 and 4 as well as the immediate surrounding geology and topography. An inferred strike-slip fault is indicated by F. The contacts between the Perdepoort- and Rooirand Member are also indicated. 85
Fig 6-40: Trough cross-bedding in Perdepoort Member close to station 3, confirms that bedding in the northern domain of zone 1 is right way up. Bedding is viewed end-on. 86
Fig 6-41: Rip-up clasts are outlined at the base of a bed, found in the vicinity of station 3; pen for scale. 86
Fig 6-42: Cross sectional overlay of the northern domain of station 2. Note numerous low angle fore- thrusts and subordinate backthrust. Abundant strike-slip faults are also present; X=movement into page, ●=movement out of page. 87
Fig 6-43: Stereogram showing poles to thrust fault plane F1. 88

Fig 6-44: Stereogram showing lineations on thrust fault plane F1. 89
Fig 6-45: Stereogram showing poles to thrust fault plane F2. 89
Fig 6-46: Stereogram showing lineations on thrust fault plane F2. 90
Fig 6-47: Stereogram showing poles to thrust fault plane F3. 90
Fig 6-48: Stereogram showing poles to backthrust plane F9. 91
Fig 6-49: Rose diagram showing orientations of strike-slip faults at station 2. 92
Fig 6-50: Stereogram showing poles to strike-slip fault planes at station 2. 92
Fig 6-51: Stereogram showing trend and plunge of slickenfibres on strike-slip fault planes F4 and F6. 93
Fig 6-52: Top: Folding in the Rooirand Member at station 2.Bottom: Blue lines indicate axial planes in cross-sectional view and surface extent is indicated in red........... 95
Fig 6-53: Stereogram showing poles to fold limbs of fold Fo1. Axial plane is indicated by AP. 96
Fig 6-54: Stereogram showing poles to fold limbs of fold Fo2. Axial plane is indicated by AP. 96
Fig 6-55: Stereogram showing poles to fold limbs of fold Fo3. Axial plane is indicated by AP. 97
Fig 6-56: Stereogram showing lineations on fold Fo1. 98
Fig 6-57: Sigmoidal shaped quartz veins fill tension gashes in rocks of the Rooirand Member. The approximate direction of σ 1 is indicated by the blue arrow; geological compass for scale. 98
Fig 6-58: South dipping rocks of the Rooirand Member. Note the distinctive red-brown surface colouration. 100
Fig 6-59: Stereogram showing contoured poles to bedding planes for station 3. 101
Fig 6-60: The southward dipping limb of a large mega-anticline that forms the main controlling structural feature in the northern sector of zone 1 (demarcated in red). Strata consist of rocks of the Rooirand Member. Station 3 is located towards the base of this outcrop. 101
Fig 6-61: Gorge opposite station 3. Note large amount of fractured angular boulders. Photo taken from the south, facing north. 102
Fig 6-62: Large open anticline in the northern half of zone 1 near station 3. Note near vertical dipping Perdepoort Member towards the south-west............................ 103
Fig 6-63: Main joints viewed from above. J1 and J2 show systematic close spaced jointing and are the dominant joint sets. J3 represents a less dominant joint set.103
Fig 6-64: Rose diagram showing strike direction of main joint sets at station 2 and 3. . 104
Fig 6-65: Stereogram showing poles to the main joint set planes at station 2 and 3. 104
Fig 6-66: Area of complex thrusting at station 4. A and B represent possible frontal and lateral thrust fault ramps and bt represents an exposed backthrust plane. The structures are viewed end-on looking from the north, facing south. 105
Fig 6-67: Cartoon cross-section depicting the main structural relationships at station 4. Fore-thrusts and backthrusts are indicated by the black lines and dip south (thick line) and north (thin line) respectively. 106
Fig 6-68: Stereogram showing contoured poles to backthrusts at station 4. 106
Fig 6-69: Photo of thrusting at station 4. Hangingwall blocks above fore-thrusts are envisaged as moving out of the page northwards and are demarcated by red lines and fault gouge (FG). Movement of the hangingwall blocks along backthrusts are towards the south (into the page). Possible frontal and lateral thrust fault ramps are indicated by A and B respectively; geological hammer for scale. 107
Fig 6-70: Stereogram showing orientation of slickenfibres on backthrust planes at station 4. 108

Fig 6-71: *Slickensided surfaces associated with backthrusting at station 4 indicate that the hanging wall has moved up (southward). Sense of movement of the hanging wall block is indicated by a red arrow; geological hammer for scale.* 108
Fig 6-72: The northern boundary of zone 2 is characterized by vertically dipping to overturned strata, associated with the northern limb of a large north verging anticline. 109
Fig 6-73: Aerial view of station 5 and 6 in zone 2. The contacts between the Perdepoort- and Rooirand Members are also indicated. Note a normal fault occurs in between station 5 and 6 (coloured in blue).. 110
Fig 6-74: Cross section of section studied at station 5. Note large amount of bedding parallel fore-thrusts and prominent normal faults the latter transecting all earlier formed faults. 112
Fig 6-75: Stereogram showing contoured poles to bedding planes at station 5............. 113
Fig 6-76: Trough cross-bedding, FD indicates facing direction; geological hammer for scale. 113
Fig 6-77: Rip-up clasts occurring at the base of a quartzite bed; pen for scale. 114
Fig 6-78: Stereogram displaying poles to thrust fault planes at station 5. 115
Fig 6-79: Stereogram displaying slickensides on all fore-thrusts at station 5................ 115
Fig 6-80: Inferred thrust fault F1 located towards the southern end of station 5; geological hammer for scale. 116
Fig 6-81: Inferred thrust faults F1 and F2. 117
Fig 6-82: Bedding parallel thrust faults F2, F3 and F4. 117
Fig 6-83: Top: Fault transects limb of an anticline; geological hammer for scale. Bottom: Structural featrures are highlighted. F7 cuts through anticline Fo2 and ends abruptly; geological hammer for scale. 118
Fig 6-84: Stereogram displaying poles to fault plane F7. 119
Fig 6-85: Top: Duplex structure. Roof-thrust F8 truncates multiple imbricates (imb) forming horse structures (h); backpack and geological hammer for scale. Bottom: Structures are highlighte in red. 120
Fig 6-86: Stereogram displaying poles to roof thrust plane F8..................................... 121
Fig 6-87: Stereogram showing slickenside orientation on roof thrust plane F8. 121
Fig 6-88: Stereogram showing poles to fault planes of imbricate faults in duplex......... 122
Fig 6-89: Top: Duplex structure displaying backthrusts cutting through earlier formed imbricates, F14 and F15. Roof thrust F8 truncates previously formed imbricates (imb). Bottom: Structures are highlighted in red. 123
Fig 6-90: Stereogram showing poles to normal fault plane F6..................................... 125
Fig 6-91: Stereogram showing slickensides on normal fault plane F6. 125
Fig 6-92: Top: A normal fault lies adjacent to a syncline. Bottom: Structures are indicated in red. Normal fault F6 clearly lies adjacent to a syncline Fo1. Bz highlights a brecciated fault zone resulting from normal faulting; geological hammer for scale. 126
Fig 6-93: Top: Inclined and folded bedding in the Perdepoort Member is cut by a normal fault. Bottom: From highlighted structures it is clear that thrust faults F3, F4 and F5, on the left (SW) truncate a syncline (Fo1) in the centre of the picture. Normal fault F6 located is located north of syncline Fo1. The axial plane of Fo1 is indicated by FP, and FZ indicates a highly brecciated fault zone associated with normal fault F6. 127
Fig 6-94: Normal fault F17 situated at the northern end of station 5 marks the end of the section. A broad zone of brecciated rocks BZ occurs adjacent to the fault F17, which cuts F8 and F16. 128

Fig 6-95: Stereogram displaying poles to fault plane of normal fault F17. 128
Fig 6-96: Stereogram displaying poles to bedding plane of syncline Fo1. AP indicates axial plane; plunge and trend of fold axis are also indicated. 129
Fig 6-97: Stereogram displaying poles to bedding plane of anticline Fo2. AP indicates axial plane plunge and trend of fold axis are also indicated. 130
Fig 6-98: Top: An anticline is cut by a normal fault. Bottom: Fold Fo4 is cut by normal fault F17 the fault geometry is distorted as a result of the angle the photo was taken at. 131
Fig 6-99: Rose diagram showing striking direction of the main joint sets at station 5... 132
Fig 6-100: Photo displaying bedding as well as two prominent jointing directions in the study section. 132
Fig 6-101: Stereogram showing poles to jointing planes at station 5. 133
Fig 6-102: Cartoon cross section showing main faults at station 6................................ 135
Fig 6-103: Sketch illustrating the position of section2 (demarcated with red) in relation to the mega anticline which forms the main mega scale feature in zone 2. 136
Fig 6-104: Stereogram showing poles to bedding at station 6. 136
Fig 6-105: Photo showing main faults (F1 to F6) at station 6 and thrust fault tF. 138
Fig 6-106: Stereogram showing poles to backthrust F5.. 139
Fig 6-107: Stereogram showing trend and plunge of slickenfibres on fault plane F5. ... 139
Fig 6-108: Well developed slickensided surface associated with backthrust F5, slickensides indicated by sl; pen for scale... 140
Fig 6-109: Stereogram showing poles to backthrust bt1.. 140
Fig 6-110: Stereogram showing poles to normal fault F1.. 141
Fig 6-111: Normal fault with large displacement located at station 6, zone 2............... 141
Fig 6-112: Close-up view of normal fault F1, note brecciated rocks demarcated by blue lines; geological hammer for scale.. 142
Fig 6-113: Stereogram showing trend and plunge of slickenfibres on fault plane F1. ... 142
Fig 6-114: Normal fault F2 transects earlier formed low angle thrust fault (tF); geological hammer for scale. 143
Fig 6-115: Stereogram showing poles to normal fault F3.. 143
Fig 6-116: Normal fault F3; geological hammer for scale.. 144
Fig 6-117: Well developed slickenside surfaces (sl) associated with normal fault F3; pen for scale. 144
Fig 6-118: Stereogram showing trend and plunge of slickenfibres on fault plane F3. ... 145
Fig 6-119: Normal fault F4 the sense of movement is clearly evident from the fault drag seen on the right of the photo; geological hammer for scale. 146
Fig 6-120: Stereogram showing poles to normal fault F4.. 146
Fig 6-121: Stereogram displaying slickenfibres on fault plane F4. 147
Fig 6-122: Normal fault F3b note displacement of marker bed indicated by red lines; geological hammer for scale. 147
Fig 6-123: Normal fault F4b; geological hammer for scale... 148
Fig 6-124: Normal faults F6 and F7 converge towards the bottom left of the photo, backthrust F5 is on the right side of the photograph; geological hammer for scale.149
Fig 6-125: Normal faults F6 and F7 viewed from a wider perspective. Displacement on F7 shows down to the south movement; geological hammer for scale.............. 149
Fig 6-126: Stereogram showing poles to normal fault plane F6.................................... 150
Fig 6-127: Stereogram showing poles to normal fault plane F7.................................... 150
Fig 6-128: A thin shale bed indicated by the red line has been “dragged” into fault F7; geological hammer for scale. 151
Fig 6-129: Stereogram showing poles to strike-slip faulting... 152

Fig 6-130: Rose diagram showing strike direction of main joint sets at station 6. 153
Fig 6-131: Aerial view showing the location of station 7 in relation to station 2 and 4 obtained from the Council for Geoscience. 155
Fig 6-132: Diagrammatic representation of station 6. The station is divided into 3 domains (D) and folds are indicated by Fo. Diagram sketched looking from the east, facing west. 156
Fig 6-133: Stereogram showing contoured poles to bedding planes in domain 1, station 7.157
Fig 6-134: Stereogram showing contoured poles to bedding planes in domain 2, station 7.157
Fig 6-135: Normal fault F1 lies between nearly vertical to overturned bedding (So) and a large brecciated zone Bz. Photo taken looking from the west, facing east; Josepha Zielke for scale. 158
Fig 6-136: Thrust faults F4 and F5 are cut by two normal faults F2 and F3, photo taken from the east, facing west; Josepha Zielke for scale. 159
Fig 6-137: Stereogram displaying poles to fault plane of backthrust F5. 160
Fig 6-138: Normal faults F2 and F3 cut earlier formed thrust faults F4 and F5 in domain 2, photo taken from the west, facing east; Josepha Zielke for scale. 160
Fig 6-139: Stereogram showing poles to fault planes of all north (foreland) verging normal faults at station 7. 161
Fig 6-140: Stereogram showing poles to fault planes of north dipping normal faults F2 and F3 at station 7. 162
Fig 6-141: Stereogram showing poles to normal fault plane F1. 162
Fig 6-142: Normal fault F1 viewed from the east. Brecciated zone (Bz) is most prominent when viewed from the east, facing west; Josepha Zielke for scale. .. 163
Fig 6-143: Normal faults F6 and F7 located in domain 2. Photo taken from the east, facing west; Josepha Zielke for scale. 163
Fig 6-144: Stereogram showing poles to normal fault plane F6. 164
Fig 6-145: Stereogram showing poles to normal fault plane F7. 164
Fig 6-146: Anticline, syncline occurring together, fold Fo1 and Fo2 viewed from the west facing approximately east. Blue lines indicate axial planes. 165
Fig 6-147: The main joint J1. Photo taken on top of bed. Geological compass for scale.166
Fig 6-148: Rose diagram showing strike directions of main joint sets at station 7......... 166
Fig 6-149: Top: Large exposure of Rooirand Member rocks located at station 8. Bottom: Overlay of structural features in the outcrop... 168
Fig 7-1: Major element Spider diagram of samples from the Perdepoort Member. Samples in red are the data obtained from S. Frost-Killian (Council for Geoscience) and those in blue are from this study. All concentration are normalized against material from upper continental crust (green line) (McLennan, 2001; as cited in Rudnick & Gao, 2003).. 174
Fig 7-2: Spider diagram showing relative concentration of trace elements in the study. Samples located near normal fault zones are all indicated in red lines and dots, all other samples are indicated in blue, these include samples from both Perdepoort- and Rooirand Members. All concentration are normalized against material from upper continental crust from Taylor and McLennan (1982) as recommended by Rollinson, (1993).. 176
Fig 7-3 : Spider diagram showing relative concentration of trace elements in the study. Samples from the Perdepoort Member are indicated in blue and from the Rooirand Member in red. All concentration are normalized against material from upper continental crust from Taylor and McLennan (1982) as recommended by Rollinson, (1993).. 178
Fig 7-4: Diagram showing the main joint planes orientations associated with folding. The

fold has been orientated according to the overall folding regime in the study area.(After Bell, (2007)).. 184
Fig 7-5: Rose diagram showing strike orientations of all joints in the structural study area. 184
Fig 7-6: Diagram illustrating the shape of and the forces experience by boudins at station 1….. 185

List of Tables

Table 2-1: The typical chemical composition (in weight %) of selected South African silica products (Agnello, 2004). 6
Table 2-2: Typical silica concentrations of deposits and mines around RSA (data extracted from Oosterhuis(1998). 6
Table 2-3: Typical impurities found in metallurgical grade silicon (Green, 1982). 9
Table 3-1: Stratigraphy of the Witteberg Group in the Eastern Cape east of 21°E after Thamm and Johnson(2006) and SACS (1980). The lithologies that crop out in the structural study zone have been shaded. 21
Table 4-1: Fold classification, after Fleuty, (1964). 30
Table 5-1: Composition of minerals scanned using energy dispersive spectroscopy. All values are in weight percentage. 41
Table 5-2: Composition of minerals scanned using energy dispersive spectroscopy. All values are in weight percentage. 42
Table 5-3: The mean weight percentages and standard deviation of major elements and loss on ignition (H_2O) in samples from the Rooirand- and Perdepoort- Members (from XRF data). 51
Table 5-4: Major elements found in Perdepoort- and Rooirand Member samples. All values are in weight percentage. 52
Table 5-5: Correlation matrix of major elements. 53
Table 5-6: Correlation matrix of major and trace elements. 53
Table 5-7: Correlation matrix of all trace elements. 54
Table 7-1: *XRF analysis of nine samples from the Perdepoort Member, obtained from S. Frost-Killian from the Council for Geoscience.* 173
Table 7-2: Chronological description of believed tectonic evolution of the study area. 186

1. Introduction

This project was initiated at the beginning of 2008 for the main purpose of identifying suitable lithological units in the vicinity of the Nelson Mandela Bay Metropole (NMBM), for extraction of silica to be used in the manufacturing of solar cells. The two most important points to consider when sourcing suitable silica are grade and location.

Generally silica sold to the market place in its various crude or processed forms possesses a purity of at least 98% quartz or higher (Agnello, 2004). For the electronics industry, which includes solar technologies, an even higher grade source material is required (Oosterhuis, 1998). The quartz source should have at least 99.5% SiO_2 and a Fe_2O_3 content of less than 0.04-0.08%. This raw material is converted into a chemical grade quartz, then a halide or halosilane, which is in turn converted to high-grade silicon (Fig 2-2) (Oosterhuis, 1998).

The geographical position of a silica mine is of great importance. This was highlighted in the review by Agnello (2004) who indicated that 87% of silica mines or millers were located within a 65km radius of their target market.

In the near vicinity of the NMBM rocks of the Cape Supergroup are potentially the most suitable for purposes of this study as they contain an abundance of quartz rich rock units (quartz arenites). In the Cape Supergroup the lowermost (Table Mountain Group) and uppermost (Witteberg Group) rock units have by far the best developed quartz arenites. Although the Table Mountain Group has potentially suitable horizons of high silica content, which also merit further study they occur mostly in the urbanized zones of Port Elizabeth and Uitenhage. Strata from the Witteberg Group are situated outside urban development zones, yet close enough to the Coega Industrial Development Zone to be exploited. These factors are directly related to grade and location and thus received greatest consideration when selecting a site for study regarding potential silica extraction.

Accessibility, although a minor consideration in terms of potential future industrial development, was a major consideration for the researcher. The study site was thus chosen for the following reasons:

- Strata form the Perdepoort Member in the Witteberg Group was targeted as it has been described by many authors as a clean white quartz arenite and is considered to possess a high SiO_2 purity.
- The chosen area exhibits good outcrops of Witteberg Group rocks.
- The study site is situated 30 km west of Kirkwood in close proximity to the Nelson Mandela Bay Metropole.
- The study site is located in an area showing minimal urban development unlike areas were the TMG crops out.
- The study site has good accessibility in the form of gravel roads and a small railway station, located on the main rail between Port Elizabeth and the Coega IDZ.

This study commenced in 2008 with field work involving mapping and sample collection for thin section analyses, as well as collecting structural data for structural analysis. Sampling of rock units chosen for geochemical analyses took place during 2009, and samples were analysed at the Council for Geosciences laboratories in Pretoria. The purpose of this approach was to demarcate the lateral and vertical extent of suitable quartz-rich horizons in order to understand their 3-D geometry brought about by deformation during the Cape orogeny some 300 My ago. Samples suspected of containing a high SiO_2 content could then be analysed geochemically, and compared to zones containing higher levels of added impurities such as iron and carbonate. These occured most frequently in areas of faulting thus suggesting these areas could be avoided in possible future sampling. Thus an area 30 km west of Kirkwood (measuring some 25 km2), and spanning the Witteberg Group, was chosen as the study site.

1.1 Aims

The aims of this study are to:

- Give a descriptive account of lithologies of the Witteberg Group as well as outlining their regional distribution in the study area.
- Give a structural analysis of folds and faults in the study area as a foundation for understanding the 3-D distribution of strata (especially SiO_2 rich horizons). Such an analysis will provide a better understanding of the modification of strata brought about as a result of the Cape Orogeny.
- Integrate mineralogical, geochemical and structural data in order to provide a framework from which suitable horizons could be targeted for the production of solar cells at an extraction plant planned for the future in the IDZ.

2. Silicon Literature review

2.1 Introduction

In 1954 the front page headlines of the New York Times and Wall street journal read, ”Vast Power of the Sun is Tapped by Battery Using Sand Ingredients”, the first efficient solar cell had been developed (Green, 2001). The demand for solar cell technology has since grown exponentially (Green, 1982).

This chapter will briefly outline the characteristics of solar cell technology, production and raw materials, as well as some general information regarding the silicon industry.

2.2 Mining and Industry

Silicon in its purest form is required for manufacturing photovoltaic cells (Ontario, 2000). In nature, however, it never occurs in its elemental form but rather bonds with oxygen forming the tetrahedral quartz molecule (SiO_2) Although quartz is a fairly common mineral in the earth‟s crust, 66.62% according to Rudnick and Goa (2003), economically viable deposits are fairly scarce. Typically mineral deposits occur as sand, quartzites, sandstone, massive quartz as in veins and pegmatites, quartz crystals as formed in vugs or cavities and silcrete (Lang, 1991, as cited in Oosterhuis, (1998)).

The principal sectors or divisions in the silicon market are chemical, metallurgical and electrical (Oosterhuis, 1998). Ten global industrial sectors are involved in the production chain of semiconductor grade silicon (Hashim, 2003). These include industries such as, coal, charcoal, silicon metal, chlorosilane compounds (used in silicon purification), polycrystalline silicon (polysilicon), semiconductor devices, solar cells and optical fibres (Fig 2-2) (Hashim, 2003). The exports of silica from the Republic of South Africa grew by 36% year on year in the period 1995 to 2004 (Agnello, 2004).

In the last decade or so, world solar cell production has increased rapidly with an annual average growth rate of 30% (Zhao, 2004). This emphasizes the demand for semiconductor silica as well as silicon for other industries (Agnello, 2004). Despite this fact solar cell technology in RSA only makes-up a minute amount of the total market and forms part of the portion designated as “other” in Fig 2-1. One can thus clearly see that solar cell silicon is a highly specialized industry.

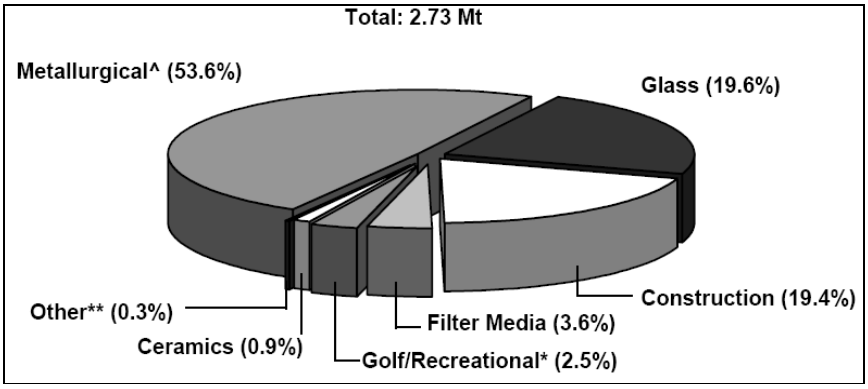

Fig 2-1: Pie chart showing a detailed breakdown of markets for all silica products in RSA in the year 2003 (modified from Agnello, 2004).

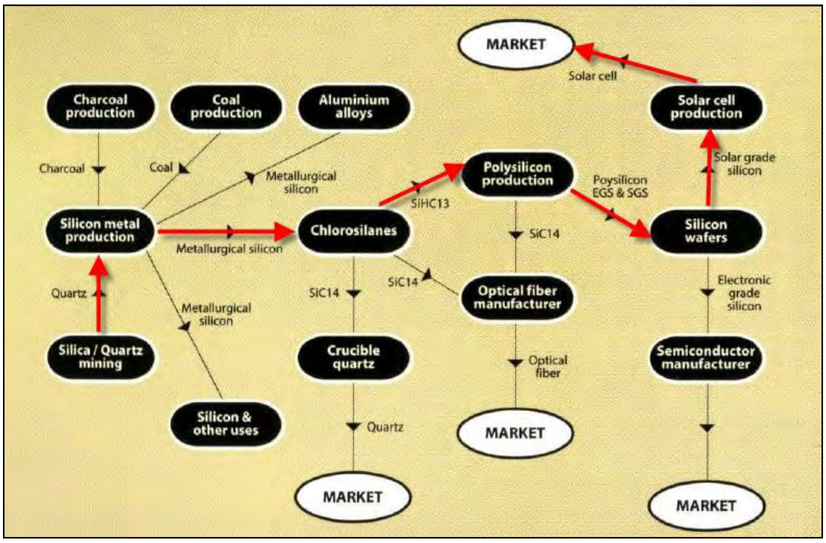

Fig 2-2: Diagram illustrating the production chain and interconnectivity of various silica end-products, the production line of solar cells is highlighted in red (after (Hashim, 2003).

The typical chemical compositions and SiO_2 content of essayed South African mines is presented in Table 2-1 and Table 2-2 respectively. The majority of silica sources in these tables show SiO_2 concentrations greater than 98% but most of these deposits would be unsuitable for use in solar cell production, as they fall below the suggested 99.5% SiO_2 purity (Oosterhuis, 1998). It is thus evident that silica sources of such high quality are extremely rare.

Table 2-1: The typical chemical composition (in weight %) of selected South African silica products (Agnello, 2004).

Chemical composition	Local producers** / mines													
	B & E Silica, Delmas Mine	Bronx Mine, amber glass	Consol Limited Glass sand	Donkerhoek Quartzite	Eggo Sand B3	Fine Industrial Minerals	Garieb Minerale, Silica 325[1]	B & E Silica, Spitskop Mine	Idwala Industrial Minerals	Silicon Smelters (Invensil)	Noel Lancaster Sands – dry	Pegmin – Milled, 200 mesh	Samquarz, D13 28/310	Container glass SiO_2 specs
SiO_2	99.1	99.2	99.7	98.1	99.6	98.5	99.2	97.4	99.8	99.5	97.8	99.3	99.5	>99.5
Al_2O_3	0.4	0.2	<0.1	0.9	0.0	0.8	0.1	0.9	<0.1	<0.1	0.8	0.3	<0.1	<0.1
Fe_2O_3	0.5	<0.1	<0.1	0.2	<0.1	0.1	0.1	0.5	<0.1	<0.1	0.4	<0.1	<0.1	<0.1
CaO	<0.1	0.1	<0.1	0.0	<0.1	<0.1	0.1	0.0	<0.1	<0.1	0.2	<0.1	<0.1	0.1
Na_2O	<0.1	0.0	na	0.0	0.0	<0.1	0.1	0.2	<0.1	na	na	<0.1	<0.1	<0.1
MnO	<0.1	<0.1	na	0.0	0.0	0.0	<0.1	na	<0.1	<0.1	na	na	<0.1	<0.1
MgO	<0.1	0.0	<0.1	0.2	0.0	<0.1	0.0	<0.1	<0.1	<0.1	0.1	na	<0.1	0.1
Moisture	na	na	<0.1	na	na	<0.3	0.0	na	na	na	0.5	na	5	na
LOI	<0.1	0.2	0.2	na	0.1	0.3	0.3	na	<0.1	na	0.8	0.2	<0.1	<0.3

Table 2-2: Typical silica concentrations of deposits and mines around RSA (data extracted from Oosterhuis(1998).

Deposit/companies	**SiO_2 wt %**
Inyoku farm pegmatite	99.8
SAMANCOR Ltd.	99.5
Tubatse Ferrochrome	97.84
Spitskop quarry	98
Iscor Ltd. quarry Donkerhoek	95
Nababeep Kloof silica quarry	92-95
Consol Glass Ltd. Philippi quarry	99
Graded Sands (Pty) Ltd.	99.5
Timeball Hill quartzite	99.36
Waterberg sandstone near Nylstroom	98.56
Wonderfontein farm	95.55

It is clearly seen in Fig 2-3 that nearly all active silica mines are located close to major industrialized zones or trade centres. The majority of these mines are located in the Western Cape, Gauteng and Mpumalanga, rich in industrial infrastructure, with minor operations located near Mossel Bay in the Western Cape and Port Elizabeth in the Eastern Cape.

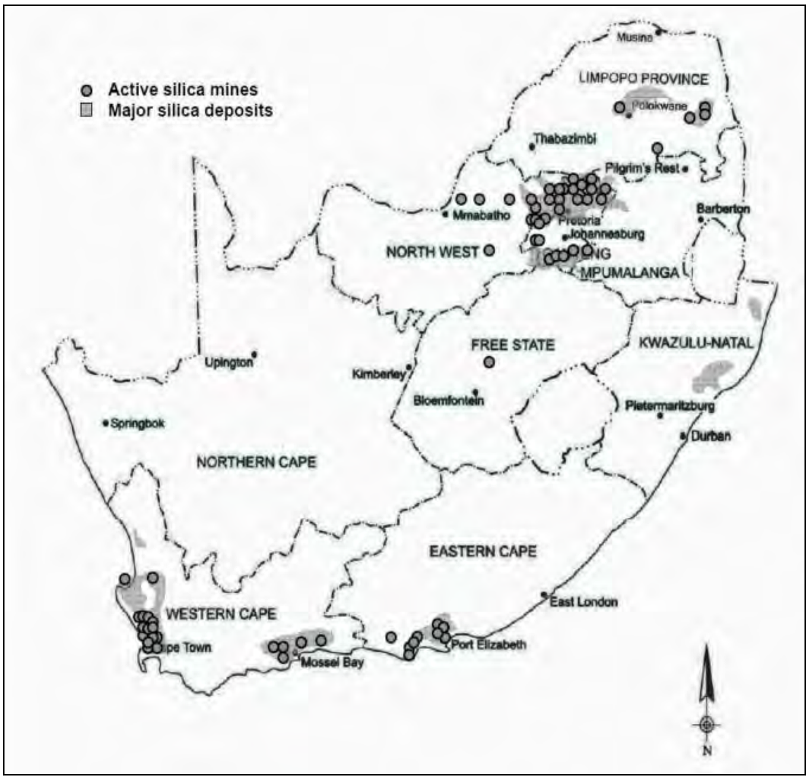

Fig 2-3: The distribution of silica mines and deposits in South Africa (Agnello, 2004).

2.3 Why silicon

According to the work of Green, (1982, 1987, 2001) a solar cell and its functions can be summarized as follows (Fig 2-4):

In basic terms a solar cell converts energy from the sun, photon energy, into an electrical current. Photon energy is converted into electrical energy when electrons, excited into higher energy levels by photon energy, make transitions from these higher energy levels to lower energy levels.

Solar cells are primarily composed of silicon, minor constituents include, boron, phosphorous, arsenic, carbon and several other impurities present in minute amounts. Silicon is part of a group of elements that are known as semiconductors. The crystal lattice arrangement of silicon possesses the *diamond lattice* configuration. This configuration allows for an electron to undergo a transition from a higher energy level to a lower energy level and vice versa. Silicon strongly absorbs short wavelength light thus its optical properties are also highly favourable for use in solar cells (Green, 1982). At these short wavelengths photons produce enough energy to excite an electron directly from a densely occupied valence band, into a sparsely occupied conduction band (Green, 1982).

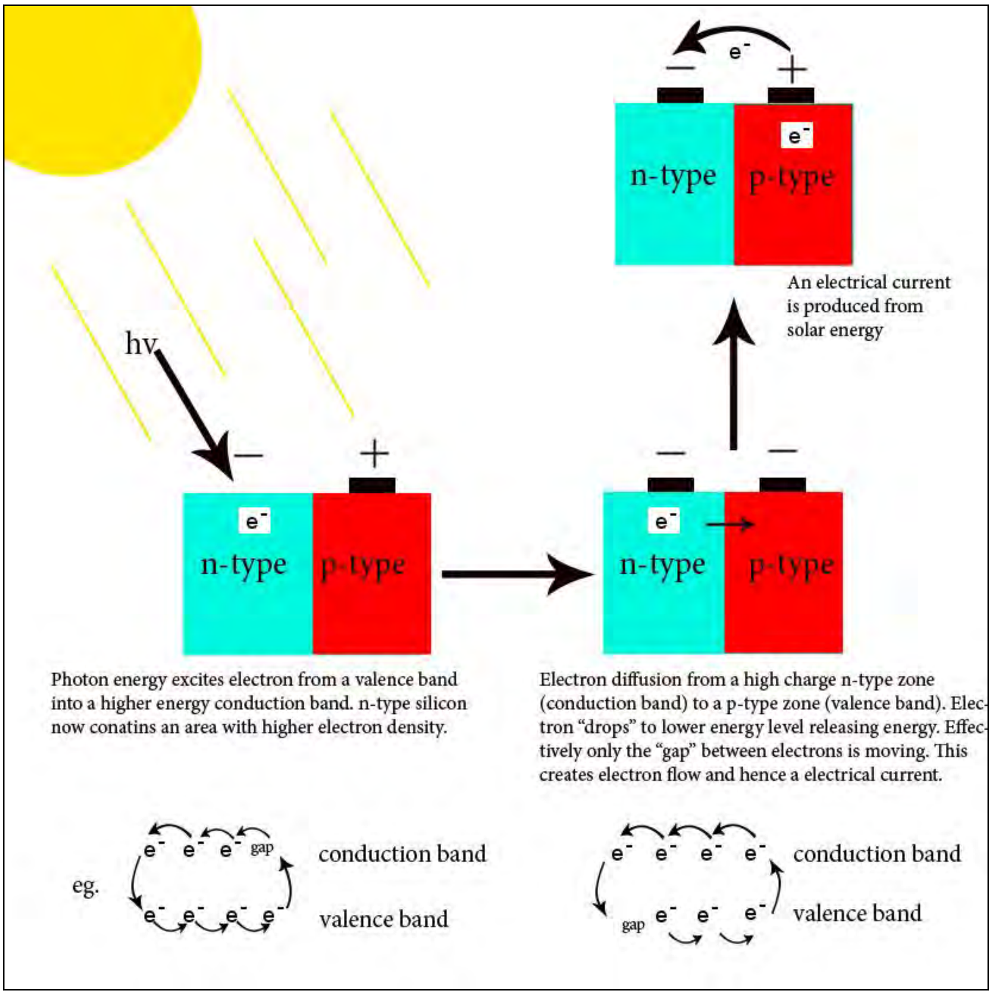

Fig 2-4: Simplified diagram displaying the process by which a solar cell converts photon energy into electrical energy.

2.4 Production of solar cell

The standard technology for solar cell production can be divided into 5 steps and is summarized in Fig 2-5:

- Reduction of raw materials such as sand and quartzite to metallurgical-grade silicon (MGS). The silicon produced in this process tends to be 98-99% pure with major impurities being Fe and Al (Green, 1982). The typical impurities for MGS can be seen in Table 2-3.

Table 2-3: Typical impurities found in metallurgical grade silicon (Green, 1982).

Impurity	Concentration range in ppm
Al	1500-4000
B	40-80
Cr	50-200
Fe	2000-3000
Mn	70-100
Ni	30-90
P	20-50
Ti	160-250
V	80-200

2.5 Summary statement

To conclude is it is clear from the literature review that the natural occurrences of SiO_2, suitable for use in the silicon industry, are rare. Most sources of SiO_2 contain large proportions of impurities such as Fe, Mn, P and S, which hamper the efficient operation of solar cells. However the beneficiation of silica ore firstly to produce MGS and thereafter through the processes of fluidization with HCl and fractional distillation may produce purity levels which are acceptable in the solar industry

Fig 2-5: The process of solar cell production from quartzitic sand to solar cell adapted from Perry (1998)

3. Geology Literature review

3.1.1 Cape Supergroup

The Cape Supergroup geology has been extensively reviewed by Thamm and Johnson, (2006). A brief overview of this review together with work by other authors is presented below.

Sedimentation commenced during the late Proterozoic to early Paleozoic extension following the Pan-Gondwanean, Saldania orogeny. The silica-clastic Cape Supergroup was deposited in a passive continental margin basin over a period of ±160Ma from the Early Ordovician ±490 Ma to Early Carboniferous ±330 Ma, in which time up to 10km of strata were preserved. Depositional environments ranged from aeolian to fluviodeltaic to shallow marine (Tankard *et al.*, 2009). The Cape Supergroup consists of three subdivisions, from the base to the top, the lower Table Mountain Group (TMG), the Bokkeveld Group, and the Witteberg Group (Fig 3-1).

Group	Age (Ma)	Lithologies	Palaeoenviroments
Witteberg	Devonian (±375 Ma) - Carboniferous (±330 Ma)	Equal mix of sandstone (quartzites) and shale with a minor diamictite.	Offshore marine shelf, beach, fluviodeltaic.
Bokkeveld	Early Devonian (±390 Ma) – Middle Devonian (±375 Ma)	Mostly siltstones and shale with less sandstone.	Offshore shelf, tidal flat , delta front, distributary channel.
Table Mountain	Ordovician (±500 Ma) – Devonian (±330 Ma)	Almost entirely sandstone with only minor shales and a diamictite.	Offshore shelf, tidal flat, fluvial braid plain and minor glacial.

Fig 3-1: The main Groups, lithologies and depositional environments in the Cape Supergroup (Thamm & Johnson, 2006).

The lowermost Table Mountain Group overlies the pre-Cape Group and consist mainly of arenaceous strata with quartz arenites making up the bulk of this Group.

The argillaceous strata of the Bokkeveld Group conformably overlies the TMG reaching a maximum thickness of 3000m (SACS, 1980). The Bokkeveld Group is envisaged as an off-lapping southward-thickening sequence, deposited in southward migrating deltaic environments, consisting almost entirely of shales (Broquet, 1992).

The Bokkeveld Group is conformably overlain by the Witteberg Group which ranges in thickness from 1100m-2200m and contains roughly equal amounts of sandstone and mudrocks (Broquet, 1992). A specific section will be dedicated to the Witteberg Group as this study focussed on strata within this Group.

The end of the Witteberg era during the Early Carboniferous marks the end of Cape sedimentation (Cole, 1992). This was followed by a lacuna of approximately 30 Ma as a result of either crustal uplift or lowering in sea level as an after effect of Dwyka glaciation in the Permo-Carboniferous (Visser, 1992).

3.1.2 Gondwana Tectonism

The late and post Precambrian events along the southern margin of Gondwana can be summarized by two first-order episodes of compression and extension spanning ±600Ma (de Wit & Ransome, 1992 b):

- The Pan-Gondwanean convergence 650 ±100Ma,
- the late Proterozoic to early Palaeozoic extension 500 ±100Ma,
- the late Paleozoic convergence 300 ±100Ma,
- and the Mesozoic extension 150 ±50 Ma.

It is during the late Paleozoic convergence, shortly after the end of Cape Supergroup deposition, that Cape folding was initiated affecting mainly the strata of the Cape Supergroup but also strata of the pre-Cape Group and lower parts of the Karoo Supergroup.

It should however be pointed out that although the effects of these Palaeozoic events are clearly visible, there have been many arguments regarding the exact model of deformation. Over the last 4 decades several authors have put forward various tectonic models to explain the formation of the Cape Fold Belt, each of these models will be discussed briefly.

3.1.3 Models for Cape Fold Belt formation

(i) Gravity slip

Newton, (1973) proposed a model based on vertical tectonics rather than conventional orogenic tectonics (Fig 3-2). Uplift occurred towards the south and west of the Cape Fold Belt due to a series of faults, which were upthrown towards the south. The author suggests it was either caused by the weight of the overlying sediments or a bulge in the mantle. This relative uplift resulted in sediments sliding over step-like fault blocks of pre-Cape basement descending on a palaeoslope towards the north. This gravity sliding of strata resulted in the deformation of the Cape Rocks and its characteristic overfolding. The Cape syntaxis is envisaged as a convergence between the eastward and northward flowing sedimentary masses.

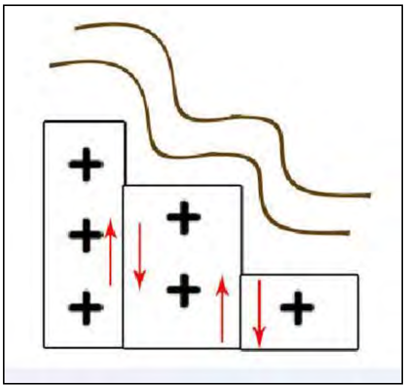

Fig 3-2: Simplified cross-section illustrating Newton's gravity slip model for the formation of the Cape Fold Belt. One can clearly see cover rocks sliding over basement rocks that have experienced normal faulting, adapted from Booth (2009).

(ii) Conventional Subduction Models

A model of conventional plate tectonics is put forward by de Beer *et al.,* (1974). This model explains geophysical anomalies such as the Southern Cape Conductive belt, Beattie magnetic anomaly, and a negative anomaly in the southeastern Cape. This theory suggests that Gondwana was underthrusted by an oceanic plate and later experienced a continental collision resulting in orogeny.

(iii) Alpine model

The model proposed by de Swardt and Rowsell (1974) suggests that the Cape Fold Belt was formed by gravity sliding of cover rocks over a more rigid basement. A median zone of uplift is thought to have facilitated this gravitational gradient. The model is similar to that of an Alpine type deformation. Folding and thrusting is seen as verging away from this median zone with basement becoming involved at a later stage.

(iv) Collision Model and Andean model

A collision type model is put forward by de Wit and Ransome (1992a), in which the authors suggest that a collision of microplates during the Late Precambrian formed the two different branches of the Cape Fold Belt (Fig 3-3). The model explains the syntaxis forming as a result of a rotation of these microplates. The model is essentially a modified version of the Andean subduction model. The authors believe this to be one of the more plausible models as it best explains the deformation in the southern branch of the fold belt as well as the presence of volcanics in the Karoo Supergroup.

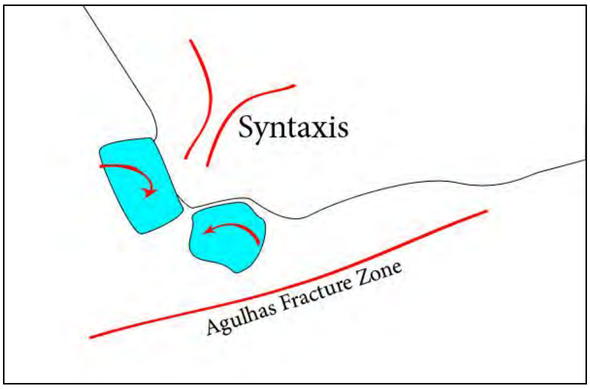

Fig 3-3: Simplified illustration of the microplate collision model put forward by de Wit and Ransome (1992a) .The rotation of two microplate is emphasized as forming the syntaxis zone, adapted from Booth (2009).

(v) Flat-plate Subduction

Lock, (1980) suggested that a Proto-African plate collided and fused with the south-western margin of Gondwana at the position of the present day southern coastline of Africa (Fig 3-4). The resultant subducted oceanic lithosphere caused major stresses at the leading edge of the proto-African plate. The fused plates continued to converge causing major friction, which resulted in tectonic deformation, shortening, and the eventual formation of the CFB (Rhodes, 1974). The fusing of the subducted oceanic plate with the proto-African plate would explain the lack of any significant volcanic activity during the formation of the Cape Fold Belt. It is also suggested that a subduction zone formed some 1000km south-east of the present day coastline.

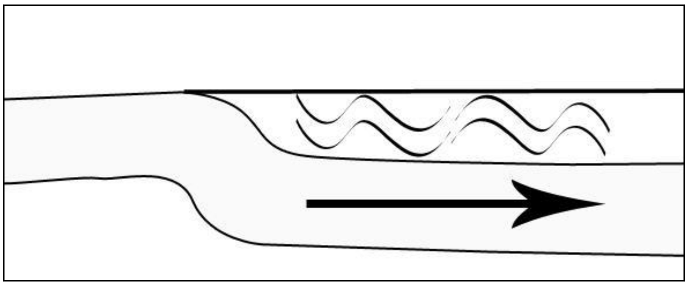

Fig 3-4: Simplified illustration showing Lock's 1980 flat plate subduction model, adapted from Lock ,(1980).

(vi) Ensialic model

Hälbich, (1983) proposed an ensialic model in which extension occurred normal to the basin axis resulting in crustal thinning and the formations of grabens. Rising mantle convection currents resulted in the formation of an aulacogen, into which terrigenous sediments were deposited. Tectonic shortening occurred at the northern extent of the graben, where faults show a decreased dip. The deformation is seen as a multiphase deformation resulting in thinning within the crust.

(vii) Transpression model

Johnston, (2000) presents a dextral transpression model for the development of the Cape Fold Belt (Fig 3-5). In this model the author proposed that the Cape Fold Belt forms the east-west trending inboard step in a larger northwest-trending dextral intracontinental transpression belt. The dextral movement in this model would also adequately explain en echelon folds and faults as well as suspected flower structures in the Karoo (Booth, 2009).

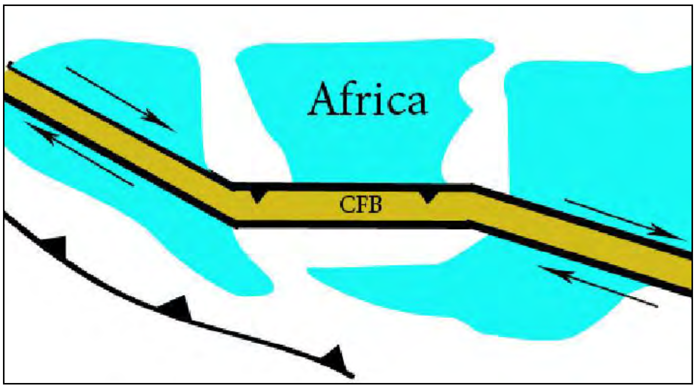

Fig 3-5: Johnston's transpression model sees the margin along the Cape Fold Belt (CFB) as an east-west trending inboard step in a larger intracontinental transpressional belt, adapted after Johnston, (2000).

Futhermore when taking into account the arcuate geometry of the later formed Mesozoic basins of southern Africa it can be argued that these follow the so-called grain of the Cape Fold Belt. This earlier work lends further support to Johnston"s transpression model. (Martin *et al*., 1981 as cited in Fouche *et al*., 1992).

3.1.3.2 Conclusion to models

The absence of a number of features expected in the case of an ideal orogenic belt should be kept in mind when considering any model put forward to explain the formation of the Cape Fold Belt (Hälbich, 1983). Models need to account for the absence of any significant igneous activity in the cover rocks, lack of carbonate rocks, lack of ocean floor derivatives, the relatively low grade of regional metamorphism, and the asymmetric nature of the fold belt.

3.1.4 Cape Fold Belt Tectonism

3.1.4.1 Cape Fold Belt Paroxysms

Despite all the differences that exist in the models that attempt to explain the Cape Fold Belt formation, authors agree that it was formed as a result of the four northward directed compressions (Tankard *et al.*, 2009). Hälbich *et al.*, (1983) made great strides in unravelling the timing of orogenic events in the Cape Fold Belt. Hälbich et al., (1983, 1992) found that during the Cape Orogeny four cycles of compressions coupled with an extension have deformed strata involved in the Cape fold belt. Broadly the deformation of the Cape Fold Belt has been described as a single phase of orogeny, with multiple events or paroxysms effecting multiple Groups and Supergroups.

(i) 1st Paroxysm Swartberg folding 278 ± 2Ma

This first phase of deformation in the Cape Fold Belt propagated through a flexure-slip mechanism and resulted in the formation of the Kango Anticlinorium and proto-Swartberge. Hälbich, (1983) suggests that contacts with high deformability contrasts formed large décollements thus facilitating an estimated 35% shortening through mechanisms such as northward overfolding. Temperatures are believed not to have exceeded 300°C (Hälbich *et al.*, 1983).

(ii) 2nd Paroxysm Outeniqua folding 258 ± 2Ma

The second phase resulted in the formation of isoclinal, almost recumbent, structures formed by northward overfolding in the Outeniqua Range (Hälbich *et al.*, 1983). The George Anticlinorium formed in this phase resulting in further horizontal shortening (Hälbich, 1983).

(iii) 3rd Paroxysm crenulations cleavage 247 ± 3Ma

The third compressive stage is represented by steeply southward dipping crenulation cleavage (Hälbich *et al.*, 1983). This event is envisaged as forming asymmetric megafolds which extend into the lower Beaufort sequence and semi-lithified Ecca beds. This is believed to be as a result of décollement in the basement or basement cover (Hälbich, 1983) .

(iv) 4th Paroxysm kink banding 230 ± 3 Ma

Kink bands and minor shears formed as a result of the last north-south compression (Hälbich *et al.*, 1983). Low amplitude, near upright folds, bear testimony to the last compressive event (Hälbich *et al.*, 1983).

(v) 5th Paroxysm relaxation 215 ± 5Ma

The final phase of deformation of the Cape Fold Belt took place along east-west trending normal faults, and according is closely associated with a set of tensional kinks (Hälbich, 1983, 1992).

3.1.5 Break-up of Gondwana

The last phase of tectonism experienced by the Cape Supergroup is the Mesozoic extension and break-up of Gondwana and is thought to have started in the Late Jurassic or Early Cretaceous. It is considered the last phase of tectonism in the Cape Fold Belt although still partially assisted with movement along the Agulhas Falkland Fracture Zone. (Booth *et al.*, 2004, Booth & Shone, 1999, Broad *et al.*, 2006, Dingle *et al.*, 1983, Fouché *et al.*, 1992, Shone, 2006, Watkeys, 2006). The break-up of southern Gondwana is considered as a two-fold process involving continental rifting followed by continental drift (Fouché *et al.*, 1992, Watkeys, 2006). The relaxation of the Cape Fold Belt can be attributed to episodes of rifting and reactivation of the older structures thought to have been initiated in the last phase or 5th paroxysm of deformation in the Cape Fold Belt (Fouché *et al.*, 1992). Fouche *et al*., (1992) have identified at least 5 episodes of both positive and negative inversion in the Bredasdorp basin since the initiation of rifting. Tankard et al., (2009) postulates that the Mesozoic Basins formed as a result of strike-slip extensional forces resulted in dextral movement along the Agulhas shear zone. This is thought to have been a result of reactivation along the Cape Fold Belt transverse zone. Strike-slip faulting identified by Booth *et al*., (2004) in the eastern sector of the Cape Fold Belt appears to be linked to the Agulhas Fracture zone which is in keeping with the general pattern of late fault development along the southern margin of Africa. These events resulted in the formation of a series of Mesozoic graben and half-graben basins developing along the southern margin of Gondwana, of which the local Algoa Basin is the largest (Broad *et al.*, 2006, Shone, 2006). Cretaceous faulting continued well into the Tertiary (Hälbich, 1992).

3.1.6 Patterns of folding and faulting in the Cape Fold Belt

The Cape Fold Belt can be divided into two branches, a western branch of open upright, megafolds, monoclines and normal faults striking roughly N-S, and a southern branch of northward verging asymmetric often overfolding folds striking approximately E-W (De Villiers, 1944, Shone & Booth, 2005, Söhnge, 1983). In the southern branch folds becomes tighter as one moves further south in the general direction of the coastline (De

Villiers, 1944, Shone & Booth, 2005, Söhnge, 1983). The southern branch is of particular interest in this study as the study area forms part of it. The southern branch extends from the Cape syntaxis to the mouth of the Fish River (De Villiers, 1944, Johnston, 2000).

The southern branch of the Cape Fold Belt is characterized by higher deformational intensity compared to the western branch, as indicated by first order north verging recumbent folds and abundant second order folds (de Beer, 1995). Second order folds are more intense compared to first order folds and appear to have been formed by an earlier event (Hälbich, 1992). These folds appear to be a result of disharmony and decoupling especially within the Nardouw Subgroup, which resulted in superimposed second order recumbent folds on north verging normal limbs of large anticlinoria (Gresse *et al.*, 1992).

Small northward bedding inversions are common in the southern branch of the fold belt and several authors have recognised thrusting as a major feature in the southern branch of the Cape Fold Belt, not only on a mesoscale but also on a megascale (Booth, 2002, Booth *et al.*, 2004, Booth & Shone, 1992, Booth & Shone, 1999). In the eastern sector duplexing is seen as the main formation mechanism of the Cape Fold Belt with the resultant thrust stacking hampering any stratigraphic study and determination of true bedding thicknesses (Booth *et al.*, 2004).

3.2 Study Area

3.2.1 The Witteberg Group

3.2.1.1 Lithostratigraphy

The argillaceous strata of the Bokkeveld Group are conformably overlain by the more arenaceous strata of the Witteberg Group (Booth *et al.*, 2004). The total thickness of the Witteberg Group in the eastern sector is thought to exceed 2200m (SACS, 1980). Within the Eastern Cape the Witteberg strata can be divided into the lower Weltevrede- and Witpoort Formations and two overlying Subgroups, the lower Lake Mentz - and upper Kommadagga Subgroups (SACS, 1980). The Weltevrede Formation in the Eastern Cape is the equivalent of the Weltevrede Subgroup encountered in the Western Cape to the west of 21°E (SACS, 1980). The resistant white and brownish quartzites of the Witpoort Member forms topographical highs, clearly marking the separation between the Weltevrede Formation and the Lake Mentz Sub group (SACS, 1980).

The middle Devonian (±380 Ma) to middle Carboniferous (±325 Ma) strata of the Witteberg Group consist of approximately equal amounts of light grey to brownish quartzitic sandstones and micaceous mudrock (Thamm & Johnson, 2006, Whittingham, 1987). The overall depositional environment of the lower Witteberg sediments is believed to be near a shoreface, in a continuous inner shelf, along a storm dominated shallow marine coastal zone (Cotter, 1999). An overall eustatic sea level change at this time resulted in a seaward progradation of fluviodeltaic sediments across a shallow marine shelf (Cotter, 1999, Thamm & Johnson, 2006). The deposition of the Witteberg Group thus took place in a variety of environments from fluviodeltaic to shallow marine shoreface deposits.

Sedimentary structures found in the Witteberg Group include trough and planar cross bedding, wave ripple structures, hummocky and swaley cross stratification, linsen, wavy and flaser bedding, and horizontal lamination (Broquet, 1992, Cotter, 1999, Shone & Booth, 2005). Although generally devoid of body fossils, the strata of the Witteberg Group contain abundant trace fossils (Cotter, 1999, Thamm & Johnson, 2006).

3.2.2 Witpoort Formation

This study focussed specifically on the Witpoort Formation, which is believed to be comprised of more than 90% sandstone (Brunsdon & Booth, 2009, Johnson, 1976). The Witpoort Formation consists of three subdivisions, two of which crop out in the study zone viz. the red-brown Rooirand Member and the white Perdepoort Member (Brunsdon

& Booth, 2009). The Skitterykloof Member, although not present in the study zone, caps the Witpoort Formation in places (Thamm & Johnson, 2006). A stratigraphic column of the Witteberg Group is presented in Table 3-1.

Table 3-1: Stratigraphy of the Witteberg Group in the Eastern Cape east of 21°E after Thamm and Johnson(2006) and SACS (1980). The lithologies that crop out in the structural study zone have been shaded.

Age	Subgroup	Formation	Member	Lithology
±330 Ma		Dirkskraal		Sandstone
		Soutkloof		Shale
Carboniferous	Kommadagga	Swartwaterpoort		Sandstone
		Miller		Diamictite
		Waaipoort		Mudrock ,sandstone
	Lake Mentz	Floriskraal		Shale, sandstone
		Kweekvlei		Shale
			Perdepoort	Sandstone
		Witpoort		
Devonian			Rooirand	Sandstone
±380 Ma		Weltevrede		Sandstone, shale

3.2.2.1 Rooirand Member

The Rooirand Member comprises medium- to thickly bedded quartzitic sandstone that shows a distinct red-brown to pinkish grey colour on weathered surfaces and contains minor intercalated shales and siltstone (Thamm & Johnson, 2006, Toerien & Hill, 1989). Strata from the Rooirand Member are thought to have been the result of longshore drift forming a coastal barrier complex. This conforms to sedimentary structures encountered in the Member viz.cross-bedding and micro-crosslaminations (Johnson, 1976, Thamm & Johnson, 2006).

3.2.2.2 Perdepoort Member

The Perdepoort Member follows the Rooirand Member and comprises up to 60m of white massive quartz arenites (Brunsdon & Booth, 2009, Thamm & Johnson, 2006). Quartzites are supermature and coarse-grained, forming a distinct marker in the field separating the Weltevrede Formation and Lake Mentz Subgroups (Thamm & Johnson, 2006, Toerien & Hill, 1989). These supermature quartzites are indicative of a beach depositional environment. This interpretation is further supported by the presence of low angle cross-bedding (Thamm & Johnson, 2006).

3.2.3 Kweekvlei Formation

A sharp contact exists between the Witpoort Formation and the overlying Kweekvlei Formation. The predominantly argillaceous Kweekvlei Formation consists of fine grained purplish-grey mudrock which becomes more micaceous and silty towards the top (Johnson, 1976, Thamm & Johnson, 2006, Whittingham, 1987). The Kweekvlei Formation shows abundant sedimentary structures and trace fossils.

3.3 Previous Work in the study area

3.3.1 Previous work

Faulting and folding within the eastern sector of the Cape Fold Belt has been extensively studied and reviewed by several authors (Booth 1996; 1998; 2002, Booth *et al.*, 2004, Booth *et al.*, 1999, Booth & Shone, 1992, Booth & Shone, 1999, Booth & Shone, 2002, Brunsdon & Booth, 2009). Most of these studies focussed on the Witteberg Group rocks in the vicinity of the town of Steytlerville, located approximately 50km west of the study zone. The above-mentioned authors found the folding in the Witteberg Group to be mainly open to close, upright to overturned, and north-verging. South-verging folds have been noted but are considered rare and appear to be associated with thrust faults. They also found pervading south dipping thrust faulting with associated backthrusts that in some instances are cut by younger thrusts. Thrusting is often noted as closely spaced and is believed to have resulted in the duplication of quartzitic strata and elimination of more argillaceous horizons (Booth & Shone, 2002). This has greatly hindered stratigraphic classification within the Cape Supergroup especially when considering lateral continuity.

A study by Goossens, (2003) conducted some 20km north of the study zone in the upper Witteberg and lower Karoo Supergroup rocks, noted folds as the dominant structure. The folds varied between tight to gentle, but were mostly north-verging. The study also found faulting in the form of thrust faults, reverse faults, and normal faults; the latter transecting other structures.

Only two authors Whittingham, (1987) and Jeffreys, (2003) have compiled information in the immediate vicinity of the study zone. The work by Whittingham, (1987) noted the structures in the Witteberg rocks to be overturned and north verging. He also observed that normal faults predominantly dip towards the south, although northward downthrown normal faults are also present. Jeffreys, (2003) carried out analysis of the northern half of the study zone in which he noted large scale thrust faulting, north verging open mesofolds, and large scale normal faulting that transect all other structures.

Thrust faulting in the Witteberg has formed numerous structures such as pop-ups, triangle zones and wedge structures. The two authors also found the faulting to be highly complex with thrusting occurring pre, -syn -and post folding. They further noted fold geometry to be directly related to thrusting and the competency of strata. Booth *et al.,*

(1999) also observed that thrust faulting is directly related to lithology as argillaceous horizons display closer spaced faulting compared to more arenaceous horizons.

4. Methodology

4.1 Study site

4.1.1 Locality

The study area is located in the Cape Fold Belt and it lies approximately 30km west-northwest of Kirkwood, 10km south of Darlington Dam and 90km north of Port Elizabeth (Fig 4-1). This area forms part of the Cacadu district, Eastern Cape, South Africa. The railway hamlet of Glenconnor is situated immediately to the south-east of the study site. The study site lies between the latitudes 25°02‘‘E to 25°‘‘12 and longitudes 33°19‘‘S to 33°21‘‘S, is bound in the North by the Klein Winterhoek mountains and is fault bounded to the South by the Mesozoic Algoa basin. The structural study focussed on the area demarcated by red lines in Fig 4-1, although geochemical samples were also collected outside this zone.

4.1.2 Topography

The Sapkammas mountain range dominates the southern half of the study area forming a narrow mountain range of low height but relatively high relief. It is comprised of more resistant Witpoort Formation of the Witteberg Group. The Klein Winterhoek mountain range extends along the northern boundary of the study area. Both these mountain ranges trend roughly east-west and form part of the Cape Fold Belt. They are drained by non-perennial rivers which form a dendritic pattern in the northern half of the study area. In the southern half of the study area the non-perennial Grootrivier dominates low lying areas. The river cuts through the Sapkammas mountains towards the south-east of the study site near Glenconnor. The lower lying areas are composed of less resistant strata. Within the southern half of the study site these consist of Lake Mentz Subgroup rocks, and in the northern half of the study site they consist of Dwyka tillite, the lowermost part of the Karoo Supergroup rocks (Fig 4-1).

4.1.3 Vegetation

Vegetation tends to be denser on south facing slopes and low-lying alluvium rich areas. This made mapping in certain areas impossible due to restricted movement and accessibility.

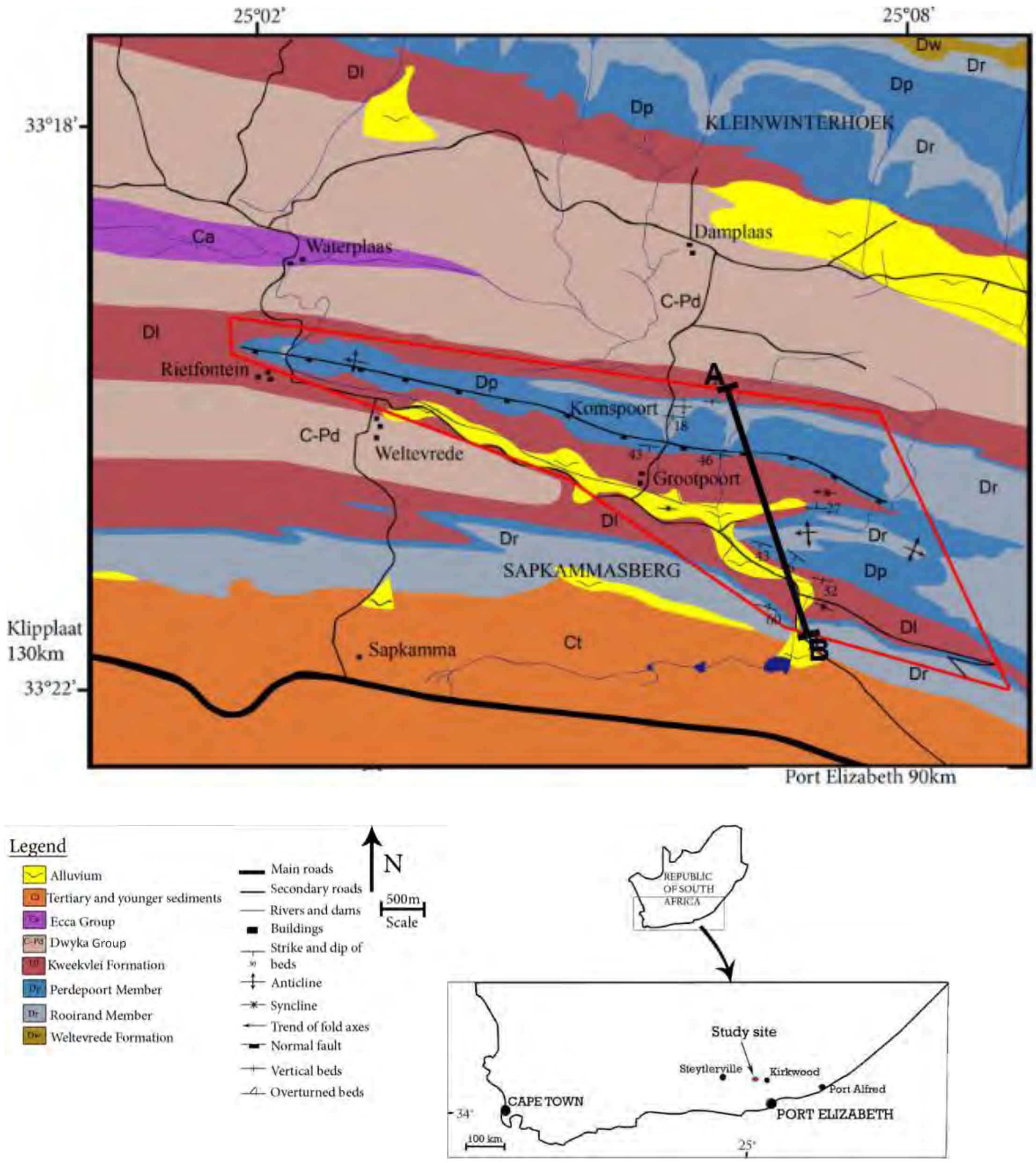

Fig 4-1: Locality and geological map of the study area, the area in which the structural study was studied is demarcated by red lines. A representative cross-section was drawn from A-B this will be referred to in the structural result section.

4.2 Materials and Methods

4.2.1 Structural geology

4.2.1.1 Desktop study

Desktop studies commenced with the analyses of the study site using the 3324 Port Elizabeth 1:250000 geological map and the 3325 AC Glenconnor 1:50000 topographical map. The latter had been obtained from the Council for Geoscience and has been modified by Whittingham (1987) who had traced in geological contacts. Aerial photos (Job 446: strip 7, 3685-3690: strip 8, 2925-2930: strip 9: 3875-3880) were also consulted in conjunction with maps to gain a more comprehensive understanding of the geology of the area. Aerial photos were also obtained in the form of high quality digital photos from the Council for Geoscience. These served to enhance interpretation and presentation of features within the study area.

4.2.1.2 Field techniques

Relevant outcrops were initially photographed and sketched. A tape measure was then used to determine the approximate dimension of outcrops. The relevant primary structural features were then noted, followed by measuring of secondary structures such as bedding, fold- and fault geometry, jointing and cleavage. The structural features were measured with the aid of a Brunton geological compass. Other important geological features such as bed thickness and strata colouration were also noted. Sections were chosen for accessibility and in such a way as to best unravel the overall geology of the structural study site.

4.2.1.3 Fold and Fault classification

(i) Faults

A fault can be defined as a discontinuity surface or plane along which rock masses on adjacent sides display clear differential movement. Faults can be grouped into three broad categories which are all summarized in Fig 4-2.

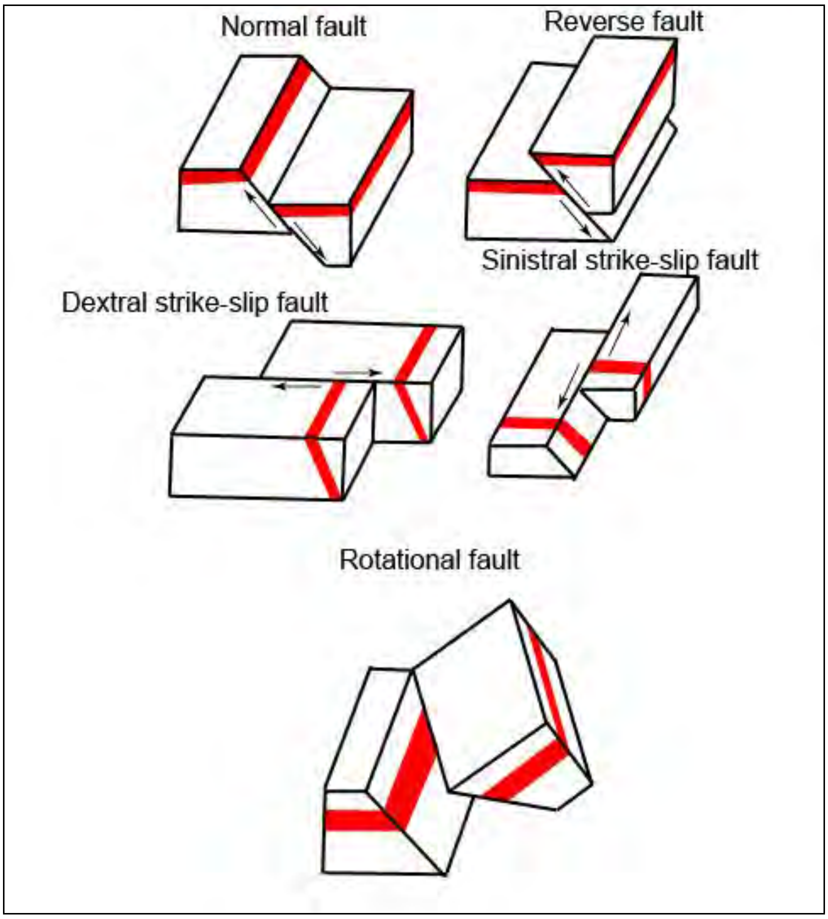

Fig 4-2: Summary of fault types, after Ghosh (1993).

A special case of reverse fault exists in which the dip is less than 45° in such cases the fault is rather classified as a thrust fault (Price, 1966) . Fault planes in this study were identified by using a combination of the following criteria:

1. Clear displacement of markers such as bedding, vein fillings and previously identified fault planes.
2. Fault gauge and breccia.
3. Fault drag or roll-overs in the case of normal faults.
4. Slickensides and or slickenfibre surfaces often formed on quartz veins.

In the case of the last two a sense of movement of a fault can readily be ascertained. Fault drag clearly indicates the direction of movement of the hanging wall as the associated bedding surface bends towards the direction of movement. In the case of slickensides a stepped-like surface is often formed consisting of a “crest” and “step” that are orthogonal to the direction of movement. The sense of movement of the particular hanging wall block may be determined by running one"s hand across the surface, the so-called smoother direction revealing the direction of movement. However, sense of movement can be ambiguous, and thus when this method is used it was combined with other criteria where possible.

(ii) Folds

Folds were classified according to the method applied by Fleuty, (1964). For the purposes of the study this method best clarified the geometry of folds and was also simple to employ. The classification method describes the various components of a fold viz. plunge of fold axis, attitude of axial plane, and interlimb angle (Table 4-1 and Fig 4-3). For example; a fold with an interlimb angle of 160°, an axial planar dip of 85°, and a fold axis plunging at 55° would be classified as a steeply inclined, moderately-plunging gentle fold. Folds can further be classified by their shape in profile, for example box, chevron folds etc., and also symmetric (equal fold limb lengths) and asymmetric (unequal fold limb lengths). Folds may also be considered as parasitic, when superimposed on folds of larger wavelength, and disharmonic when folds in different layers display varying wavelengths.

Other methods of fold classification require a profile that is perpendicular to that of the fold axis in order to determine dip isogons. This method was not utilized as all folds were observed in profile at angles that were most probably not perpendicular to the fold axis

Table 4-1: Fold classification, after Fleuty, (1964).

Interlimb angle in °	Description	Axial plane dip in °	Term	Description	Fold axis plunge in °	Term	Description
180°-120°	Gentle	90°	Vertical	Upright fold	90°	Vertical	Vertical fold
120°-70°	Open	89°-80°	Sub-vertical	Upright fold	89°-80°	Sub-vertical	Vertical fold
70°-30°	Closed	80°-60°	Steep	Steeply inclined fold	80°-60°	Steep	Steeply plunging fold
30°-0°	Tight	60°-30°	Moderate	Moderately inclined fold	60°-30°	Moderat e	Moderately plunging fold
0	Isoclinal	30°-10°	Gentle	Gently inclined fold	30°-10°	Gentle	Gently plunging fold
negative angles	Mushroom	10°-01°	Sub-Horizontal	Recumbant	10°-01°	Sub-Horizont al	Sub-horizontally plunging fold
		0°	Horizontal		0°	Horizont al	Horizontal fold

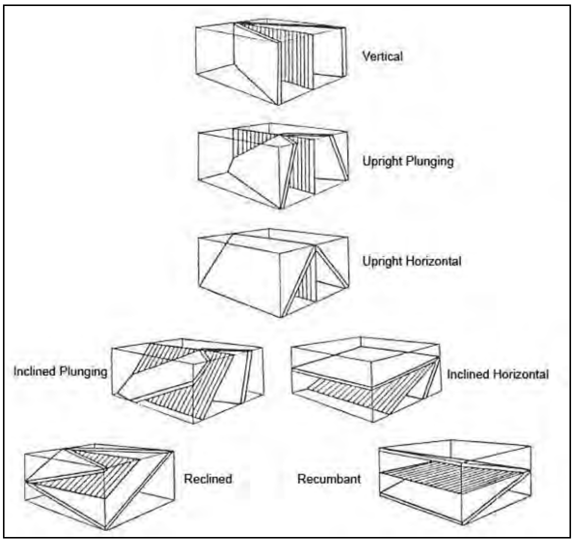

Fig 4-3: Attitudes of folds derived from the reorientation of a upright antiform, after Fleuty, (1964).

4.2.1.4 Interpretation of structural data

The relevant readings were plotted on equal area and equal angle stereonett using Stereo32 version 0.9.4. All readings were corrected for magnetic declination and N indicates true north in all stereograms in the study. The average magnetic declination for the study site is 24°W of true north (as calculated in November 2008, Hermanus Magnetic Observation pers. comm.).

4.2.2 Mineralogy and Geochemistry

4.2.2.1 Sample Collection

One hundred samples in total were collected from the Rooirand- and Perdepoort Members (Fig 4-4). Some of the samples were collected in areas outside of the structural study zone. Samples were spaced along strike and at different latitudinal outcrops of Perdepoort- and Rooirand Member strata. Samples were collected using an 8 pound sledge hammer and in some instances a hammer and chisel were also employed.

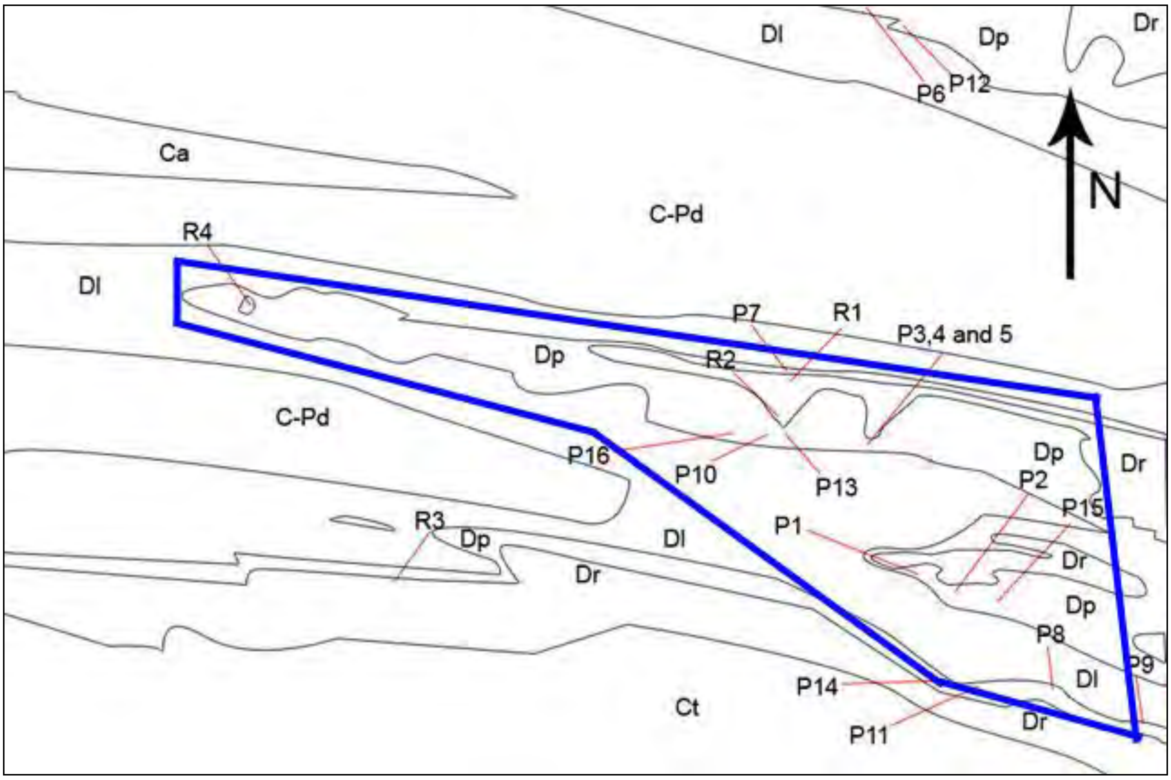

Fig 4-4: Simplified map showing the approximate locations of samples from the Rooirand-(R) and Perdepoort (P) Members. See Fig 4-1 legend for symbol explanations.

4.2.2.2 Petrographic Light Microscopy

Representative hand samples from both the Perdepoort- and Rooirand Member were cut and polished by the researcher using university equipment in order to produce thin sections. These thin sections were analyzed to determine general mineralogy and any structural and/or metamorphic textures. A Leica DM EP polarising microscope was used for thin section analysis and a Cannon PowerShot S40 digital camera, connected via a Leica Dc 150 camera adapter, was used for taking photos of the thin sections.

4.2.2.3 Scanning Electron Microscopy

Four samples from the Perdepoort Member, as this lithology was the main focus of this study, and one from the Rooirand Member were analysed using a Philips XL 30 Scanning Electron Microscope (SEM). An EDAX DX-4 model was used for Energy Dispersive X-ray Spectroscopy, which allows one to scan specific areas of a sample surface. The method is particularly useful as it allows one to analyze specific minerals or areas in a sample. However, as the analysis scans a certain volume of rock the elemental analysis of a small mineral might be erroneous due to the composition of surrounding minerals. SEM enables the detection of minerals which are not readily seen or identifieble using normal light microscopy. These included among other opaques such as rutile and haematite, as well as rare earth minerals such as monazite.

(i) Sample preparation for Scanning Electron Microscope analysis

Samples were cut from hand samples using an abrasive rock saw into blocks with approximate dimensions of 2-5mm thick, and 4x4cm length and width. Samples were then mounted in an epoxy resin using a plastic cylindrical shaped mould and allowed 2 to 3 minutes to harden. The epoxy blocks were then removed from the mould and one end of the epoxy block enclosing the samples was ground down by hand using p240 (58.6µm) sandpaper. The samples were manually ground down until enough resin was removed so as to expose the sample to the surface. Each sample was then ground for approximately five minutes in a series of steps, each step utilizing a lower abrasive grade of sandpaper. Samples were ground in a rotational motion to avoid unidirectional scratches. The grinding steps were as follows, p240 (58.6µm) to p400 (35µm) to p800 (21.8µm) to p1200 (15.8µm) and then the samples were then ground to 6µm using a Buehler polisher. Some samples were ground using the Buehler sample holder and some were ground manually by rotating them on the Buehler"s rotating grinding disc. The samples were finally ground down to 3µm. The last two grounding steps used special doulube 6µm and 3µm diamond containing lubricant.

The samples were then coated with a thin 20-30nm carbon coating in order to avoid excessive surface charging. This was done using an Emitech K 950 X high vacuum turbo coater.

A silver epoxy contact was then painted from the edge of the sample, on the resin block surface, to the base of the resin block in order to earth the sample to the stand in the

Scanning Electron Microscope. This was done to provide a conduit for electrons excited at the surface of the samples.

4.2.2.4 XRF analysis

Hand samples were sent to the Council for Geoscience laboratory in Pretoria for X-ray Fluorescent (XRF) Spectroscopy analysis. Initially it was planned that 100 samples would be analysed but due to unforeseen financial constraints only 20 samples were finally analysed. Through this method a powdered rock sample is analysed thus providing a whole rock chemical composition. The Council for Geoscience laboratory utilizes fusion disks and/or pressed powder pellets to analyze elements in conjunction with an international reference material. The latter is done to ensure the accuracy of the method of analyses. The following elements were tested for using XRF; Si, Ti, Al, Mn, Mg, Ca, Na, K, P, As, Ba, Bi, Br, Ce, Co, Cs, Cr, Cu, Ga, Ge, Hf, La, Mo, Nd, Nb, Ni, Pb, Rb, Sc, Se, Sm, Sr, Ta , Th, Tl, U, V, W, Y, Yb, Zn and Zr. Major elements were reported in weight percentage, while trace elements were reported in parts per million (ppm).

5. Results: Mineralogy and Geochemistry

5.1 Mineralogy

5.1.1 Petrography

5.1.1.1 Perdepoort Member

Petrographic light microscopy and scanning electron microscopy of the Perdepoort Member reveal a lithology that consists almost entirely of quartz framework grains with minor rock fragments (Fig 5-1). Accessories include biotite, muscovite, chlorite, apatite, rutile, hematite, baryte and monazite. Quartz grains are subrounded to sub-angular, have an average grain size of 0.2-0.8 mm and show no preferred orientation. Many quartz grains display undulose extinction with sutured, embayed and straight grain boundaries; the latter occurring in areas where triple junctions were noted (Fig 5-2 and Fig 5-3). Recrystallization is clearly visible although it doesn"t seem to indicate a preferred orientation. Mica minerals form the major matrix component, and occur in cracks and spaces between quartz grains. Biotite laths and larger crystals are present. The larger crystals are rare with most biotite occurring as small grains between quartz grains. (Fig 5-3 and Fig 5-4). Micas do not possess a predominant preferred orientation although some grains are aligned. These minerals occur as both subangular grains and aborescent aggregates. Opaque minerals mostly occupy cracks in the rocks, clearly indicating the position of microfractures. Opaques form a significant portion of the matrix, exact percentages are indicated in the section related to geochemistry. Using the Scanning Electron Microscopy techniques a distinction could be made between hematite that dominates areas with high fracture density, and rutiles that dominates areas with lower fracture density. Quartz grains did not show any inclusions in the specific samples that were analyzed. Feldspars appear to be totally absent, although one highly weathered feldspar was noted which could not be positively identified.

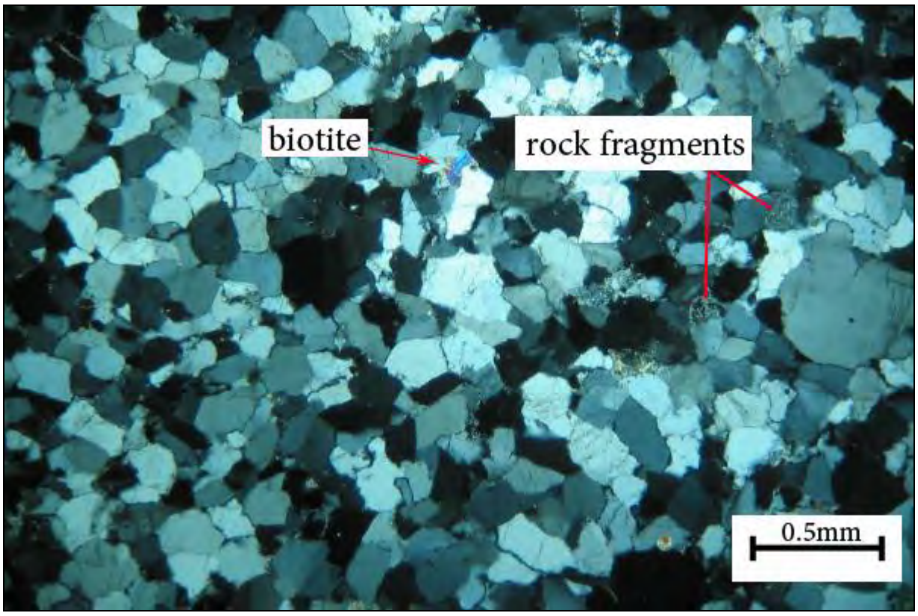

Fig 5-1: Photomicrograph showing overall composition of a typical sample from the Perdepoort Member. Note only a few rock fragments and a single biotite grain are present. Photomicrograph taken under crossed nicols.

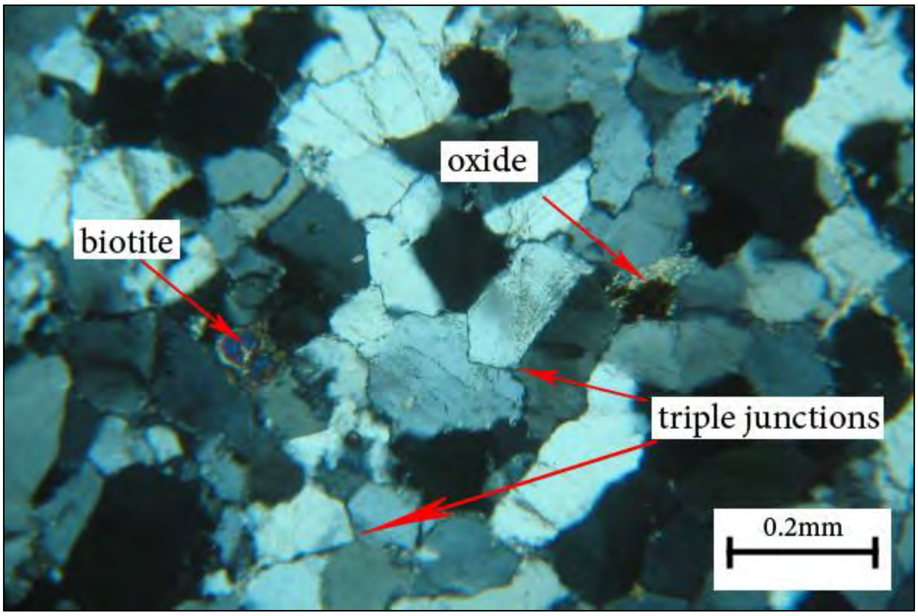

Fig 5-2: Photomicrograph showing triple junctions between quartz grains. Note the overall composition consists almost exclusively of quartz grains. Photomicrograph taken under crossed nicols.

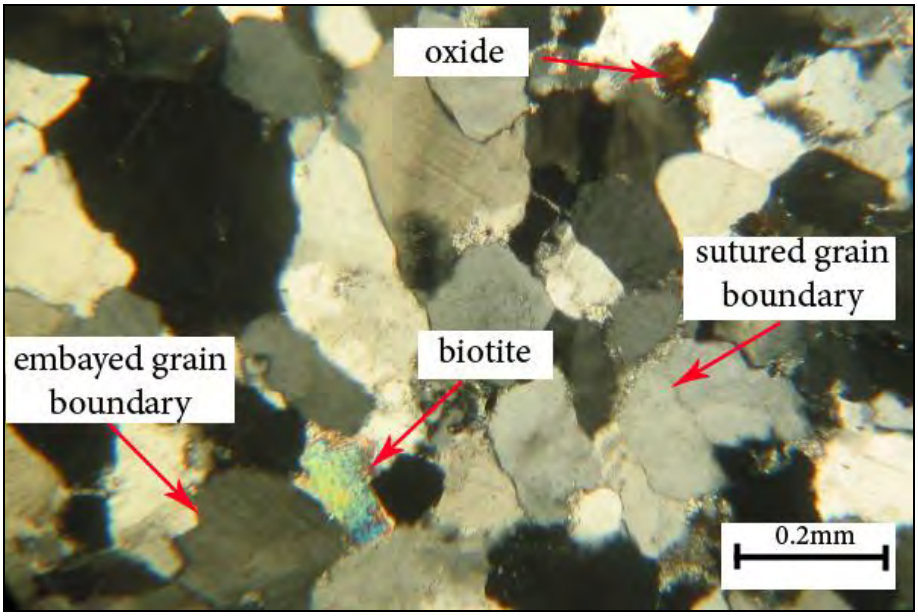

Fig 5-3: Photomicrograph showing a single biotite grain in a slide comprised largely of quartz. Grain boundary relations are also indicated. Oxide mineral also occur as microcrystalline grain between quartz grains providing a brown tinge to the slide when viewed under normal light. Photomicrograph taken under crossed nicols.

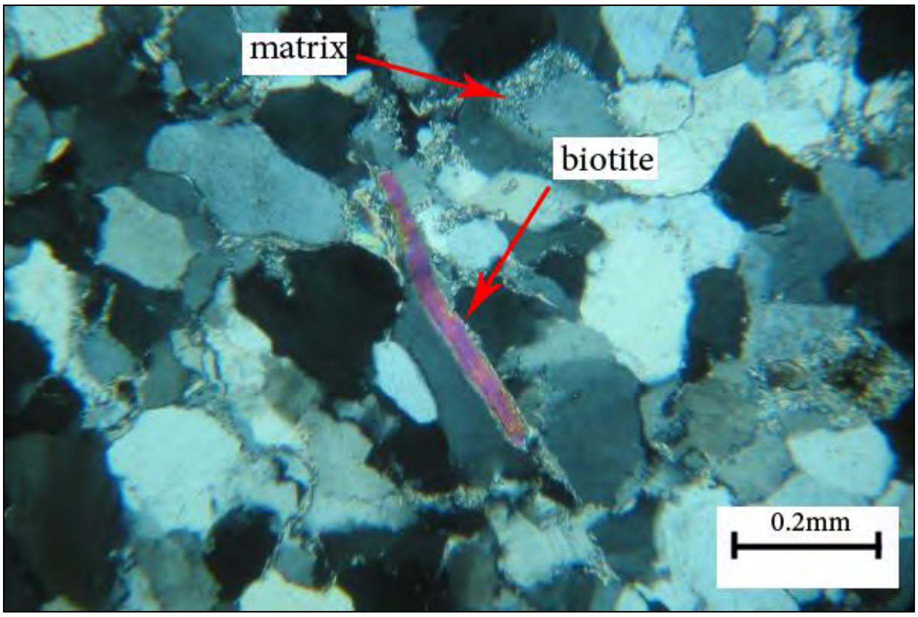

Fig 5-4: Photomicrograph showing a biotite lath surrounded by quartz framework grains note the small amount of fine mica matrix. Photomicrograph taken under crossed nicols.

5.1.1.2 Rooirand Member

The Rooirand Member forms the basal unit of the Witpoort Formation and contains a distinctive red-brown surface weathering. Just by observing thin sections with the naked eye one can clearly observe that it contains increased amounts of oxides hence its red-brown colour. This is in clear contrast to the Perdepoort Member. The Rooirand Member still contains a high percentage of quartz which is also confirmed by XRF analysis (Section 5.2). The Rooirand Member also shows a relatively high concentration of biotite compared to the Perdepoort Member (Fig 5-5 and Fig 5-6). Opaques oxides are also more abundant in the Rooirand Member, often filling fractures as dark red masses in the rocks (Fig 5-5). An increase in matrix and accessories is clearly visible in the Rooirand Member (Fig 5-7). Micas are abundant in microfractures and in-between quartz grains (Fig 5-5 and Fig 5-6). Rutiles are also abundant in Rooirand Member rocks (see section 5.1.2). Quartz possesses an average size similar to that of quartz in the Perdepoort Member, 0.2-0.8mm, and grain boundaries are sutured and straight with numerous triple junctions. Quartz also occurs as fine grains, especially between larger grains forming a triple junction and at the centre of triple junction points and thus should rather be classified as chert (Fig 5-7). Quartz grains show undulose extinction and recrystallization, although no preferred orientations are observed. Some quartz grains are highly strained. This is, however, not a common occurrence. Most of the rutile grains appear to be original detrital framework grains (Fig 5-6). One such detrital grain appears to have been fractured post-depositionally (Fig 5-6).

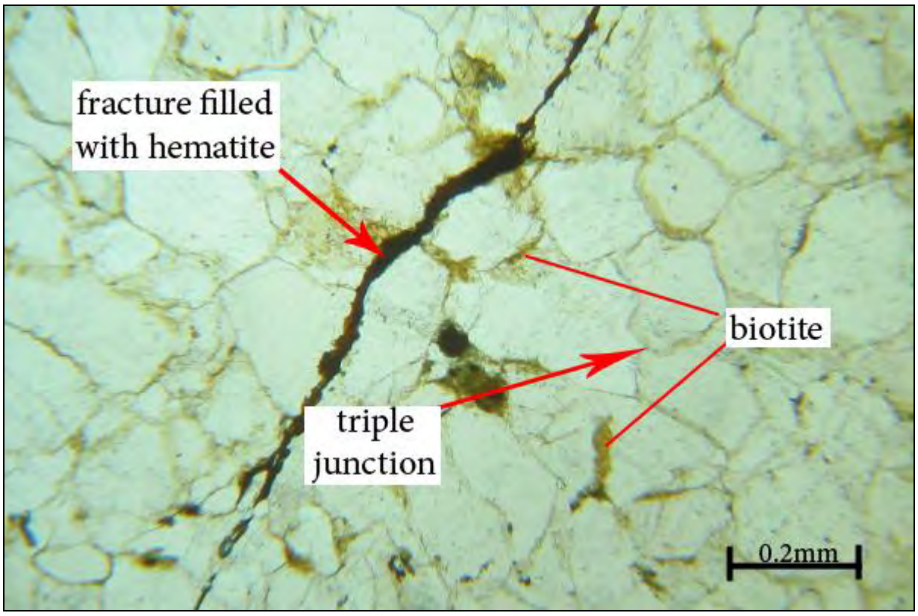

Fig 5-5: Photomicrograph showing a fractured that has been filled with hematite in quartzite of the Rooirand Member. Note the increased amount of matrix primarily as biotite. Photomicrograph taken under plane polarised light.

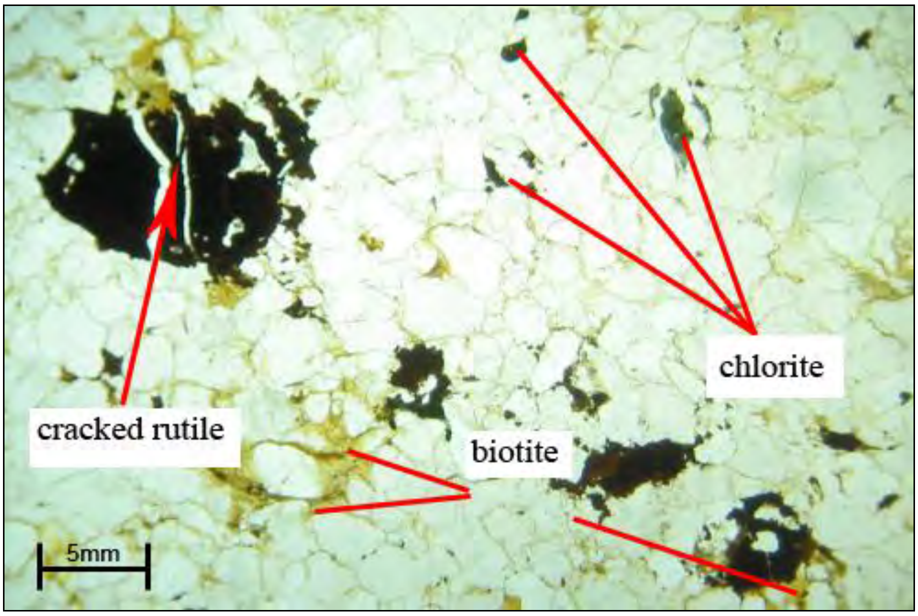

Fig 5-6: Photomicrograph showing detrital rutile which has been cracked (sample from the Rooirand Member). Chlorite grains are present towards the top right. Note the increased percentage matrix and oxides when compared to the Perdepoort Member. Photomicrograph taken under plane polarised light.

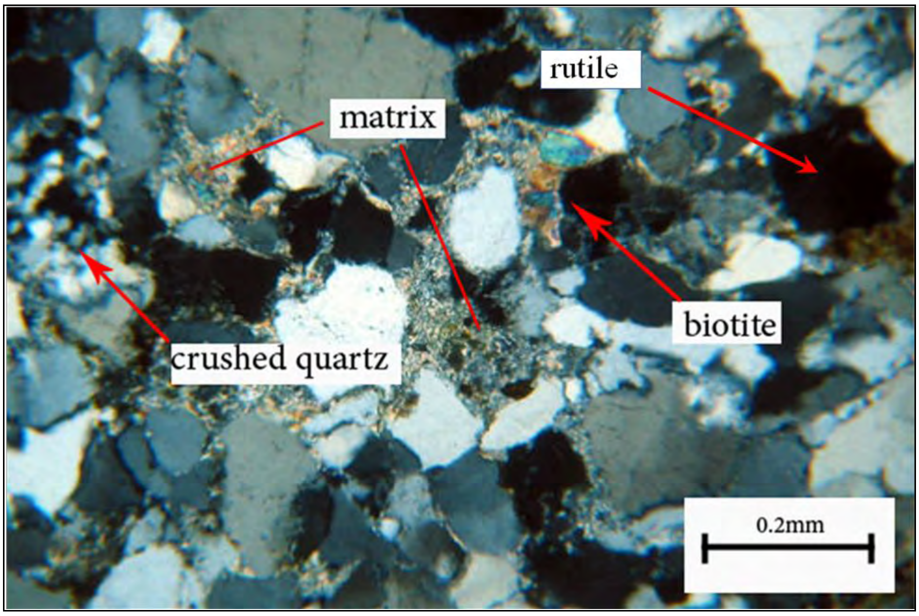

Fig 5-7: Photomicrograph showing the overall composition of the Rooirand Member. Note the increased amount of matrix and biotite when compared to the Perdepoort Member.A rutile grain is present towards the top right of the photomicrograph, remaining dark under crossed-nicols. Photomicrograph taken under crossed nicols.

5.1.2 Scanning Electron Microscopy

The data in Table 5-1 and Table 5-2 show the various elemental weight percentages for the minerals analyzed. The individual quartz grains analyzed were very pure and did not show any other elements or any significant inclusions in their crystal structures. Minerals were identified by comparing the weight percentage obtained in the analysis with ideal formula percentages of minerals. Minerals such as monazite and rutile did however show some variation in weight percentages. These variations may be reflected in Table 5-1 and Table 5-2. In Table 5-1 minerals designated as rutiles vary considerably in elemental composition. Hematite is also abundant in these rocks and except for slight compositional difference show a constant chemical composition. Zircons are abundant in the Perdepoort and Rooirand Members, and show slight variations in the Zr and SiO_2 percentages. Other minerals found include biotite and baryte. Some of the variations in certain minerals might be due to interference produced by backround minerals.

Table 5-1: Composition of minerals scanned using energy dispersive spectroscopy. All values are in weight percentage.

	RM1	RM2	RH1	RZ1	RR1	RH2	RM3	PH3	PH4	PZ2	PH5	PR2	PR3	PR4	PQ1
Al_2O_3	0.79	0.2	2.66	bdl	0.96	5.26	bdl	7.47	bdl	bdl	11.37	8.89	7.54	21.08	0.02
SiO_2	4.54	1.31	5.47	33.91	1.33	9.15	1.14	10.09	10.28	32.1	8.09	3.85	1.26	28.54	99.98
P_2O_5	13.33	27.29	1.27	bdl	bdl	1.6	29.55	2.82	bdl	bdl	1.87	4.02	4.49	bdl	bdl
ThO_2	6.48	5.31	bdl	bdl	bdl	bdl	7.97	bdl	bdl	bdl	bdl	bdl	bdl	bdl	bdl
K_2O	0.36	bdl	bdl	bdl	bdl	bdl	bdl	1.18	bdl	bdl	0.96	0.89	2.07	4.53	bdl
Na_2O	bdl	1.19	bdl	bdl	bdl	1.08	bdl	bdl	bdl	bdl	bdl	bdl	0.19	0.4	bdl
MgO	bdl	bdl	bdl	bdl	bdl	bdl	bdl	bdl	bdl	bdl	bdl	bdl	0.62	0.7	bdl
CaO	0.6	1.07	bdl	bdl	bdl	bdl	1.48	bdl	bdl	bdl	bdl	1.04	1.21	bdl	bdl
SrO	bdl	bdl	bdl	bdl	bdl	bdl	bdl	bdl	bdl	bdl	bdl	bdl	bdl	bdl	bdl
La_2O_3	10.68	15.8	bdl	bdl	bdl	bdl	15.67	bdl	bdl	bdl	bdl	bdl	bdl	bdl	bdl
Ce_2O_3	31.08	31.48	bdl	bdl	bdl	bdl	28.01	bdl	bdl	bdl	bdl	bdl	bdl	bdl	bdl
Pr_2O_3	4.46	2.07	bdl	bdl	bdl	bdl	1.86	bdl	bdl	bdl	bdl	bdl	bdl	bdl	bdl
Nd_2O_3	16.28	9.7	bdl	bdl	bdl	bdl	8.18	bdl	bdl	bdl	bdl	bdl	bdl	bdl	bdl
Sm_2O_3	4.11	bdl	bdl	bdl	bdl	bdl	1.76	bdl	bdl	bdl	bdl	bdl	bdl	bdl	bdl
NiO	bdl	bdl	bdl	bdl	bdl	bdl	bdl	bdl	10.07	bdl	bdl	bdl	bdl	bdl	bdl
MnO	bdl	bdl	bdl	bdl	bdl	bdl	bdl	bdl	1.27	bdl	bdl	bdl	bdl	bdl	bdl
FeO	7.29	bdl	90.6	bdl	3.77	82.91	bdl	78.43	61.78	bdl	77.71	35.37	14.55	1.47	bdl
Cr_2O_3	bdl	bdl	bdl	bdl	bdl	bdl	bdl	bdl	16.6	bdl	bdl	bdl	bdl	bdl	bdl
ZrO_2	bdl	4.6	bdl	66.09	bdl	bdl	4.39	bdl	bdl	67.9	bdl	bdl	bdl	bdl	bdl
TiO_2	bdl	bdl	bdl	bdl	93.94	bdl	bdl	bdl	bdl	bdl	bdl	45.94	68.08	43.28	bdl
BaO	bdl	bdl	bdl	bdl	bdl	bdl	bdl	bdl	bdl	bdl	bdl	bdl	bdl	bdl	bdl
SO_3	bdl	bdl	bdl	bdl	bdl	bdl	bdl	bdl	bdl	bdl	bdl	bdl	bdl	bdl	bdl
CoO	bdl	bdl	bdl	bdl	bdl	bdl	bdl	bdl	bdl	bdl	bdl	bdl	bdl	bdl	bdl

** I: P=Perdepoort Member sample; R=Rooirand Member sample; M=monazite; Z=zircon; H=hematite; Mi=mica; R=rutile; B=baryte; Q=Quartz; bdl=below detection limit.*

Table 5-2: Composition of minerals scanned using energy dispersive spectroscopy. All values are in weight percentage.

	PQ2	PQ3	PZ3	PMi1	PZ4	PR5	PM4	PM5	PB1	PB2	PR6	PB3	PMi2	PR7	PA1
Al_2O_3	0.03	bdl	bdl	37.73	bdl	bdl	34.64	33.77	0.6	2.63	bdl	1.2	36.53	bdl	bdl
SiO_2	99.94	99.99	31.87	50.35	35.05	4.89	bdl	7.27	7.8	bdl	1.04	bdl	52	2.1	7.09
P_2O_5	bdl	bdl	bdl	bdl	bdl	bdl	32.54	32.08	1.12	3.9	bdl	bdl	bdl	bdl	37.87
ThO_2	bdl	bdl	bdl	bdl	bdl	bdl	bdl	bdl	bdl	bdl	bdl	bdl	bdl	bdl	bdl
K_2O	0.01	bdl	bdl	10.15	bdl	bdl	bdl	bdl	0.36	1.59	bdl	bdl	8.84	bdl	bdl
Na_2O	bdl	bdl	bdl	bdl	bdl	bdl	bdl	bdl	bdl	bdl	bdl	bdl	0.64	bdl	bdl
MgO	bdl	bdl	bdl	0.54	bdl	bdl	bdl	bdl	bdl	bdl	bdl	bdl	0.76	bdl	bdl
CaO	bdl	bdl	bdl	bdl	bdl	bdl	bdl	bdl	bdl	bdl	bdl	bdl	bdl	bdl	46.75
SrO	bdl	bdl	bdl	bdl	bdl	bdl	1.81	bdl	bdl	27.07	bdl	bdl	bdl	bdl	bdl
La_2O_3	bdl	bdl	bdl	bdl	bdl	bdl	6.16	5.67	bdl	bdl	bdl	bdl	bdl	bdl	bdl
Ce_2O_3	bdl	bdl	bdl	bdl	bdl	bdl	15.15	13.53	bdl	bdl	bdl	bdl	bdl	bdl	bdl
Pr_2O_3	bdl	bdl	bdl	bdl	bdl	bdl	bdl	bdl	bdl	3.9	bdl	bdl	bdl	bdl	bdl
Nd_2O_3	bdl	bdl	bdl	bdl	bdl	bdl	9.7	7.69	bdl	bdl	bdl	bdl	bdl	bdl	bdl
Sm_2O_3	bdl	bdl	bdl	bdl	bdl	bdl	bdl	bdl	bdl	bdl	bdl	bdl	bdl	bdl	bdl
NiO	bdl	bdl	bdl	bdl	bdl	bdl	bdl	bdl	bdl	bdl	bdl	bdl	bdl	bdl	bdl
MnO	bdl	bdl	bdl	bdl	bdl	bdl	bdl	bdl	bdl	bdl	bdl	bdl	bdl	bdl	bdl
FeO	0.02	bdl	bdl	1.23	bdl	bdl	bdl	bdl	bdl	bdl	bdl	bdl	1.18	bdl	8.29
Cr_2O_3	bdl	bdl	bdl	bdl	bdl	bdl	bdl	bdl	bdl	bdl	bdl	bdl	bdl	bdl	bdl
ZrO_2	bdl	bdl	68.13	bdl	64.95	bdl	bdl	bdl	bdl	bdl	bdl	bdl	bdl	bdl	bdl
TiO_2	bdl	bdl	bdl	bdl	bdl	95.11	bdl	bdl	bdl	bdl	98.96	bdl	bdl	97.9	bdl
BaO	bdl	bdl	bdl	bdl	bdl	bdl	bdl	bdl	55.98	48.6	bdl	67.67	bdl	bdl	bdl
SO_3	bdl	bdl	bdl	bdl	bdl	bdl	bdl	bdl	26.92	27.07	bdl	31.13	bdl	bdl	bdl
CoO	bdl	bdl	bdl	bdl	bdl	bdl	bdl	bdl	6.29	bdl	bdl	bdl	bdl	bdl	bdl

** II: P=Perdepoort Member sample; R=Rooirand Member sample; M=monazite; Q=quartz; Z=zircon; H=hematite; Mi=mica; R=rutile; A=apatite; B=baryte; Q=Quartz; bdl=below detection limit.*

5.1.2.1 Perdepoort Member

The high proportion of quartz in these quartzites can be seen in the SEM photomicrographs (Fig 5-8 and Fig 5-9).

It is clear that accessories are a minor component in these samples. Accessories, besides biotite and muscovite, comprise approximately 5-15 % of samples, and although only representing a small component of the overall composition, less than 5%, are important for identifying a potentially pure silica source.

Baryte is frequently observed between quartz grains in the Perdepoort Member (Fig 5-14). Rutile grains consist of detrital grains and epigenetic aggregates between quartz grains. This is evident as Fig 5-13 clearly shows that some rutiles are syn-deformational. Rutiles have a wide size range; from microcrystalline aggregates between quartz grains, to 0.1mm detrital grains (Fig 5-12). Biotite, muscovite and hematite are also often seen as a fine grained aggregate mixture between quartz grains (Fig 5-11).

Zircons are easily observed on a SEM image and appear as bright spots (Fig 5-9 and Fig 5-15). Most biotite is found as fine crystals between quartz grains although large biotites are also observed (Fig 5-10).

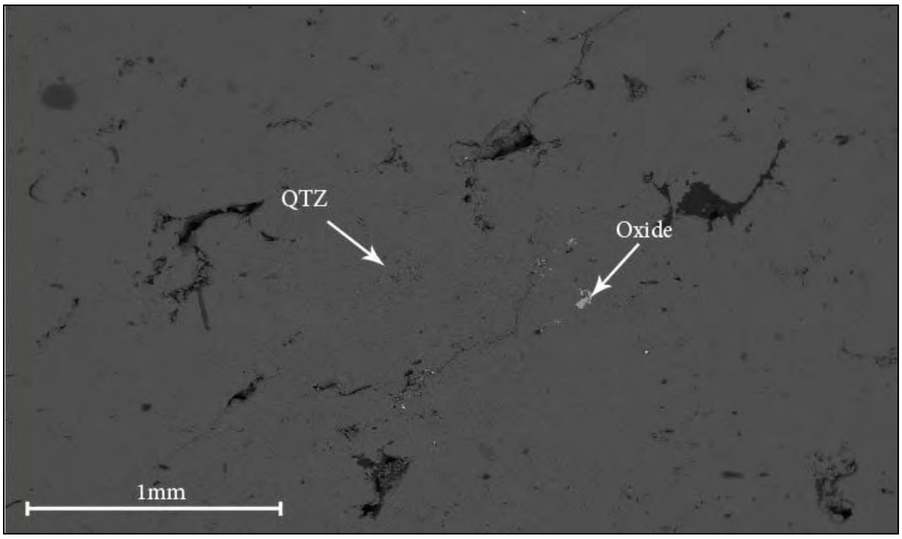

Fig 5-8: Scanning electron photomicrograph showing the overall composition of the Perdepoort Member. The quartz, identifiable by its grey tone, covers almost the entire slide. Brighter areas indicate other minerals, in this case oxides in the form of rutile. Photomicrograph taken in backscatter electron mode.

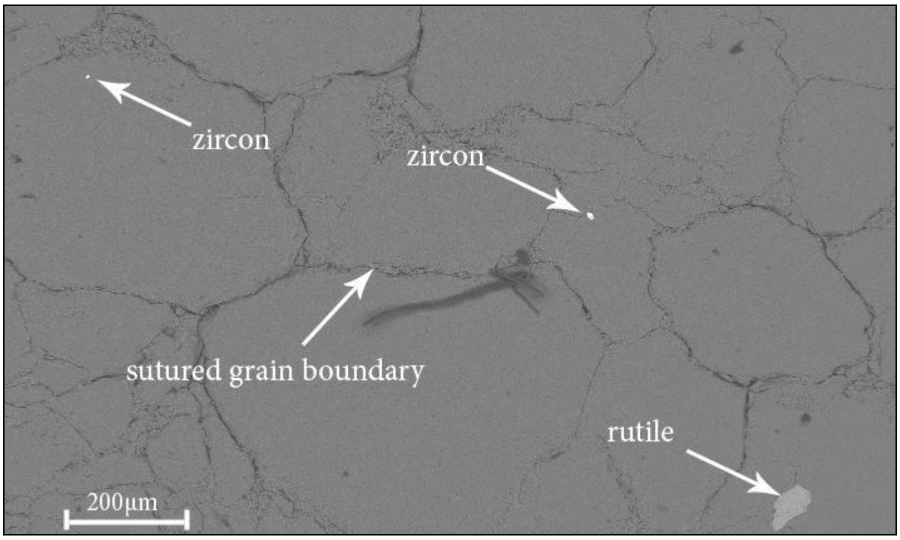

Fig 5-9: Scanning electron photomicrograph clearly showing an example of sutured grain boundaries. Zircons and rutile are also visible in photomicrograph. Photomicrograph taken in backscatter electron mode.

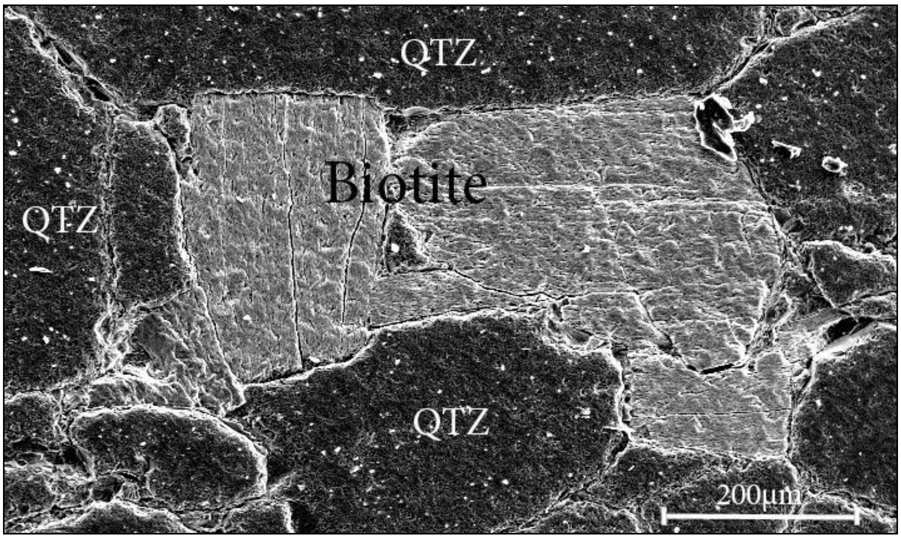

Fig 5-10: Scanning electron photomicrograph showing biotite laths between quartz grains. Photomicrograph taken in backscatter electron mode.

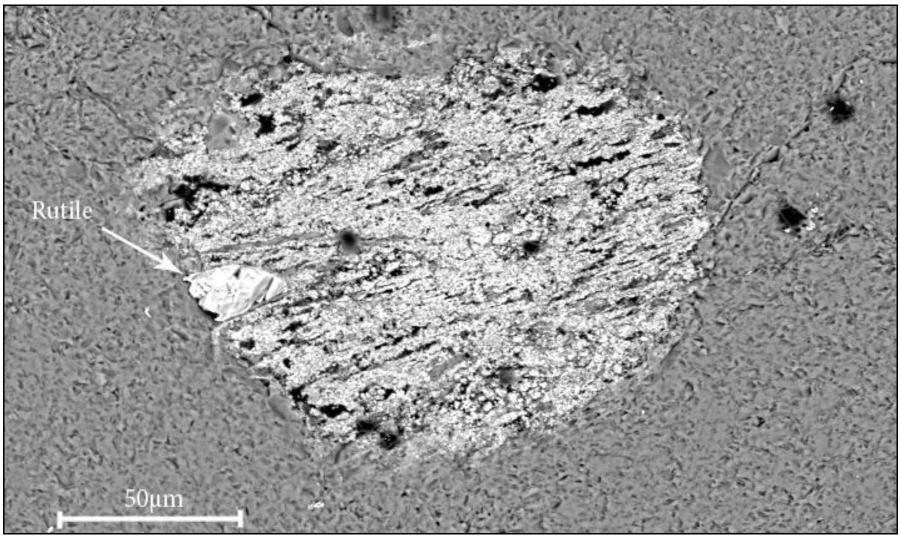

Fig 5-11: Interlayered rutile, hematite and biotite surrounded by quartz grains. A larger rutile grain is indicated on the left. Photomicrograph taken in backscatter electron mode.

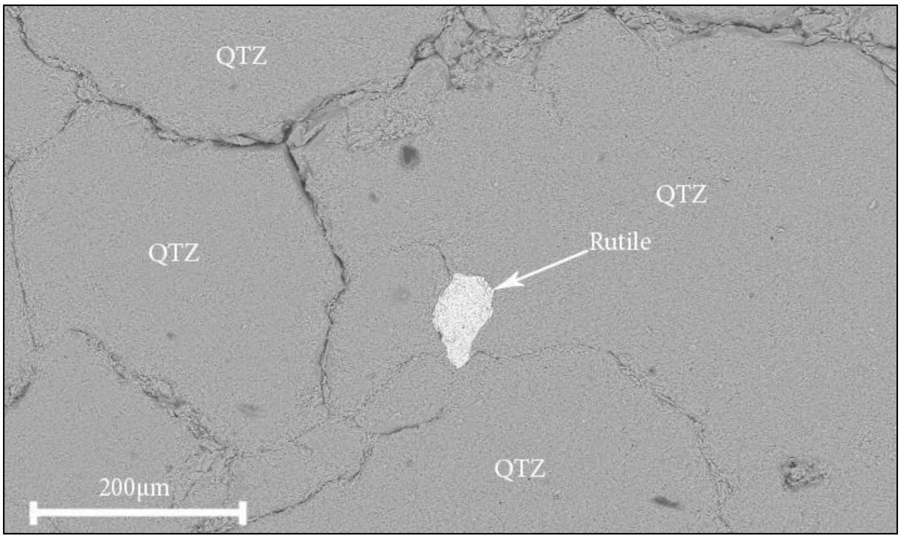

Fig 5-12: Scanning electron photomicrograph showing a rutile grain in the centre of the slide comprised almost exclusively of quartz. Photomicrograph taken in backscatter electron mode.

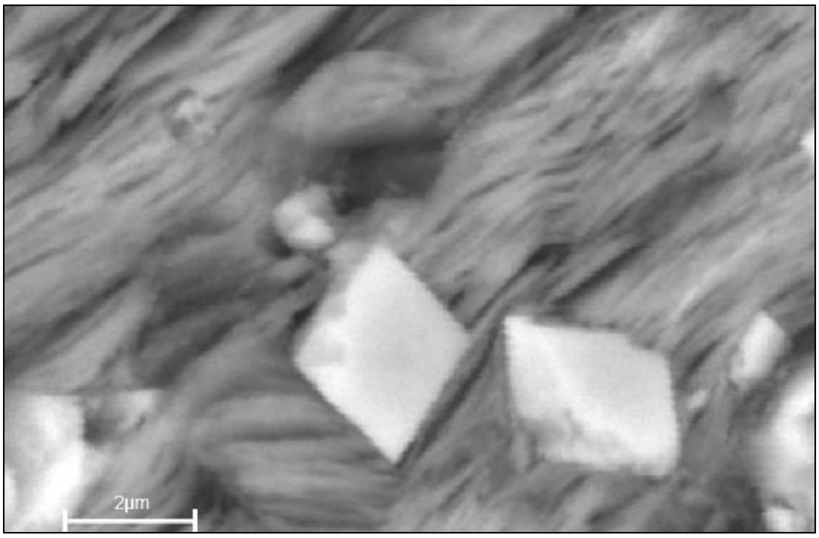

Fig 5-13: Euhedral possibly syn-deformational rutiles in a biotite matrix. This foliation appears to have been formed during growth of the rutile grains as evident by foliation bending around these rutiles. Photomicrograph taken in backscatter electron mode.

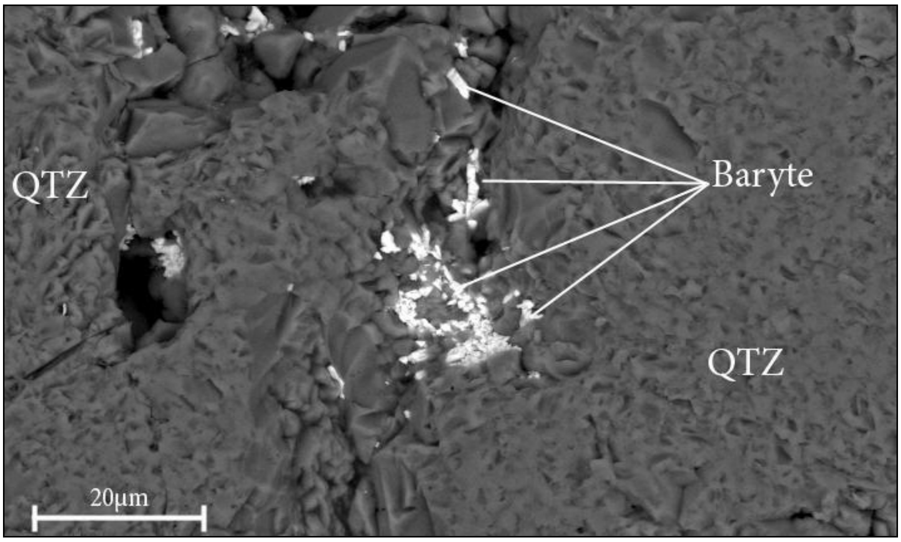

Fig 5-14: Scanning electron photomicrograph showing baryte in cracks between quartz grains. Photomicrograph taken in backscatter electron mode.

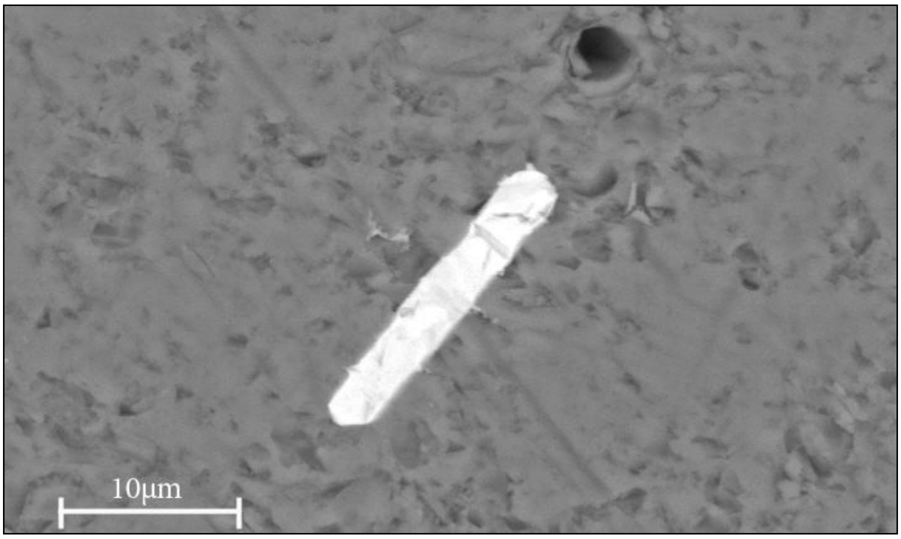

Fig 5-15: Scanning electron photomicrograph of a zircon in Perdepoort Member. Photomicrograph taken in backscatter detection mode.

5.1.2.2 Rooirand Member

SEM analyses of the Rooirand Member confirm findings using petrographic microscopes. Although the rocks still contains a large amount of quartz, there is a substantial increase in the proportion of mica, rutile, hematite, apatite, baryte, and rare earth minerals (REM) as compared to the Perdepoort Member. This increase in the proportion of matrix minerals is clearly visible in Fig 5-16.

Hematite largely occupies cracks as can be seen in Fig 5-5 and Fig 5-17. Close up views of monazite can be seen in Fig 5-19 and Fig 5-20. In the case of the Rooirand Member it appears that many of the accessory minerals are detrital (Fig 5-19 and Fig 5-20), however some also show a faint foliation (Fig 5-18).

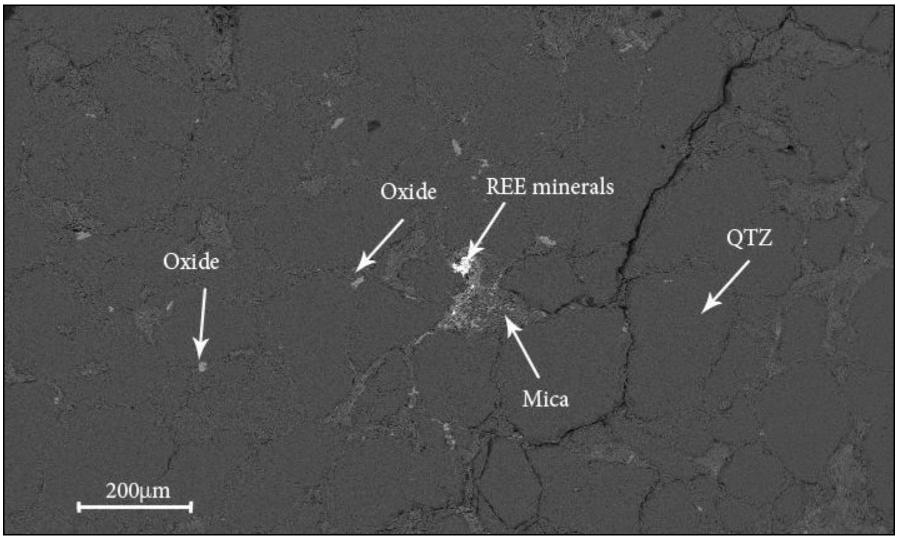

Fig 5-16: Scanning electron photomicrograph showing the overall composition of the Rooirand Member. Quartz commonly constitutes a large component of the sample. Brighter areas indicate different minerals which possess higher atomic numbers such as mica, oxides such as hematite and rutile. The very bright area in the middle of the photomicrograph indicates rare earth elements predominantly in the form of monazite. Photomicrograph taken in backscatter electron mode.

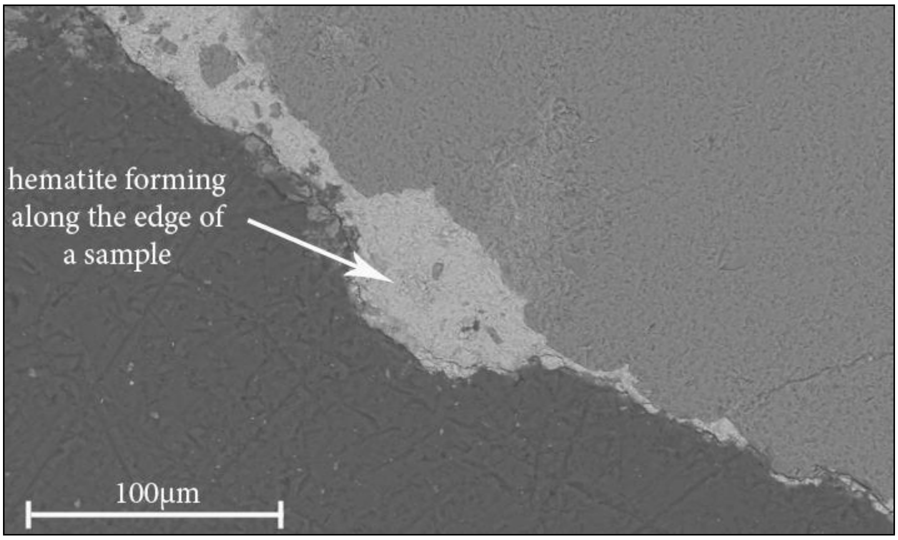

Fig 5-17: Scanning electron photomicrograph showing iron oxides filling a crack located at the edge of a sample of Rooirand Member rock. Photomicrograph taken in backscatter electron mode.

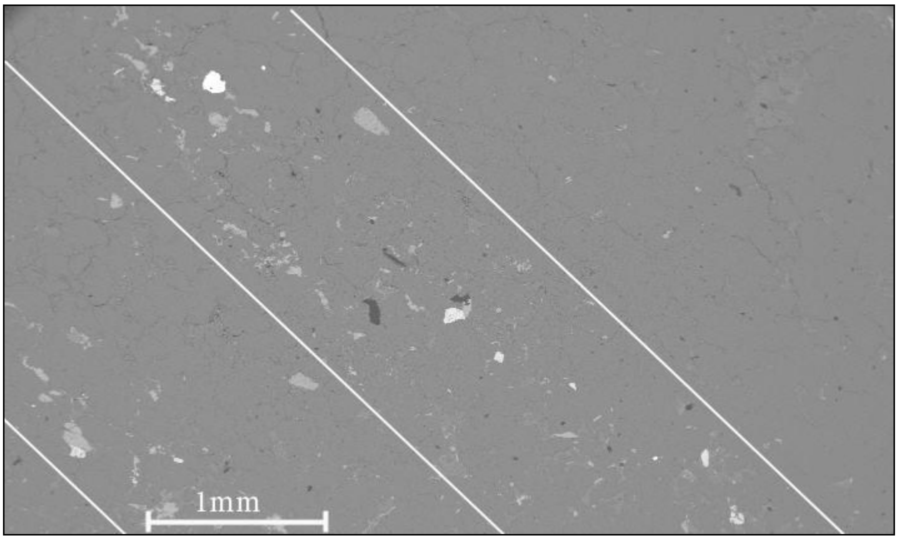

Fig 5-18: Scanning electron photomicrograph showing a lineation, possibly a bedding plane, formed by oxides and rare earth minerals (indicated by white lines). Photomicrograph taken in backscatter electron mode.

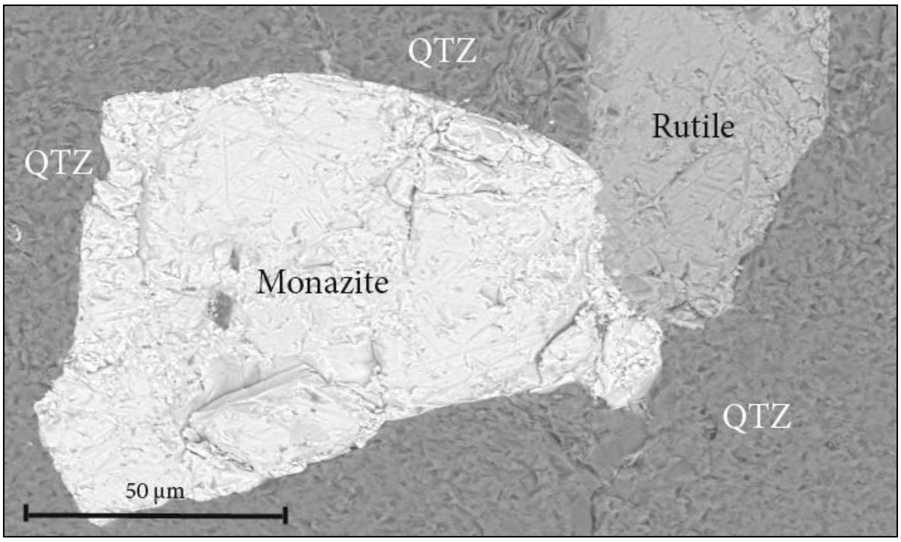

Fig 5-19: Scanning electron photomicrograph showing a rutile grain adjacent to a monazite surrounded by quartz, these oxides and rare earth minerals are more abundant in the quartzites of the Rooirand Member than the Perdepoort Member. Photomicrograph taken in backscatter electron mode.

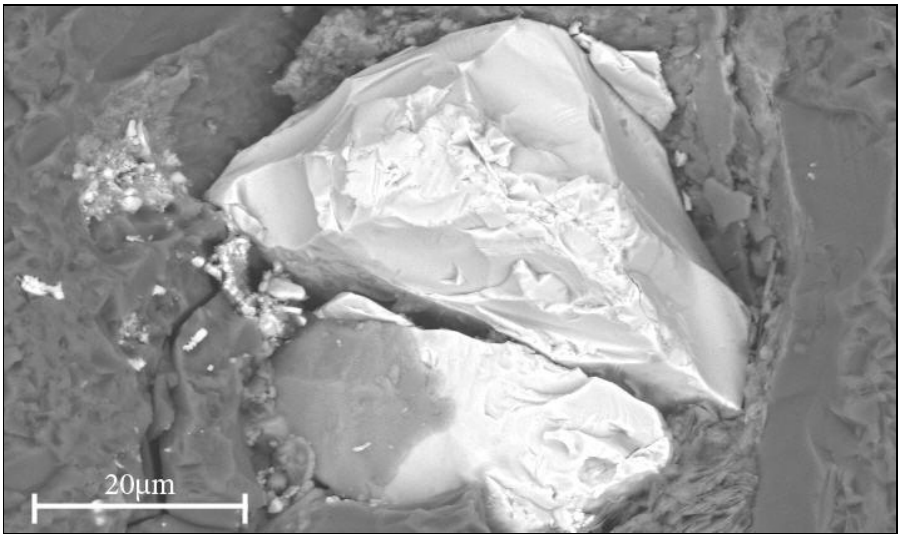

Fig 5-20: Scanning electron photomicrograph showing another rare earth mineral which displaying a composition suggestive of monazite. Photomicrograph taken in backscatter electron mode

5.2 Geochemistry

The mean weight percentage and standard deviation of major elements and H_2O loss on ignition for samples from the Rooirand- and Perdepoort Members are presented in Table 5-3. The analysis for all samples is presented in Table 5-4.

Table 5-3: The mean weight percentages and standard deviation of major elements and loss on ignition (H_2O) in samples from the Rooirand- and Perdepoort- Members (from XRF

	Perdepoort n=16		Rooirand n=4	
	Mean	Std. Dev.	Mean	Std. Dev.
SiO_2	98.09	1.34	93.88	2.25
TiO_2	0.16	0.17	0.50	0.35
Al_2O_3	1.15	0.76	3.03	1.44
Fe_2O_3(t)	0.43	0.15	1.09	0.66
MnO	0.01	0.00	0.01	0.00
MgO	0.03	0.02	0.08	0.06
CaO	0.01	0.01	0.02	0.01
Na_2O	0.00	0.00	0.00	0.00
K_2O	0.27	0.21	0.96	0.75
P_2O_5	0.06	0.01	0.03	0.01
Cr_2O_3	0.00	0.00	0.00	0.00
L.O.I.	0.32	0.15	0.62	0.19

Table 5-4: Major elements found in Perdepoort- and Rooirand Member samples. All values are in weight percentage.

	P1	P2	P3	P4	P5	P6	P7	R1	R2	P8	P9	P10	R3	R4	P11	P12	P13	P14	P15	P16	P17	P18
SiO_2	99.48	97.33	99.49	99.34	98.84	99.28	96.12	94.41	90.57	99.63	98.99	96.46	95.46	95.09	97.45	98.61	96.90	95.43	98.33	97.76	98.33	97.76
TiO_2	0.15	0.44	0.19	0.01	0.02	0.01	0.16	1.01	0.39	0.03	0.18	0.21	0.23	0.37	0.37	bdl	0.07	0.58	0.15	0.13	0.15	0.13
Al_2O_3	0.39	1.29	0.19	0.15	0.76	0.64	1.91	2.81	4.93	0.50	0.87	2.34	1.43	2.94	1.31	0.77	2.44	2.30	1.11	1.51	1.11	1.51
Fe_2O_3(t)	0.38	0.33	0.40	0.52	0.38	0.32	0.47	0.85	1.33	0.29	0.41	0.56	1.87	0.32	0.48	0.34	0.38	0.91	0.29	0.48	0.29	0.48
MnO	0.005	0.005	0.012	0.009	0.009	0.011	0.007	0.008	0.014	0.006	0.008	0.009	0.012	0.004	0.007	0.004	0.006	0.008	0.005	0.007	0.005	0.007
MgO	0.01	0.03	0.01	0.01	0.02	0.01	0.06	0.09	0.15	bdl	0.01	0.04	0.03	0.04	0.04	0.01	0.05	0.06	0.02	0.03	0.02	0.03
CaO	bdl	bdl	0.02	0.01	0.01	bdl	0.15	0.03	0.02	bdl	bdl	bdl	0.01	0.01	0.01	bdl	0.01	0.02	0.03	bdl	0.03	bdl
Na_2O	bdl	bdl	bdl	bdl	bdl	bdl	bdl	bdl	bdl	bdl	bdl	bdl	bdl	0.06	bdl	bdl	bdl	bdl	bdl	bdl	bdl	bdl
K_2O	0.05	0.32	0.01	0.01	0.13	0.14	0.50	0.76	2.05	0.09	0.20	0.61	0.38	0.63	0.34	0.16	0.57	0.57	0.24	0.39	0.24	0.39
P_2O_5	0.006	0.056	0.149	0.194	0.033	0.009	0.251	0.032	0.026	0.033	0.029	0.013	0.033	0.016	0.025	0.071	0.009	0.038	0.018	0.026	0.018	0.026
Cr_2O_3	0.001	0.001	0.002	bdl	0.001	0.001	bdl	0.003	0.002	0.001	0.001	0.002	bdl	bdl	0.002	bdl	bdl	0.001	0.001	0.001	0.001	0.001
L.O.I.	0.12	0.38	0.14	0.26	0.27	0.15	0.62	0.57	0.88	0.22	0.29	0.45	0.43	0.59	0.34	0.15	0.44	0.60	0.38	0.38	0.38	0.38

** III: P=Perdepoort Member sample; R=Rooirand Member sample; bdl=below detection limit*

The r^2 correlation matrices in Table 5-5, Table 5-6, and Table 5-7 highlight any correlations between both major and trace elements, indicating possible chemical or physical relationships. Element correlations are colour coded; elements that correlate extremely well are highlighted in blue ($r^2 > 0.9$), good correlations are highlighted in green ($r^2 <0.9>0.8$) and reasonable correlations in yellow ($r^2 <0.8>0.6$).

Table 5-5: Correlation matrix of major elements.

	SiO_2	TiO_2	Al_2O_3	Fe_2O_3(t)	MnO	MgO	CaO	K_2O	P_2O_5	Cr_2O_3	L.O.I.
SiO_2	1.00	0.37	0.91	0.44	0.10	0.88	0.01	0.88	0.02	0.40	0.88
TiO_2		1.00	0.29	0.12	0.00	0.30	0.00	0.20	0.02	0.42	0.29
Al_2O_3			1.00	0.22	0.04	0.84	0.01	0.91	0.06	0.37	0.86
Fe_2O_3(t)				1.00	0.38	0.30	0.02	0.28	0.01	0.36	0.26
MnO					1.00	0.15	0.02	0.15	0.01	0.21	0.04
MgO						1.00	0.04	0.92	0.00	0.41	0.79
CaO							1.00	0.00	0.44	0.11	0.11
K_2O								1.00	0.04	0.28	0.77
P_2O_5									1.00	0.01	0.00
Cr_2O_3										1.00	0.29
L.O.I.											1.00

Table 5-6: Correlation matrix of major and trace elements.

	Ba	Ce	Cr	Cu	Ga	Hf	La	Nb	Nd	Pb	Rb	Sr	Th	V	Y	Zn	Zr
SiO_2	0.82	0.21	0.00	0.15	0.86	0.01	0.00	0.40	0.04	0.71	0.89	0.46	0.15	0.75	0.42	0.13	0.22
TiO_2	0.13	0.77	0.01	0.02	0.21	0.82	0.19	0.99	0.69	0.61	0.20	0.05	0.84	0.70	0.95	0.13	0.91
Al_2O_3	0.84	0.15	0.00	0.09	0.95	0.01	0.00	0.33	0.05	0.65	0.96	0.46	0.13	0.70	0.33	0.16	0.15
Fe_2O_3(t)	0.29	0.05	0.03	0.19	0.14	0.00	0.00	0.12	0.00	0.30	0.26	0.03	0.01	0.23	0.18	0.00	0.08
MnO	0.11	0.00	0.00	0.01	0.17	0.02	0.02	0.00	0.01	0.09	0.22	0.02	0.02	0.03	0.02	0.01	0.00
MgO	0.83	0.17	0.06	0.14	0.78	0.04	0.10	0.34	0.07	0.68	0.91	0.49	0.21	0.66	0.38	0.19	0.20
CaO	0.00	0.00	0.00	0.33	0.00	0.08	0.18	0.00	0.06	0.00	0.00	0.18	0.57	0.00	0.01	0.80	0.00
K_2O	0.92	0.09	0.00	0.06	0.82	0.00	0.02	0.24	0.02	0.63	0.99	0.52	0.07	0.61	0.26	0.17	0.10
P_2O_5	0.04	0.00	0.01	0.05	0.00	0.07	0.02	0.03	0.05	0.03	0.00	0.03	0.01	0.07	0.04	0.03	0.02
Cr_2O_3	0.22	0.32	0.01	0.03	0.47	0.09	0.03	0.42	0.23	0.49	0.33	0.08	0.49	0.48	0.52	0.00	0.36
L.O.I.	0.71	0.21	0.00	0.22	0.83	0.00	0.02	0.34	0.04	0.60	0.80	0.47	0.16	0.69	0.33	0.23	0.18

Table 5-7: Correlation matrix of all trace elements.

	Ba	Ce	Cr	Cu	Ga	Hf	La	Nb	Nd	Pb	Rb	Sr	Th	V	Y	Zn	Zr
Ba	1.00	0.05	0.01	0.06	0.78	0.00	0.07	0.16	0.01	0.46	0.92	0.58	0.03	0.55	0.18	0.16	0.05
Ce		1.00	0.05	0.05	0.13	0.62	0.64	0.80	0.93	0.38	0.12	0.04	0.82	0.54	0.81	0.35	0.83
Cr			1.00	0.01	0.00	0.06	0.66	0.04	0.01	0.00	0.00	0.06	0.02	0.08	0.04	0.15	0.05
Cu				1.00	0.05	0.07	0.01	0.02	0.02	0.09	0.03	0.07	0.03	0.08	0.03	0.09	0.01
Ga					1.00	0.00	0.00	0.24	0.10	0.54	0.88	0.51	0.13	0.66	0.28	0.16	0.09
Hf						1.00	0.05	0.84	0.59	0.22	0.00	0.05	0.87	0.27	0.77	0.09	0.96
La							1.00	0.19	0.42	0.02	0.00	0.11	0.16	0.02	0.19	0.11	0.24
Nb								1.00	0.72	0.63	0.25	0.06	0.85	0.74	0.94	0.18	0.92
Nd									1.00	0.16	0.04	0.02	0.80	0.38	0.79	0.30	0.71
Pb										1.00	0.60	0.20	0.49	0.73	0.64	0.08	0.51
Rb											1.00	0.47	0.07	0.62	0.26	0.18	0.11
Sr												1.00	0.00	0.32	0.04	0.24	0.00
Th													1.00	0.45	0.89	0.19	0.94
V														1.00	0.75	0.26	0.54
Y															1.00	0.19	0.91
Zn																1.00	0.15
Zr																	1.00

6. Results: Structural Geology

6.1 Introduction

The study area is divided into two zones. Zone 1 is located in the southern half of the study area and Zone 2 the northern half (Fig 6-1 and Fig 6-2). On a megascale zone 1 contains a large overturned anticline/syncline/anticline coupling while zone 2 shows a nearly upright syncline to overturned anticline coupling (Fig 6-2).

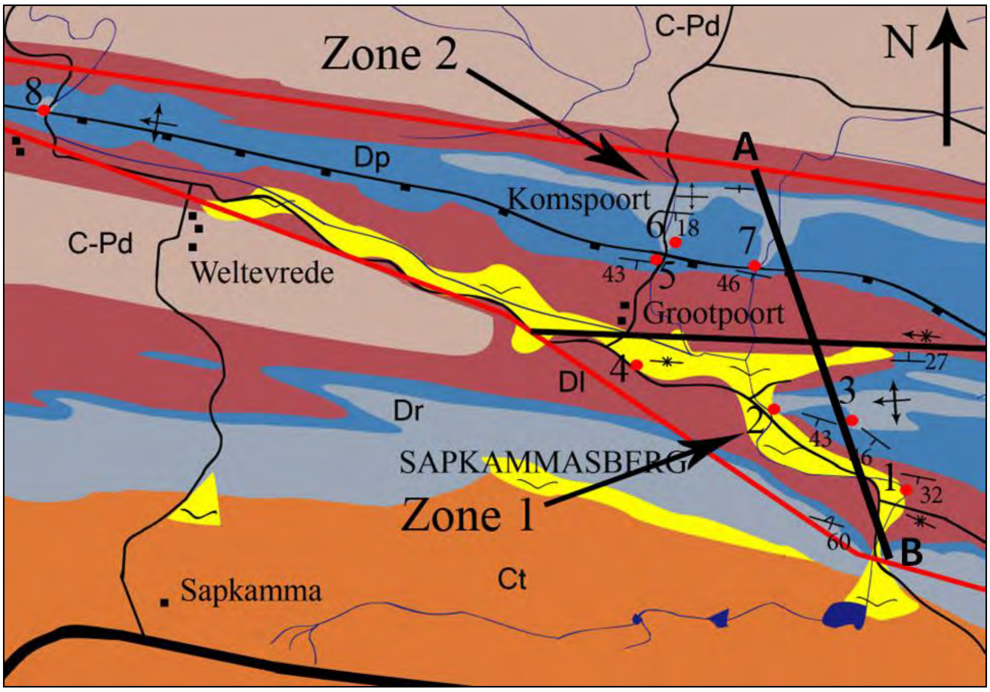

Fig 6-1: Magnified view of geological map. Zone 1 and 2 are indicated with black arrows and are separated by a line running from east to west, the positions of stations 1 to 8 are marked by red dots.

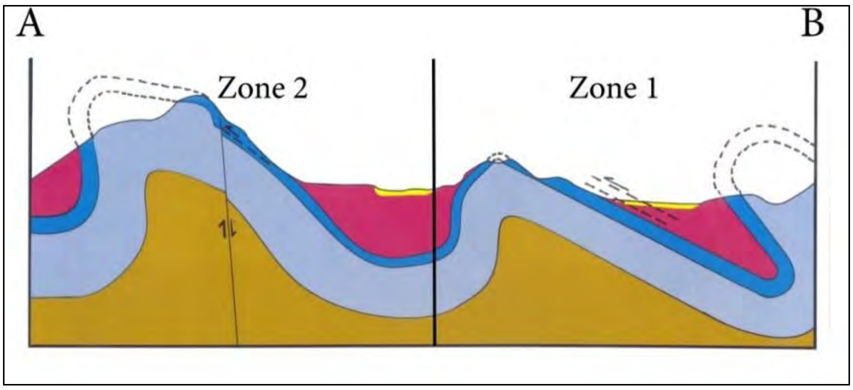

Fig 6-2: Cross sectional view showing the separation between zone 1 and 2

6.2 Zone1

6.2.1 Introduction

Zone 1 (Fig 6-1, Fig 6-2 and Fig 6-3) was mapped by measuring bedding and structural features on outcrop, supplemented by sketches, drawings and photographs. The Rooirand Member outcrops towards the southern extent of zone 1. This is followed by the Perdepoort Member towards the north and finally the more argillaceous strata of the Kweekvlei Formation.

Bedding in zone 1 was found to dip at moderate to steep inclinations in a south-easterly direction (Fig 6-5). Bedding generally displayed an increased dip towards the south.

The main structural controlling factor of zone 1 is an asymmetric overturned syncline (Fig 6-7). Bedding is overturned in the southern part of zone 1. This was confirmed by the presence of trough cross-bedding which is located in the zone demarcated as Dp in Fig 6-4 (Fig 6-6). The megasyncline has an interlimb angle of 28° and an axial plane that dips at 46°. The fold axis plunges at 5° and the fold can thus be classified as a moderate, sub-horizontally plunging tight fold (Fig 6-7).

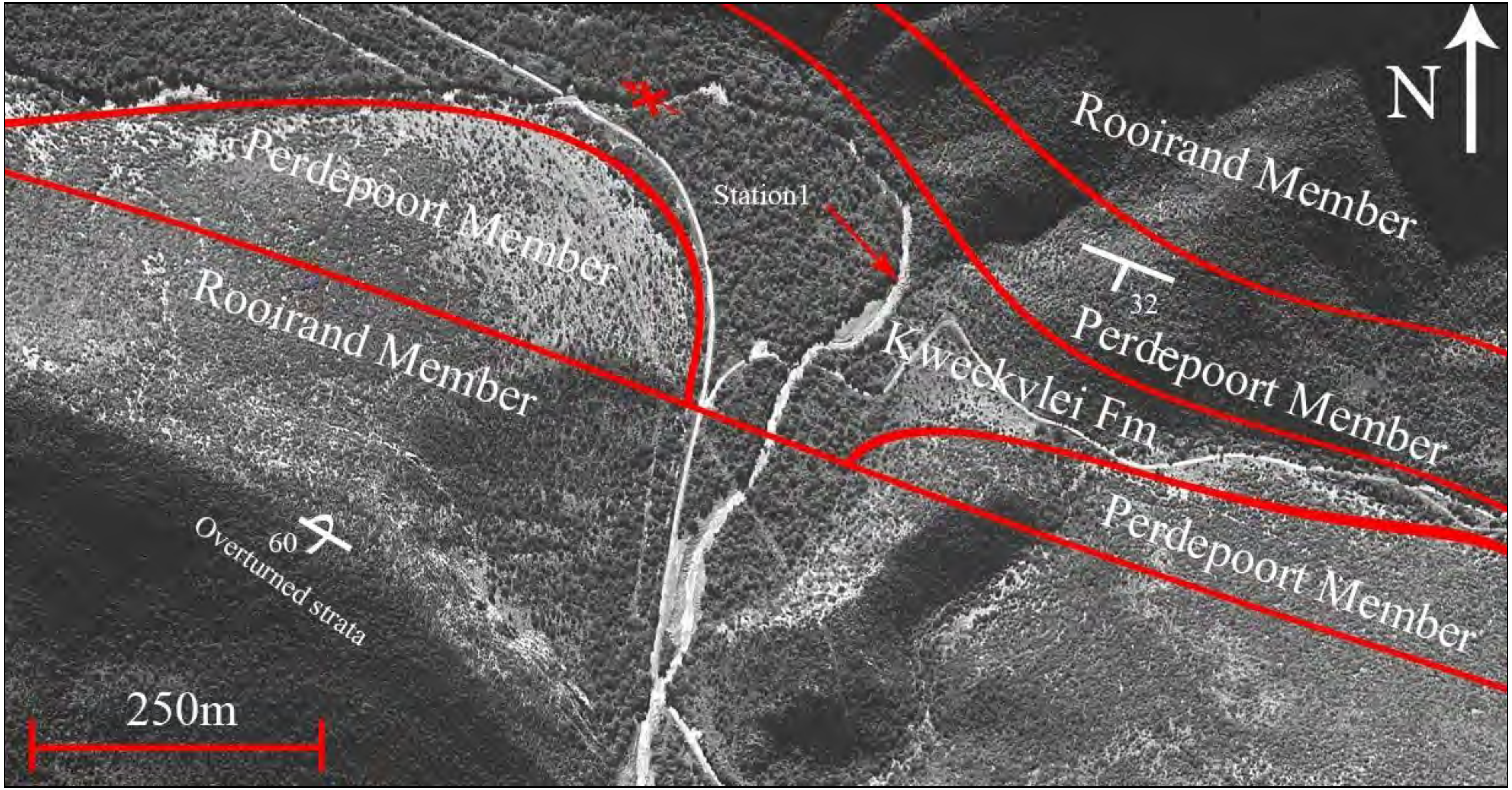

Fig 6-3: Aerial overview of part of zone 1. Contacts between lithologies are indicated as well as the position of station1.

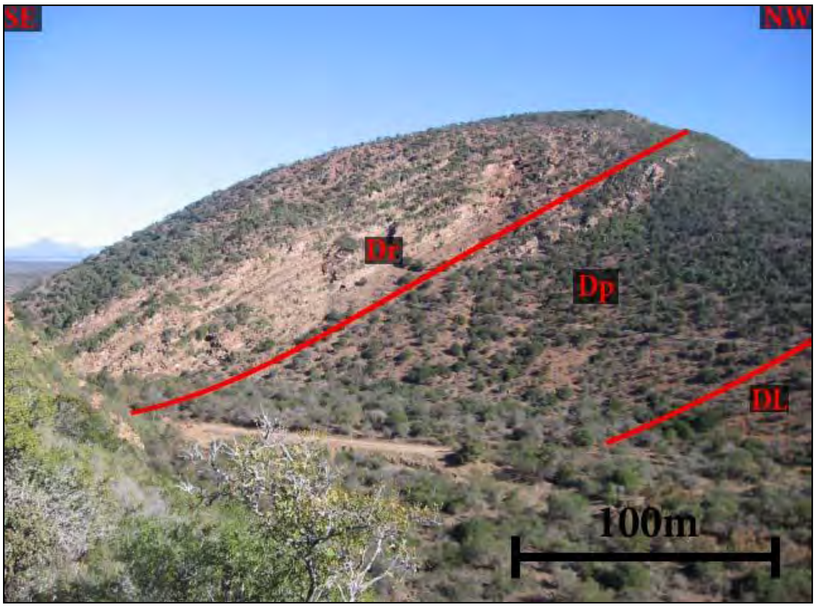

Fig 6-4: The limb of a large overturned syncline is located towards the southern extent of the study area. The succession is Kweekvlei Formation (Dl), Perdepoort-(Dp) and Rooirand Member (Dr). The stratigraphic order is clearly reversed.

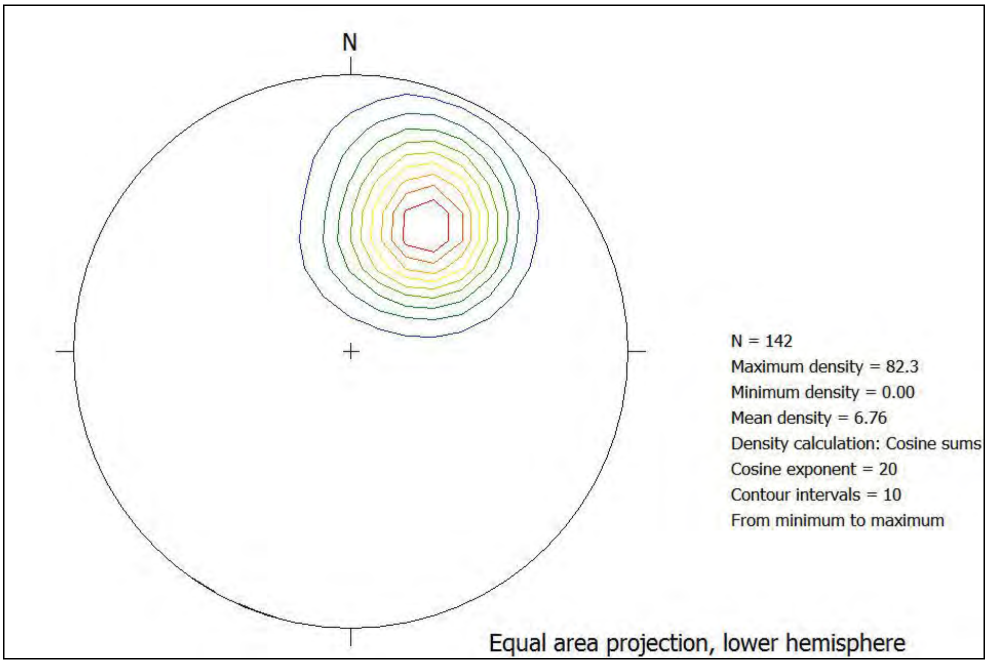

Fig 6-5: Stereogram showing contoured poles to bedding planes in the southern domain of zone 1.

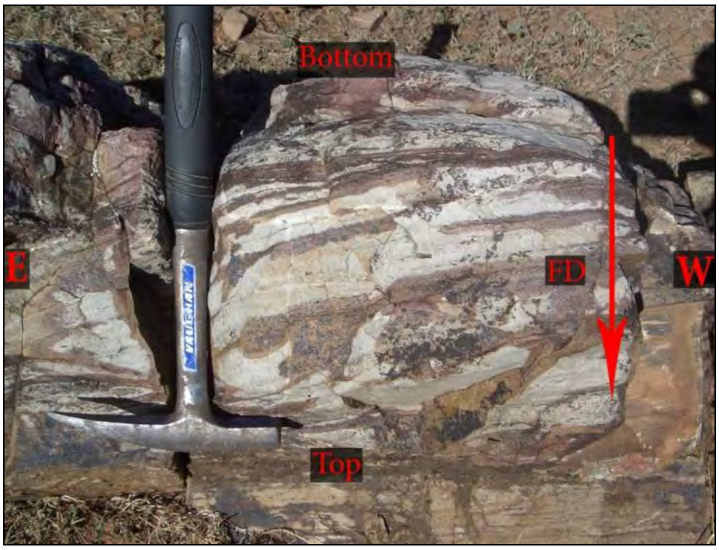

Fig 6-6: Trough cross-bedding indicates that bedding is overturned in the southern extent of zone 1, thus confirming the position of an overturned syncline in zone 1; geological hammer for scale.

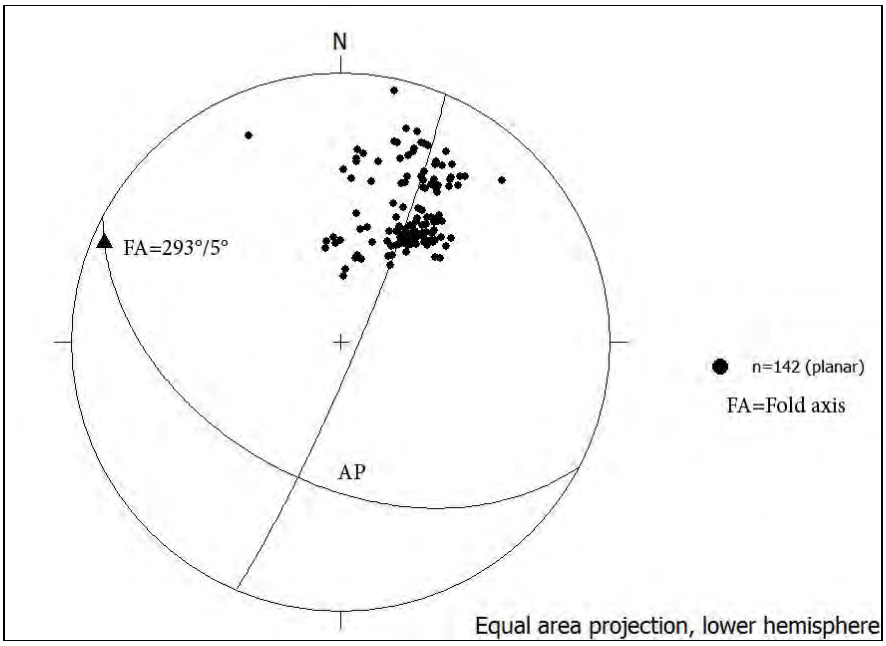

Fig 6-7: Stereogram showing poles to fold limbs of a large overturned syncline which forms the main macroscale feature in zone 1.

6.3 Station 1

6.3.1 Introduction

This station comprises a good outcrop on the eastern bank of a non-perennial riverbed. It is located on the northern, non-overturned limb (long limb) of a large overturned syncline, which forms the main macroscale feature in zone 1 (Fig 6-2 and Fig 6-8). The study section extends for approximately 35m. The dark grey, to black, organic rich shales, which make up the Kweekvlei Formation, constitute the whole outcrop. Average thickness of laminae are estimated at 1cm. Arenaceous horizons are also present. These, also have an average thicknesses of 1cm. Pervasive iron staining was observed and concretions containing increased amounts of what appears to be iron minerals were also observed (Fig 6-23).

Secondary structures observed include thrusting, strike-slip faulting, well-developed cleavage and boundinage. Fore-thrusts are the most abundant secondary structure encountered in the section. Strike-slip faulting appear to have utilized previously formed fore-thrusts and is a major feature of the section. Axial planar cleavage is well developed throughout the section and dips to the south. The cleavage is associated with an overturned syncline, which is the megascale structural feature in zone 1 (Fig 6-2).

Boudins and mullions were also noted in the northern and southern extremities of the section respectively. Boudins display a well-developed boudin train, with boundins being visible in all three dimensions

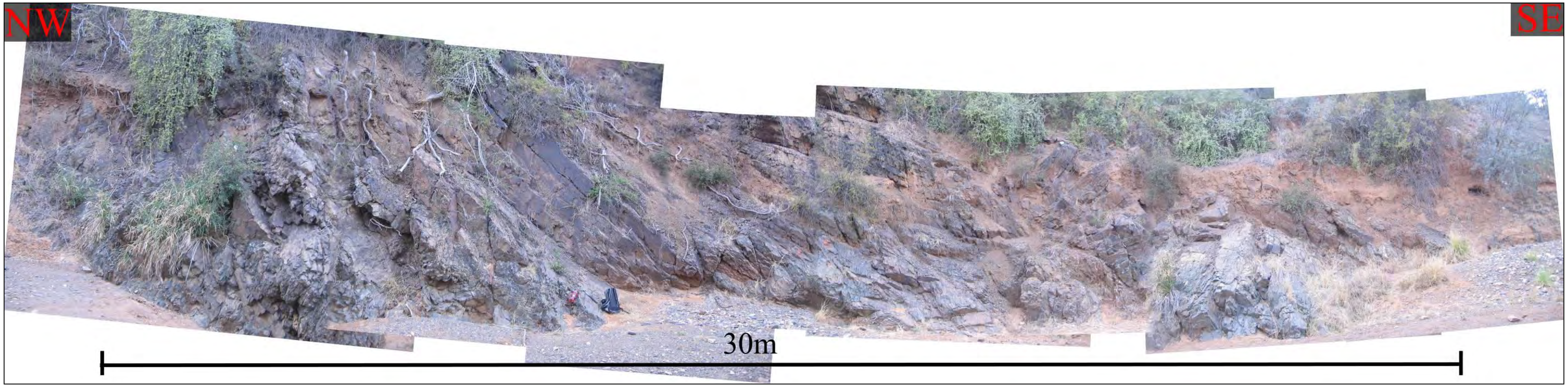

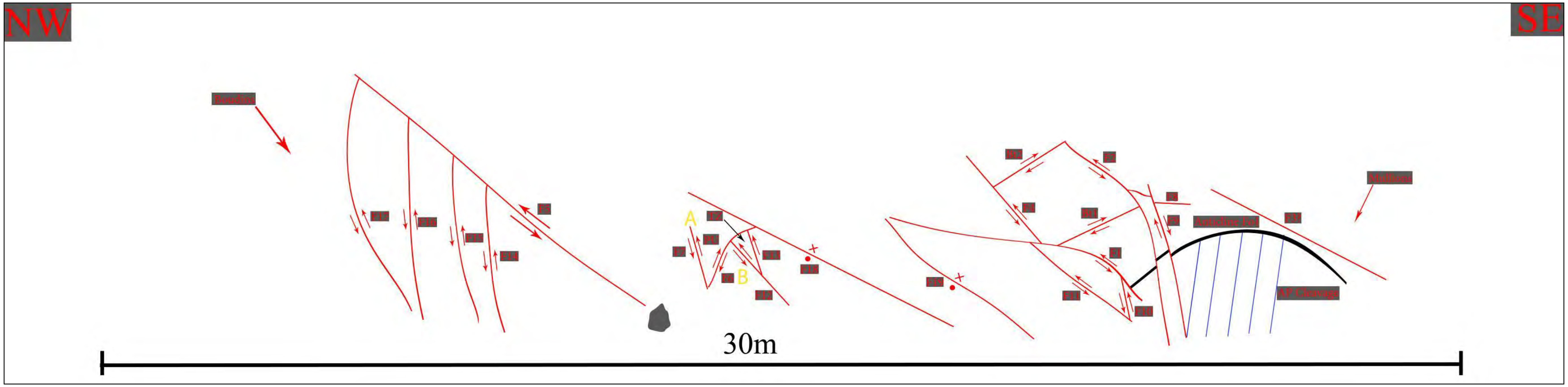

Fig 6-8:Top: Photo showing outcrop of Kweekvlei Shale Formation. Bottom: Cross-sectional overlay of Kweekvlei Shale Formation at station 1. Note complex structural relationship in the centre of the cross-section where a pop-up (A) structure and triangle zone (B) are present as a result of fore- and backthrust cut-off relationships.

6.3.2 Bedding

Bedding is convolute and was identified using evidence such as mineral laminations, ambiguous wave ripples, and load cast structures; the latter two being used as indicators of facing direction (Fig 6-9). Boudinage indicates separation between more competent and less competent layers and may thus designate bedding orientation but not younging direction. Bedding is inferred as being right way-up, correlating with the normal, northern limb of a large overturned syncline which is the macroscale structural feature in zone 1. Bedding dips at moderate angles to the south-west (Fig 6-10).

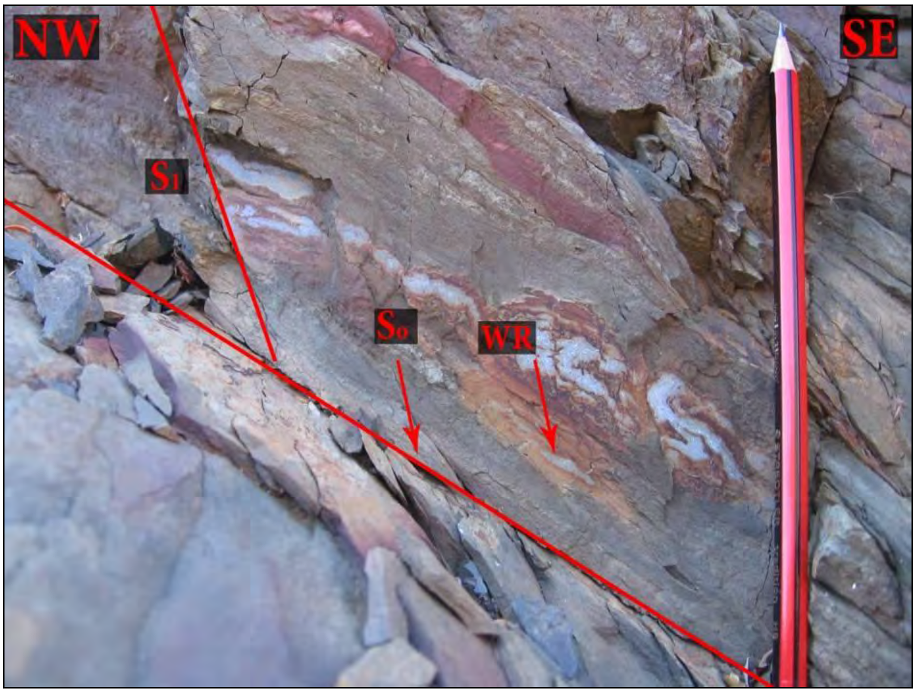

Fig 6-9: Mineral laminations indication bedding (So) orientation in shales of the Kweekvlei Formation. Note southward dipping cleavage (S1) and possible wave ripple (WR).

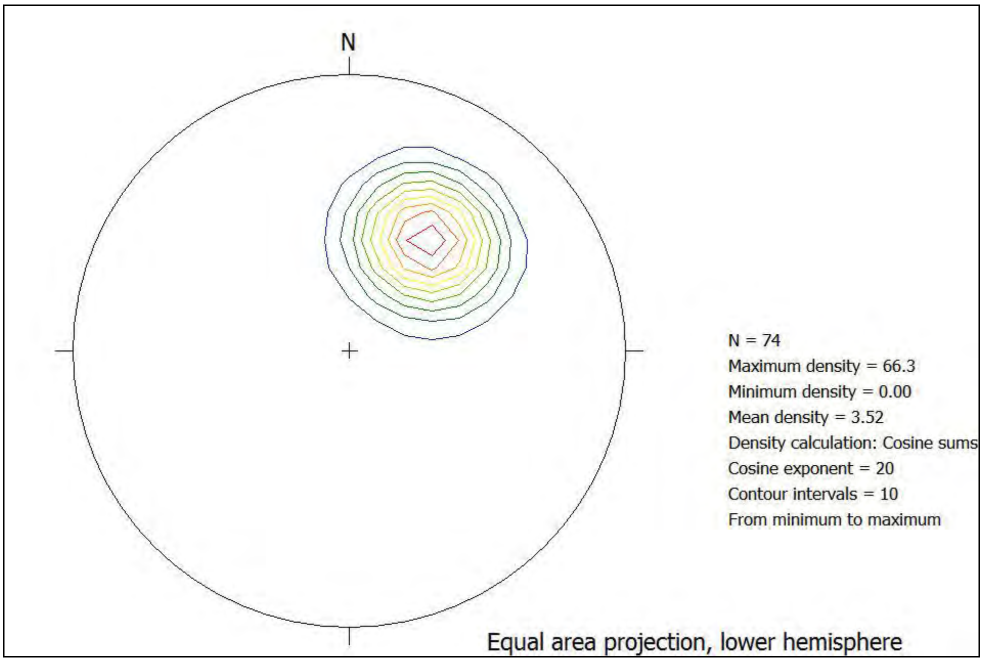

Fig 6-10: Stereogram showing contoured poles to bedding planes at station 1.

6.3.3 Faults

Criteria such as slickensides, fault breccia and fault gouge were utilized in order to determine fault geometry and relative movement. Slickensides are well developed in most instances. However, in certain cases the positions of faults were inferred with the help of observed displacement of known faults by previously suspected faults and vice versa.

Faulting in this section consists primarily of south west dipping fore-thrusts (Fig 6-11), strike-slip faults and minor backthrusts. Only one normal fault is noted, F9 in (Fig 6-8 and Fig 6-14). Thrusting is more closely spaced when compared to the thrusts in quartzites studied at stations 5 to 8 of zone 2. Thrusts frequently display bedding parallel relationships with well developed ramp and flat geometry in places. In certain areas fault cut-off relationships are highly complex making exact determination of the order of development difficult. Several backthrusts are present in the section, two are transected by fore-thrusts and the other forms part of a pop-up structure and triangle zone (Fig 6-12 and Fig 6-16). Two strike-slip faults are noted in the section, these appear to have utilized weaknesses along previously formed thrust fault planes. Two duplex structures are also identified in the section, with F1 and F5 forming the roof thrusts to the imbricate stacks (Fig 6-14 and Fig 6-15).

6.3.3.1 Thrust-faults

Fore-thrusts all dip approximately south-west (Fig 6-11). Thrust fault F1 displays ramp and flat geometry (Fig 6-14). Evidence from slickensides indicates that hanging wall blocks were displaced towards the north-east in fore-thrusts and towards the south-west in backthrusts. The main fore-thrusts at station 1 are F5, F1 and F4 (Fig 6-11, Fig 6-12, Fig 6-13, Fig 6-14 and Fig 6-15). F5 represents a bedding parallel thrust, horizontal principal stresses appear to have taken advantage of pre-existing weaknesses in the bedding plane. In this section this bedding plane weakness enjoys preference over the usual 20° to 25° inclination associated with thrusts formed by horizontal principal stresses (compare Fig 6-11 and Fig 6-19). Simlar features were also noted by Price (1966).

F1 forms the roof-thrust in a duplex structure with F10 and F11. F5 forms the roof thrust in a duplex structure with imbricates F14, F15, F16 and F17 (Fig 6-15). A pop-up structure is formed between F6 and F7 (Fig 6-16).

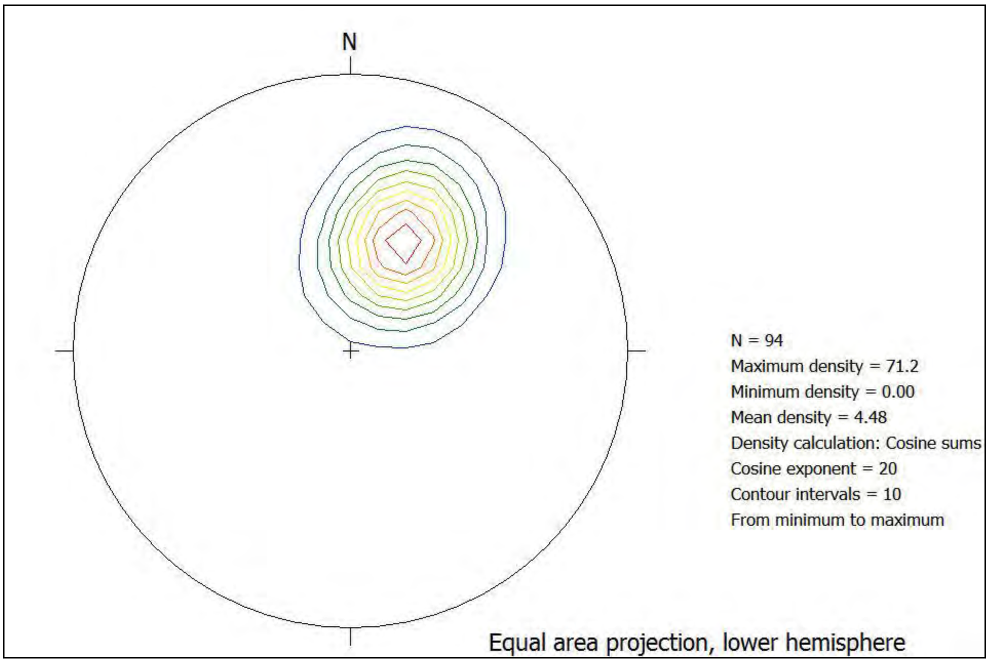

Fig 6-11: Stereogram showing contoured poles to all fore-thrust planes measured at station 1.

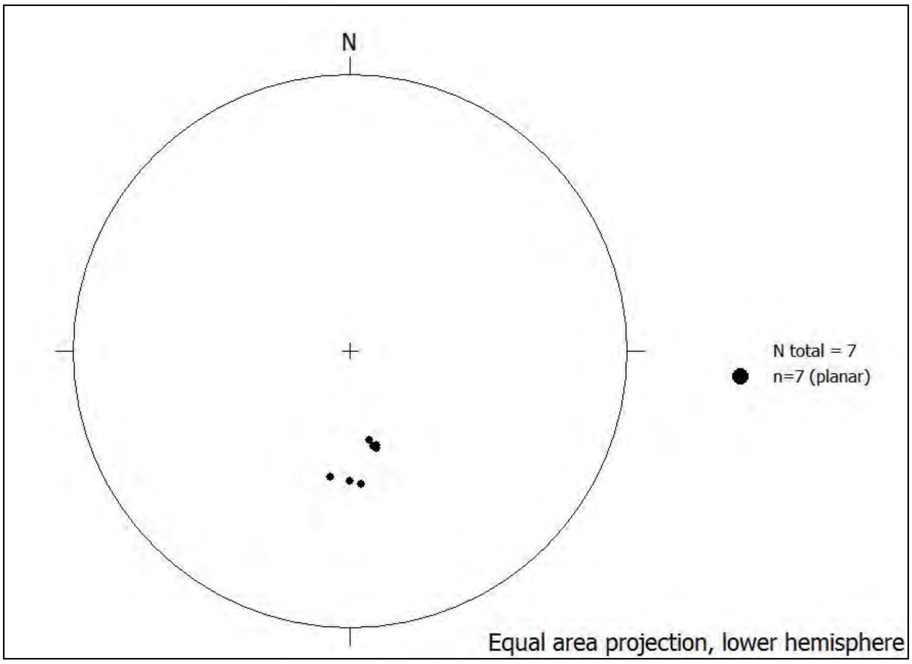

Fig 6-12: Stereogram showing poles to all measured backthrust planes at station 1.

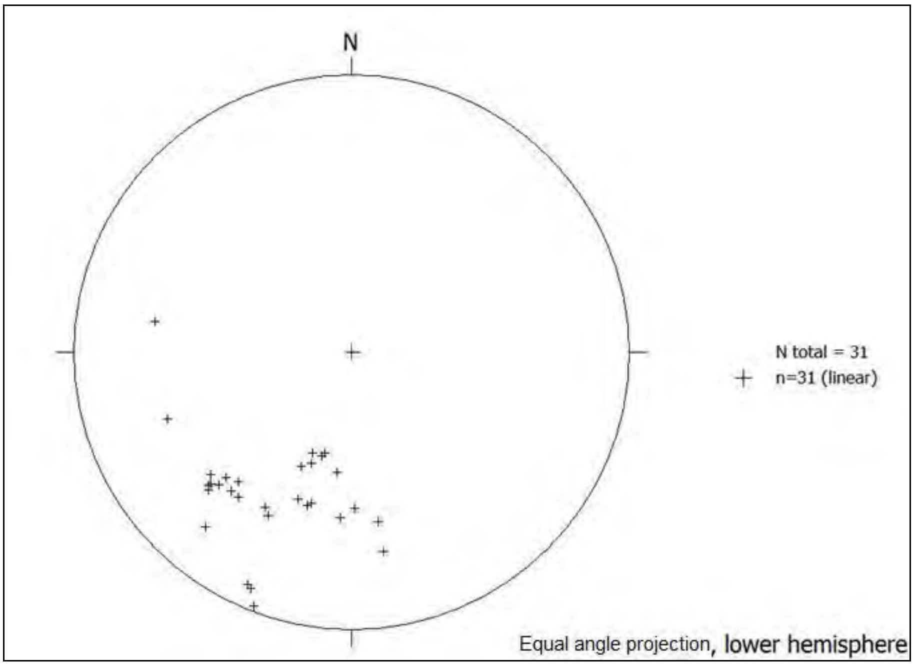

Fig 6-13: Stereogram showing trend and plunge of slickensides on all measured fore-thrust planes at station 1.

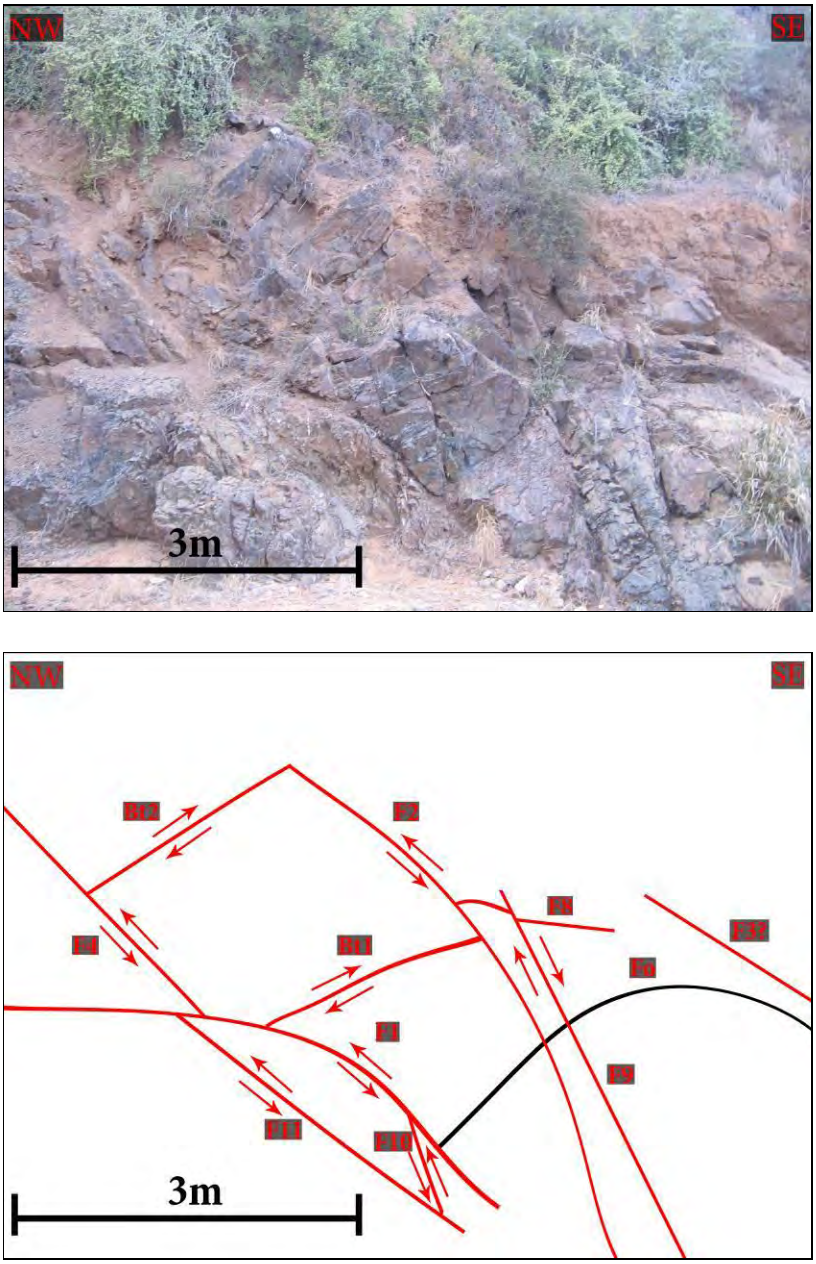

Fig 6-14: Top: Photo showing complex structural relationships towards the south-eastern end of station 1. Bottom: Structural features are highlighte. Note the duplex structure between F1, F10 and F11. Note anticline (Fo) towards the south-east appear to have been cut by F2 and F9. An inferred fault is indicated by F3?, and two backthrusts (Bt) are also present.

A triangle zone was observed adjacent to the pop-up forming between F12 and F13 (Fig 6-8 and Fig 6-16). As shown in Fig 6-14, F2 and F9 are inferred to cut through anticline Fo1. The fault planes only appear to have fractured anticline Fo 1 with minimal movement observed (Fig 6-8 and Fig 6-14). F3 in Fig 6-14 is also an inferred fault.

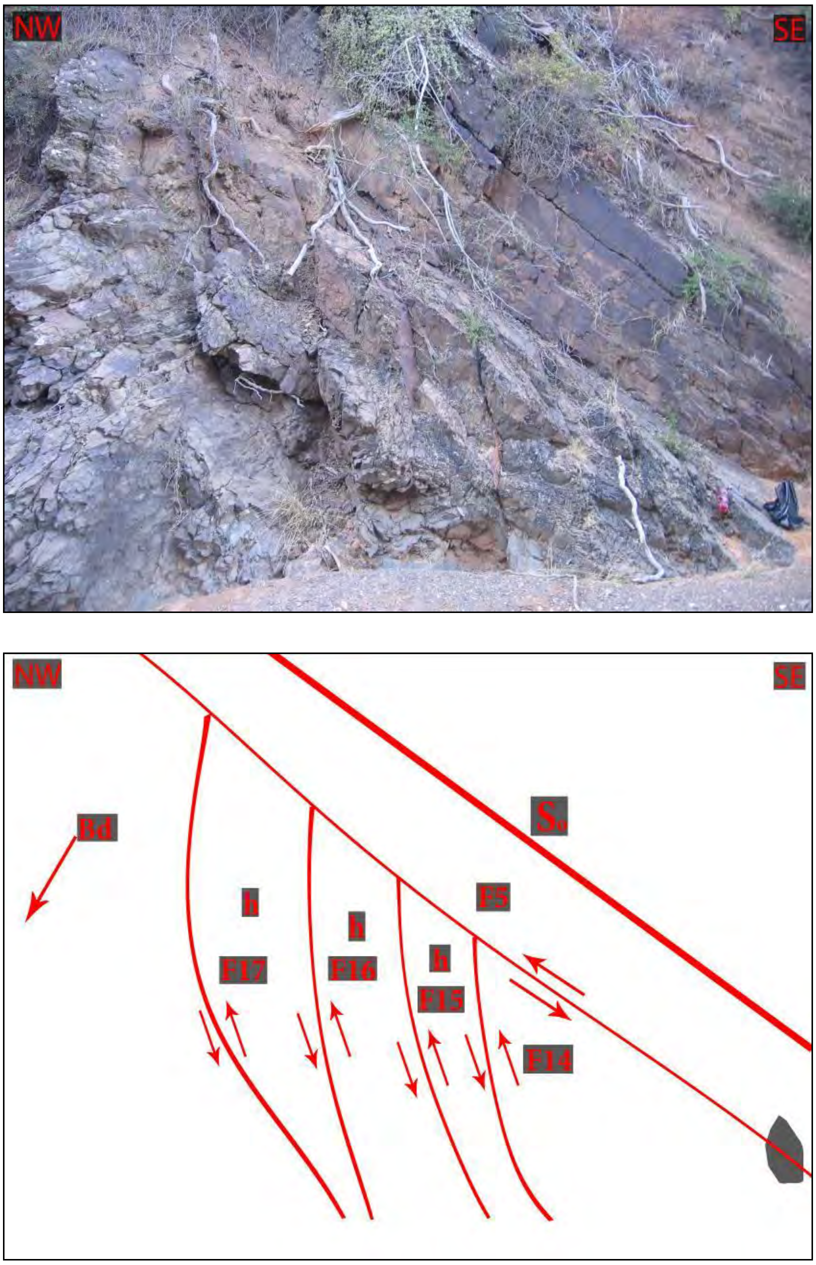

Fig 6-15:Top: Kweekvlei shale Formation showing showingimbricates joining roof thust Bottom: Structural features are indicated. F5 forms the roof thrust to a duplex structure situated at the north-western end of station 1. Multiple imbricates join F5 forming horse structures (h). Bedding orientation is indicated by S_0. The position of boudins is indicated by Bd; backpack, located on the bottom right of the frame, for scale.

The orientations of the more prominent thrust faults differ to some extent. F1 displays differing orientation on its flat compared to its ramp surface. The ramp surface dips in a south south-westerly direction, while the flat dips in a southerly direction (Fig 6-17). Thrust fault F4 on the other hand displays quite variable dip inclinations, but all in a north-westerly direction (Fig 6-18). Thrust fault F5 displays a south-westerly dip (Fig 6-19). The dense grouping of stereo readings indicates a planar shaped fault plane for F5, with no ramp and flat geometry. Imbricate thrusts F14-F17 join F5 flattening out towards the horizontal, at the base of the section (Fig 6-15). At their base they show dips similar to roof thrust F5 (compare Fig 6-19 and Fig 6-20).

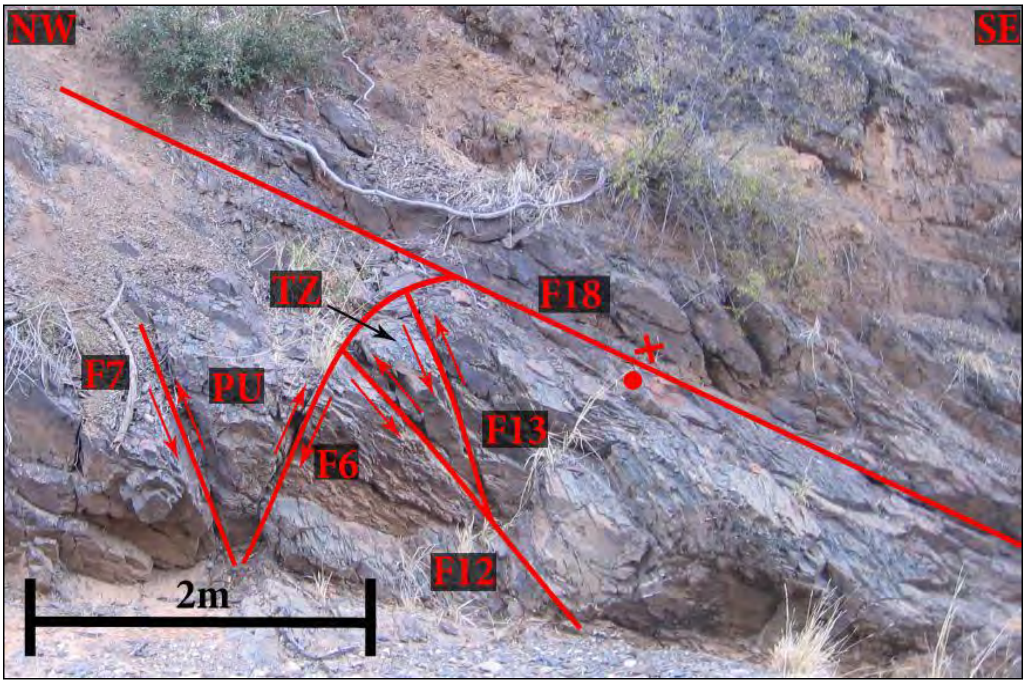

Fig 6-16: High angle fore- and backthrust cut-offs form a pop-up structure (PU) and triangle zone (TZ). Slickensides record strike-slip as the most recent component of movement for F18 (X=eastward displacement, into page ●=westward displacement, out of page).

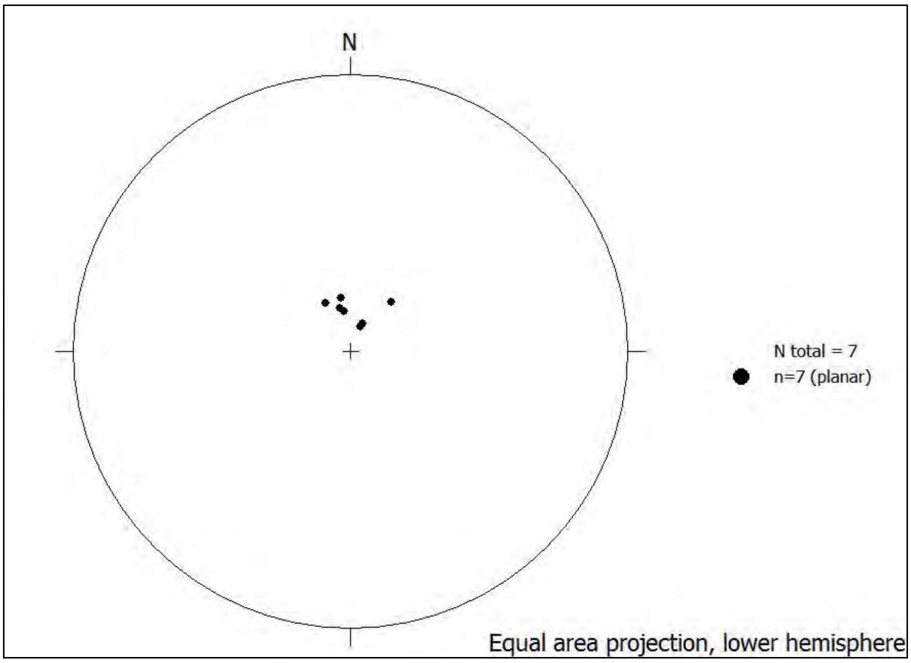

Fig 6-17: Stereogram showing poles to thrust fault plane F1.

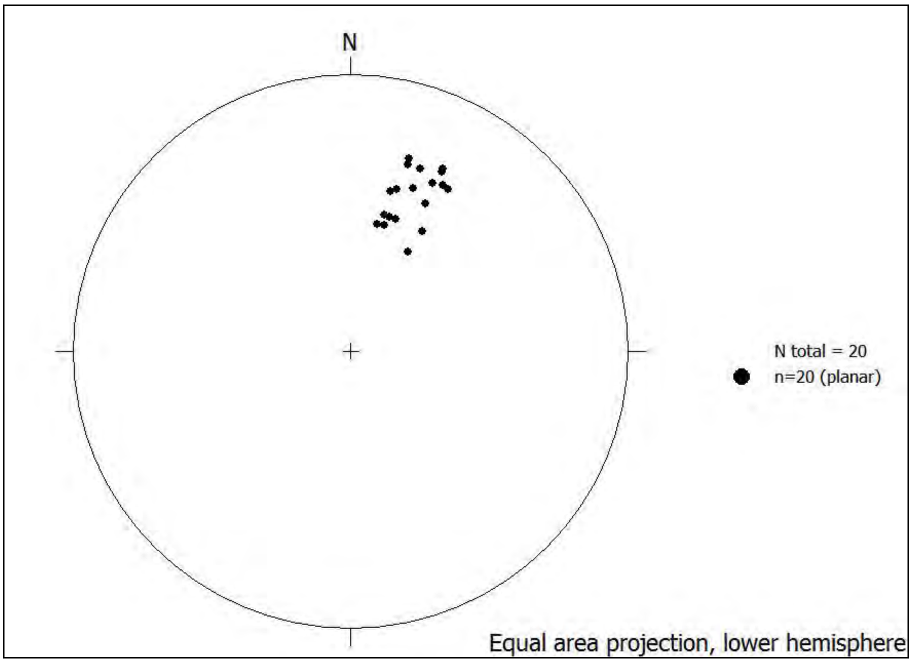

Fig 6-18: Stereogram showing poles to thrust fault plane F4.

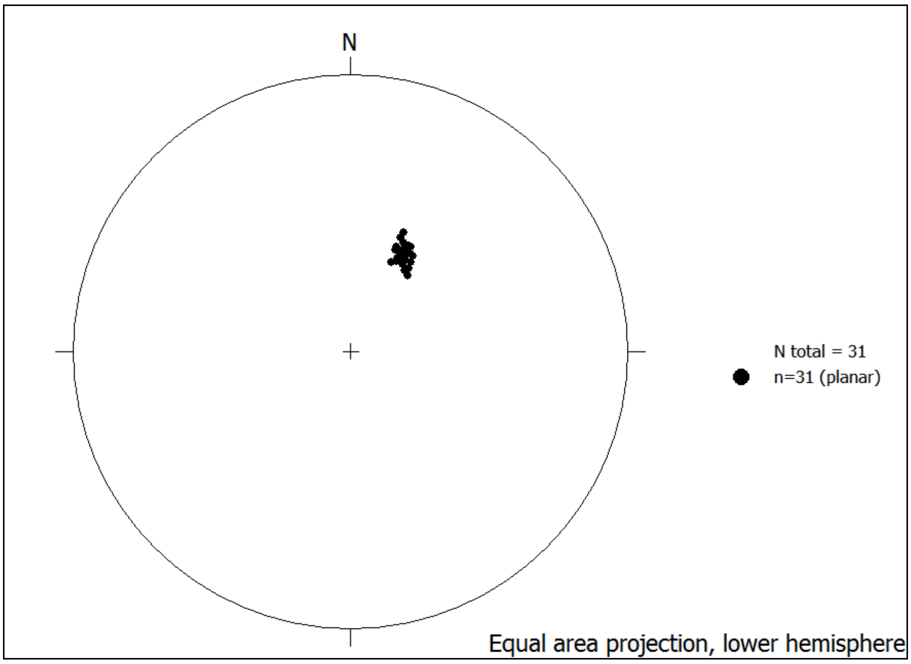

Fig 6-19: Stereogram showing poles to thrust fault plane F5.

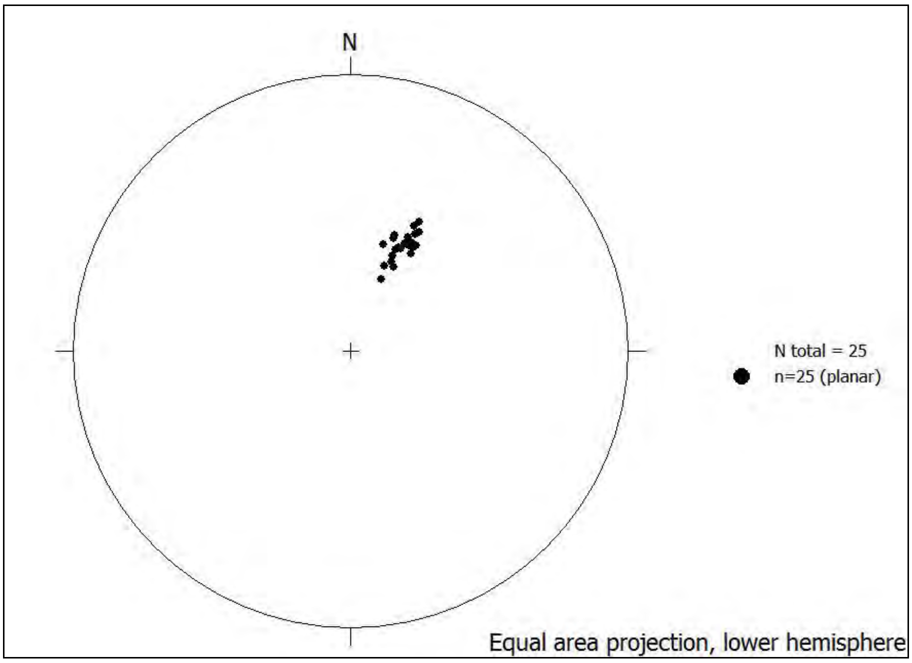

Fig 6-20: Stereogram showing poles to imbricate thrust fault planes F16 and F17.

Subordinate backthrusts are located within the south-eastern and central sectors of station 1. Backthrusts dip north, approximately opposite to fore-thrusts (Fig 6-14 and Fig 6-21). Backthrusts display moderate dips of approximately 45°. Three back-thrusts were observed in the study section, but sense of movement could not be confirmed for F6 as slickensides are poorly developed (Fig 6-14 and Fig 6-16).

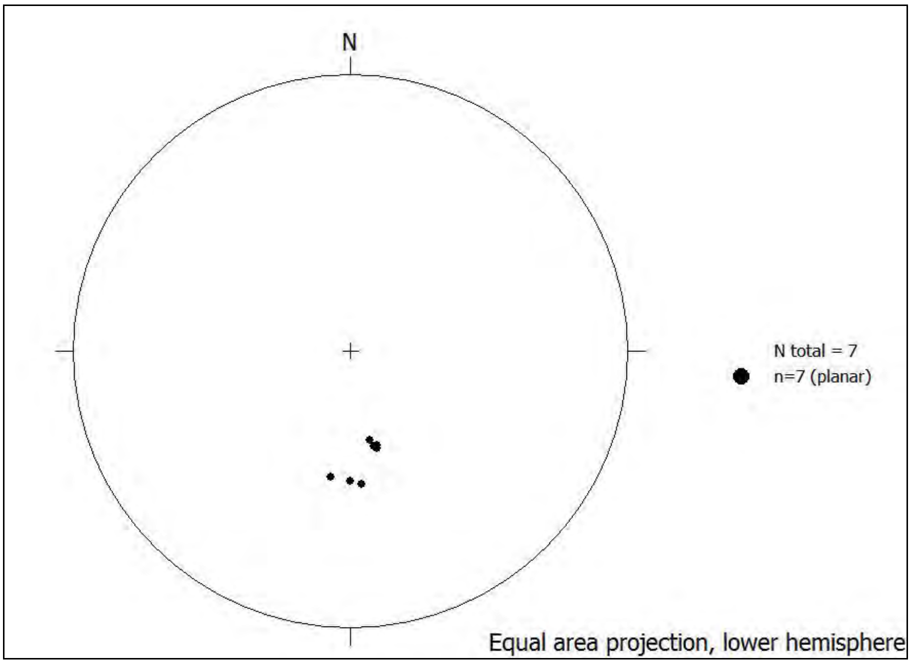

Fig 6-21: Stereogram showing poles to all measured backthrust planes at station 1.

6.3.3.2 Strike-slip faults

F18 has a characteristic thrust fault geometry, although the most recent component indicates strike-slip movement (Fig 6-22 and Fig 6-24). Both strike–slip faults F18 and F19 possess fault planes which show orientations sub-parallel to both bedding and fore thrusts (Fig 6-23, Fig 6-25 and Fig 6-27). However, the most recent movement, as indicated by slickenside evidence, is east-west (Fig 6-24). This is at an angle of approximately 90° to the dip direction of the fault plane, thus the strike-slip component is dominant. Both F18 and F19 are classified as left-lateral (or sinistral) strike- slip faults (Fig 6-23 and Fig 6-24).

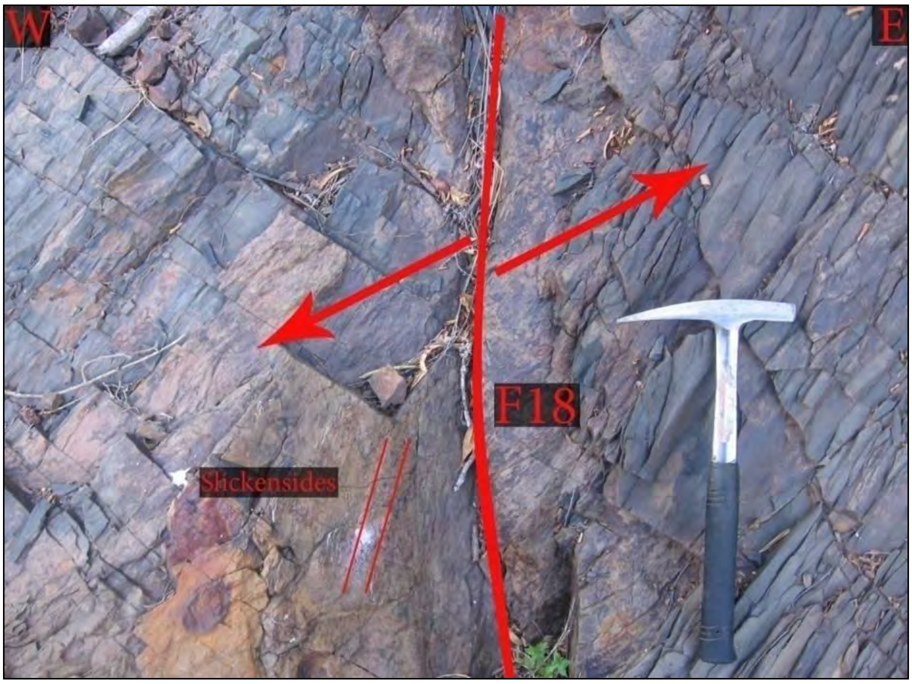

Fig 6-22: Strike-slip fault F18 is classified as a sinistral fault. The footwall block, located on the left of the photo, has clearly moved towards the left, relative to the hanging wall block. Slickensides are also indicated by coloured lines; geological hammer for scale.

Fig 6-23: Strike-slip fault F19 shows sinistral movement. Concretions c are also present on the fault plane; geological hammer for scale. The footwall block, located on the left of the photo, has clearly moved towards the left, relative to the hanging wall block.

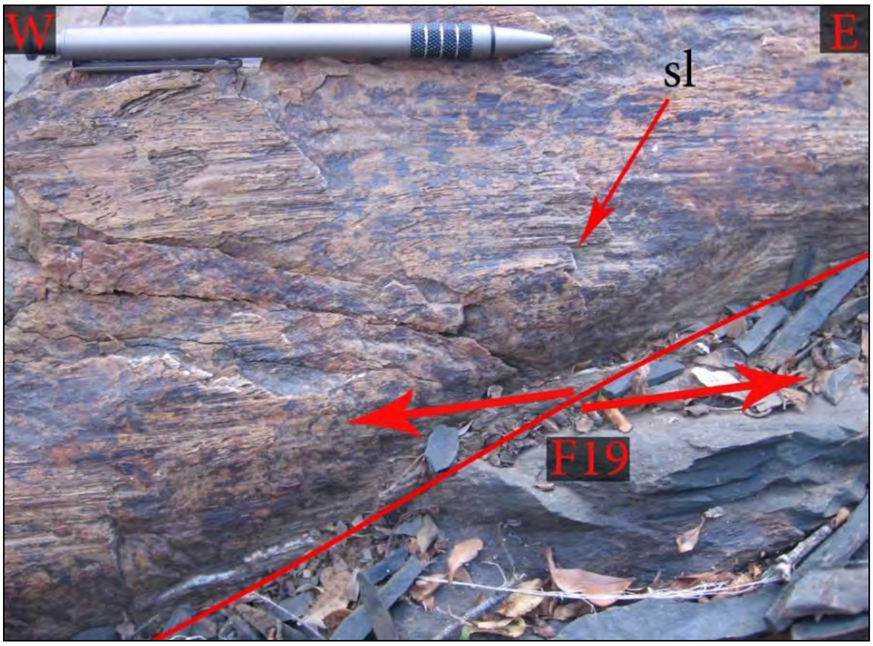

Fig 6-24: Well developed slickenfibres sl associated with strike-slip fault F18. The relative sense of movement is indicated by arrows and slickensides are indicated by sl; pen for scale.

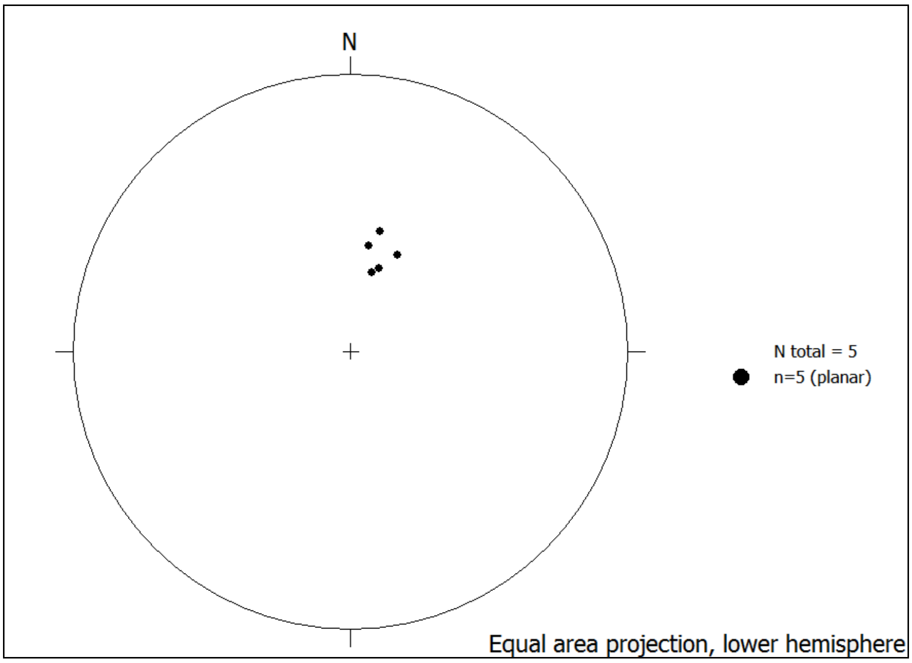

Fig 6-25: Stereogram showing poles to strike-slip fault plane F19.

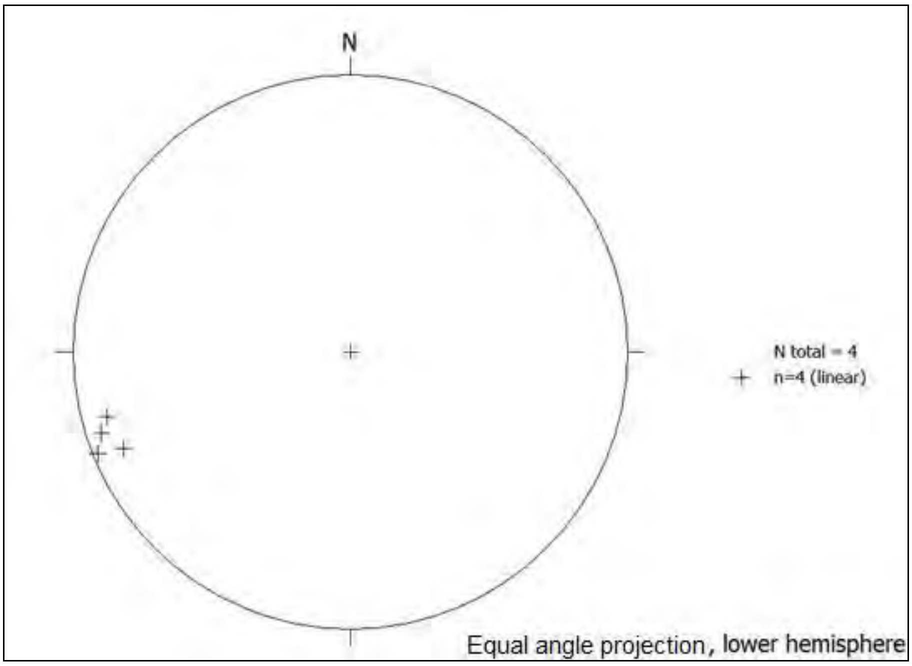

Fig 6-26: Stereogram showing trend and plunge of slickensides on fault plane F19.

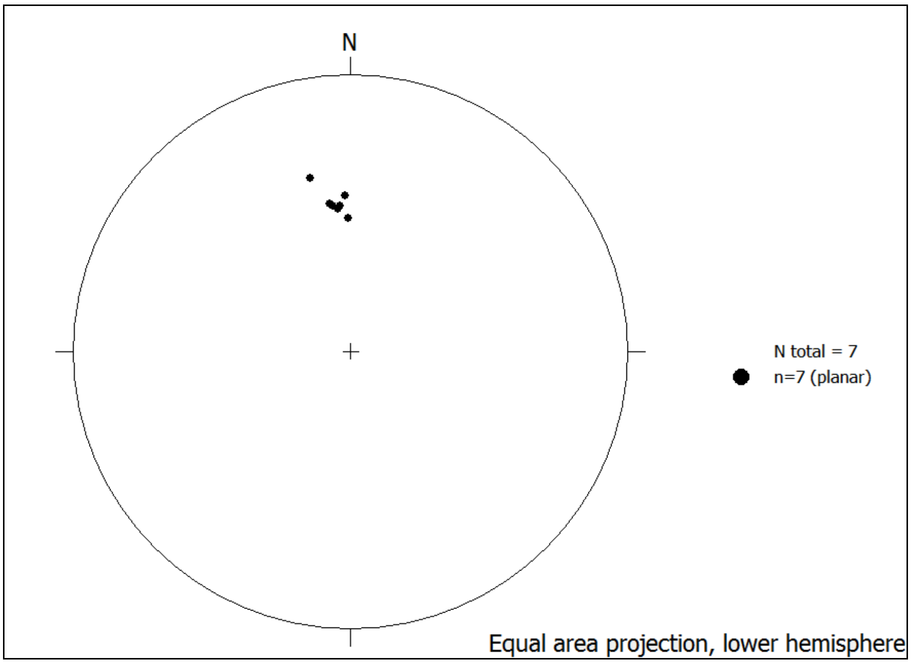

Fig 6-27: Stereogram showing poles to strike-slip fault plane F18.

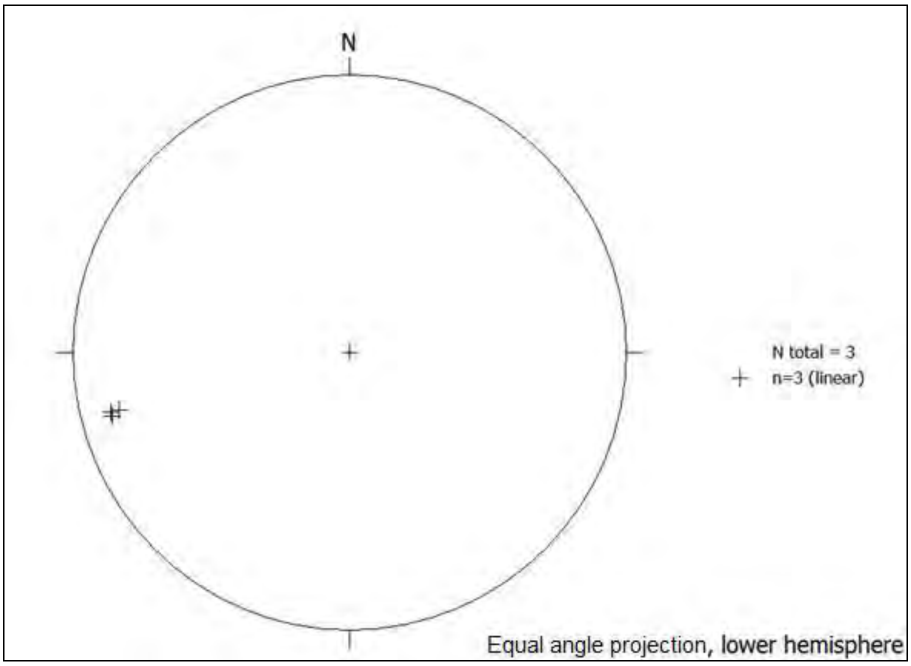

Fig 6-28: Stereogram showing trend and plunge of slickenside on fault plane F18.

6.3.3.3 Normal faults

Only one normal fault F9 is observed at station 1. F9 clearly displaces F8 (Fig 6-14 and Fig 6-29).

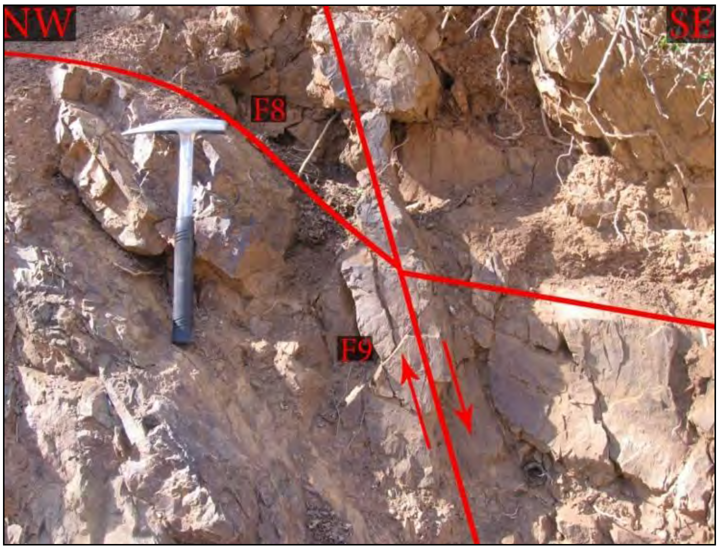

Fig 6-29: Normal fault F9 cut through fault F8; geological hammer for scale.

6.3.4 Lineations

Lineations were found in the form of slickenfibres on fault planes and fold limbs (Fig 6-30). These served mainly to determine the direction of the most recent movement on fault planes. In most cases slickenfibres were well developed, and sense of movement could be deduced. Slickenfibres plunge towards the south and south-west in fore-thrusts, north-northwest in backthrusts, and east-northeast in strike-slip faults. Fore- and backthrusts display similar degrees of plunge regarding slickenfibres, but slickenfibres plunge at a lower inclination on strike-slip faults. Lineations are also present in the form of mullions which are found in the proximity of anticline Fo1, in the south-eastern sector of station 1 (Fig 6-31).

Fig 6-30: Well developed slickenfibres on fault plane F5. Red lines indicate last recorded phase of movement on the fault plane; pen for scale.

Fig 6-31: Mullions on what appears to be a bedding surface; geological hammer for scale.

6.3.5 Folding

Folding at station 1 consists of a single anticline, Fo, located towards the south-eastern end of the section (Fig 6-32). Station 1 is located on the normal limb of a large overturned anticline that forms the main macroscale feature in zone 1. The fold axis of anticline Fo has a trend and plunge of 271°/30° (Fig 6-33). The axial plane has an azimuth and dip of 181°/89° and the interlimb angle is 41°. Fo can thus be classified as a moderately inclined, gently-plunging close fold.

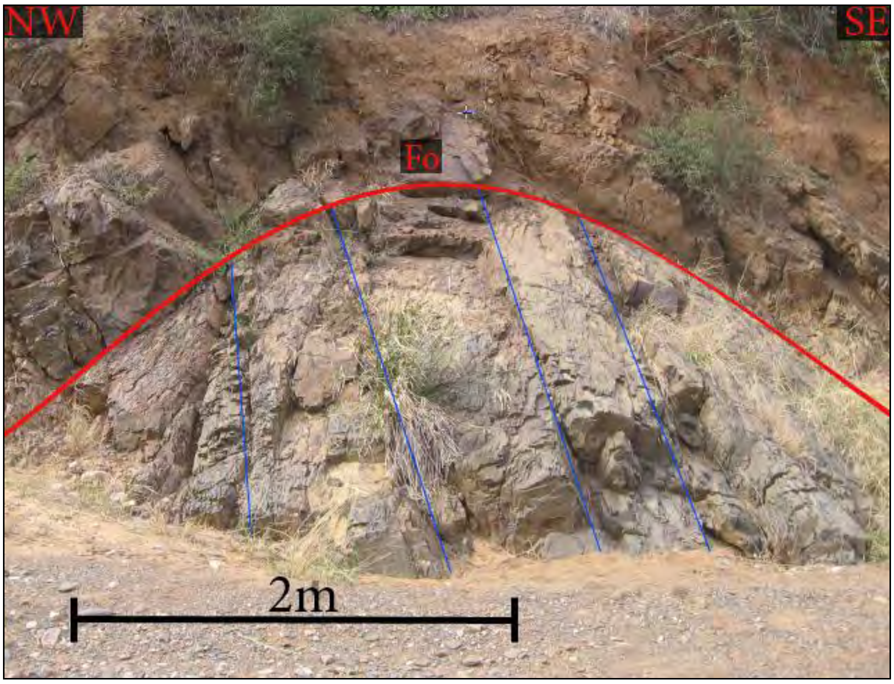

Fig 6-32: Anticline Fo in Kweekvlei shale Fromation, blue lines indicate axial planar cleavage of Fo.

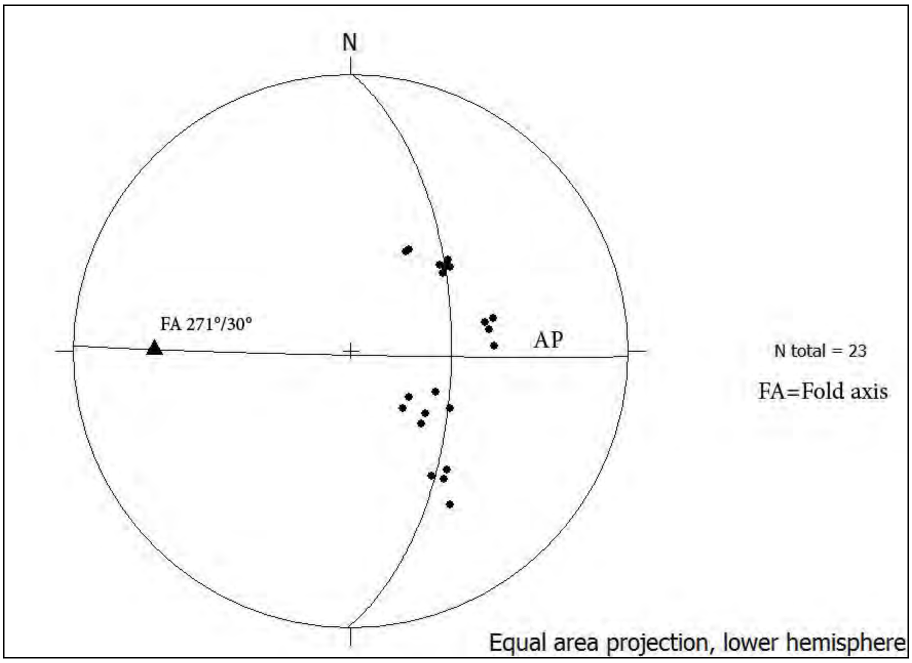

Fig 6-33: Stereogram showing poles to fold limbs of fold Fo. Axial plane is indicated by AP.

6.3.6 Cleavage

Cleavage is well developed in the argillaceous rocks at station 1. Cleavage planes dip steeply to the south-southwest (Fig 6-34). Cleavage is identified as axial planar and developed as a result of a macroscale overturned syncline located within zone1. The cleavage planes show an average azimuth and dip of 200°/65°.

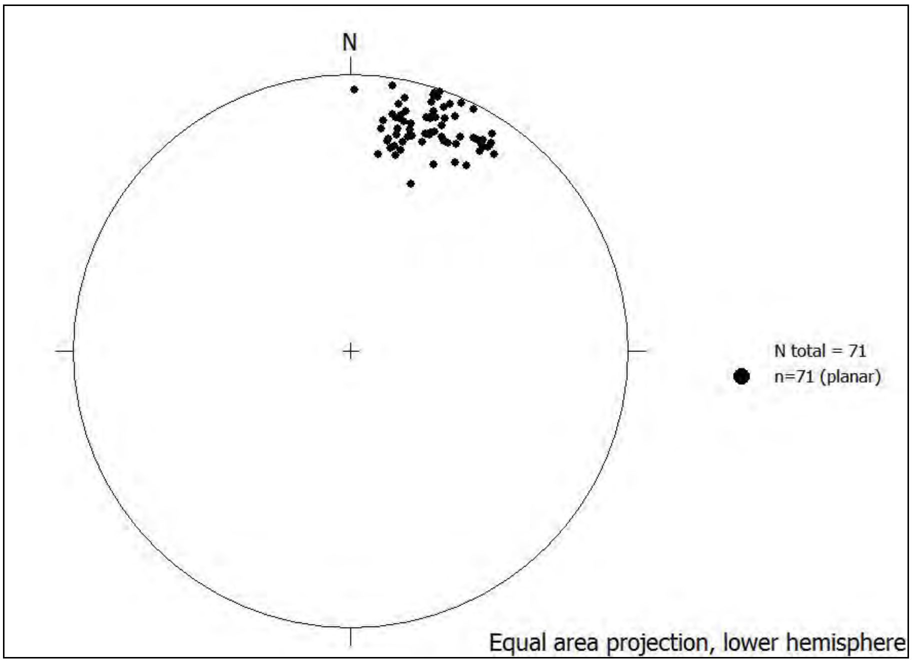

Fig 6-34: Stereogram showing poles to cleavage planes at station 1.

6.3.7 Joints

Joints are not as well developed in the Kweekvlei Formation as in the more competent quartzitic formation of the Perdepoort- and Rooirand Members. Joints could only be located in areas where cleavage was less pronounced and more competent layers were present. The only area that displays convincing joint planes is located in the centre of the study section, close to a pop-up and triangle zone (Fig 6-16). Joint readings are summarized in Fig 6-35. Two joint sets are recognized; one prominent, J1, and one less prominent, J2 (Fig 6-35). Joint planes dip at steep inclinations in a southerly direction (Fig 6-36). Joints have a general east-west orientation, with J1 striking at 75° and J2 at 95°.

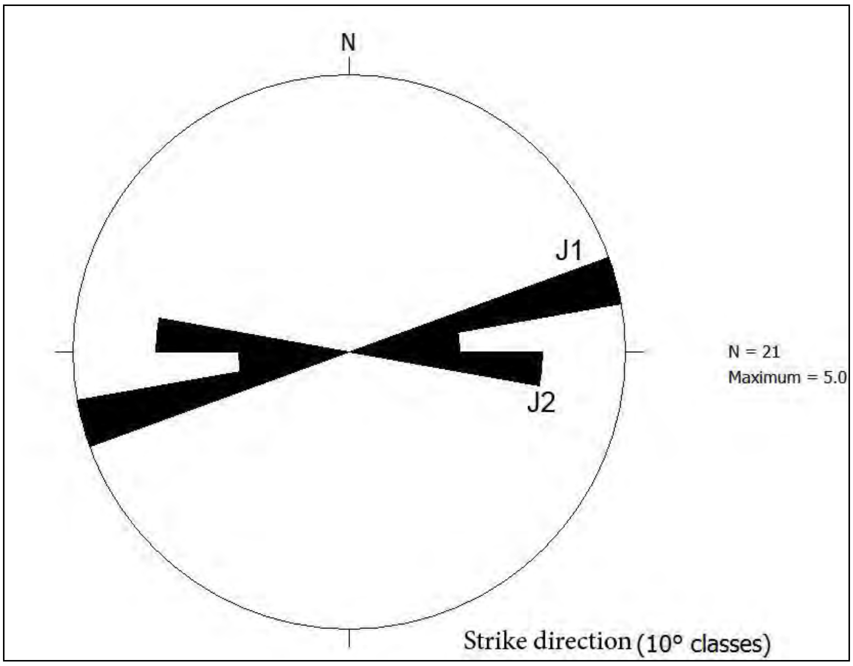

Fig 6-35: Rose diagram showing main joint strike directions at station 1.

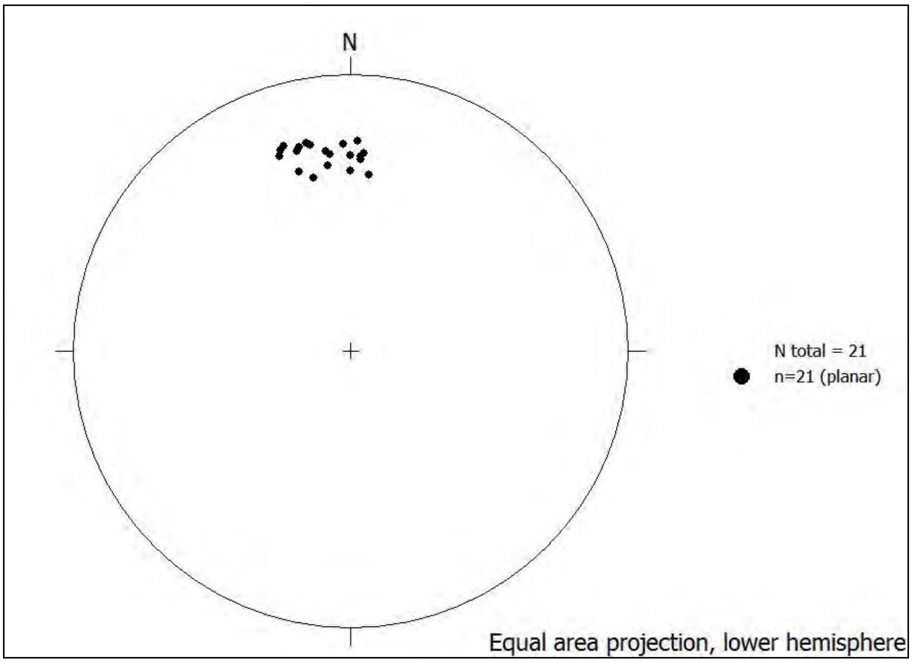

Fig 6-36: Stereogram showing poles to joint planes at station 1.

6.3.8 Boudinage

Boudins are formed in layers of brittle or more competent rocks which are encased by layers of ductile or less competent rocks (Ghosh, 1993). The brittle layer in this case has separated into fragments as a result of the process known as extension fracture boudinage (Ghosh, 1993). Boudins display a clear boudin termination and symmetry with respect to boudin train geometry. Boudins at station 1 can be classified as symmetric torn boudins.

The boudins can further be classified as barrel-shaped when viewed end-on (Ghosh, 1993) (Fig 6-37). Less competent host rock has clearly infiltrated the spaces between boudins (Fig 6-38).

Fig 6-37: Boundin train located in a competent layer of argillaceous strata. The red line indicates the separation of the brittle, competent layer from the underlying, relatively less competent layer; geological hammer for scale.

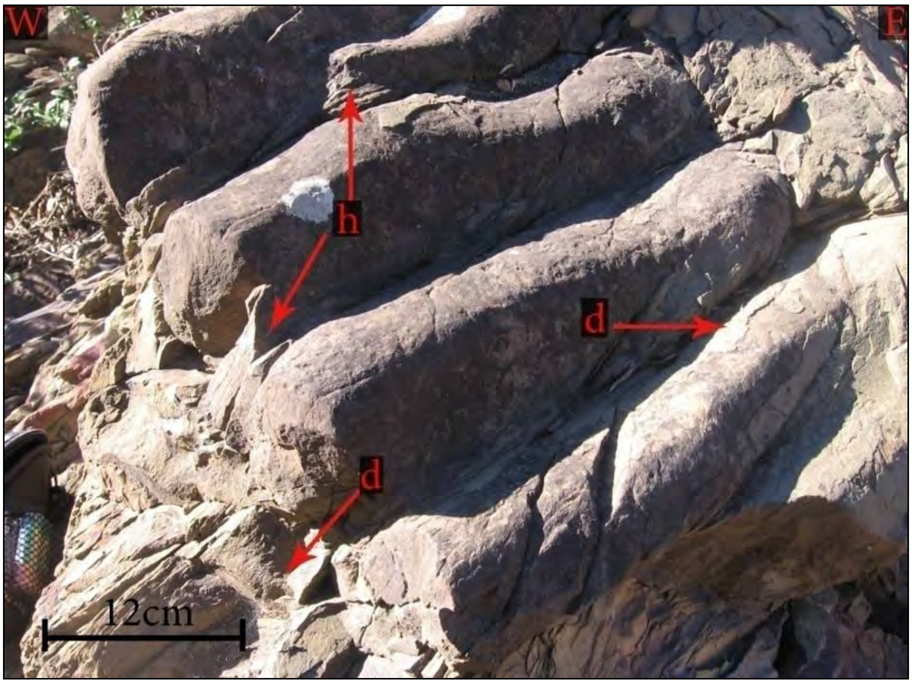

Fig 6-38: Boudin train viewed from an upper angle. Host inflow is clearly visible and is indicated by h. Ductile or relatively less competent layers and remnants of these incompetent layers on boudin surfaces are indicated by d. Camera bag is an additional indicator of scale.

6.4 Station 2

6.4.1 Introduction

Rocks at this station crop out on the eastern bank of a southward flowing non-perennial riverbed, located immediately north of an eastward bend in the river (Fig 6-39). It is situated 800m west-northwest of station 1 along approximately the same strike. The section consists of khaki-clay coloured quartzites which make-up the Rooirand Member. Average bed thickness is estimated at 40cm (Fig 6-42). Beds appear to be highly fractured in places and iron staining is also pervasive within the outcrop. On a macroscale station 2 is situated near a large anticlinal fold nose, the anticline marking the northern termination of zone 1 (Fig 6-39). The northern normal limb of a large overturned syncline constitutes the southern limb of this fold nose. Sedimentary structures in the area include cross-bedding (trough and planar) and rip-up clasts (Fig 6-41). Although the area shows that abundant folds are present bedding could not be measured directly in most places. Structures are considered right way up based on evidence for younging direction which was noted immediately down strike at station 3 in the form of trough-cross bedding (Fig 6-40). The northern half of the section is dominated by low-angle fore-thrusts, and a minor components of strike-slip movement (Fig 6-42). In the southern half of the outcrop folding is the dominant secondary structure, consisting of multiple anticlines and a single syncline.

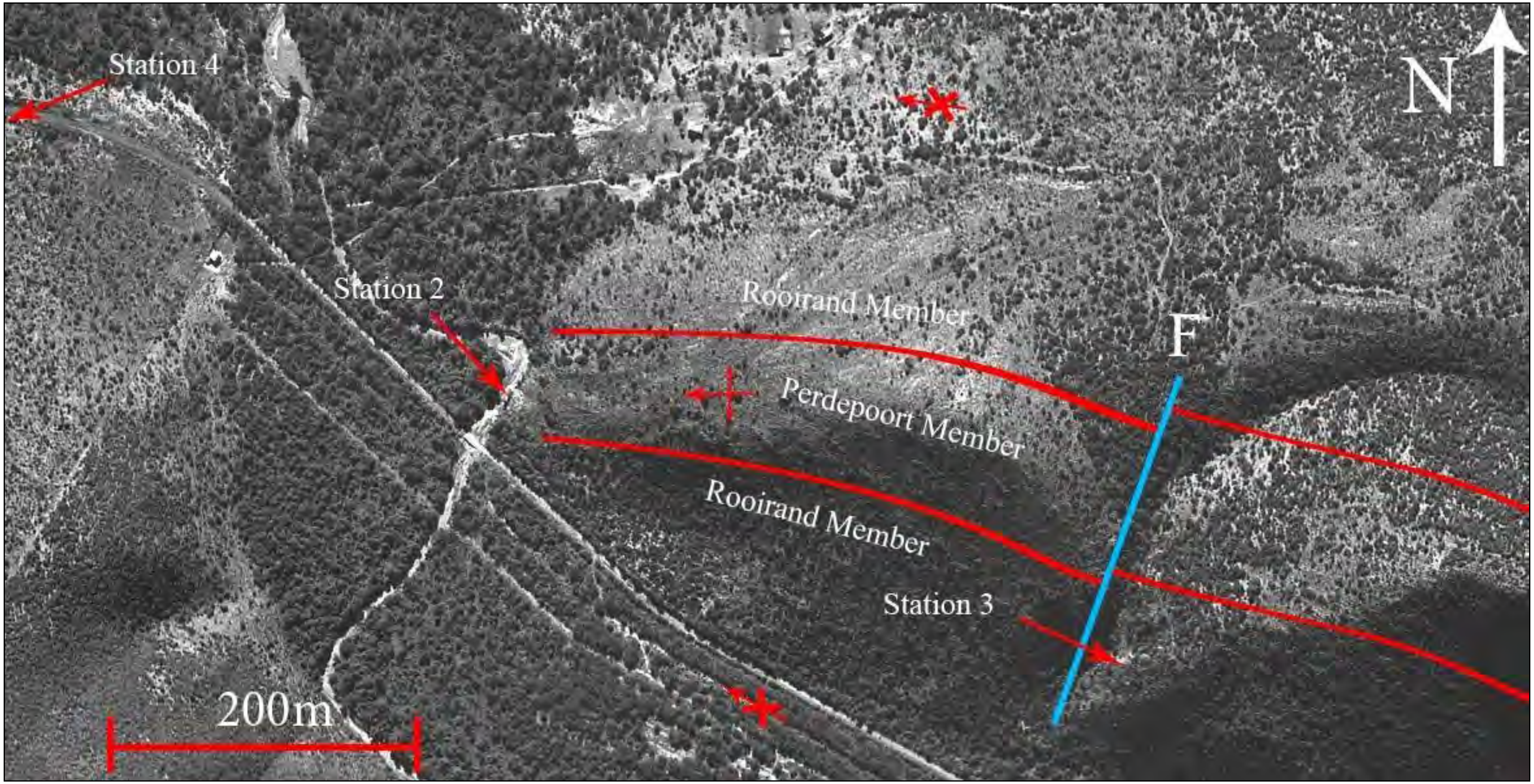

Fig 6-39: Aerial view delineating stations 2, 3 and 4 as well as the immediate surrounding geology and topography. An inferred strike-slip fault is indicated by F. The contacts between the Perdepoort- and Rooirand Member are also indicated.

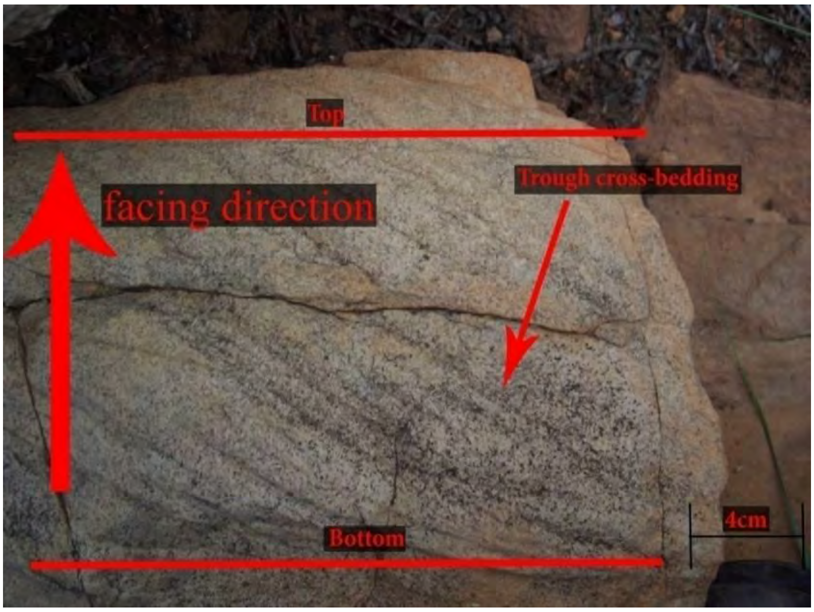

Fig 6-40: Trough cross-bedding in Perdepoort Member close to station 3, confirms that bedding in the northern domain of zone 1 is right way up. Bedding is viewed end-on.

Fig 6-41: Rip-up clasts are outlined at the base of a bed, found in the vicinity of station 3; pen for scale.

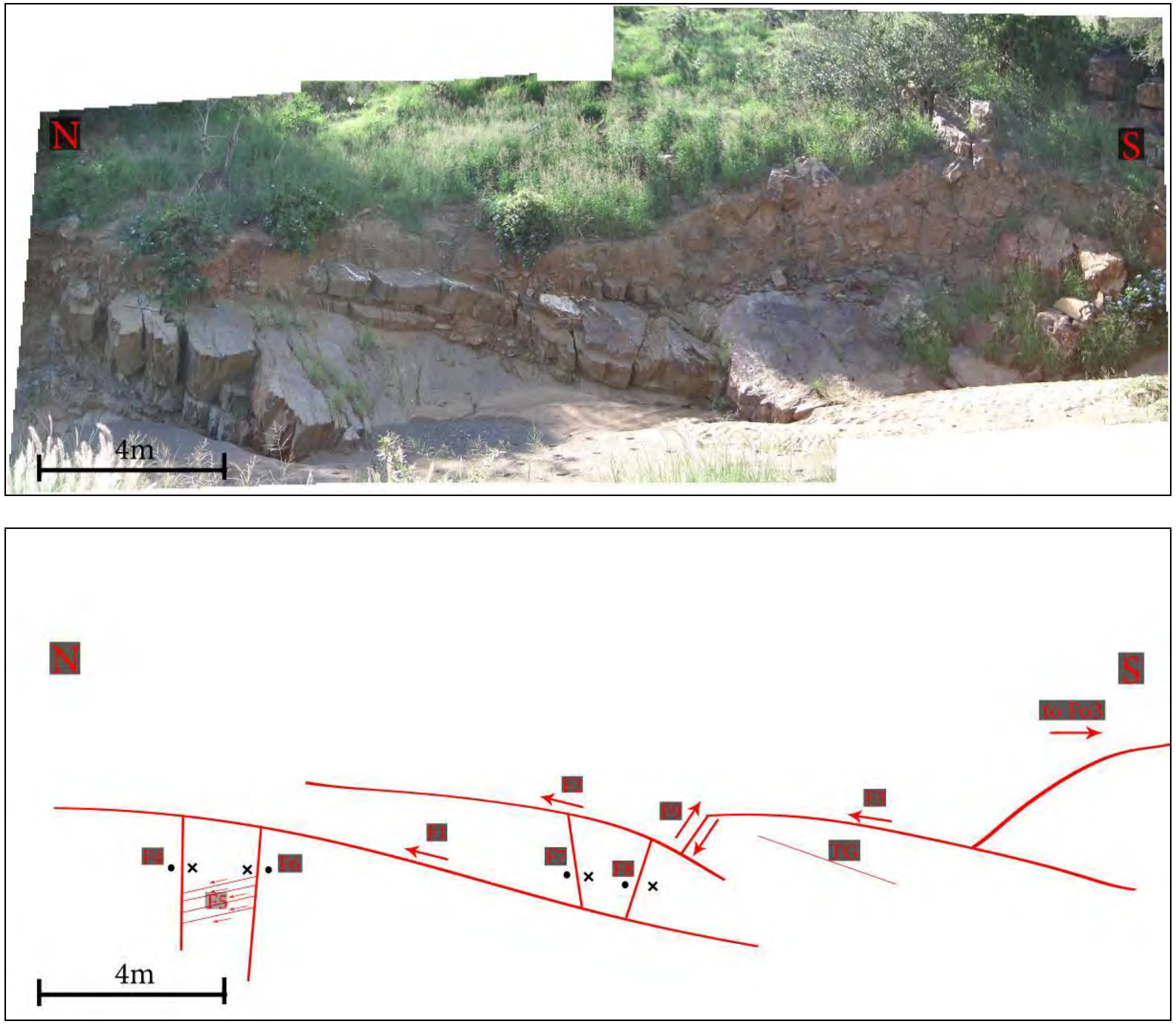

Fig 6-42: Cross sectional overlay of the northern domain of station 2. Note numerous low angle fore- thrusts and subordinate backthrust. Abundant strike-slip faults are also present; X=movement into page, ●=movement out of page.

6.4.2 Faults

The positions of faults were ascertained with the aid of slickenfibres that are particularly well developed throughout the section. Nine faults are identified at station 2 (Fig 6-42). Faults in the section consist of fore-thrusts, backthrusts and strike-slip faults. Three low angle fore-thrusts dominate the section (Fig 6-42). F7 and F8 appear to have been a high angle imbricate and backthrust respectively, although the last component of movement, as indicated by slickensides, is strike-slip. F4 and F6 also appear to have been developed as a result of thrusting; however slickensides indicate strike-slip as the final component of movement. F4, F5, F7 and F8 represent sinistral strike-slip faults, while F6 represents a dextral strike-slip fault. Some thrust faults in the section cut through strike-slip faults and are thus considered as younger.

6.4.2.1 Thrust faults

Three fore-thrusts are present in the section, F1, F2 and F3 (Fig 6-43, Fig 6-45 and Fig 6-47). All verge east and exhibit low dips, with an average azimuth and dip of 256°/23°. Thrust fault F1 displays components of strike- slip movement in certain areas of its fault plane. This is synonymous with features noted at station 1.

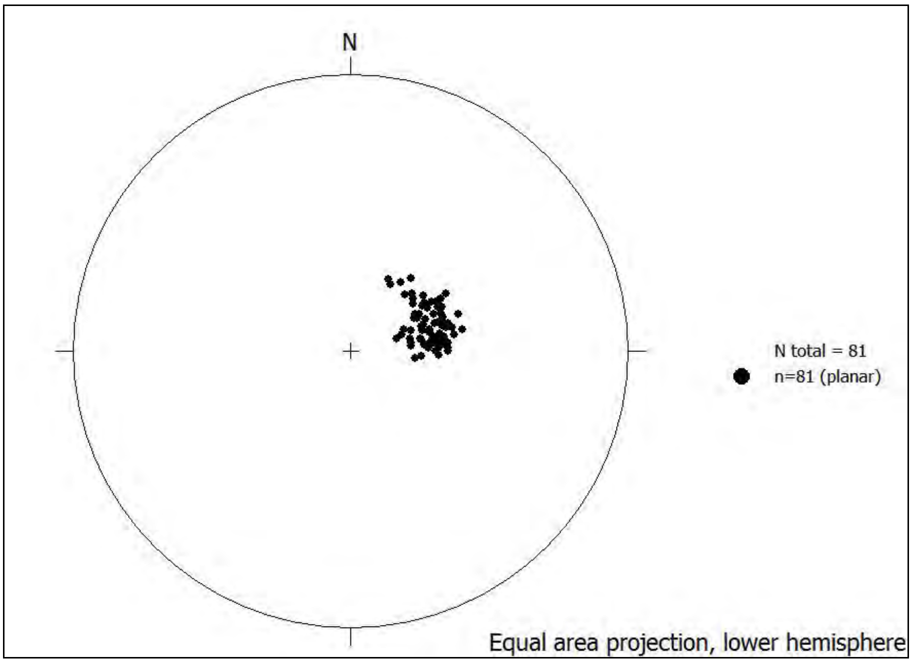

Fig 6-43: Stereogram showing poles to thrust fault plane F1.

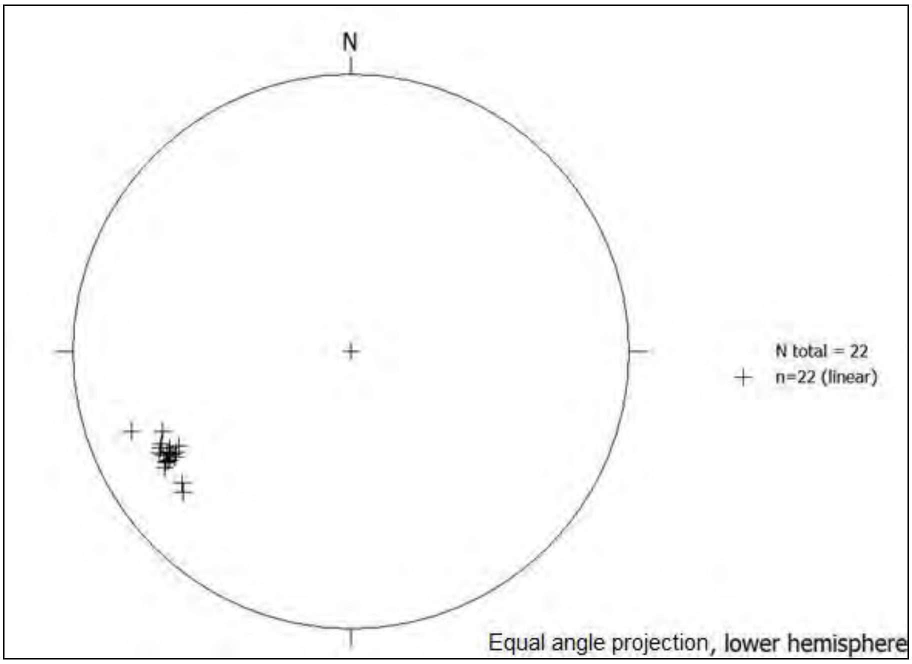

Fig 6-44: Stereogram showing lineations on thrust fault plane F1.

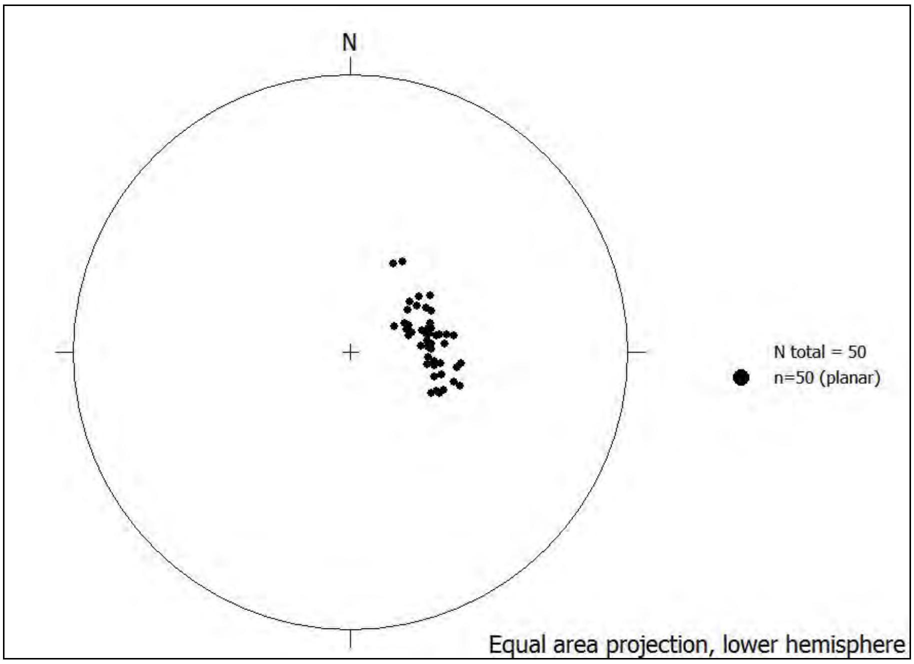

Fig 6-45: Stereogram showing poles to thrust fault plane F2.

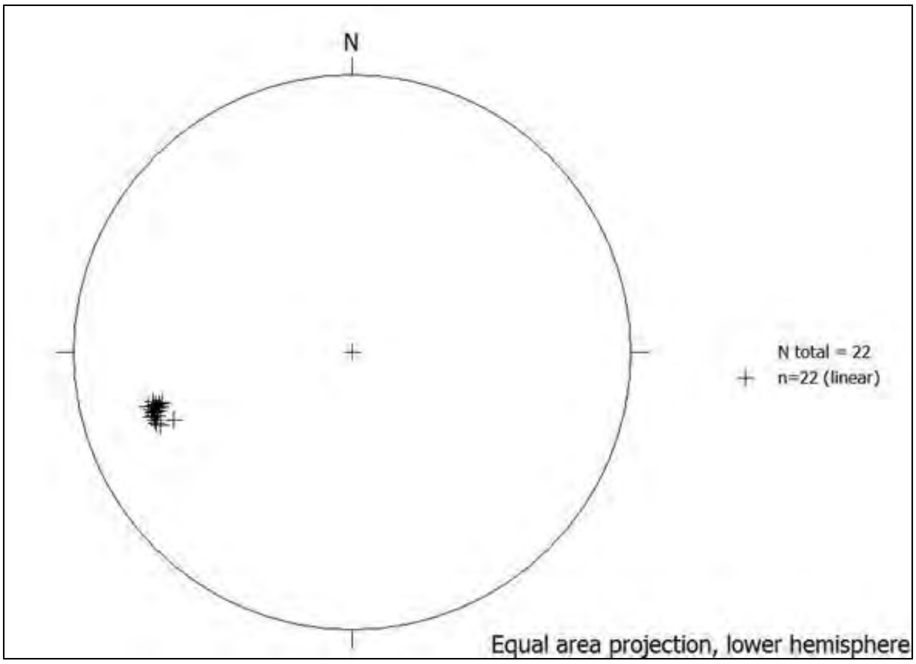

Fig 6-46: Stereogram showing lineations on thrust fault plane F2.

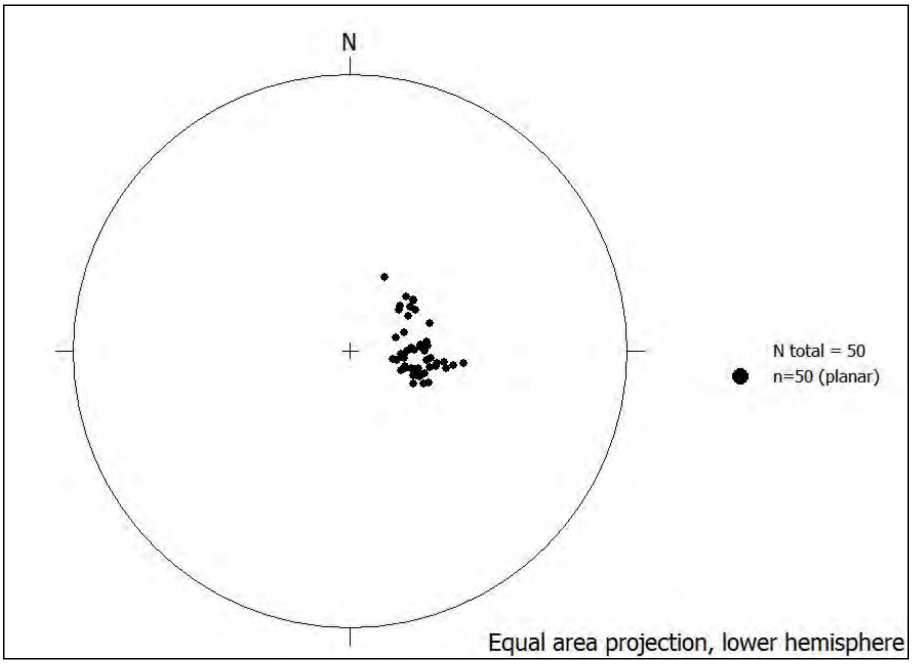

Fig 6-47: Stereogram showing poles to thrust fault plane F3.

Lineations in the form of slickenfibres measured on F1 and F2 all plunge in an approximately west-southwesterly direction (Fig 6-44 and Fig 6-46).

Only one backhthrust, F9 was noted in the section. F9 shows a southward vergence and thus dips at moderate inclinations to the north (Fig 6-48). It is truncated by a younger thrust fault F3 (Fig 6-42).

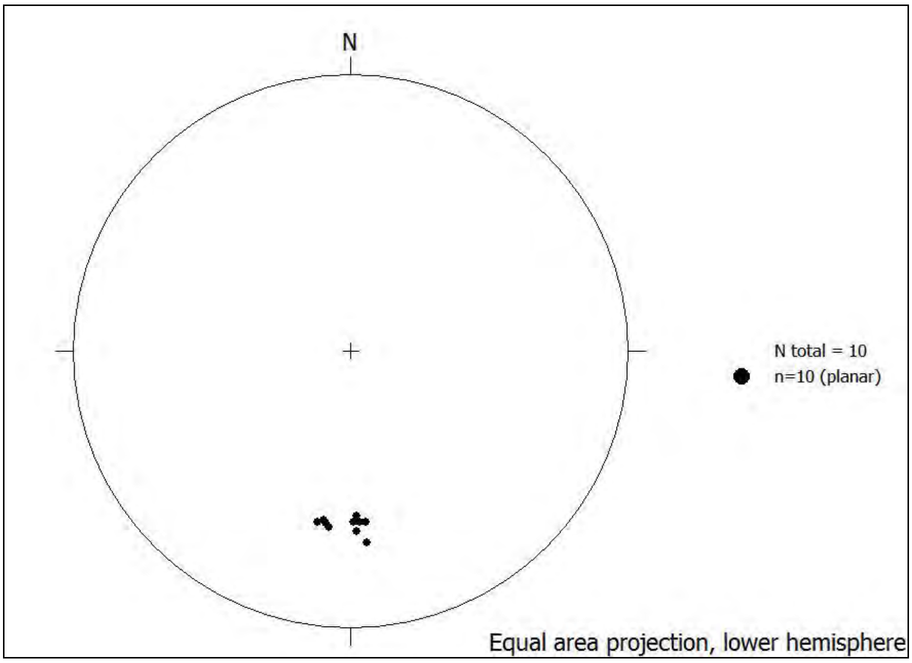

Fig 6-48: Stereogram showing poles to backthrust plane F9.

6.4.2.2 Normal faults

No normal faults were observed at station 2.

6.4.2.3 Strike-slip faults

Five strike-slip faults were observed at station 2 (Fig 6-32). As can be seen in Fig 6-49 and Fig 6-50, strike-slip faults strike in three directions. F4, F5, F7 and F8 all exhibit sinistral movement, whereas F6 exhibits dextral movement, as indicated by slickensides. The relative ages of F4, F5 and F6 may be deduced by determining cut-off relationships. F5 cuts F6 and F4 cuts F5; thus the order of development is from oldest to youngest, F6, F5 and F4. Lineations in the form of slickenfibres were only observed on two of the 5 strike-slip fault planes. Slickenfibres measured on F4 and F6 plunge at steep angles in an approximate westerly direction (Fig 6-51).

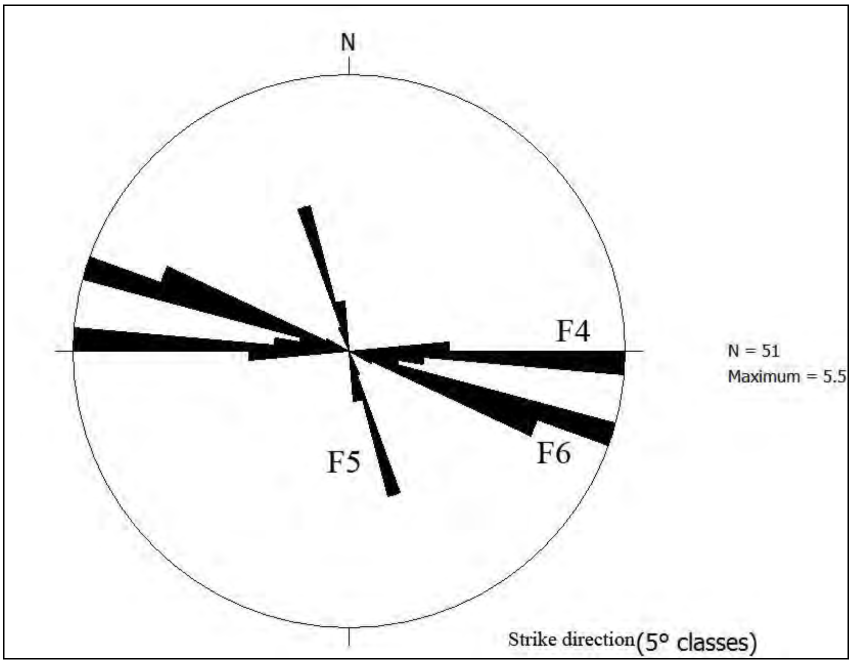

Fig 6-49: Rose diagram showing orientations of strike-slip faults at station 2.

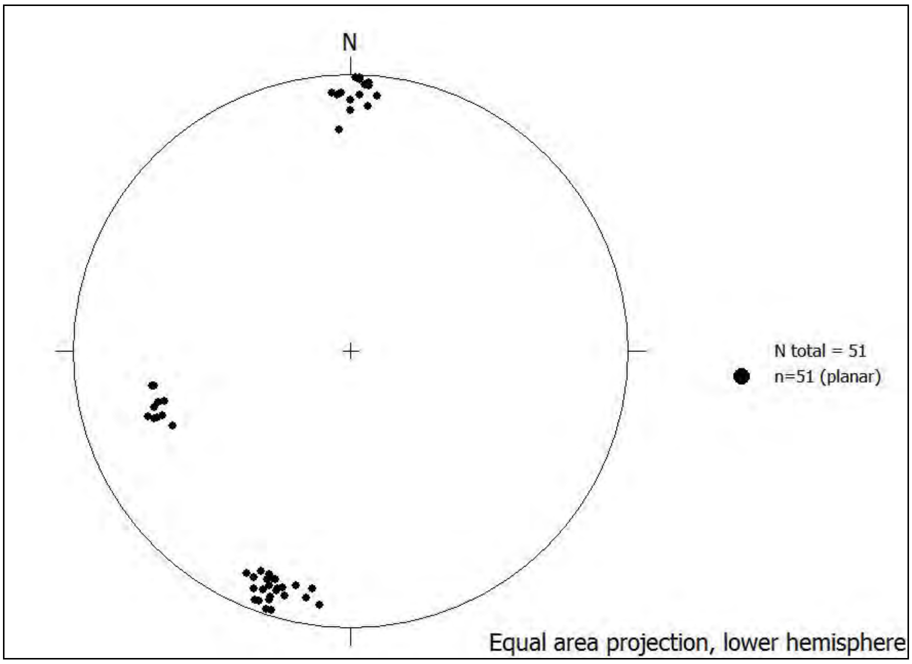

Fig 6-50: Stereogram showing poles to strike-slip fault planes at station 2.

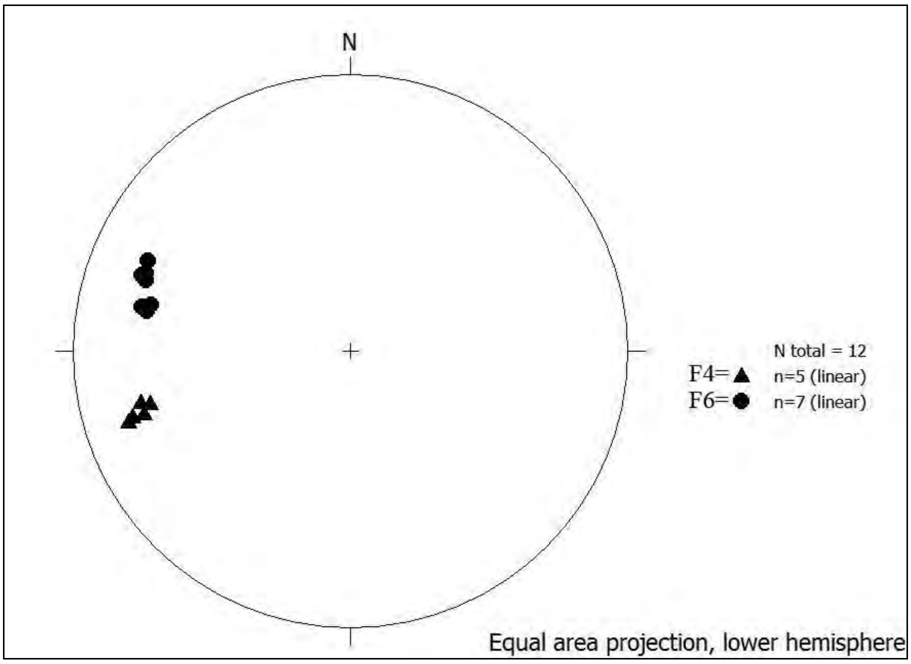

Fig 6-51: Stereogram showing trend and plunge of slickenfibres on strike-slip fault planes F4 and F6.

6.4.3 Folding

Tilted strata at station 2 are located within a fold nose marking the boundary between zone 1 and 2. Folding is prevalent within the southern half of the section and is cut by thrust fault F3 . F3 forms the boundary between the respective faulting domain towards the north and folding domain to the south (Fig 6-42). Folding is comprised of an anticline/syncline/anticline sequence represented by Fo1 to Fo3 (Fig 6-52). All axial planes are steeply inclined southwards (Fig 6-52). Fo1 represents an anticline with an interlimb angle of 42°, and the fold axis has a trend and plunge of 281°/19°. It can therfore be defined as a steeply-inclined, gentle-plunging, closed fold (Fig 6-53). Fo2 represents a syncline that has an interlimb angle of 56°, and fold axis plunging in the direction 259°/5°. It is thus defined as a steeply-inclined, horizontal- plunging, close fold (Fig 6-54). Fo3 denotes an anticline with an interlimb angle of 50° and fold axis plunging in the direction 260°/6°. Accordingly, this fold is defined as a subvertical, horizontal-plunging, close fold (Fig 6-55).

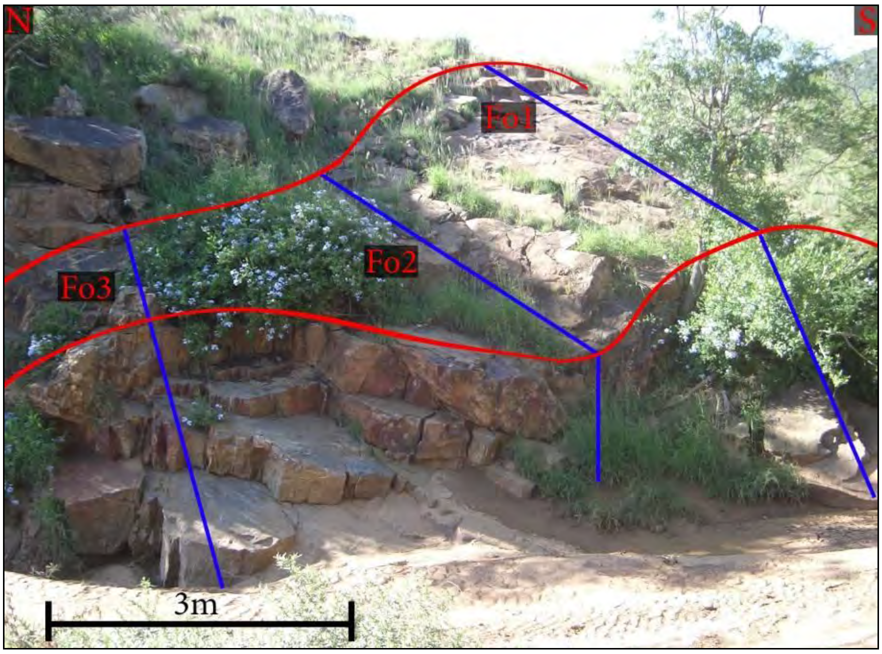

Fig 6-52: Top: Folding in the Rooirand Member at station 2.Bottom: Blue lines indicate axial planes in cross-sectional view and surface extent is indicated in red..

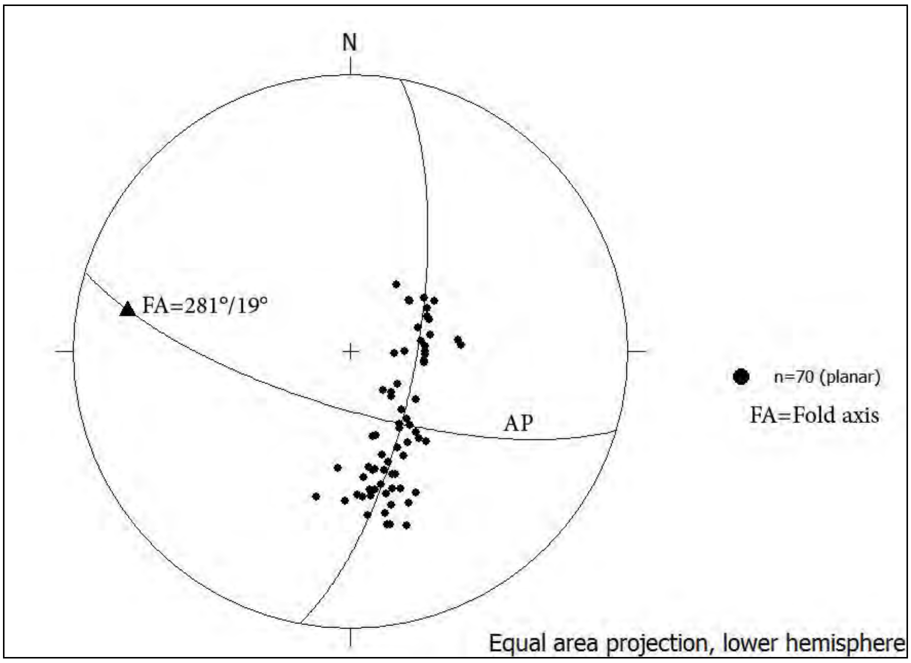

Fig 6-53: Stereogram showing poles to fold limbs of fold Fo1. Axial plane is indicated by AP.

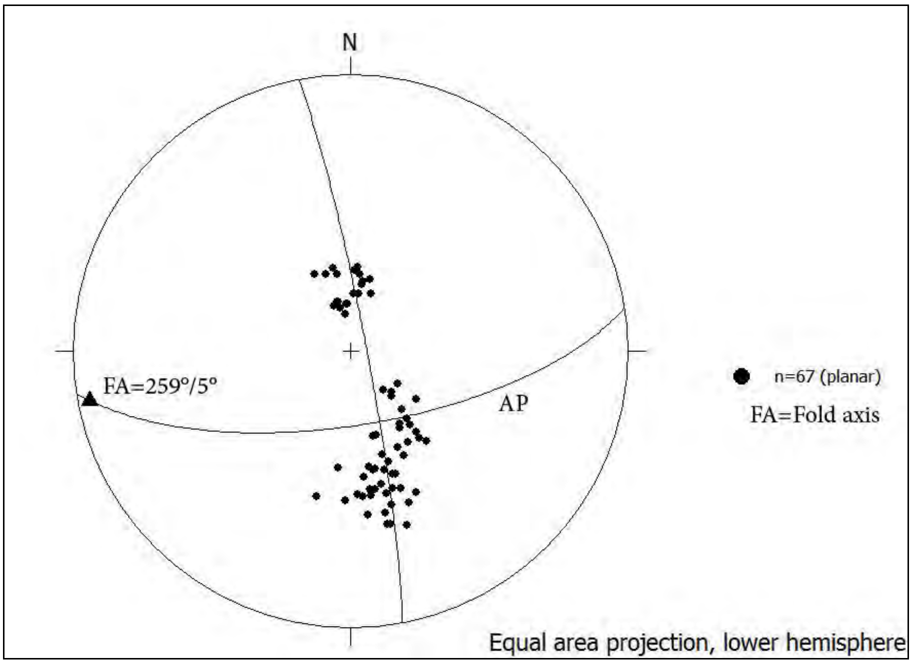

Fig 6-54: Stereogram showing poles to fold limbs of fold Fo2. Axial plane is indicated by AP.

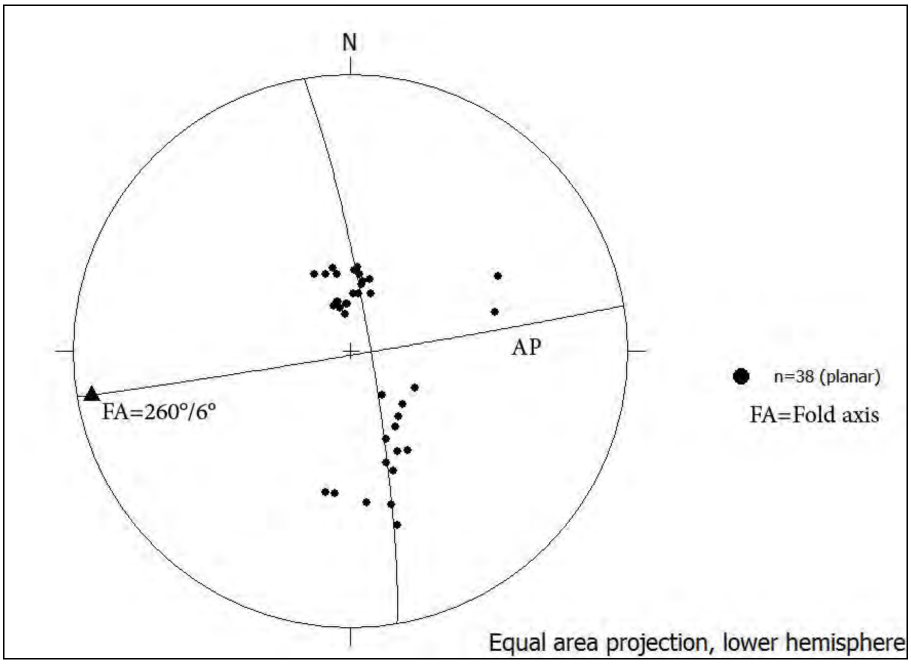

Fig 6-55: Stereogram showing poles to fold limbs of fold Fo3. Axial plane is indicated by AP.

6.4.4 Lineations

Lineations at station 2 consist of slickenfibres. These are encountered both on fault planes and fold limbs. In the case of fault planes they served to elucidate position and relative sense of movement. Lineations on fold Fo1 are particularly well developed and all slickenside measurements on this fold are summarized in a Fig 6-56. In certain instances slickensides that had developed on quartz veins displayed two trend directions. This resulted in the wide range of trend and plunge readings observed for fold Fo1 (Fig 6-56).

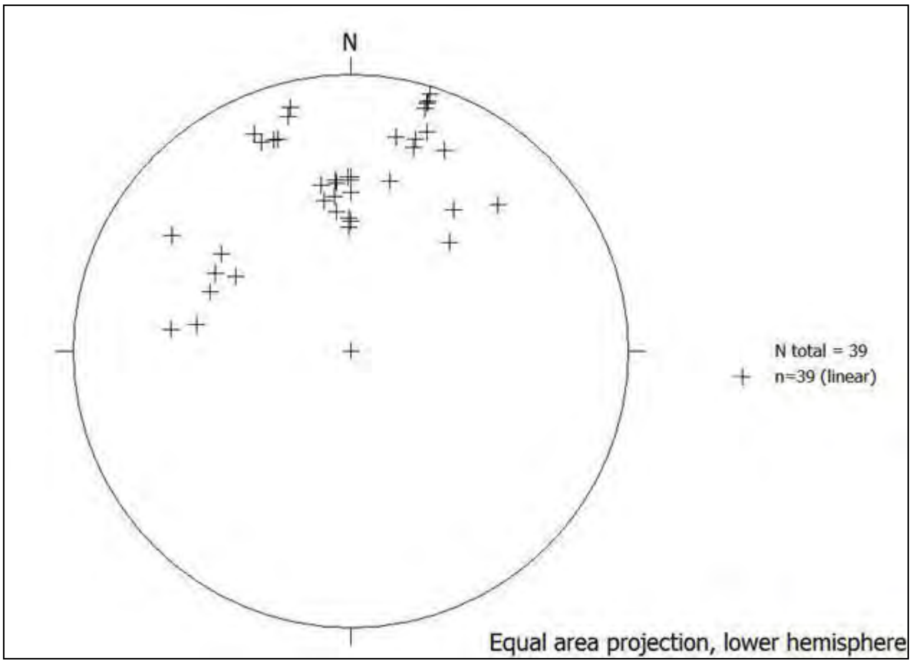

Fig 6-56: Stereogram showing lineations on fold Fo1.

6.4.5 Veins

Tension gashes filled with sigmoidal quartz veins are present at station 2 these may be utilized in order to determine the approximate orientation of σ 1 (Fig 6-57). At station 2 the approximate orientation of σ 1 is north-south (Fig 6-57).

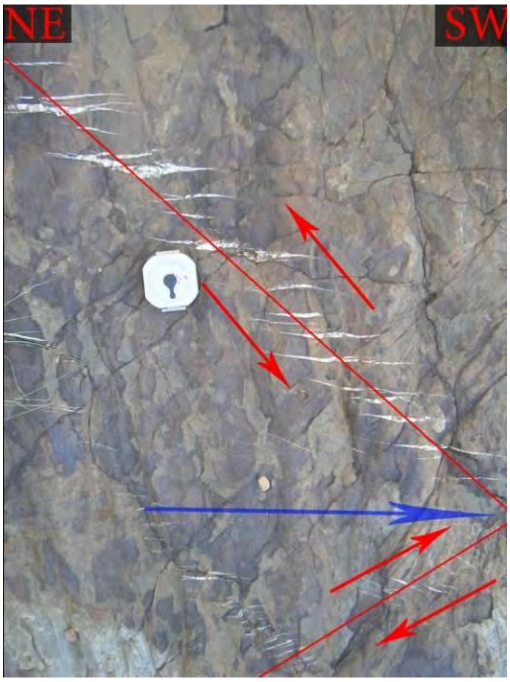

Fig 6-57: Sigmoidal shaped quartz veins fill tension gashes in rocks of the Rooirand Member. The approximate direction of σ 1 is indicated by the blue arrow; geological compass for scale.

6.4.6 Joints

Joint readings from this station are amalgamated with readings from station 3 and are presented in section 6.5.4.

6.5 Station 3

Station 3 is located in zone 1 of the study site, east of station 2 and west of station 1 (Fig 6-39). It is located along approximately the same strike as station 2. It forms part of south-dipping rocks making up the Rooirand Member, which in turn form part of the same northern limb of a large overturned syncline as was previously mentioned in station 2. The section is situated on the side of a small gorge formed by what is believed to be a large strike-slip fault (Fig 6-39 and Fig 6-60).

6.5.1 Bedding

Bedding was measured along a 30m outcrop consisting of the Rooirand Member rocks. Sedimentary structures are rare and younging direction was determined with the aid of trough cross-bedding (Fig 6-40). Beds dip at moderate angles to the south-west and form part of a mega-anticline in zone 1 (Fig 6-59 and Fig 6-60). Beds range in thickness from approximately 30cm to 50cm and show pervasive iron-oxide staining (Fig 6-58).

Fig 6-58: South dipping rocks of the Rooirand Member. Note the distinctive red-brown surface colouration.

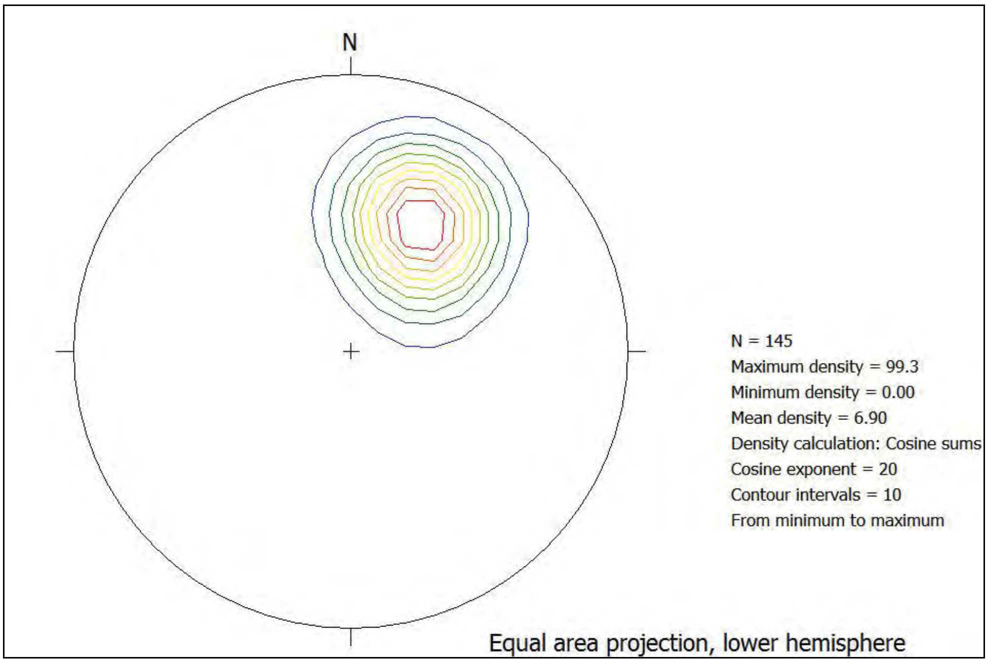

Fig 6-59: Stereogram showing contoured poles to bedding planes for station 3.

Fig 6-60: The southward dipping limb of a large mega-anticline that forms the main controlling structural feature in the northern sector of zone 1 (demarcated in red). Strata consist of rocks of the Rooirand Member. Station 3 is located towards the base of this outcrop.

6.5.2 Faults

No direct evidence in the form of slickensides or fault gouge of faulting was observed in the area. A large gorge occurs immediately adjacent to station 3, (Fig 6-39) where large amounts of fractured rocks suggest that a fault is present (Fig 6-61). From lithological distribution of rocks of the Witpoort Formation in Fig 6-39 it is inferred that this is a strike-slip fault.

Fig 6-61: Gorge opposite station 3. Note large amount of fractured angular boulders. Photo taken from the south, facing north.

6.5.3 Folds

Folding at station 3 was documented from photographs because fold limbs were inaccessible in the field. Folding consists of south verging mega anticlines with moderate dipping northern limbs developing into steep to almost vertical dipping southern limbs (Fig 6-62).

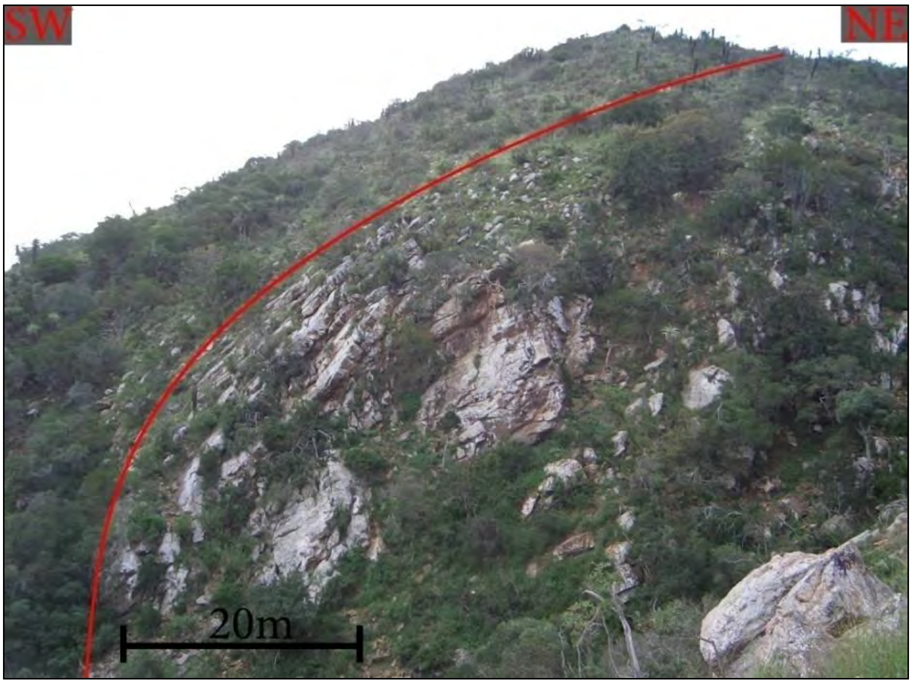

Fig 6-62: Large open anticline in the northern half of zone 1 near station 3. Note near vertical dipping Perdepoort Member towards the south-west.

6.5.4 Joints

Joint readings for station 2 and 3 are amalgamated into one rose diagram and stereogram (Fig 6-64 and Fig 6-65). The sections show systematic jointing with two prominent and one less prominent joint set (Fig 6-63). The cross cutting relationships of joints in the area can clearly be seen from Fig 6-63. Joint set J1 strikes nearly north-south whereas joints J2 and J3 strike west-northwest and west-southwest respectively.

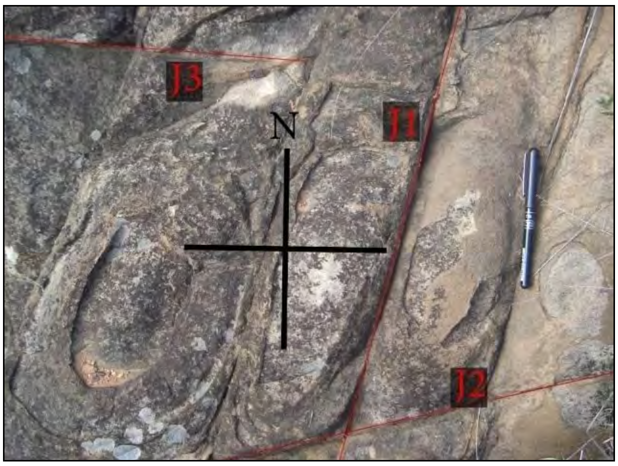

Fig 6-63: Main joints viewed from above. J1 and J2 show systematic close spaced jointing and are the dominant joint sets. J3 represents a less dominant joint set.

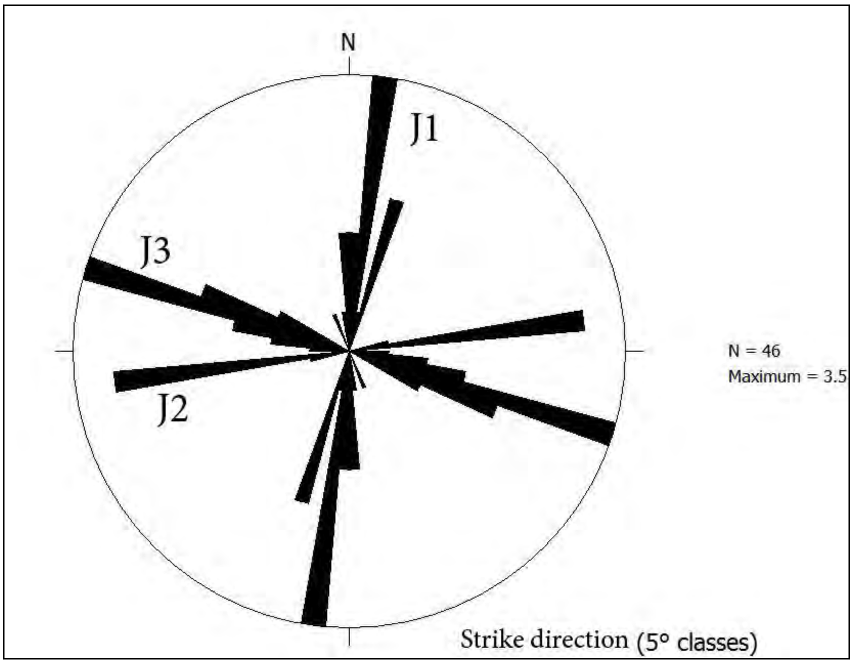

Fig 6-64: Rose diagram showing strike direction of main joint sets at station 2 and 3.

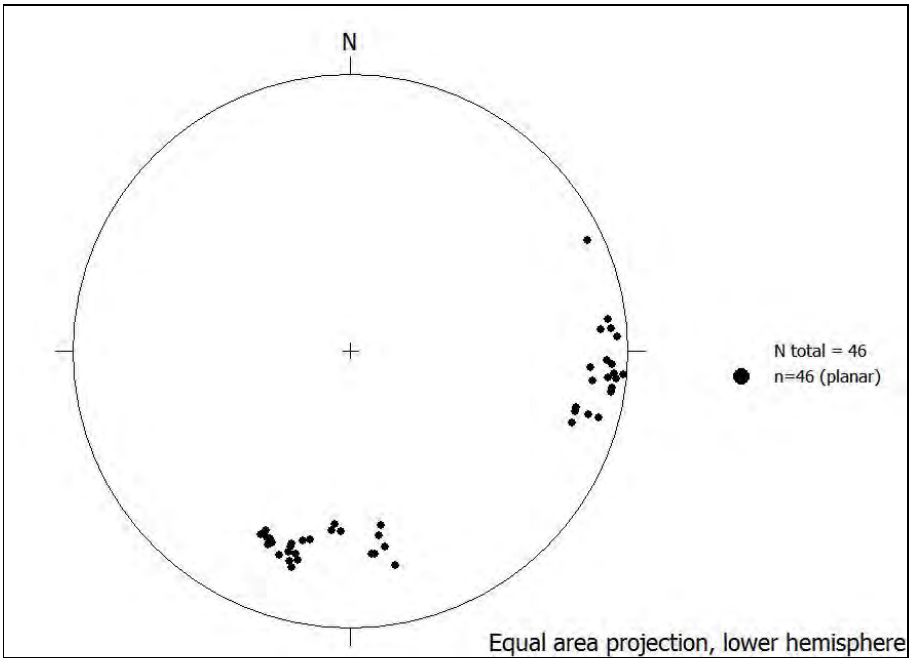

Fig 6-65: Stereogram showing poles to the main joint set planes at station 2 and 3.

6.6 Station 4

6.6.1 Introduction

Station 4 represents an area of complex thrusting in strata of the Kweekvlei Formation. Fore-thrusts are viewed end-on and dip into the page with subordinate backthrusts dipping in the opposite direction. Evidence for thrusting was found in the form of fault gouge in fore-thrusts and slickensided surfaces in the case of backthrusts. Possible frontal ramps and lateral ramps are clearly demarcated by fault gouge as can be seen from A and B in Fig 6-66.

Bedding was impossible to determine from macroscale observations as the dark-grey shales have also been extensively fractured.

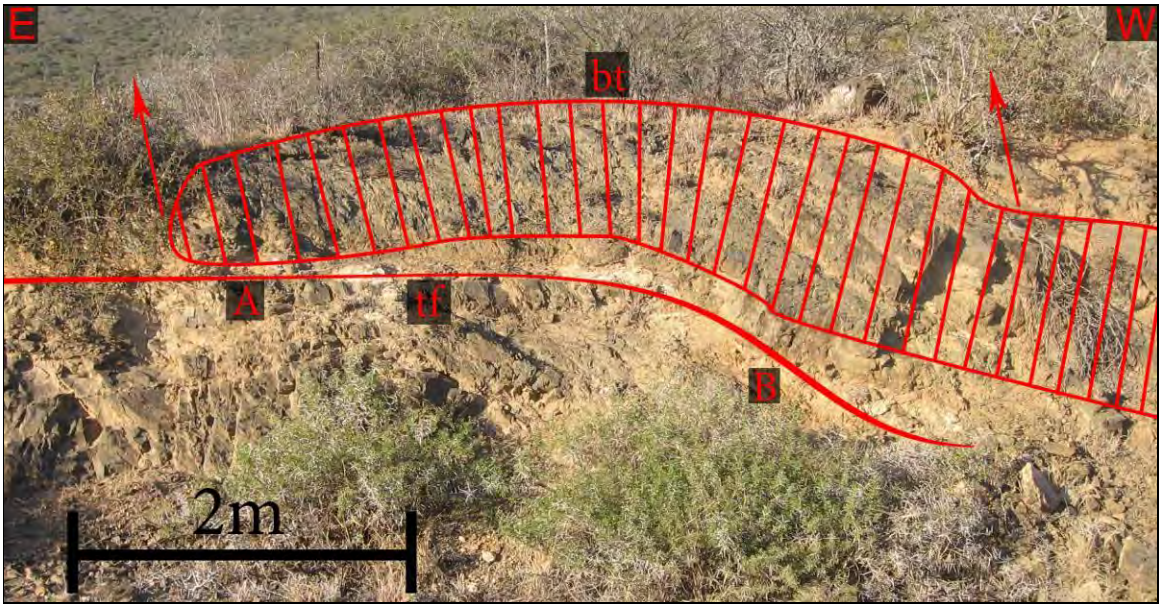

Fig 6-66: Area of complex thrusting at station 4. A and B represent possible frontal and lateral thrust fault ramps and bt represents an exposed backthrust plane. The structures are viewed end-on looking from the north, facing south.

6.6.2 Structure

The outcrop is envisaged as multiple fore-thrusts and backthrusts viewed end-on (Fig 6-67). Erosion has transected fore-thrusts utilizing backthrusts as preferential planes of weakness (Fig 6-67). Only backthrust surfaces could be measured at station 4 as these were the only surfaces that were adequately exposed to facilitate stereogram data acquisition (Fig 6-68 and Fig 6-69).

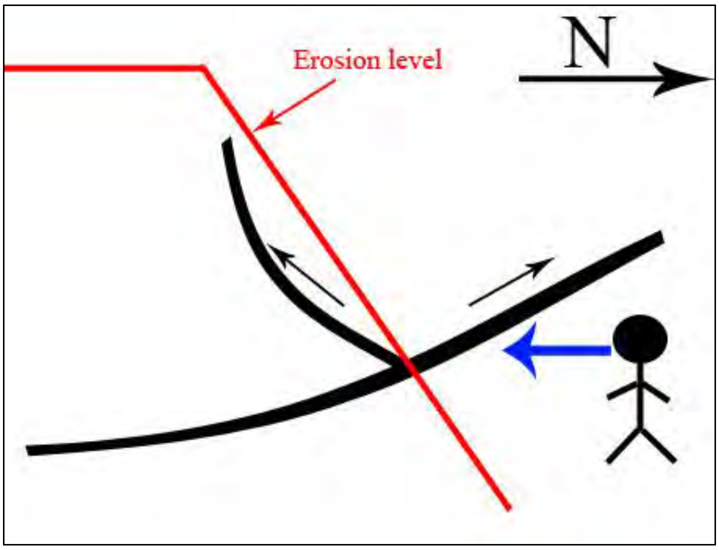

Fig 6-67: Cartoon cross-section depicting the main structural relationships at station 4. Fore-thrusts and backthrusts are indicated by the black lines and dip south (thick line) and north (thin line) respectively.

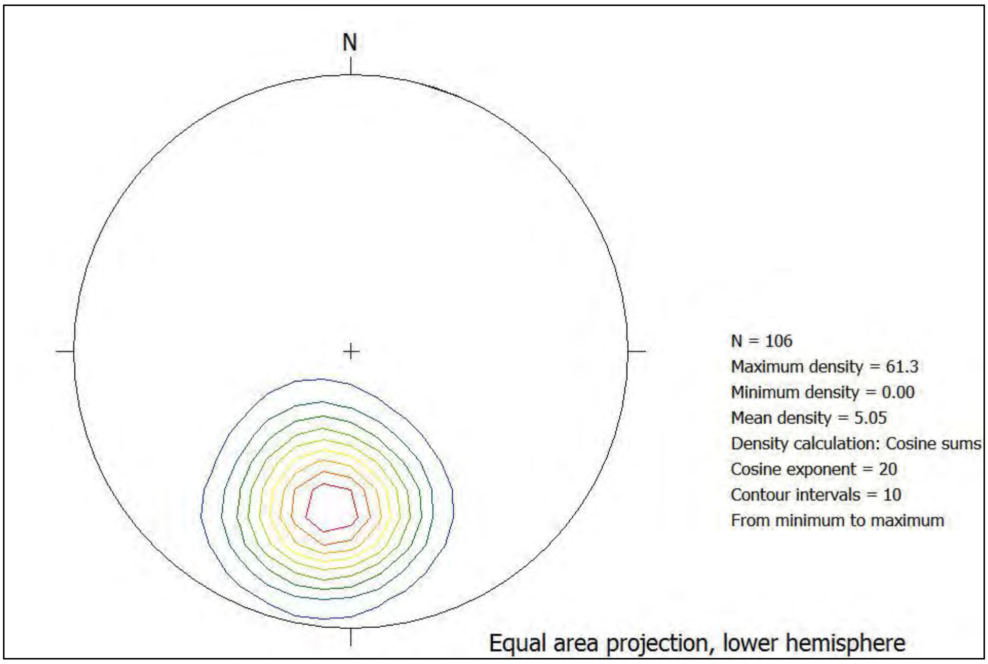

Fig 6-68: Stereogram showing contoured poles to backthrusts at station 4.

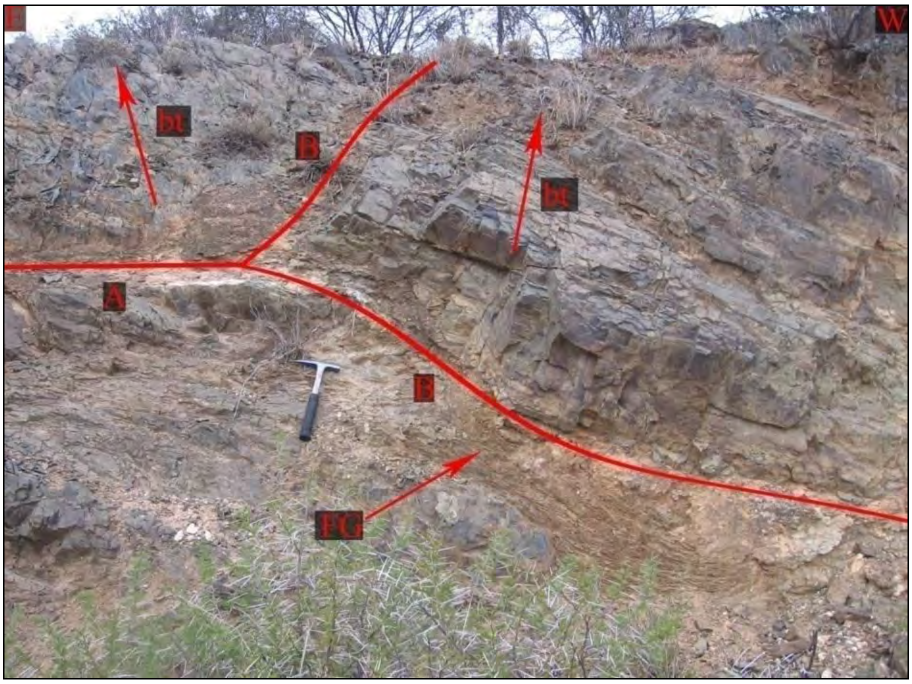

Fig 6-69: Photo of thrusting at station 4. Hangingwall blocks above fore-thrusts are envisaged as moving out of the page northwards and are demarcated by red lines and fault gouge (FG). Movement of the hangingwall blocks along backthrusts are towards the south (into the page). Possible frontal and lateral thrust fault ramps are indicated by A and B respectively; geological hammer for scale.

6.6.3 Lineations

Lineations are well developed in station 4 and occur in the form of slickensided surfaces on quartz veins. Slickensides were found only on well exposed backthrust surfaces. Slickenfibres served to determine sense of movement as well as position of backthrust planes (Fig 6-70 and Fig 6-71).

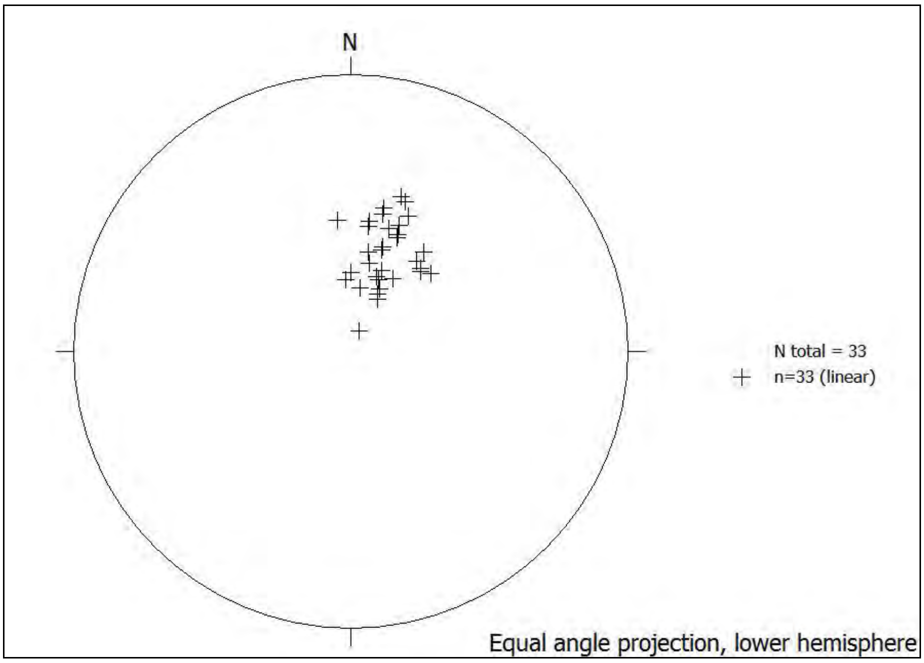

Fig 6-70: Stereogram showing orientation of slickenfibres on backthrust planes at station 4.

Fig 6-71: *Slickensided surfaces associated with backthrusting at station 4 indicate that the hanging wall has moved up (southward). Sense of movement of the hanging wall block is indicated by a red arrow; geological hammer for scale.*

6.7 Zone 2

6.7.1 Introduction

Zone 2 is located in the northern half of the study area (Fig 6-1). On a megascale it contains a large nearly upright syncline near its southern boundary and an overturned anticline towards its northern boundary (Fig 6-2). The southern limb of this overturned anticline dips gently in an approximate southerly direction and station 5 and 6 form part of this dipping fold limb (Fig 6-73). Towards the northern extent of zone 2 strata show vertical dip, forming part of an overturned fold limb associated with the previously mentioned overturned anticline (Fig 6-72). The main megascale controlling feature in zone 2 is thus north-verging overturned folding. A large normal fault showing a large strike extension is also noted at station 5 and 7 and is indicated in Fig 6-73.

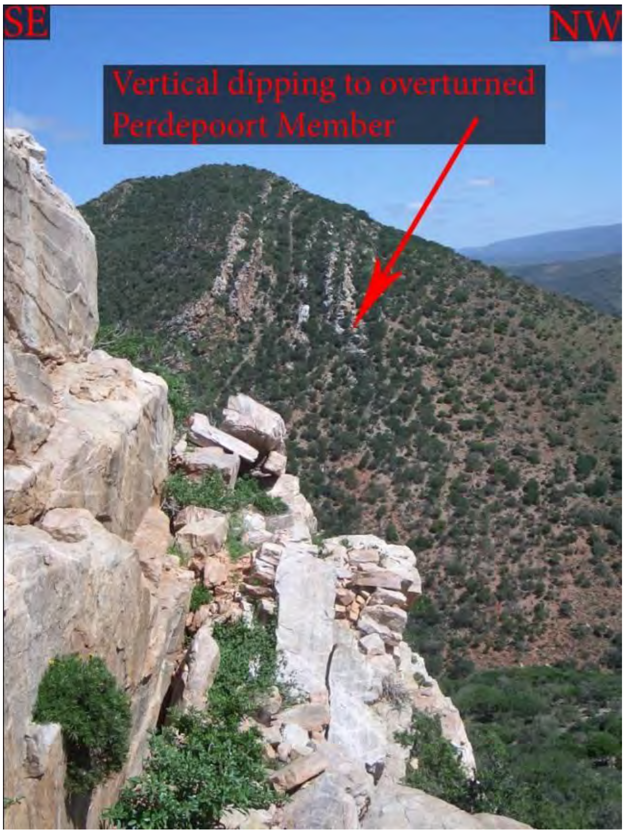

Fig 6-72: The northern boundary of zone 2 is characterized by vertically dipping to overturned strata, associated with the northern limb of a large north verging anticline.

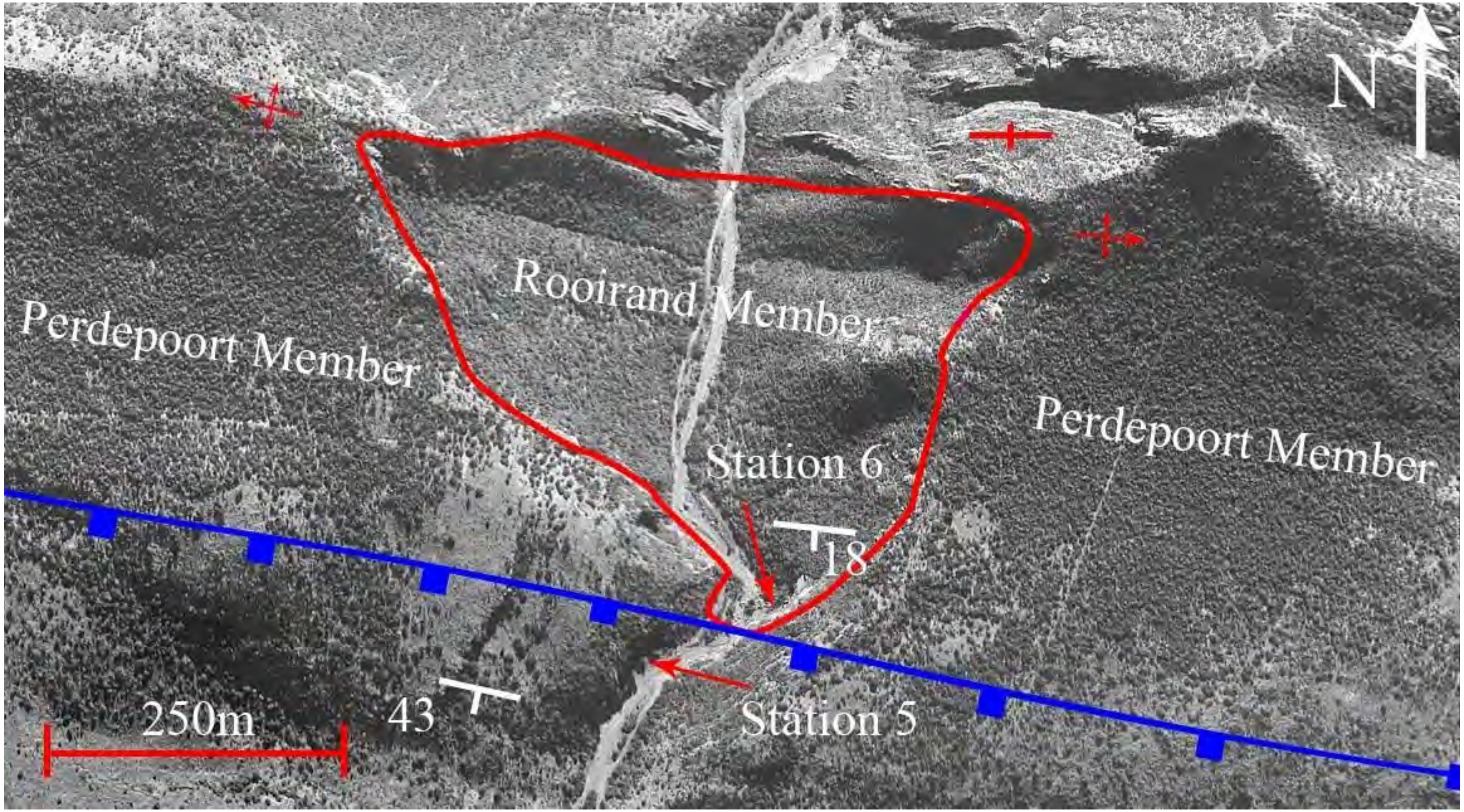

Fig 6-73: Aerial view of station 5 and 6 in zone 2. The contacts between the Perdepoort- and Rooirand Members are also indicated. Note a normal fault occurs in between station 5 and 6 (coloured in blue).

6.8 Station 5

6.8.1 Introduction

Station 5 lies on the western bank of a non-perennial southward flowing river (Fig 6-73). The rocks in the area are comprised almost exclusively of quartzites of the Perdepoort Member. Bed thickness varies greatly, with most quartzites ranging in thickness from 5cm to 70cm. Shale horizons are rare and where present are extremely thin, in the order of 2cm. Quartzites are predominantly light grey in colour with some zones displaying iron staining. Breccia is a prominent feature of this section as the area is dominated by two normal faults (Fig 6-74). The section also displays abundant sedimentary structures such as cross-bedding (both planar and tangential) and rip-up clasts (Fig 6-76 and Fig 6-77). The section is defined by two domains which are separated by normal faults. The southern domain shows bedding which dips at moderate angles to the south-west. The northern domain is characterized by faulting, folding and duplexing (Fig 6-74).

6.8.2 Bedding

Bedding is best developed towards the southern end of the section (Fig 6-74). Bedding is right way up and dips at moderate to steep inclinations in a south-southwesterly direction (Fig 6-75).

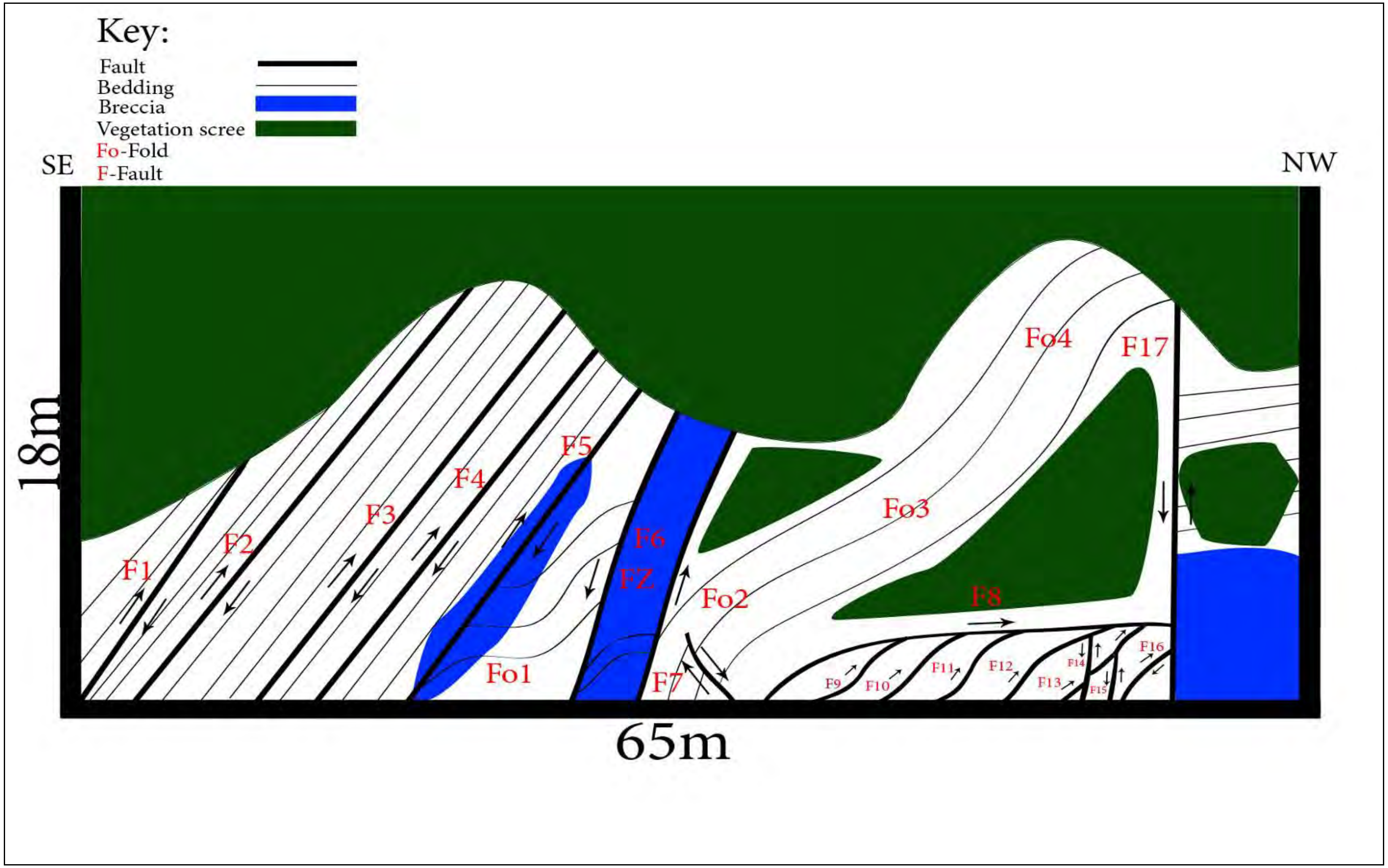

Fig 6-74: Cross section of section studied at station 5. Note large amount of bedding parallel fore-thrusts and prominent normal faults the latter transecting all earlier formed faults.

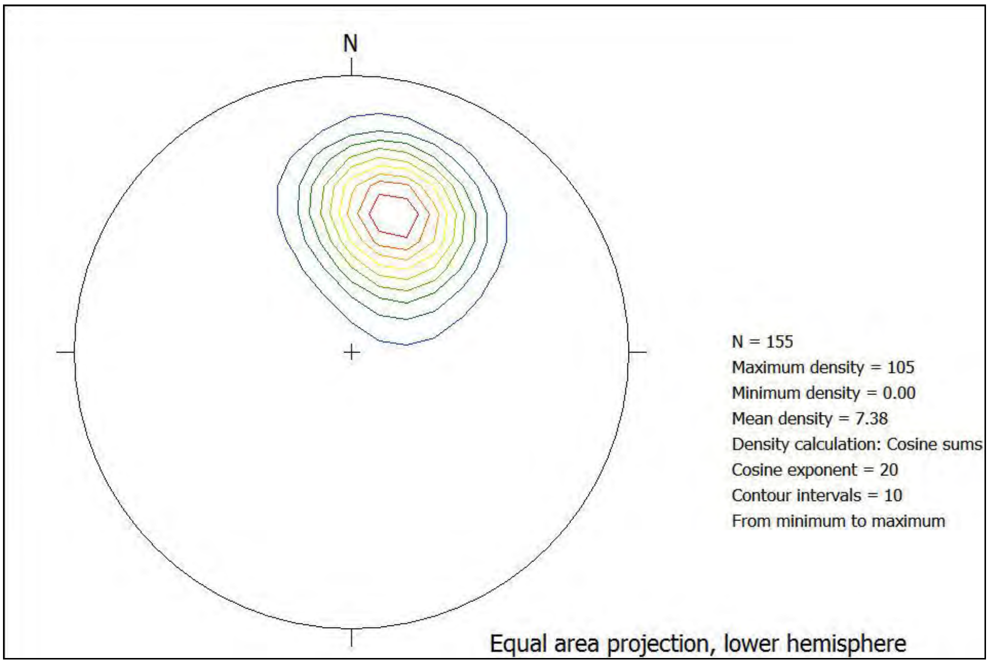

Fig 6-75: Stereogram showing contoured poles to bedding planes at station 5.

Bedding orientation is observed to change adjacent to a large normal fault that occurs approxamitely in the centre of the section (Fig 6-74). Evidence of facing direction and bedding was obtained in the form of trough cross-bedding and rip-up clasts (Fig 6-76 and Fig 6-77). These features indicate that bedding in the general vicinity is right way up.

Fig 6-76: Trough cross-bedding, FD indicates facing direction; geological hammer for scale.

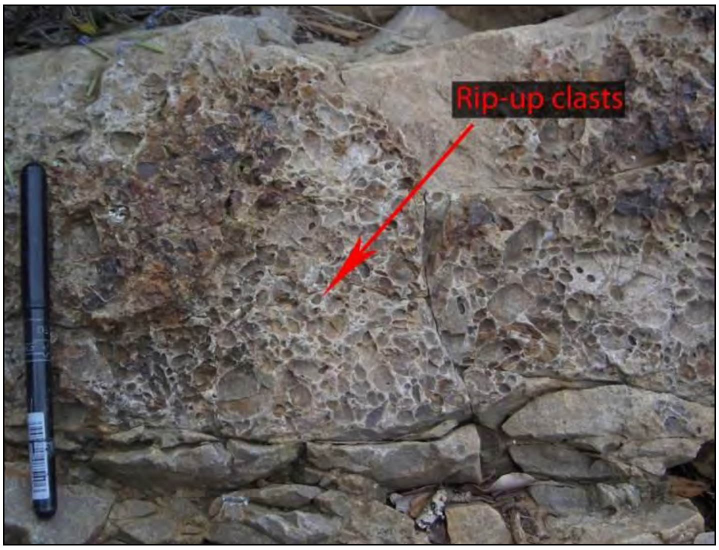

Fig 6-77: Rip-up clasts occurring at the base of a quartzite bed; pen for scale.

6.8.3 Faults

The location of faults was determined with the help of indicators including slickenfibres, breccia and cut-off relationships. The section contains 16 faults, with most faults displaying bedding parallel geometry (Fig 6-74, Fig 6-81 and Fig 6-82). Thrust faults are all fore-land verging and dip gently to moderately southward (Fig 6-78). A duplex structure is present towards the north-western end of the study section (Fig 6-74 and Fig 6-85).

Two normal faults cut through earlier formed thrust faults and divide the section into a zone of moderately dipping beds south of normal fault F6, and a zone of folding and thrusting between F6 and F17 (Fig 6-74).

Backthrusts also occur towards the northern end of the section and cut through earlier formed imbricates, forming part of a duplex structure located north of normal fault F6 (Fig 6-74 and Fig 6-89).

6.8.3.1 Thrust faults

Thrust faults are almost all bedding parallel, foreland-verging and dip at low to moderate angles southward (Fig 6-78).

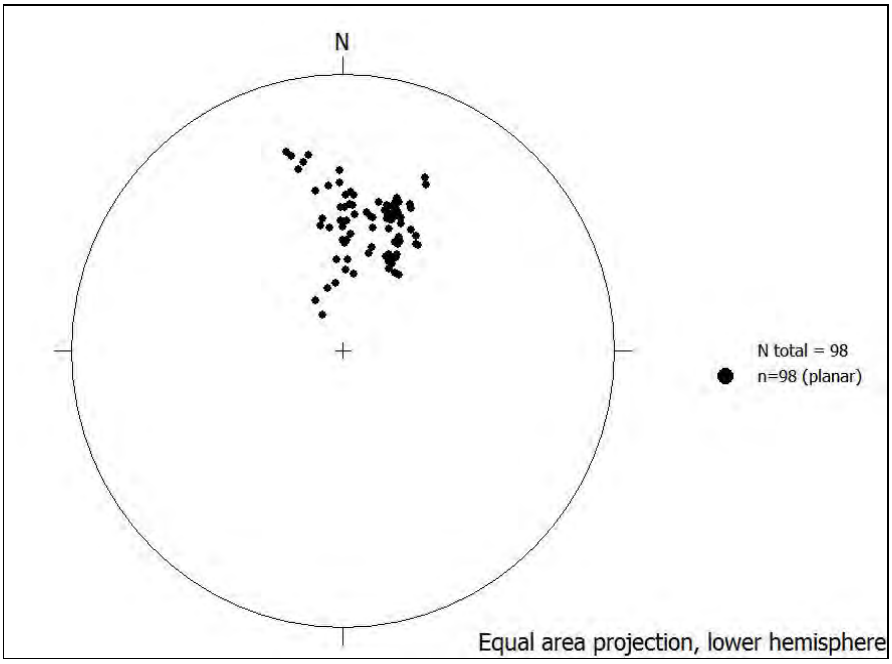

Fig 6-78: Stereogram displaying poles to thrust fault planes at station 5.

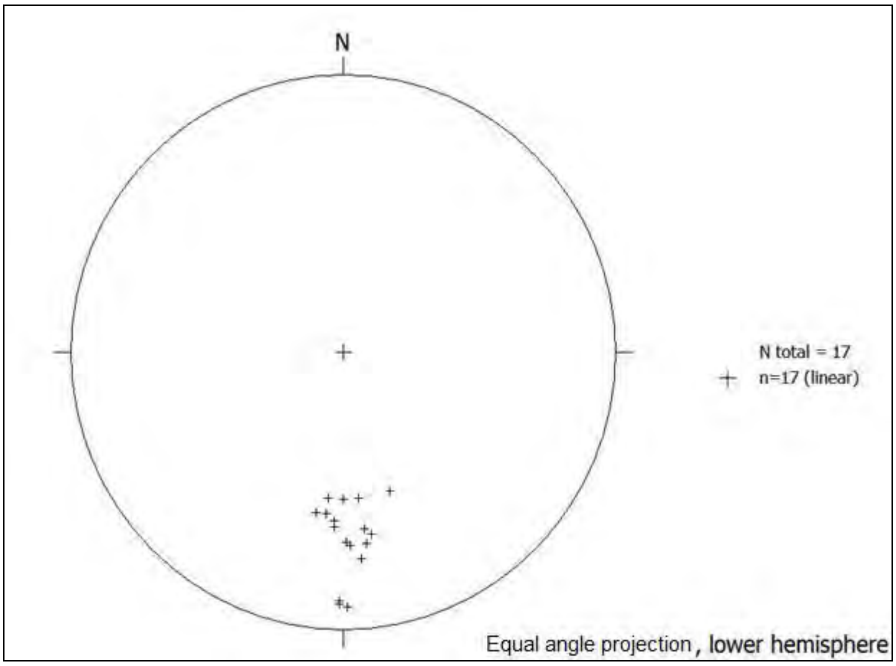

Fig 6-79: Stereogram displaying slickensides on all fore-thrusts at station 5.

Slickensides on fore-thrusts indicate southward dip (Fig 6-79). Evidence of faulting in the form of slickensides is present in F1, F2 and F3. However these slickensides are poorly developed and hamper the determination of sense of movement. These faults are presumed to be low angle thrust faults correlating with the general sense of vergence noted in the northern end of the section (Fig 6-80, Fig 6-81 and Fig 6-82).

Fig 6-80: Inferred thrust fault F1 located towards the southern end of station 5; geological hammer for scale.

Thrust fault F1 dips at a moderate angle towards the south-west. F1 is identified by a brecciated zone towards the bottom of the section. Thrust fault F2, although not outcropping, can be inferred from indicators such as slickenfibres, breccia and rock debris that has accumulated at the base of the fault (Fig 6-81).

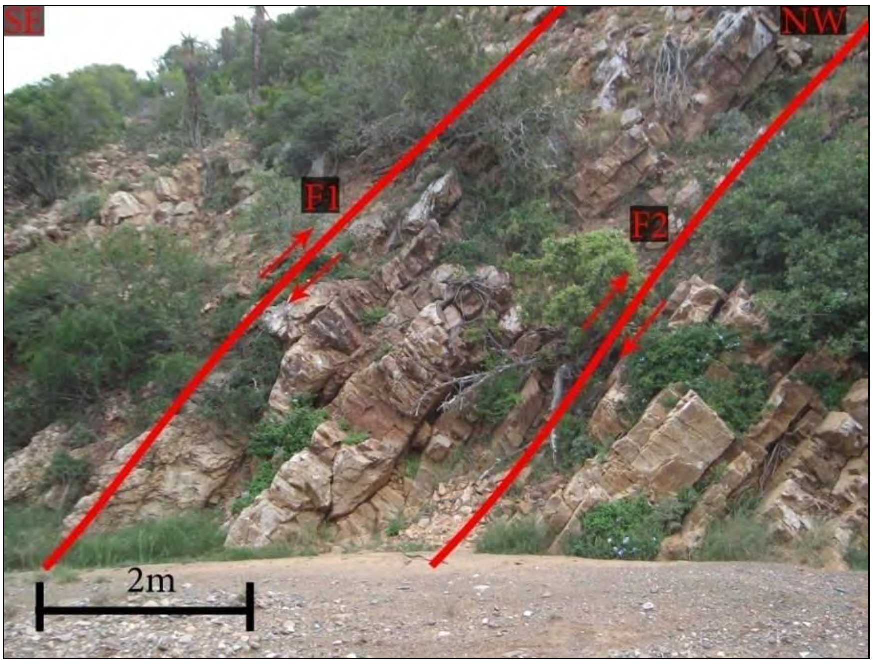

Fig 6-81: Inferred thrust faults F1 and F2.

Thrust faults F2, F3 and F4 are all bedding parallel and verge towards the northwest (Fig 6-82).

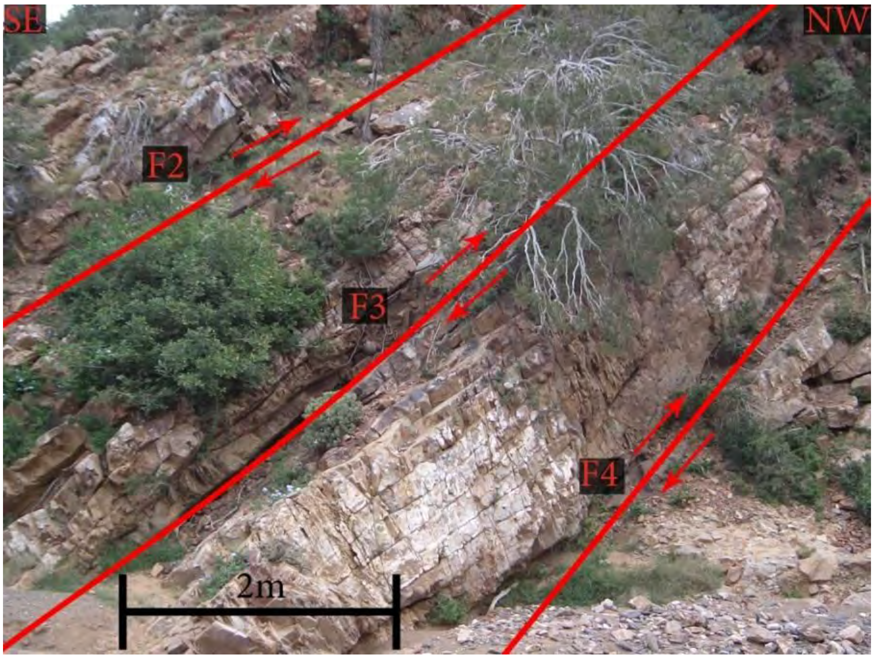

Fig 6-82: Bedding parallel thrust faults F2, F3 and F4.

F7 cuts through the southern limb of anticline Fo2 and ends abruptly (Fig 6-83). F7 dips steeply in a south- southwesterly direction (Fig 6-84).

Fig 6-83: Top: Fault transects limb of an anticline; geological hammer for scale. Bottom: Structural featrures are highlighted. F7 cuts through anticline Fo2 and ends abruptly; geological hammer for scale.

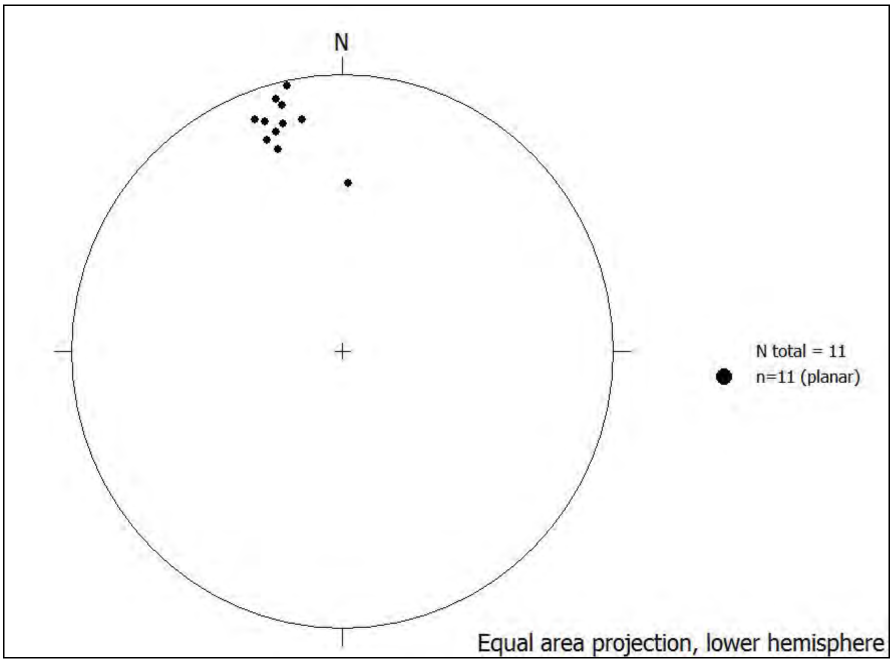

Fig 6-84: Stereogram displaying poles to fault plane F7.

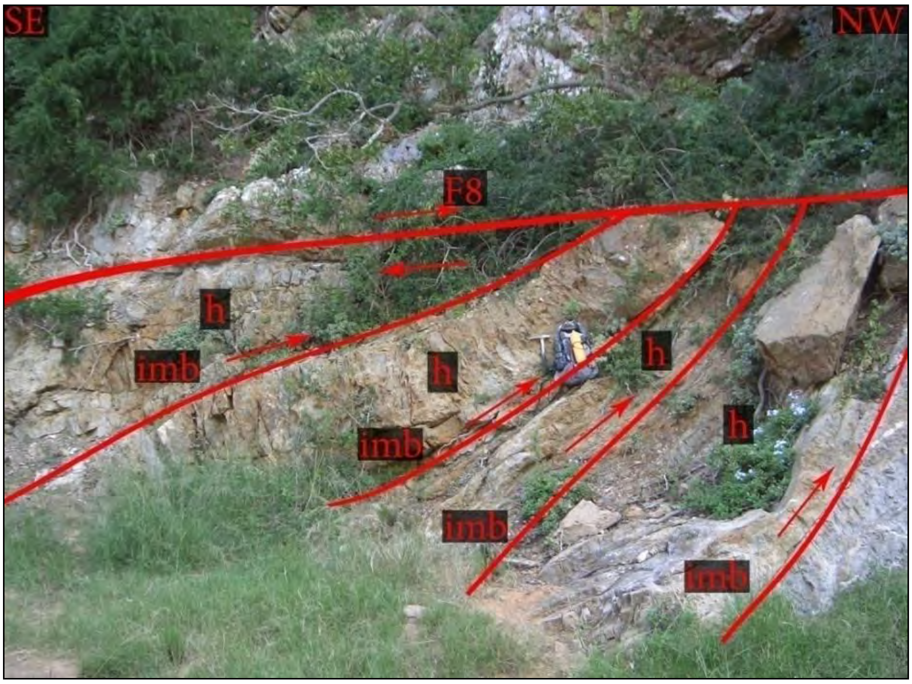

Fig 6-85: Top: Duplex structure. Roof-thrust F8 truncates multiple imbricates (imb) *forming horse structures (h); backpack and geological hammer for scale. Bottom: Structures are highlighte in red.*

A duplex structure is visible towards the north-western end of station 5 (Fig 6-85). Imbricates are truncated by roof thrust F8. F8 dips at a moderate angle towards the south (Fig 6-86). Lineations in imbricates plunge at shallow to steep angles to the south-southeast (Fig 6-87).

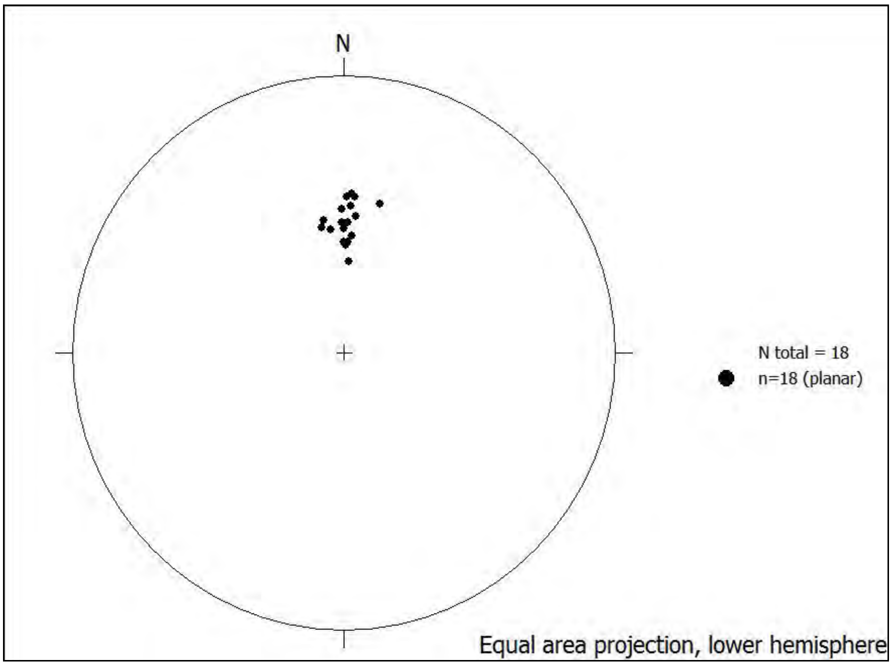

Fig 6-86: Stereogram displaying poles to roof thrust plane F8.

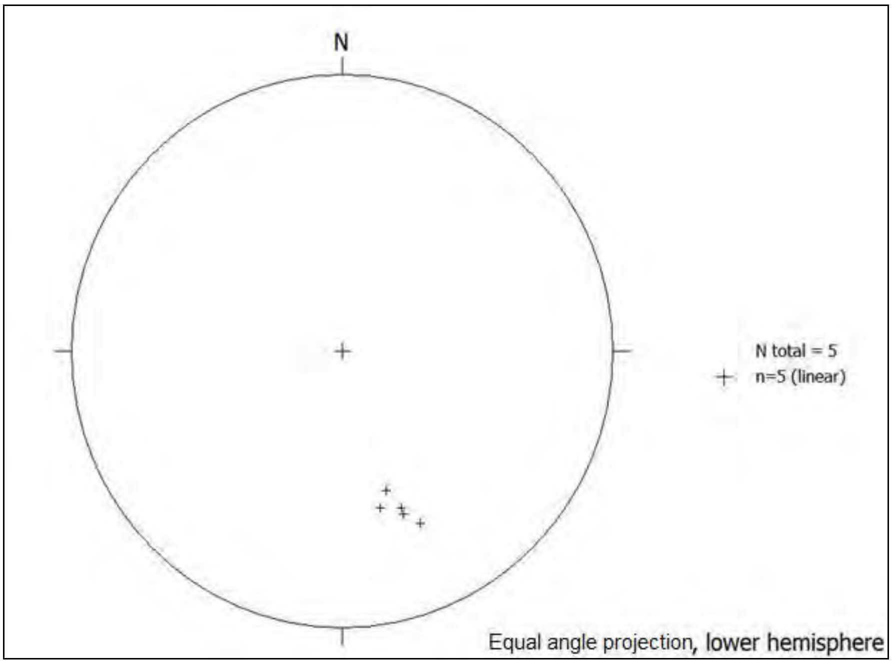

Fig 6-87: Stereogram showing slickenside orientation on roof thrust plane F8.

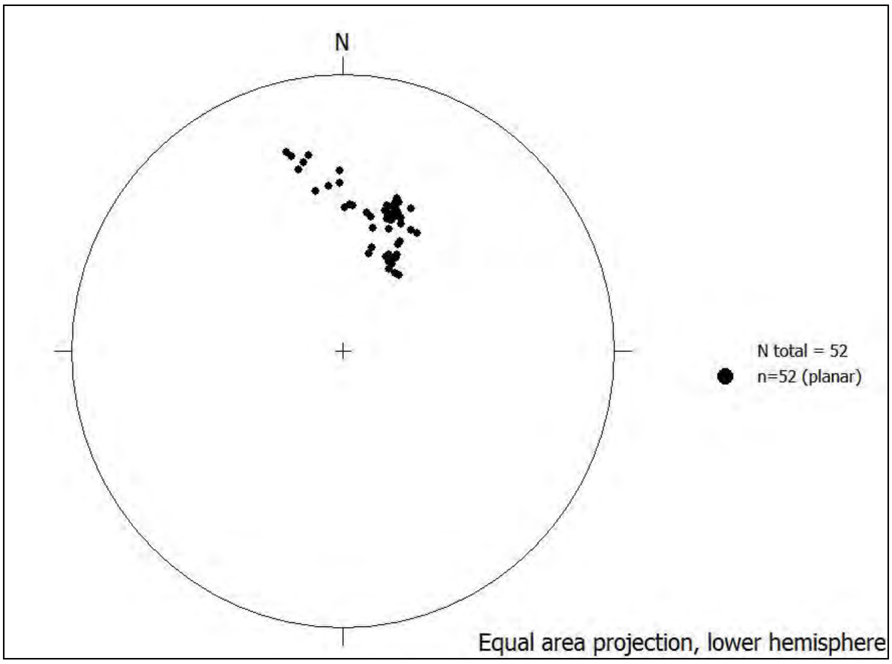

Fig 6-88: Stereogram showing poles to fault planes of imbricate faults in duplex.

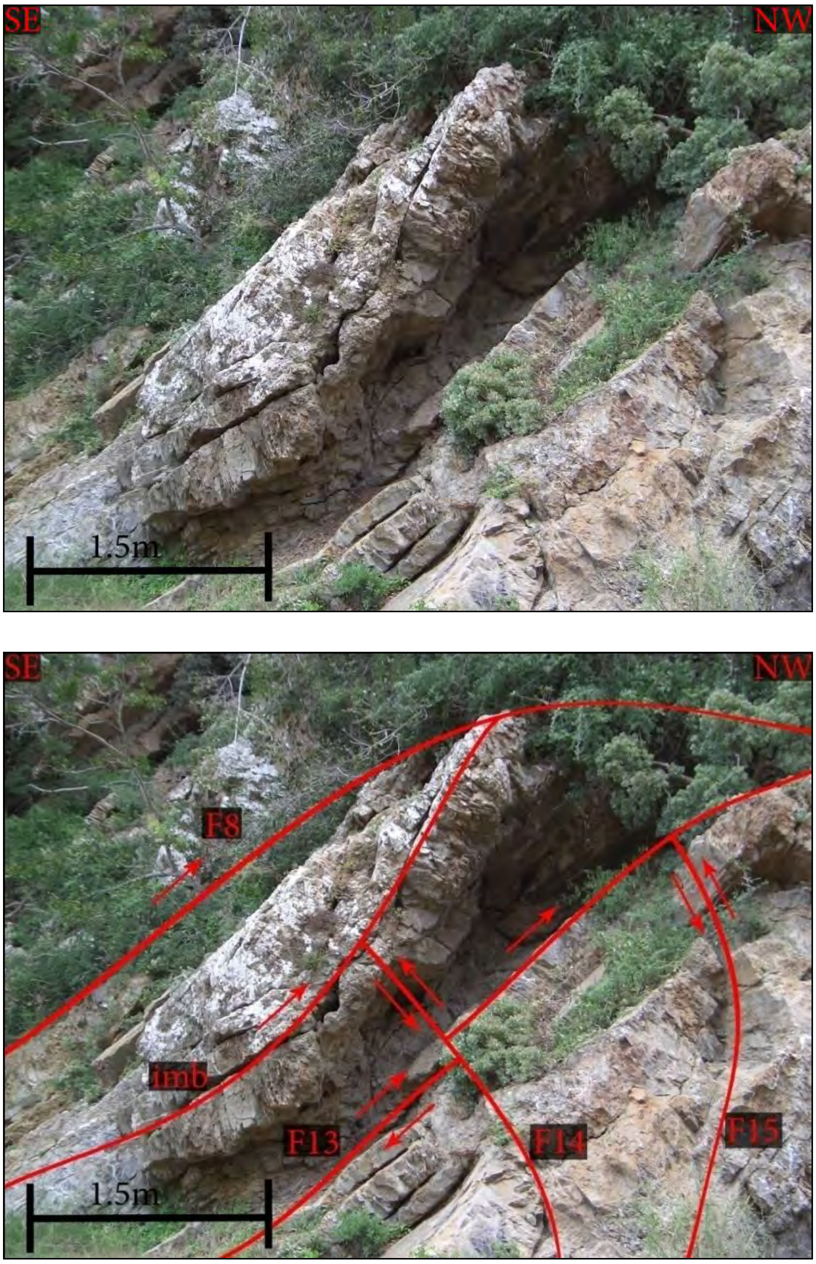

Fig 6-89: Top: Duplex structure displaying backthrusts cutting through earlier formed imbricates, F14 and F15. Roof thrust F8 truncates previously formed imbricates (imb). Bottom: Structures are highlighted in red.

6.8.3.2 Normal faults

Normal fault F6 is the main feature at station 5. A large brecciated zone is associated with F6 and cuts through multiple structures at station 5 (Fig 6-90, Fig 6-92 and Fig 6-93). F6 dips at a steep angle to the southeast (Fig 6-90). F6 dips south and both display large brecciated zones (Fig 6-74, Fig 6-90, Fig 6-92, Fig 6-93 and Fig 6-94). Slickensides on F6 indicate that the hangingwall moved southward (Fig 6-91). Normal fault F17 marks the end of the section (northern extent). The fault cuts through roof thrust F8 and a suspected imbricate fault F16 (Fig 6-94). F17 dips at a steep angle to the south (Fig 6-95). Two normal faults occur at station 5 (F6 and F13).

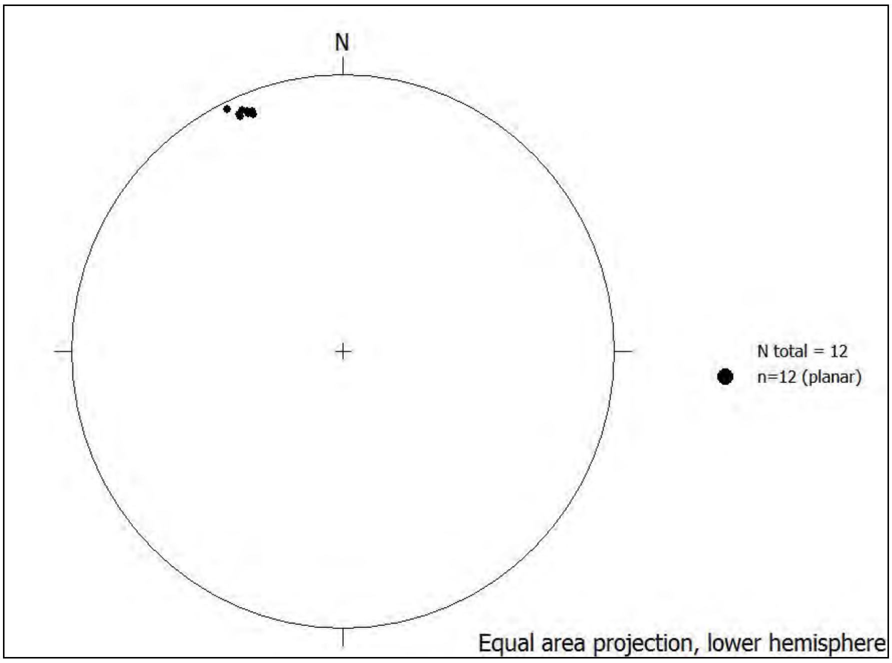

Fig 6-90: Stereogram showing poles to normal fault plane F6.

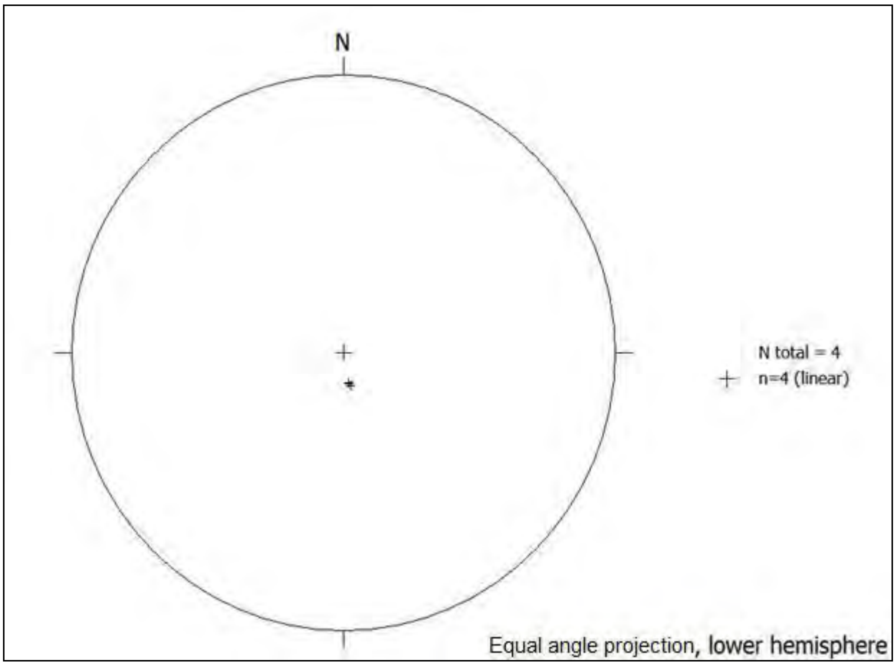

Fig 6-91: Stereogram showing slickensides on normal fault plane F6.

Fig 6-92: Top: A normal fault lies adjacent to a syncline. Bottom: Structures are indicated in red. Normal fault F6 clearly lies adjacent to a syncline Fo1. Bz highlights a brecciated fault zone resulting from normal faulting; geological hammer for scale.

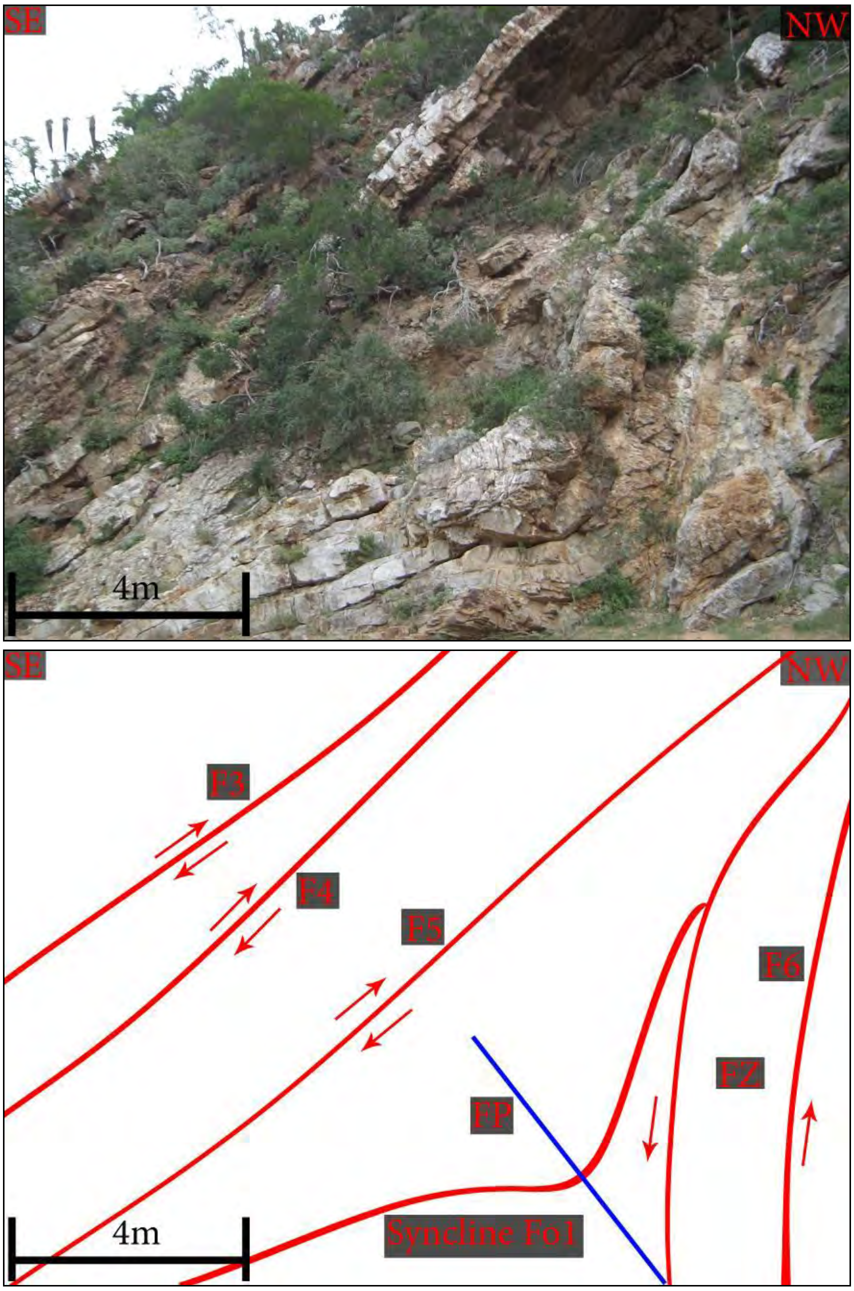

Fig 6-93: Top: Inclined and folded bedding in the Perdepoort Member is cut by a normal fault. Bottom: From highlighted structures it is clear that thrust faults F3, F4 and F5, on the left (SW) truncate a syncline (Fo1) in the centre of the picture. Normal fault F6 located is located north of syncline Fo1. The axial plane of Fo1 is indicated by FP, and FZ indicates a highly brecciated fault zone associated with normal fault F6.

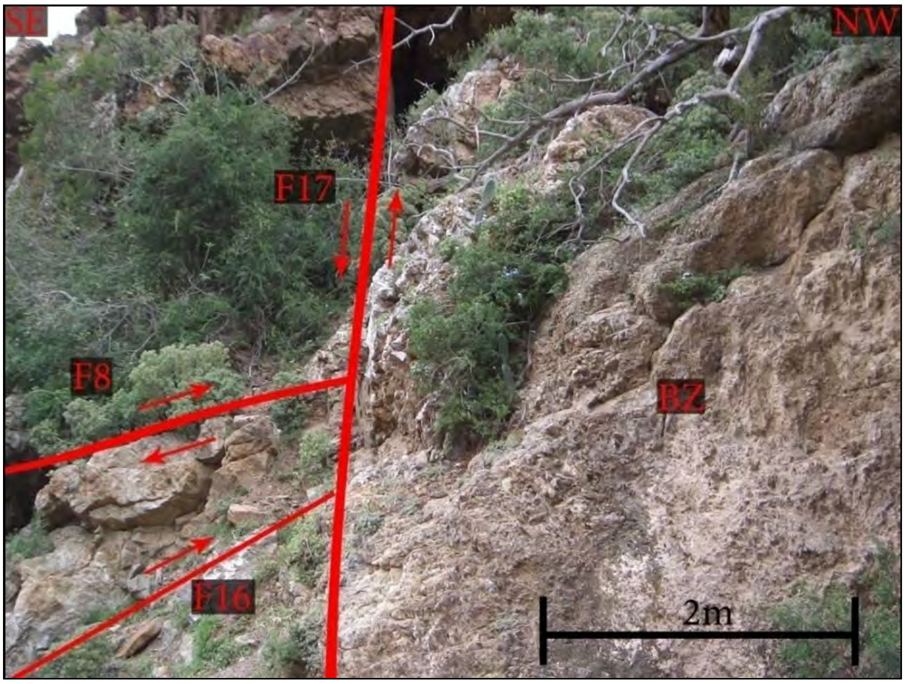

Fig 6-94: Normal fault F17 situated at the northern end of station 5 marks the end of the section. A broad zone of brecciated rocks BZ occurs adjacent to the fault F17, which cuts F8 and F16.

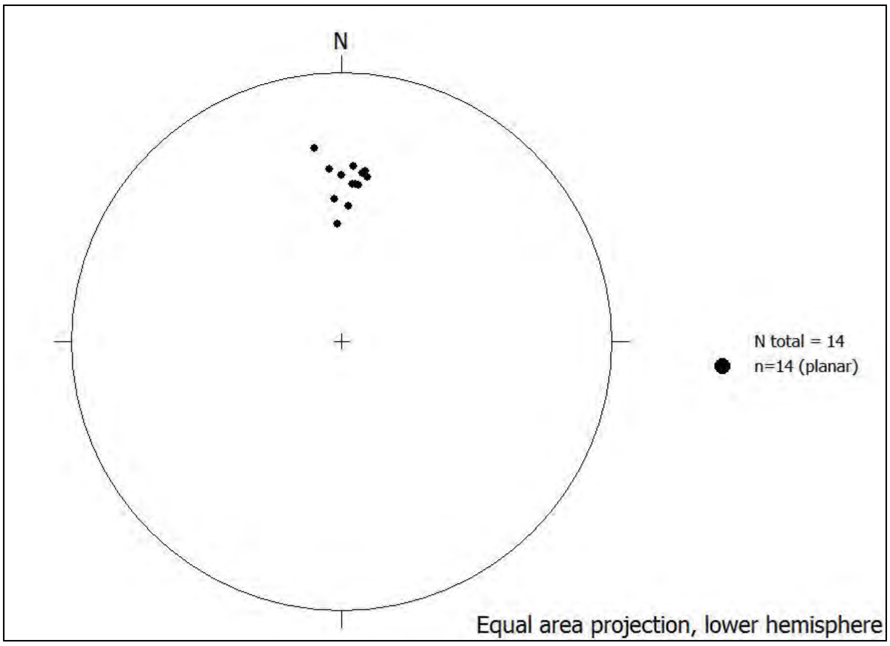

Fig 6-95: Stereogram displaying poles to fault plane of normal fault F17.

6.8.4 Folds

Folding is well developed at station 5. The section contains two synclines, Fo1 and Fo3 and two anticlines, Fo2 and Fo4 (Fig 6-74). Syncline Fo1 is closely associated with normal fault F6 (Fig 6-92 and Fig 6-93). Fo1 displays a component of fault drag (Fig 6-92). Syncline Fo1 has an interlimb angle of 37° and a fold axis plunging at 27° in an approximate westerly direction. Fo1 can be classified as a subvertical, gently plunging close fold. Anticline Fo2 plunges at 8° in a roughly west-southwesterly direction and has an interlimb angle of approximately 126°. Fo2 can be classified as a moderately inclined, sub-horizontally plunging gentle fold. An open syncline Fo3 is also present towards the centre of the section (Fig 6-74). Fold Fo4 appears to have been a tight overturned anticline that has been cut by normal fault F13 (Fig 6-98).

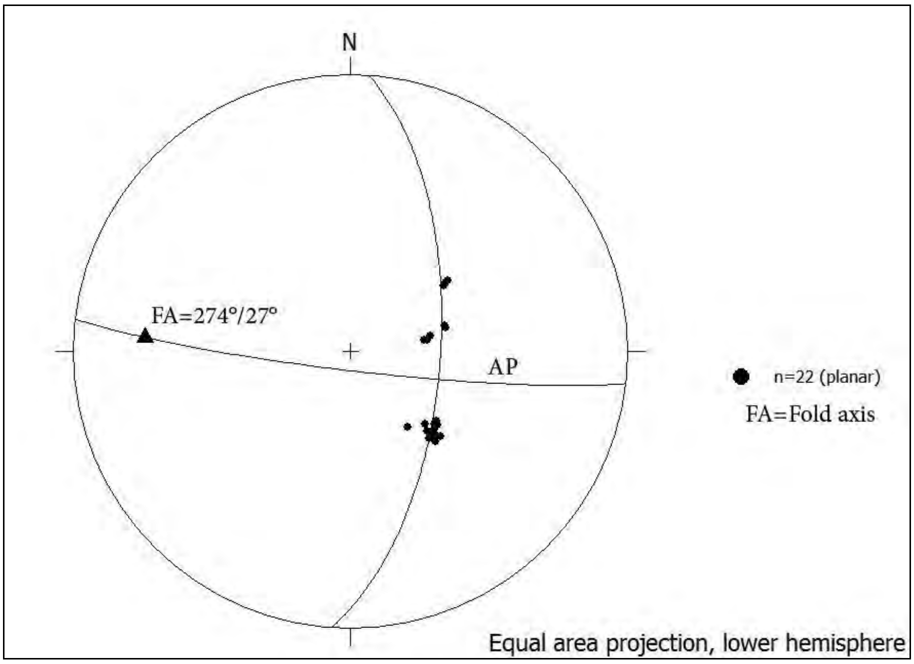

Fig 6-96: Stereogram displaying poles to bedding plane of syncline Fo1. AP indicates axial plane; plunge and trend of fold axis are also indicated.

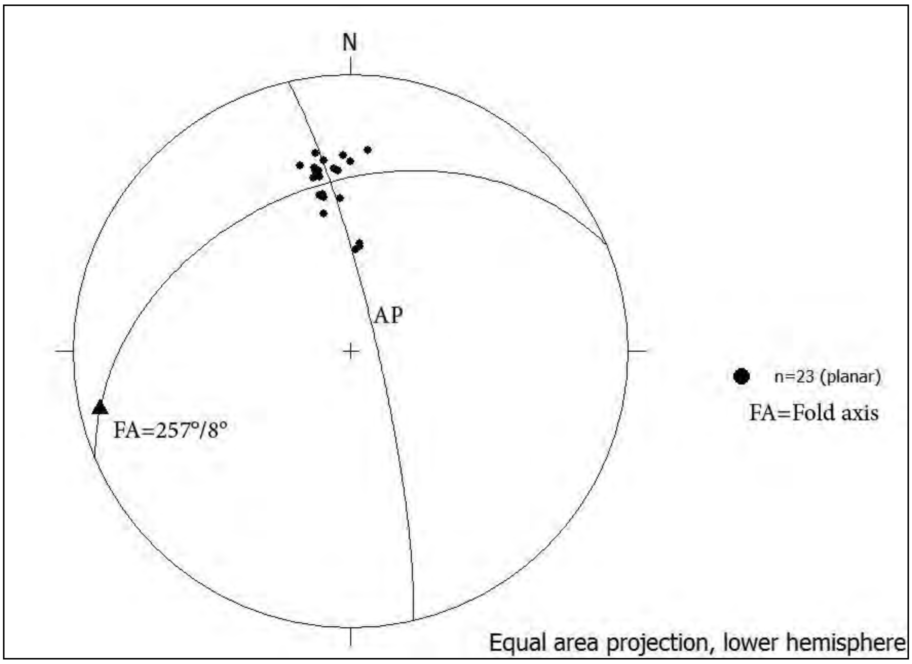

Fig 6-97: Stereogram displaying poles to bedding plane of anticline Fo2. AP indicates axial plane plunge and trend of fold axis are also indicated.

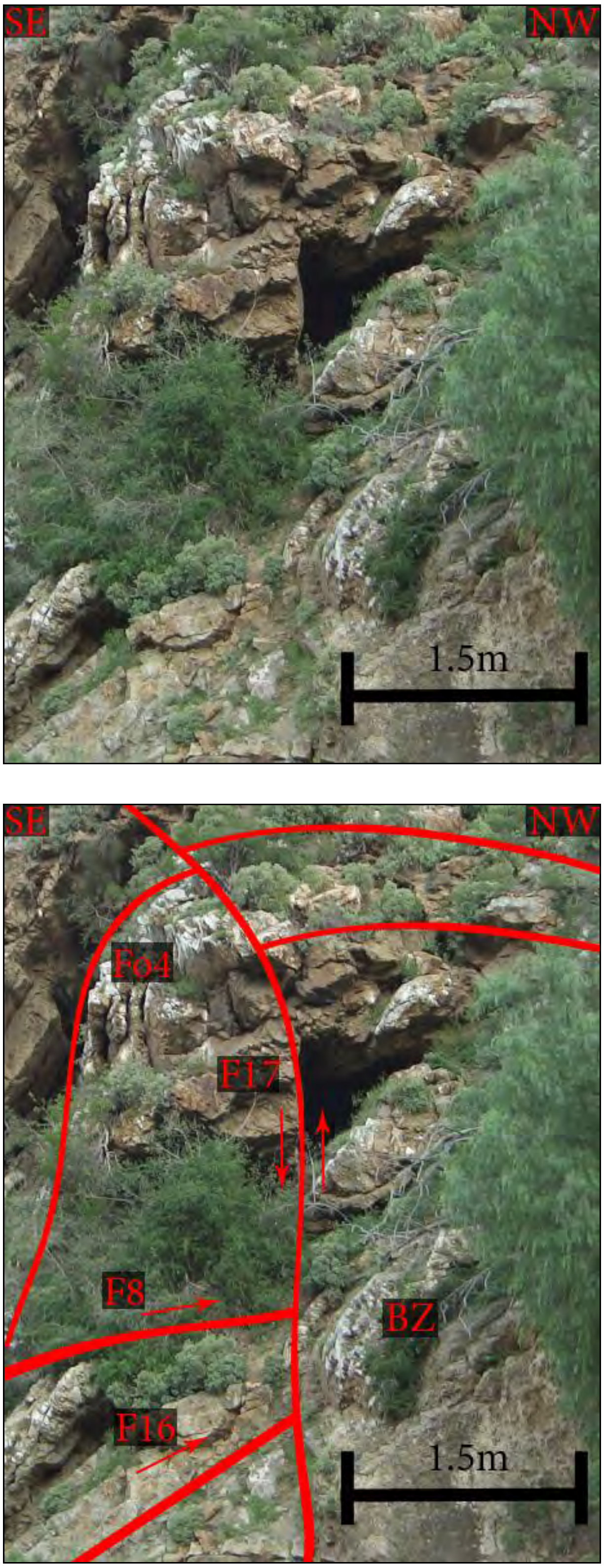

Fig 6-98: Top: An anticline is cut by a normal fault. Bottom: Fold Fo4 is cut by normal fault F17 the fault geometry is distorted as a result of the angle the photo was taken at.

6.8.5 Joints

The section contains systematic jointing with one prominent (J1) and one less prominent joint set (J2). Joints dip mostly at moderate inclinations to the north (Fig 6-99, Fig 6-100 and Fig 6-101).

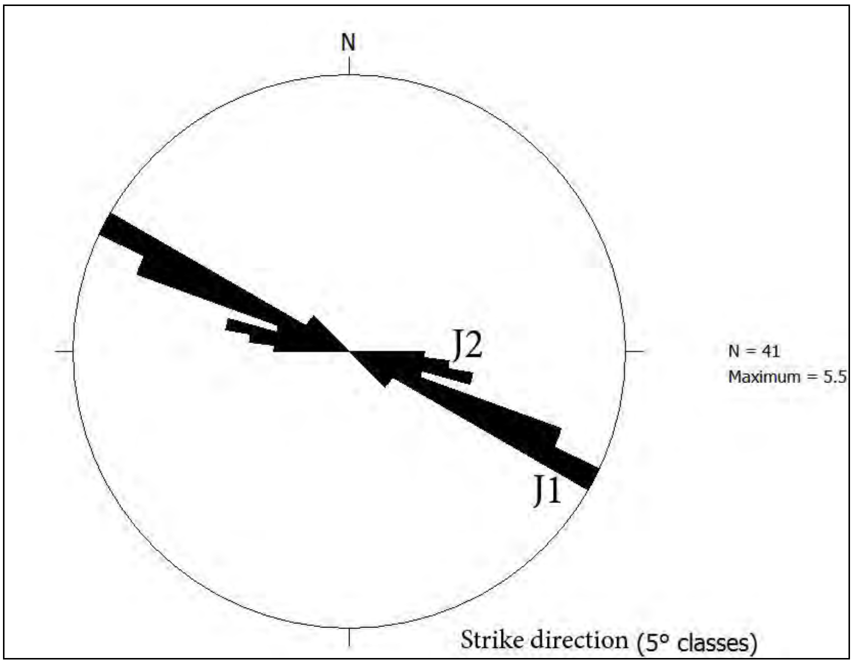

Fig 6-99: Rose diagram showing striking direction of the main joint sets at station 5.

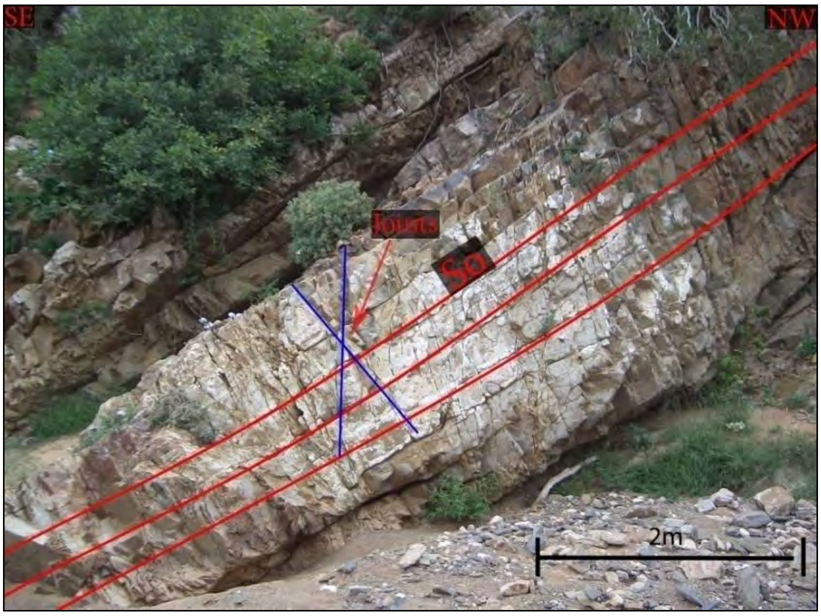

Fig 6-100: Photo displaying bedding as well as two prominent jointing directions in the study section.

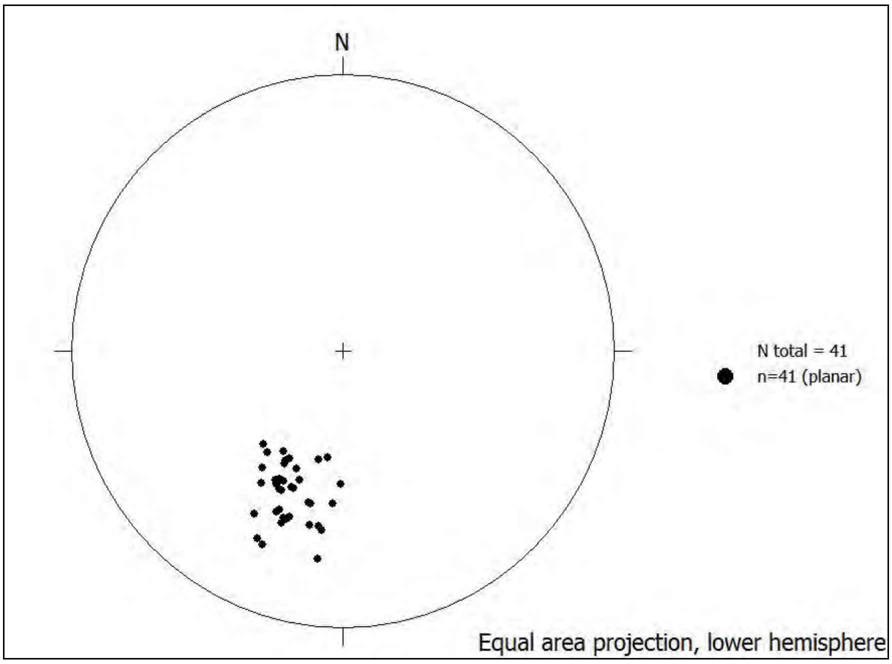

Fig 6-101: Stereogram showing poles to jointing planes at station 5.

6.9 Station 6

6.9.1 Introduction

Station 6 is located to the north of station 5 on the eastern side of a south flowing non-perennial river Fig 6-73. The section consists of red-brown, clay coloured quartzites which make up the Rooirand Member. Quartzites are fine grained and sedimentary structures are not as prevalent when compared to the Perdepoort Member. Consequently sedimentary structures were difficult to identify and facing direction was inferred as right way up correlating with the stratigraphic seqeunce noted at station 5 which is located immediately to the south. Quartzite beds range in thickness from 10cm to 1.5m. Fine grained dark-grey argillaceous beds are also noted and range in thickness from 1cm to 20cm. The section is dominated by faulting with no significant folding (Fig 6-102). The area contains both lower and higher angle thrust faults and north and south dipping normal faults (Fig 6-102). The area forms part of the gentle dipping southern limb of a northward verging, overturned anticline (Fig 6-1, Fig 6-2 and Fig 6-103). The fold axis of this anticline occurs near the northern extent of the study area. The infolded Dwyka Group is encountered slightly further north.

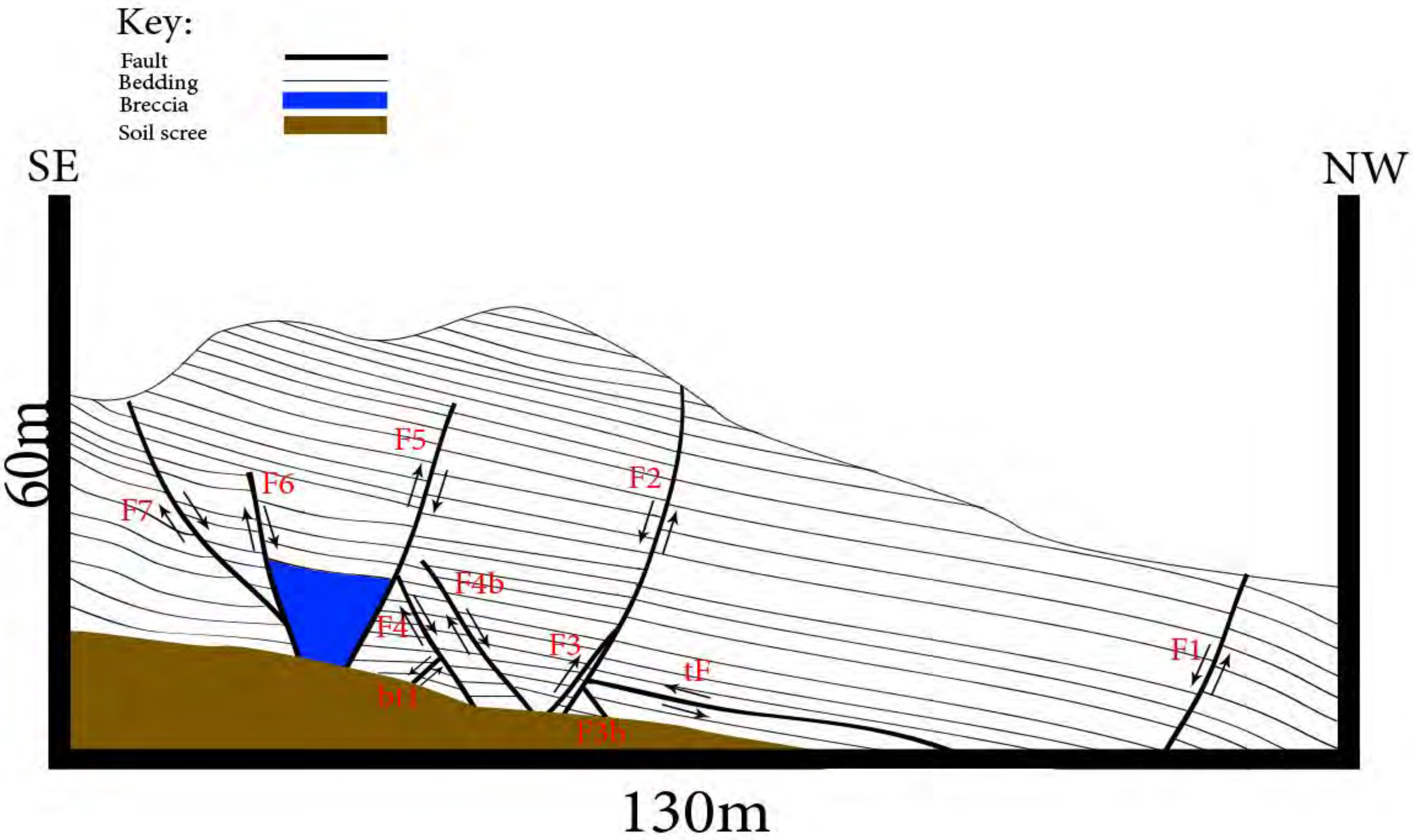

Fig 6-102: Cartoon cross section showing main faults at station 6.

6.9.2 Bedding

Bedding is well developed throughout the section and dips in a southerly direction (Fig 6-104). Bedding is inferred as right way up by correlation with station 5 (Perdepoort Member) which is located immediately south of station 6 (Fig 6-73). Bedding forms part of the gentle south dipping limb of a north-verging mega-anticline.

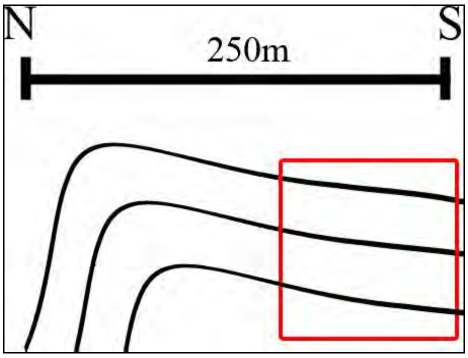

Fig 6-103: Sketch illustrating the position of section2 (demarcated with red) in relation to the mega anticline which forms the main mega scale feature in zone 2.

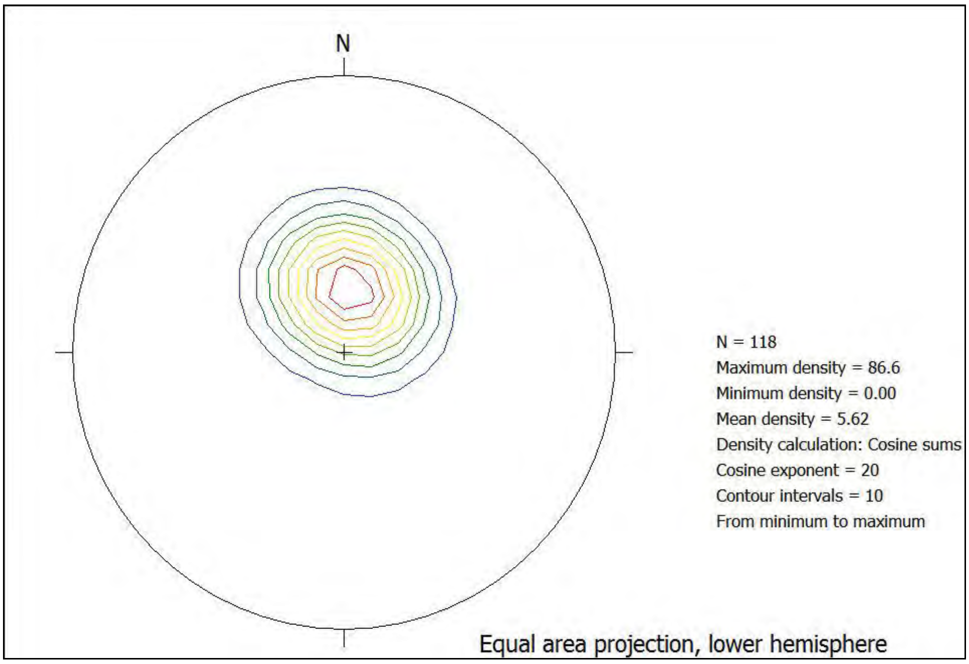

Fig 6-104: Stereogram showing poles to bedding at station 6.

6.9.3 Faults

Faults are clearly visible in the section as they displace bedding. Slickensided surfaces are well developed on most fault planes and also serve to reveal the location of less obvious faults in the section. The relative sense of movement was determined through sense of movement on slickensided surfaces, marker bed displacement and fault drag. The section contains a total of 11 faults including fore- and back thrusts as well as south- and north dipping normal faults, which dominate the section (Fig 6-102 and Fig 6-105). Faults are not as closely spaced when compared to faulting in the Perdepoort Member. Thrust fault tF shows bedding parallel geometry in cross-sectional view but most faults cut bedding at moderate to steep angles (Fig 6-102, Fig 6-105 and Fig 6-114). Minor strike-slip faults are also noted in the section. Normal faults are considered the youngest secondary structures in the area as normal fault F2 transects three other faults in the section (Fig 6-102, Fig 6-105 and Fig 6-114). Most normal faults possess steep inclinations but some also display moderate dipping fault planes (Fig 6-105, Fig 6-110, Fig 6-115, Fig 6-126 and Fig 6-127). Thrust propagation could not be determined. However, backthrust bt1 is truncated by a younger fore-thrust F4, suggesting a break-back sequence of propagation (Fig 6-102 and Fig 6-105). F5 on the other hand, might be a subordinate backthrust to a younger fore-thrust which has broken into the footwall of F4, suggesting piggy-back propagation.

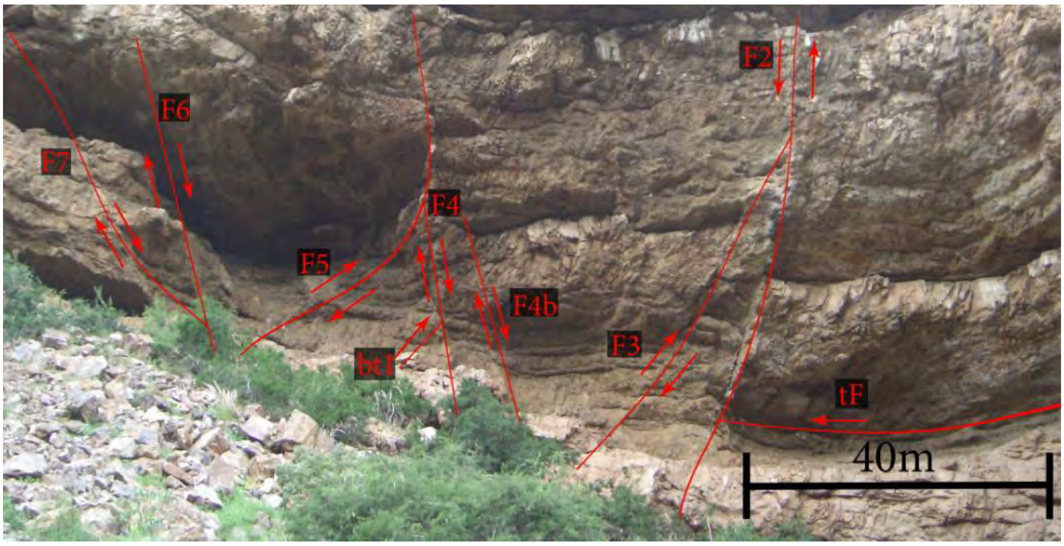

Fig 6-105: Photo showing main faults (F1 to F6) at station 6 and thrust fault tF.

6.9.3.1 Thrust faults and reverse faults

Three thrust faults can be observed within the section F5, bt1 and tF (Fig 6-102 and Fig 6-105). F4 and tF represent high angle and low angle reverse and fore-thrust respectively. F5 represents a backthrust probably associated with an earlier formed fore-thrust. Fore-thrusts show north-eastward vergence whereas backthrusts verge in approximately the opposite direction. Backthrusts F5 and bt1 dip at moderate inclinations to the south-east. Thrust fault tF could not be adequately measured because its fault plane was not appropriately exposed, being only visible in cross-section. F5 appears to be the youngest thrust fault in the section as no other faults transect F5.

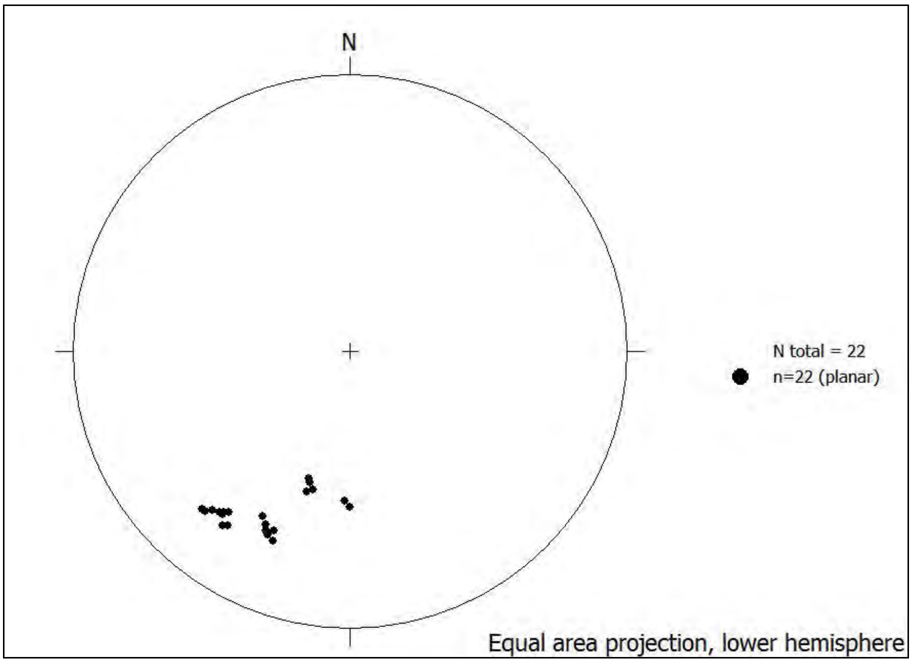

Fig 6-106: Stereogram showing poles to backthrust F5.

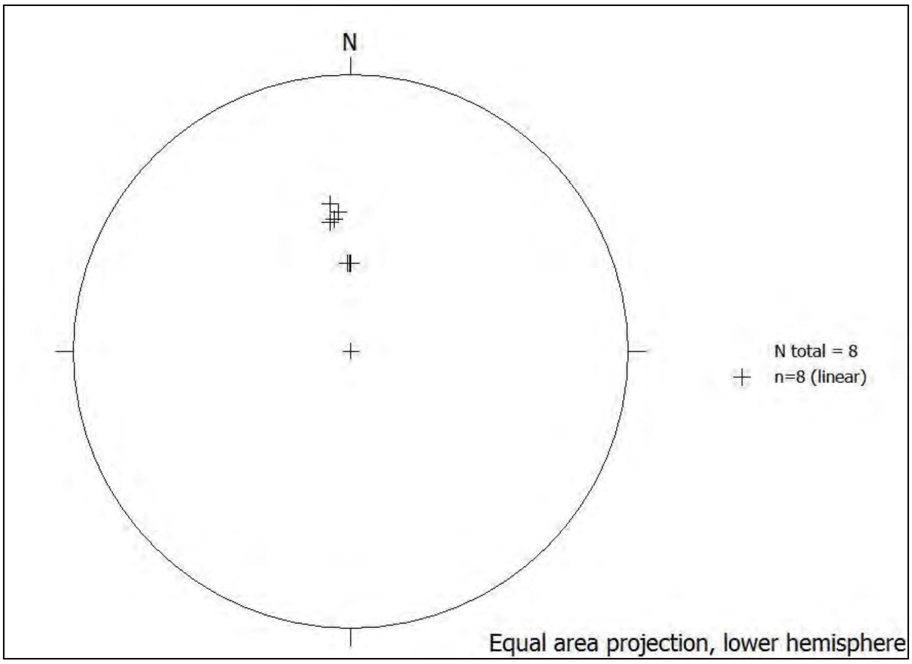

Fig 6-107: Stereogram showing trend and plunge of slickenfibres on fault plane F5.

Fig 6-108: Well developed slickensided surface associated with backthrust F5, slickensides indicated by sl; pen for scale.

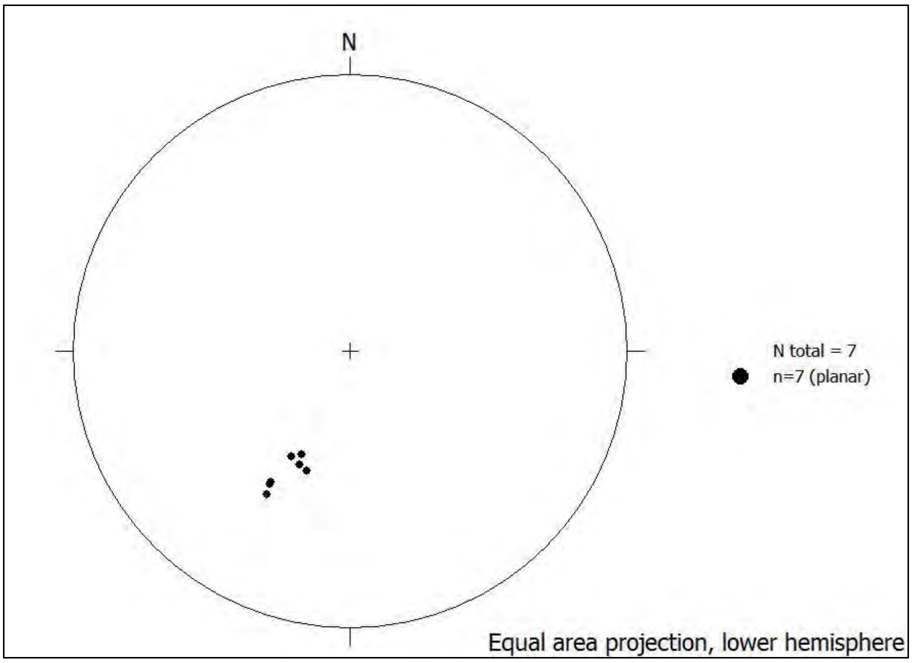

Fig 6-109: Stereogram showing poles to backthrust bt1.

6.9.3.2 Normal faults

The section is dominated by normal faults. Eight normal faults are present in the section, F1, F2, F3, F3b, F4, F4b, F6 and F7 (Fig 6-102 and Fig 6-105). Normal faults dip both towards the south and north (Fig 6-105). Normal fault F2 transects thrust faults tF and F3 thus confirming that it is a younger normal fault (Fig 6-105 and Fig 6-114). F1 dips at moderate to steep inclination in an approximately north-easterly direction (Fig 6-110). F1 clearly disrupts and displaces bedding and a zone of brecciated strata can also be observed in its fault plane (Fig 6-111 and Fig 6-112). Lineations on F1 show a steep plunge trending in a north-northwesterly direction (Fig 6-113).

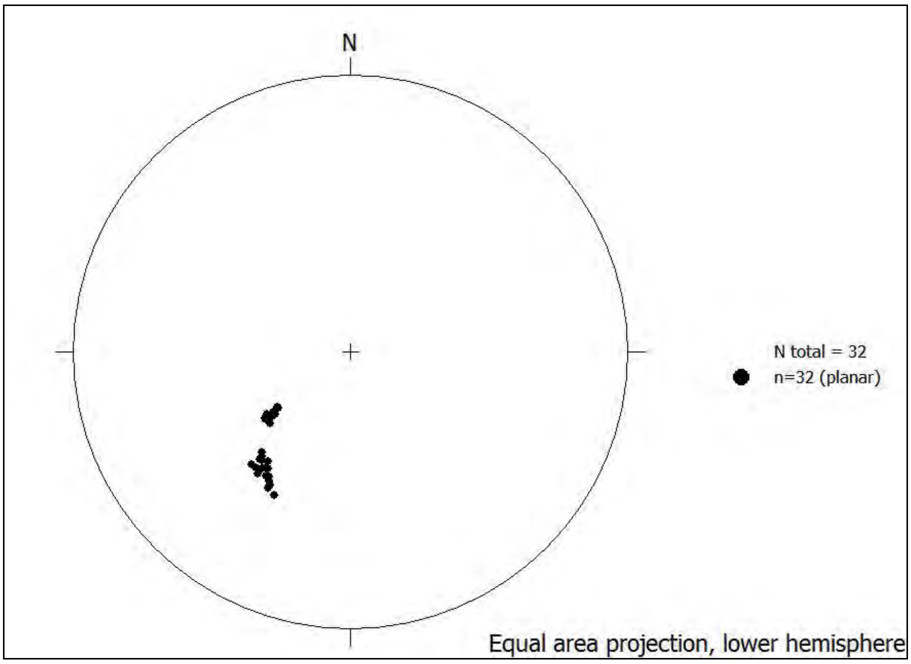

Fig 6-110: Stereogram showing poles to normal fault F1.

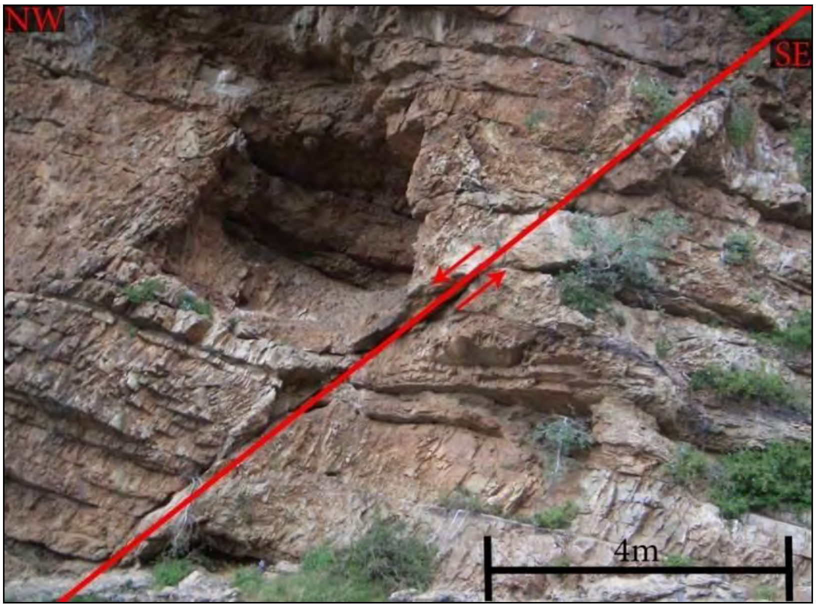

Fig 6-111: Normal fault with large displacement located at station 6, zone 2.

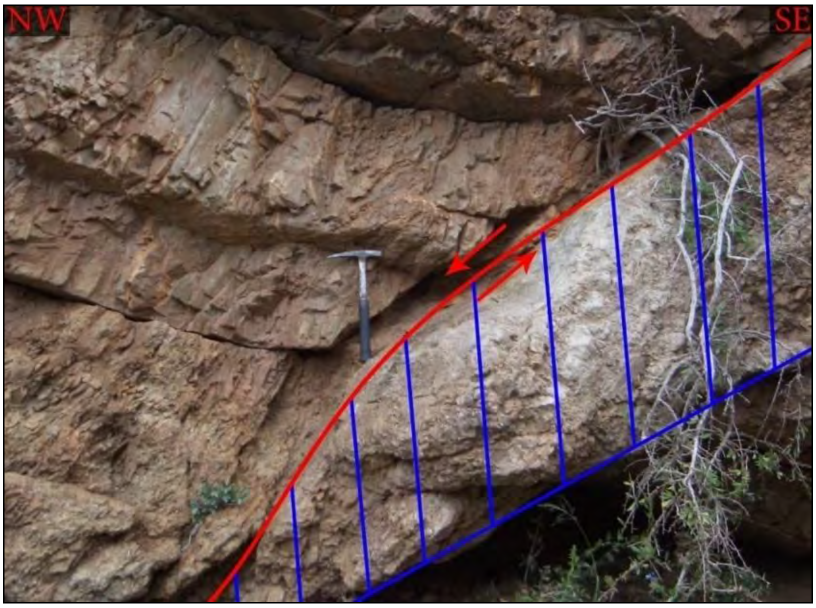

Fig 6-112: Close-up view of normal fault F1, note brecciated rocks demarcated by blue lines; geological hammer for scale.

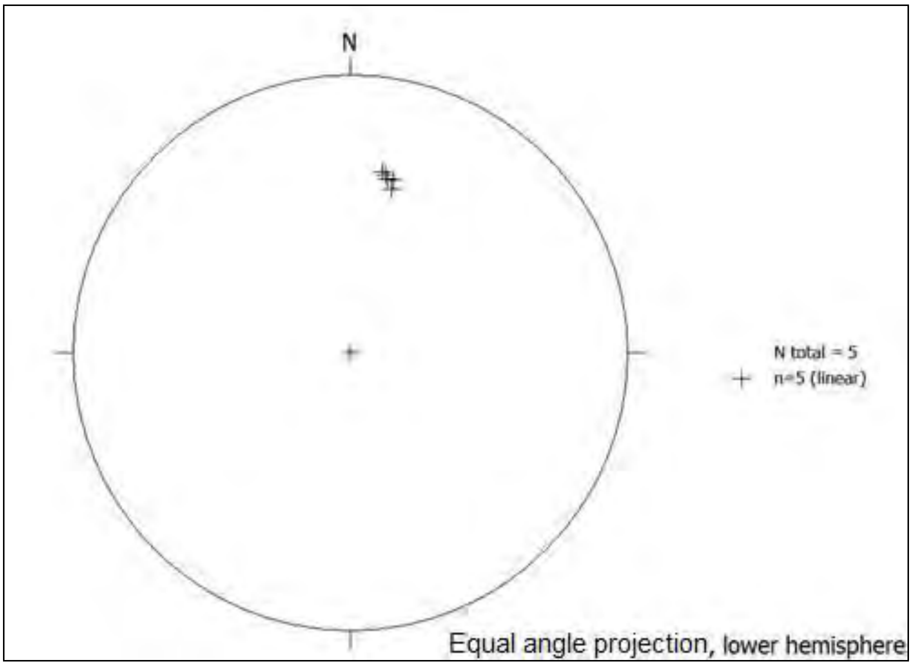

Fig 6-113: Stereogram showing trend and plunge of slickenfibres on fault plane F1.

Fig 6-114: Normal fault F2 transects earlier formed low angle thrust fault (tF); geological hammer for scale.

Normal fault F3 dips at steep angles in a north-easterly direction (Fig 6-115). Large amounts of fractured rocks are also present in and adjacent to its fault plane (Fig 6-116). Lineations on F3 plunge steeply in a north-northeasterly direction (Fig 6-117 and Fig 6-118).

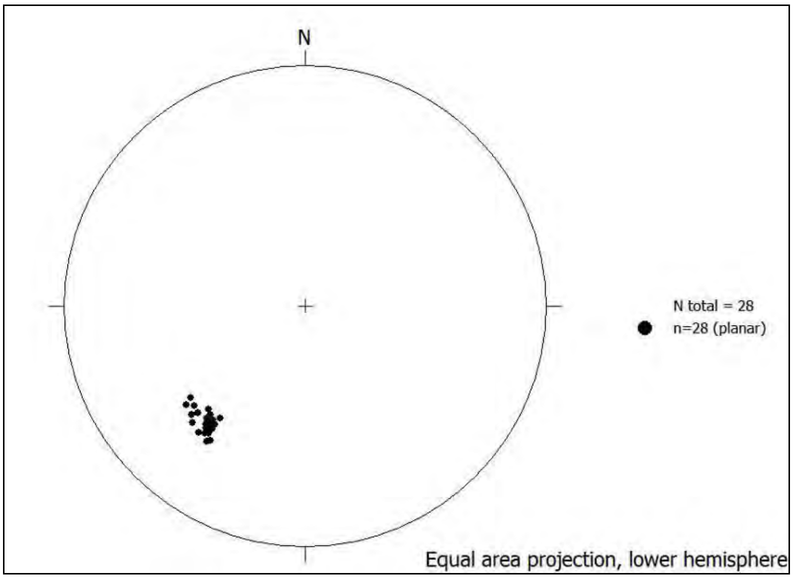

Fig 6-115: Stereogram showing poles to normal fault F3.

Fig 6-116: Normal fault F3; geological hammer for scale.

Fig 6-117: Well developed slickenside surfaces (sl) associated with normal fault F3; pen for scale.

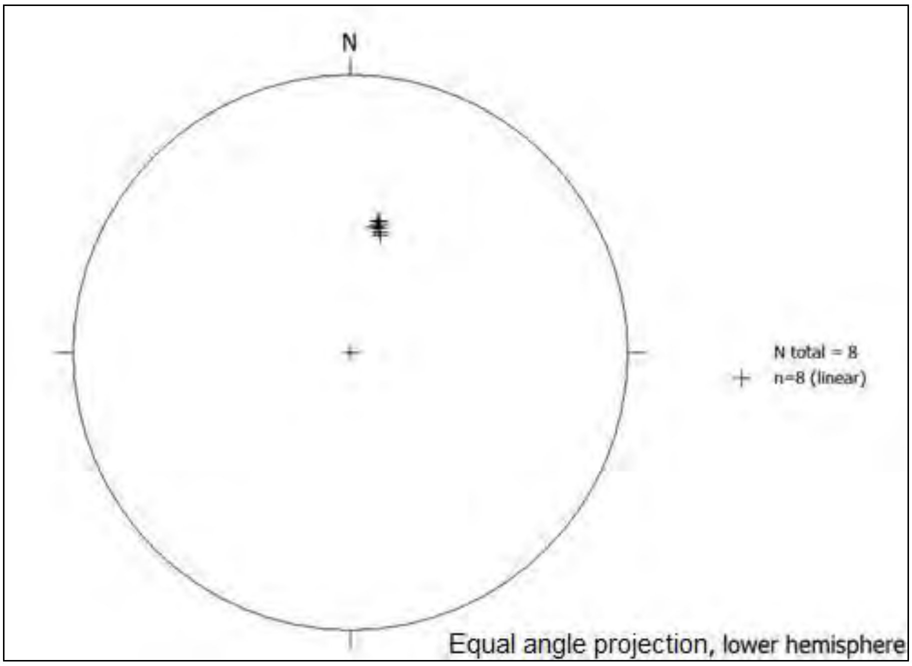

Fig 6-118: Stereogram showing trend and plunge of slickenfibres on fault plane F3.

F3b represents a normal fault that has undergone a minimal movement (Fig 6-122). The fault clearly displaces a dark marker bed with its hanging wall being downthrown to the north-west (Fig 6-122). Normal fault F4 dips at a steep angle in a south westerly direction with near vertically plunging slickensides (Fig 6-119, Fig 6-120 and Fig 6-121). Normal fault F4b also clearly disrupts bedding (Fig 6-123).

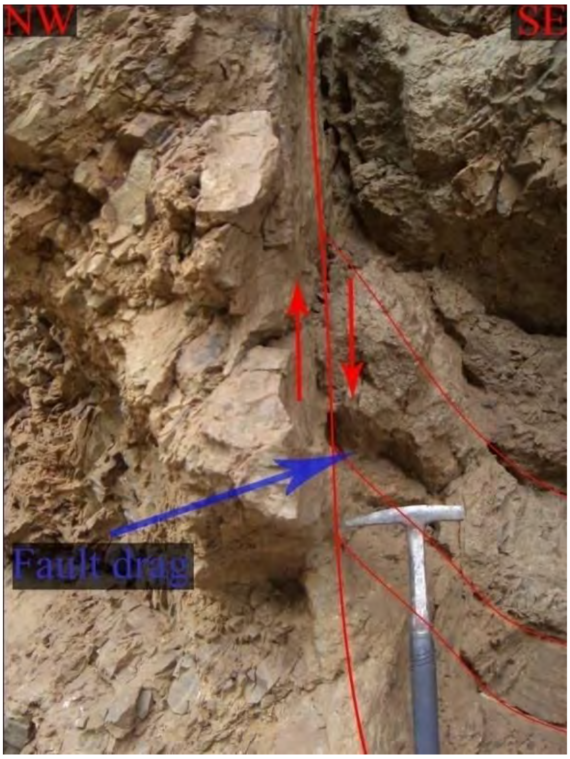

Fig 6-119: Normal fault F4 the sense of movement is clearly evident from the fault drag seen on the right of the photo; geological hammer for scale.

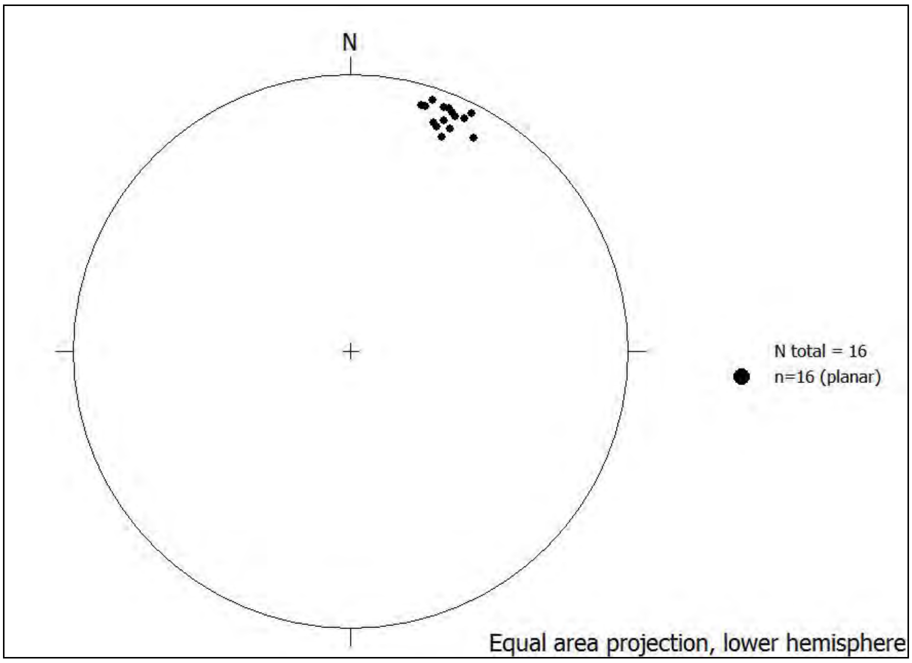

Fig 6-120: Stereogram showing poles to normal fault F4.

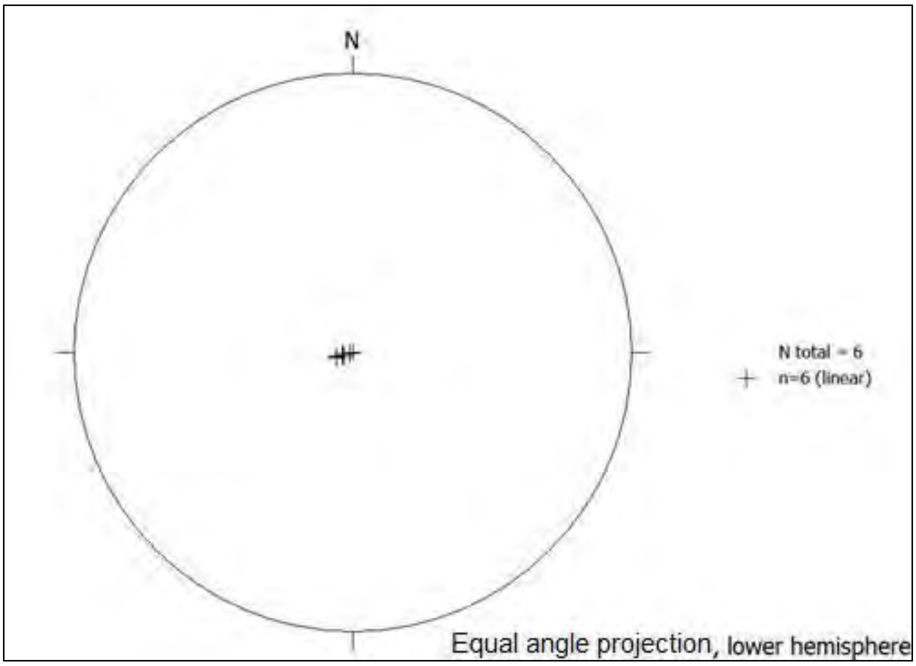

Fig 6-121: Stereogram displaying slickenfibres on fault plane F4.

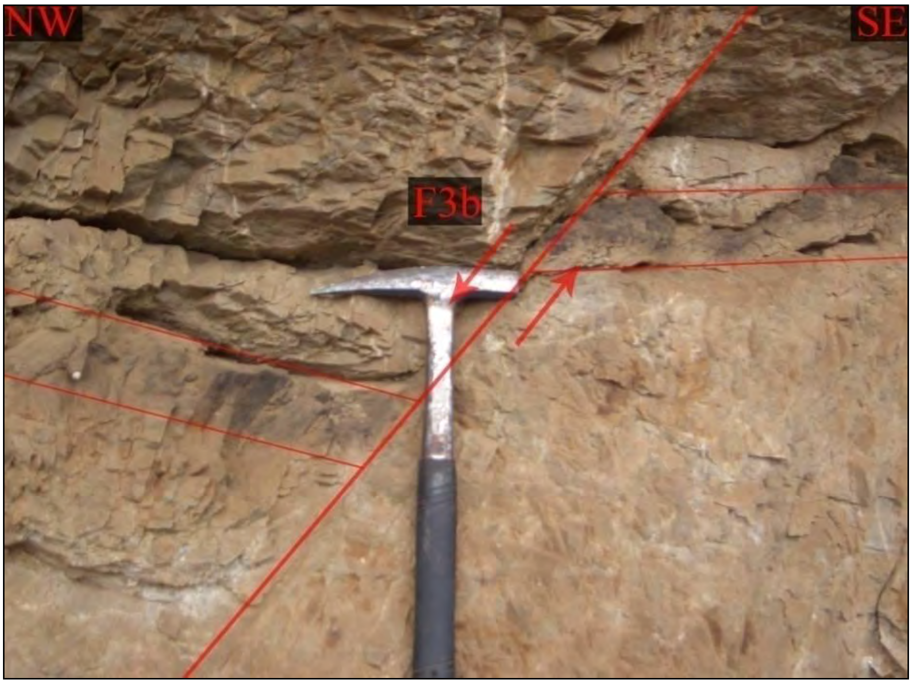

Fig 6-122: Normal fault F3b note displacement of marker bed indicated by red lines; geological hammer for scale.

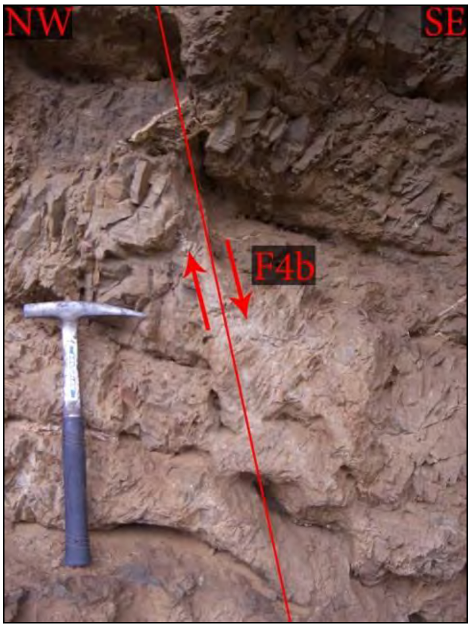

Fig 6-123: Normal fault F4b; geological hammer for scale.

Normal faults F6 and F7 are clearly visible where they disrupt bedding. They both contain abundant slickenside surfaces and in the case of F7 display fault drag (Fig 6-124, Fig 6-125 and Fig 6-128). Normal fault F7 is transected by F6 towards the base of the outcrop (Fig 6-125). Backthrust F5 and normal fault F6 enclose a zone of highly fractured rocks which show cleavage planes with a steeply inclined orientation (Fig 6-124). Normal fault F7 dips at a steep angle in a south-westerly direction, whereas the azimuth and dip of F6 varies slightly from south, at steep inclinations, to south–southwest at less steeper inclinations (Fig 6-126 and Fig 6-127).

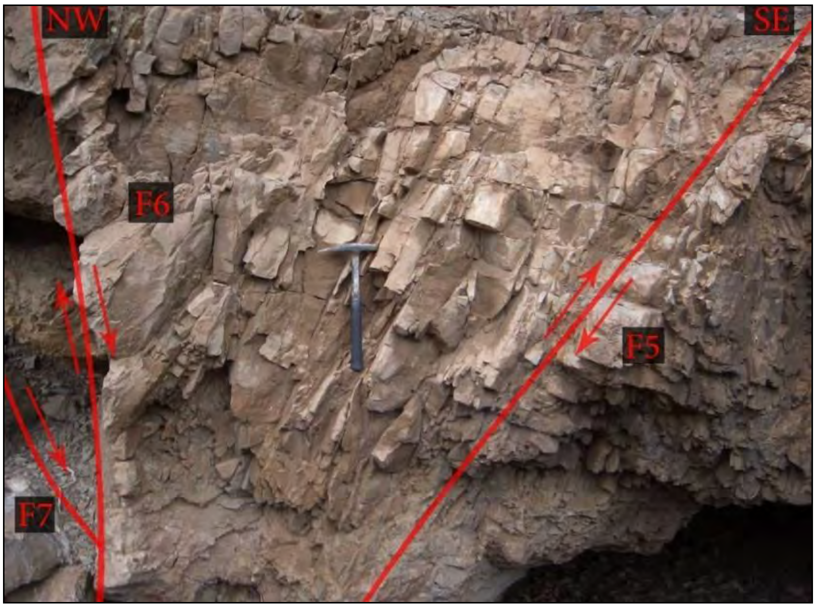

Fig 6-124: Normal faults F6 and F7 converge towards the bottom left of the photo, backthrust F5 is on the right side of the photograph; geological hammer for scale.

Fig 6-125: Normal faults F6 and F7 viewed from a wider perspective. Displacement on F7 shows down to the south movement; geological hammer for scale.

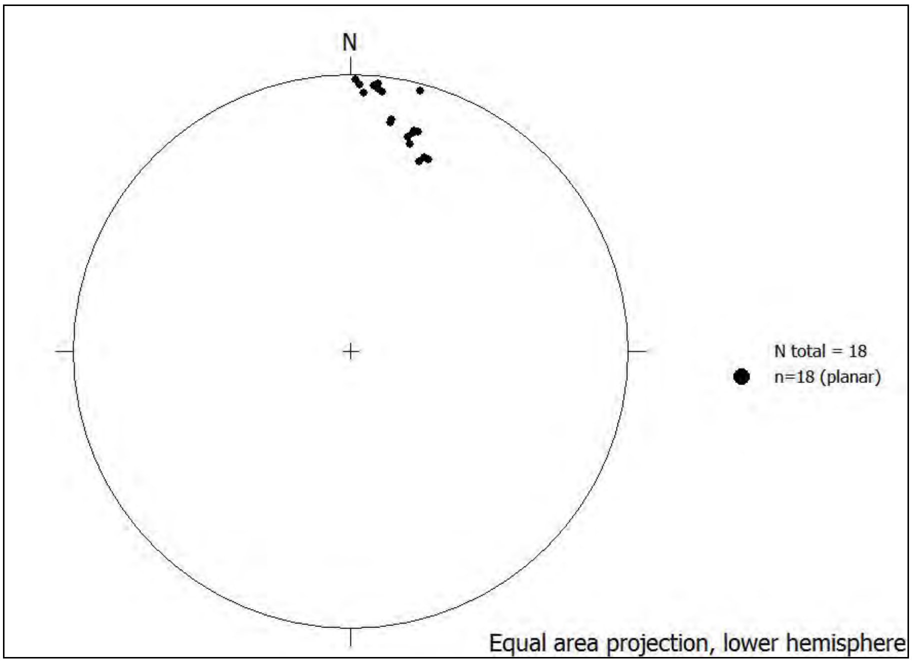

Fig 6-126: Stereogram showing poles to normal fault plane F6.

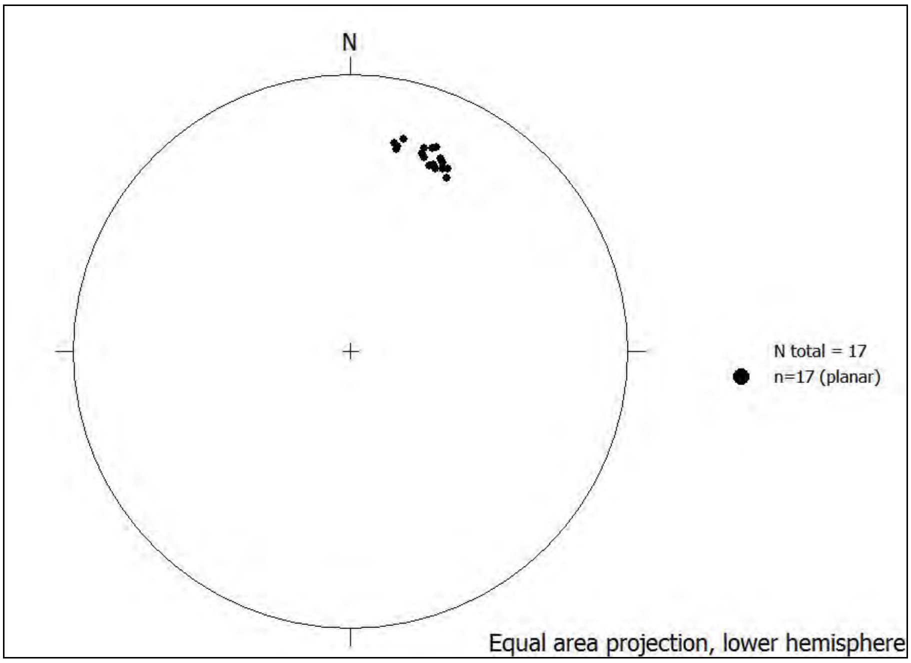

Fig 6-127: Stereogram showing poles to normal fault plane F7.

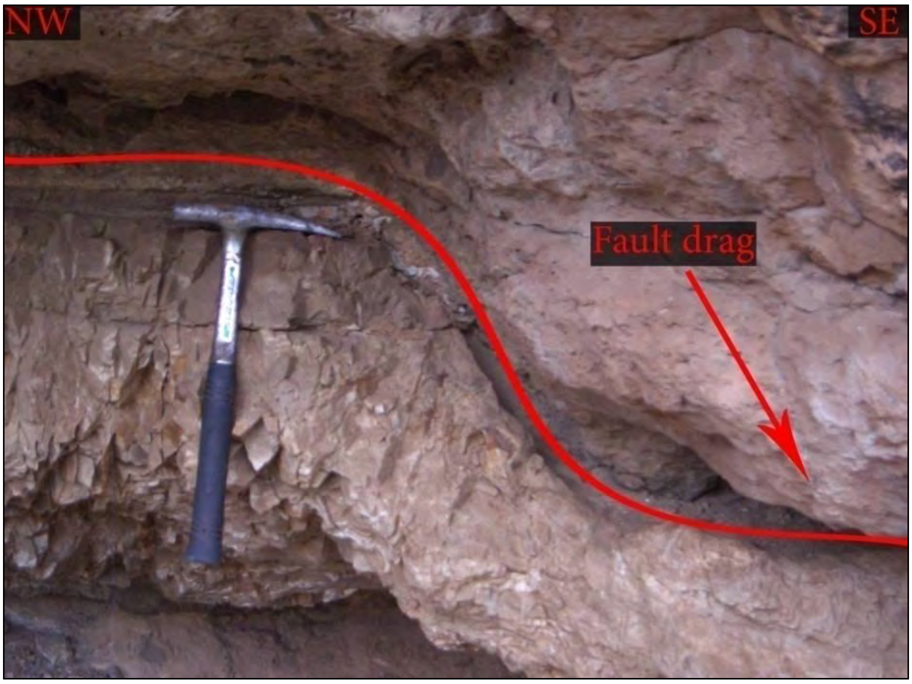

Fig 6-128: A thin shale bed indicated by the red line has been "dragged" into fault F7; geological hammer for scale.

6.9.4 Strike-slip faults

Small components of strike-slip movement were observed in various areas throughout the section these were combined and resolved into one stereogram (Fig 6-129).

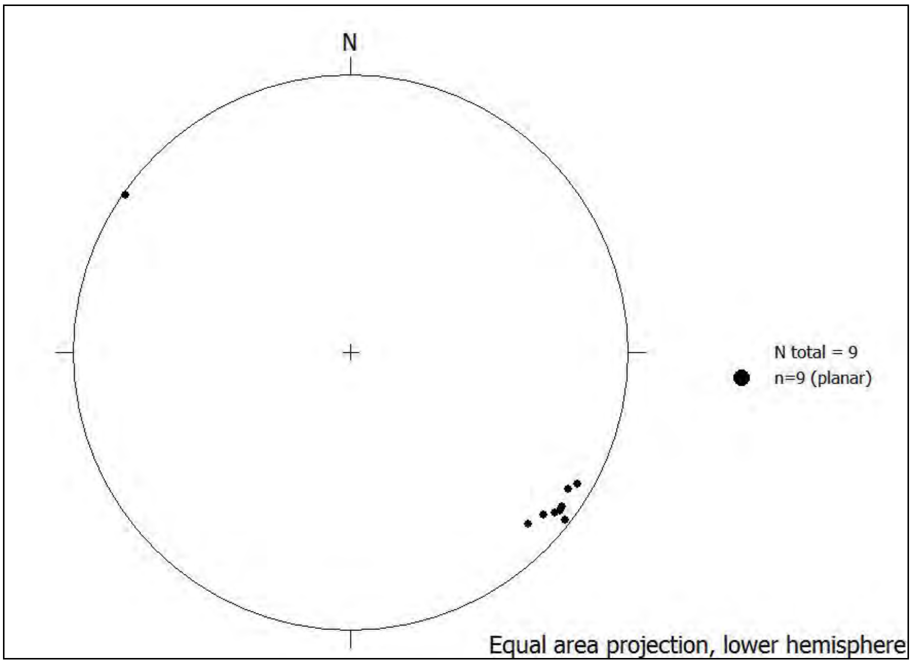

Fig 6-129: Stereogram showing poles to strike-slip faulting.

6.9.5 Folds

Although beds are tilted in places, this section shows no significant folding.

6.9.6 Joints

The section shows systematic jointing with two dominant and one less dominant joint set (Fig 6-130). Joint set J1 strikes nearly north-south whereas joints J2 and J3 strike west-northwest and west-southwest respectively. Jointing in this section shows similarities to jointing recorded at station 2 and 3.

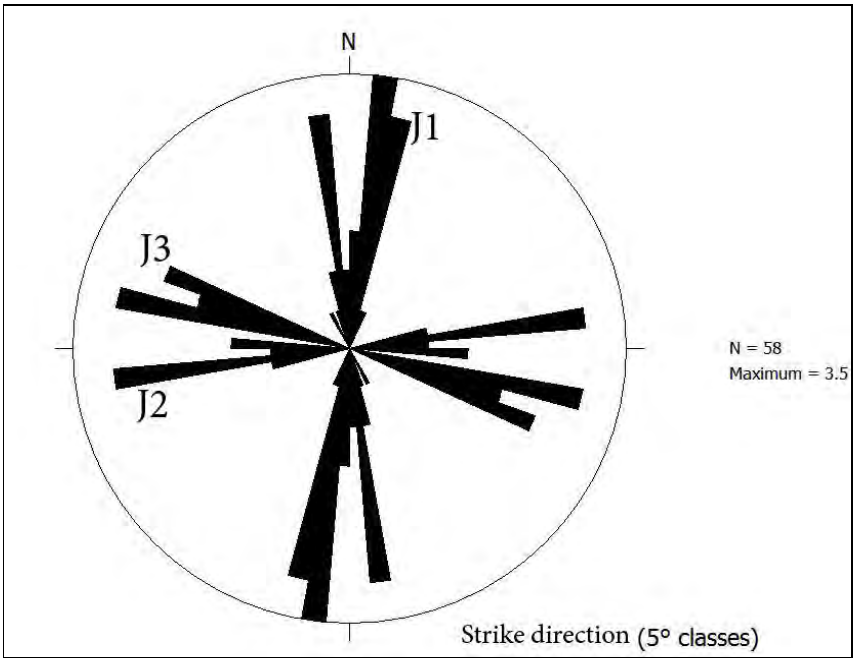

Fig 6-130: Rose diagram showing strike direction of main joint sets at station 6.

6.10 Station 7

6.10.1 Introduction

Station 7 is located along a narrow gorge approximately 3km east-southeast of station 5 and north of station 2 and 4 (Fig 6-1 and Fig 6-131). The area consists of quartzites which make up the Perdepoort Member. The section is comparable to station 5, which is located along the same strike. Quartzites which make-up the Perdepoort Member are the predominant lithology and no argillaceous horizons were noted. However, "gaps" between quartzite beds may have once been filled with shale beds. Average thickness of quartzite beds ranges from 12cm to 60cm. Quartzites are a light grey colour and iron staining is virtually absent. The section is divided into 3 domains separated on the basis of bedding orientations, faulting and folding. The area is dominated by a large normal fault (F1), which is associated with a considerable amount of brecciated rock (Fig 6-132, domain 3). Domain 2 shows a normal fault zone displaying complex cut-off relationships with earlier formed thrust faults (Fig 6-132). Domain 1 contains an anticline-syncline couple, both possessing north verging axial planes. Sedimentary structures are difficult to identify due to weathering of outcrops. Bedding is inferred as being right way-up corresponding to Perdepoort Member quartzites located along strike at station 5. The gorge is narrow thus in certain places structural features can be seen from the East or from the West.

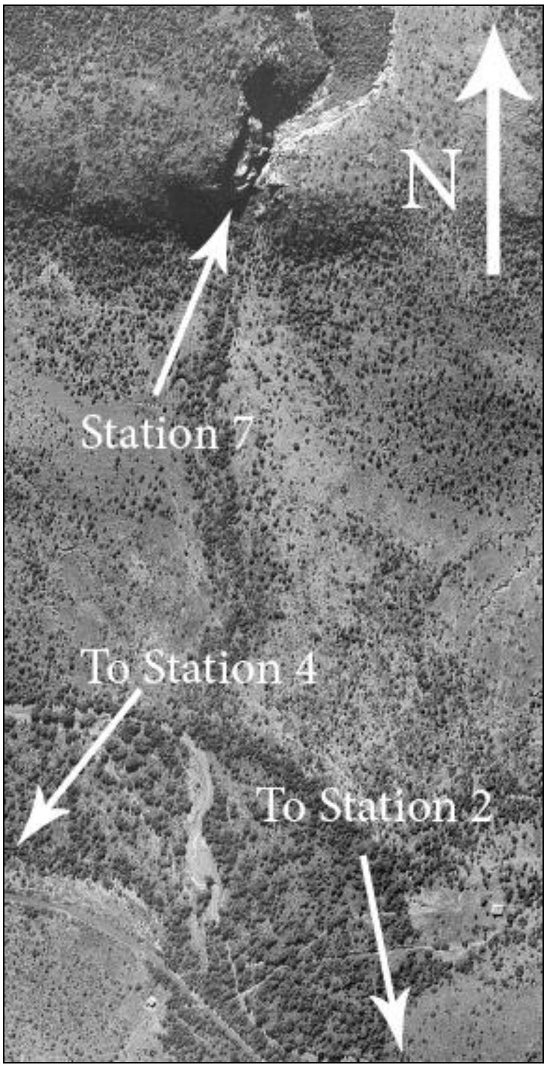

Fig 6-131: Aerial view showing the location of station 7 in relation to station 2 and 4 obtained from the Council for Geoscience.

6.10.2 Bedding

Bedding was measured in two domains. Domain 1 contains moderately south-southwest dipping bedding (Fig 6-132 and Fig 6-133). Domain 2 displays bedding dipping at moderate angles to the north-east (Fig 6-134). This change in bedding orientation is due to folding of Fo1 and Fo2. Bedding is inferred as being right way-up correlating with facing direction of Perdepoort Member quartzites located along strike at station 5. Bedding orientation has a near vertical dip in domain 3, observed between two normal faults F2 and F3 (Fig 6-132 and Fig 6-135).

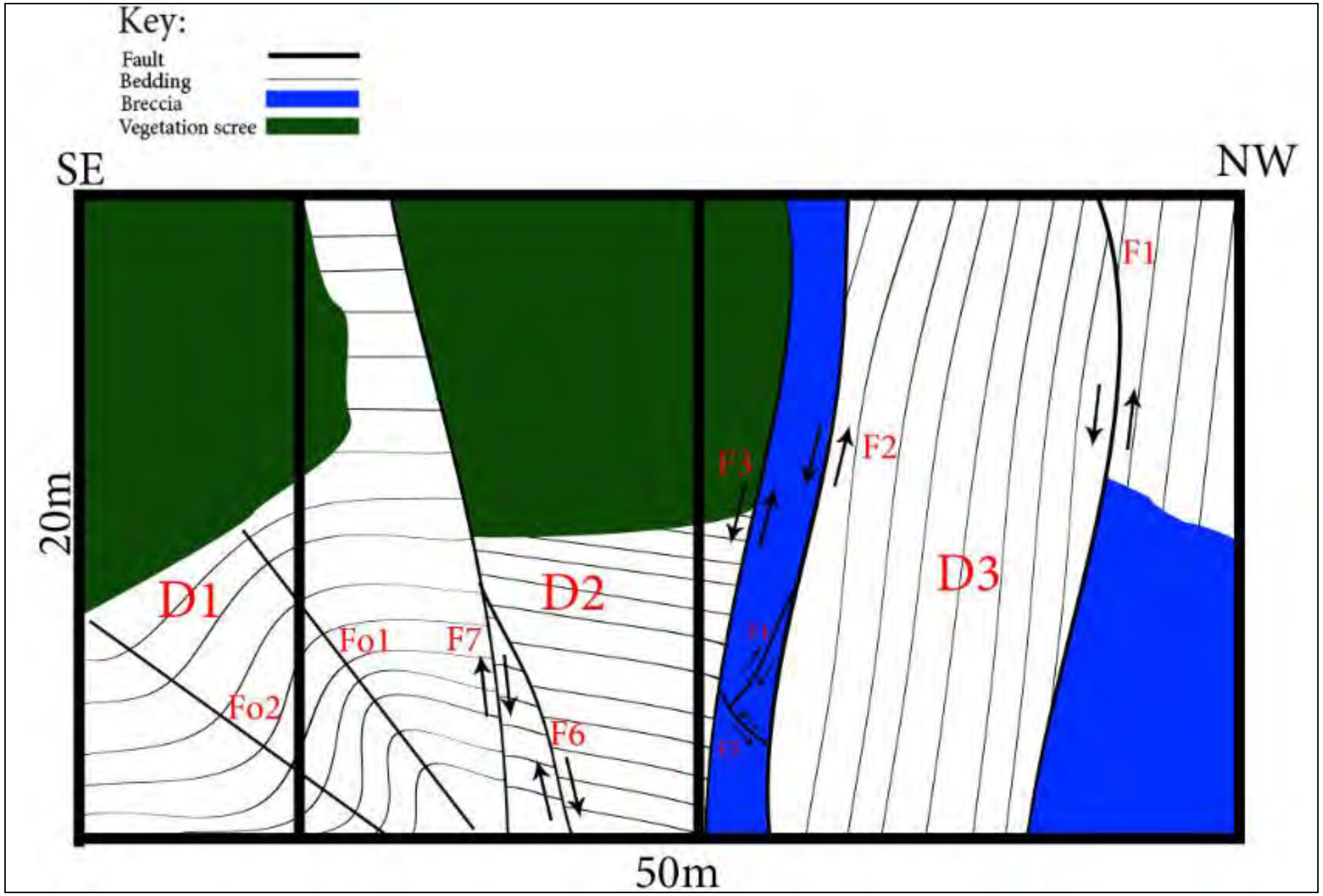

Fig 6-132: Diagrammatic representation of station 6. The station is divided into 3 domains (D) and folds are indicated by Fo. Diagram sketched looking from the east, facing west.

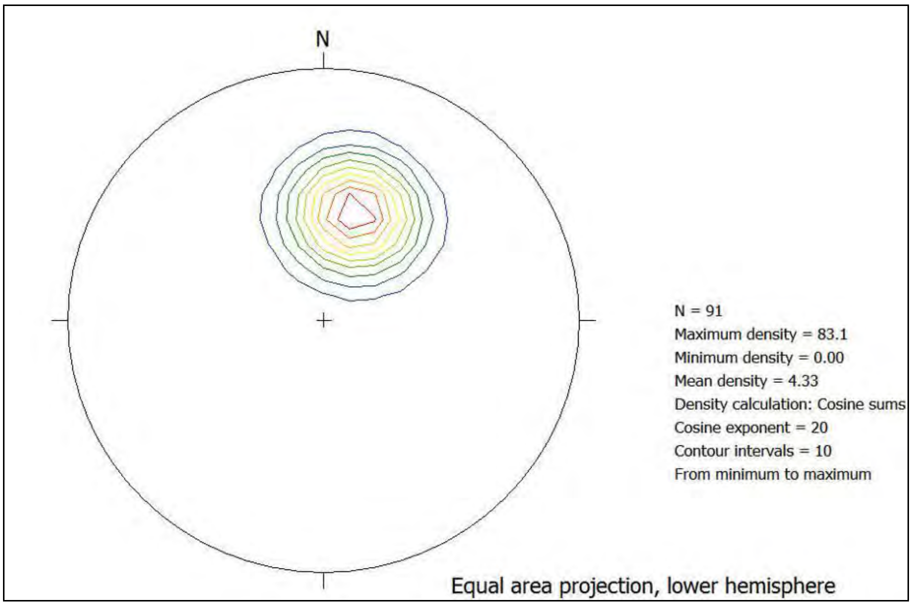

Fig 6-133: Stereogram showing contoured poles to bedding planes in domain 1, station 7.

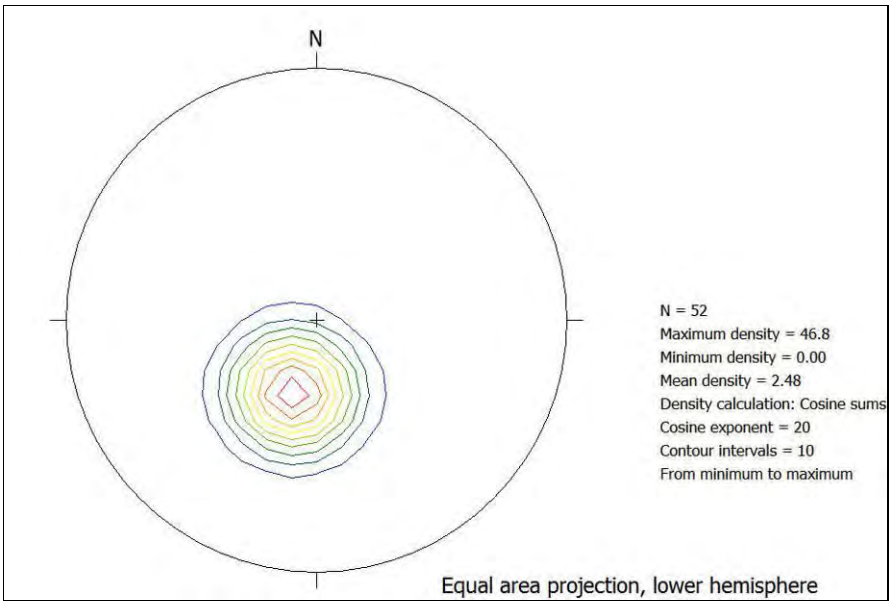

Fig 6-134: Stereogram showing contoured poles to bedding planes in domain 2, station 7.

6.10.3 Faults

Faults are clearly visible in the strata as they displace bedding and effect sudden changes in bedding orientation (Fig 6-132). Evidence such as brecciated rock and slickenside surfaces also aid in determining the presence of faults. Although slickenside surfaces are visible they are highly weathered, thus slickensides were only utilized as a secondary confirmation when identifying faults. The study site contains 7 faults. Faults mostly display high angle normal fault geometry, with hanging wall blocks moved down relative to footwall blocks. F4 and F5 appear to be fore- and backthrusts which are transected by younger normal faults F2 and F3 (Fig 6-132, Fig 6-136 and Fig 6-138)

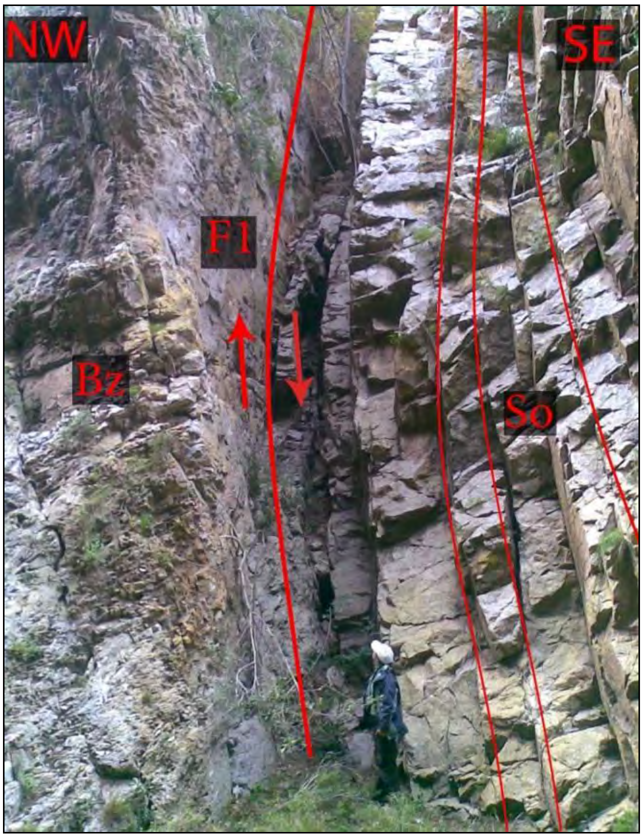

Fig 6-135: Normal fault F1 lies between nearly vertical to overturned bedding (So) and a large brecciated zone Bz. Photo taken looking from the west, facing east; Josepha Zielke for scale.

6.10.3.1 Thrust faults

Thrust faults are minor features in the section as only two inferred thrust faults are present F4 and F5, a fore-thrust and backthrust respectively (Fig 6-132). Thrust faults are cut by normal faults F2 and F3 (Fig 6-132 and Fig 6-136). Backthrust F5 has a steep northward dip (Fig 6-132 and Fig 6-137). Fore thrust F4 could not be measured but generally dips steeply in a southward direction (Fig 6-136).

Fig 6-136: Thrust faults F4 and F5 are cut by two normal faults F2 and F3, photo taken from the east, facing west; Josepha Zielke for scale.

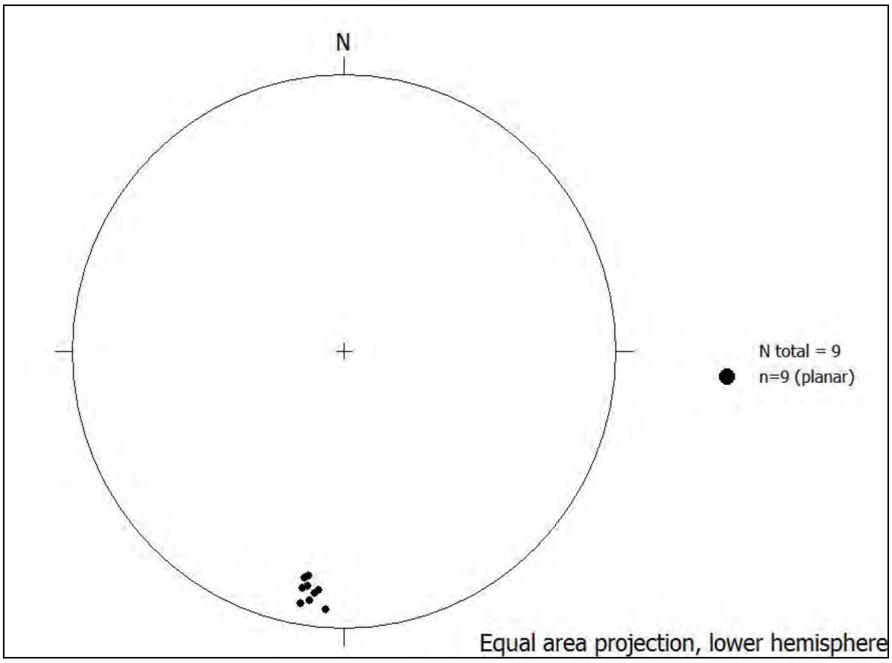

Fig 6-137: Stereogram displaying poles to fault plane of backthrust F5.

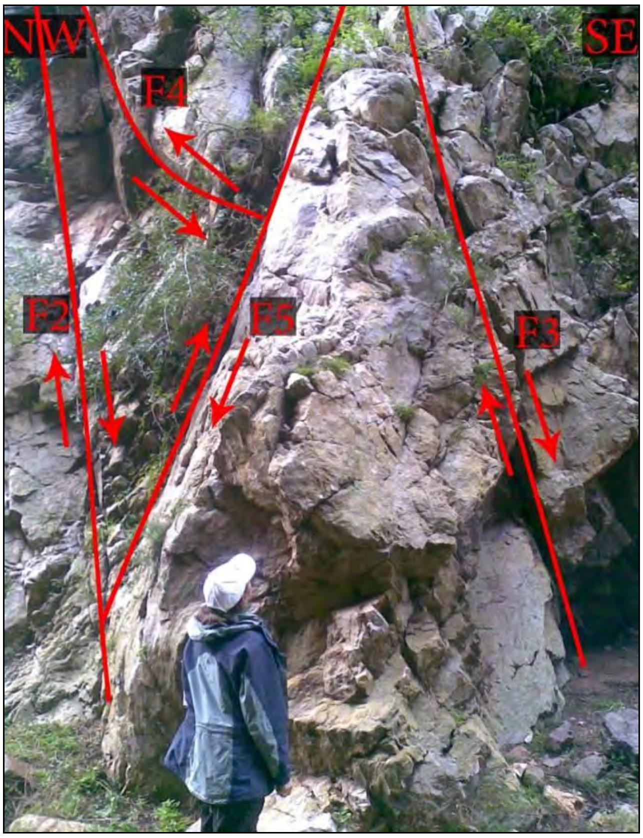

Fig 6-138: Normal faults F2 and F3 cut earlier formed thrust faults F4 and F5 in domain 2, photo taken from the west, facing east; Josepha Zielke for scale.

6.10.3.2 Normal faults

The study site contains 5 normal faults, all possess high angle dips, and normal faults dip both north and south (Fig 6-132, Fig 6-139 and Fig 6-140).

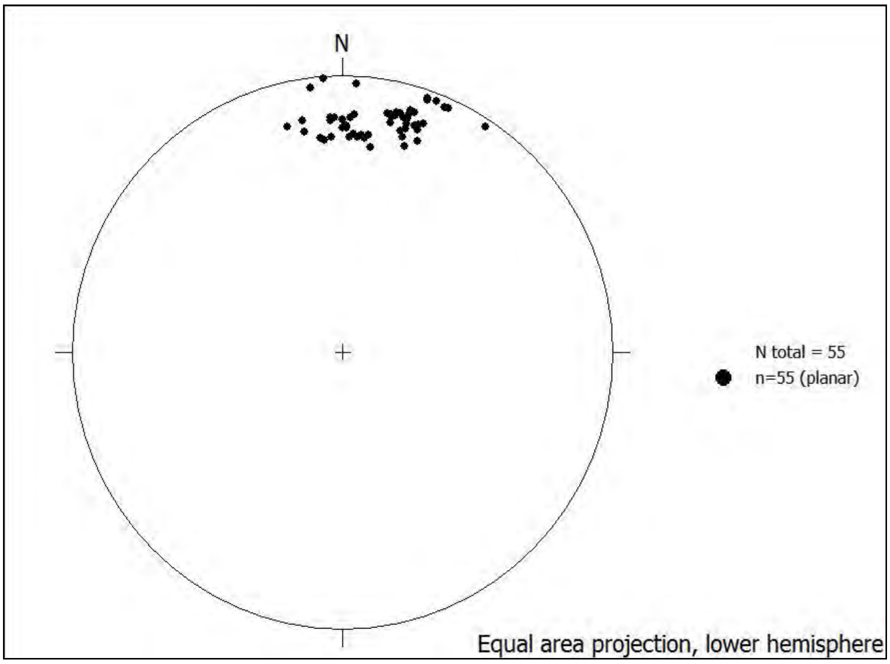

Fig 6-139: Stereogram showing poles to fault planes of all north (foreland) verging normal faults at station 7.

Normal fault F1, F2 and F3 dips south while normal faults F6 and F7 display opposite northward dip (Fig 6-139 and Fig 6-140). Normal fault F1 dominates the study section, dipping at a steep angle to the south, its footwall block contains highly brecciated rock (Fig 6-135, Fig 6-141 and Fig 6-142). The significant amount of breccia and sudden change in bedding geometry strengthens the assumption that the displacement on F1 is considerable. Normal faults F6 and F7 are located in domain 2 and show opposite vergence compared to F2 and F3 (Fig 6-132, Fig 6-140 and Fig 6-143). F7 is cut by F6 and, both faults display well developed fault planes. The slickenside surfaces slickenfibres are however poorly developed. F7 clearly displaces bedding and it is immediatly evident that its hanging wall has moved down relative to its footwall block. Normal fault F6 dips steeply south-southwest (Fig 6-144). F7 displays a similar dip to that of F6, dipping at a steep angle to the south-southwest (Fig 6-145).

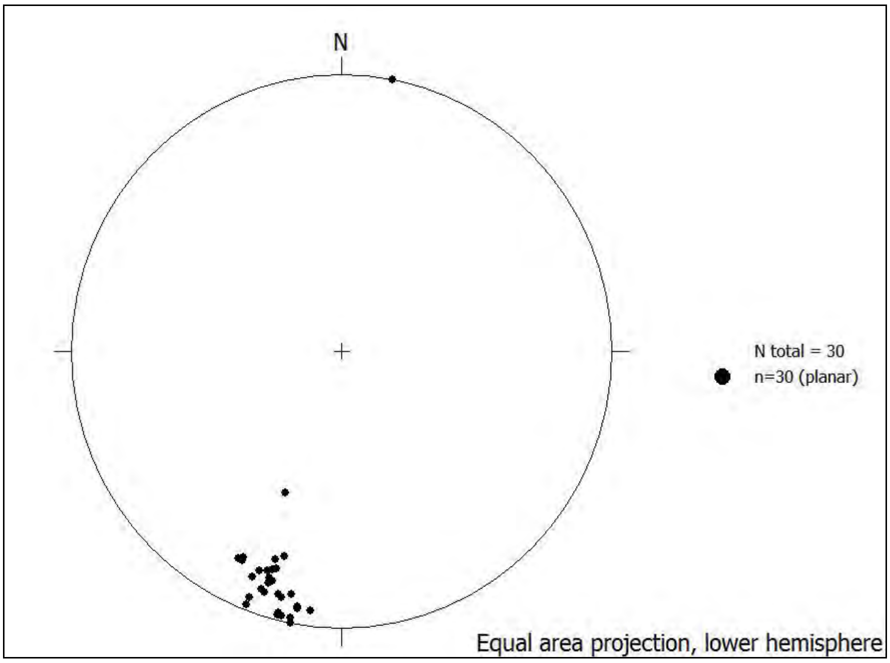

Fig 6-140: Stereogram showing poles to fault planes of north dipping normal faults F2 and F3 at station 7.

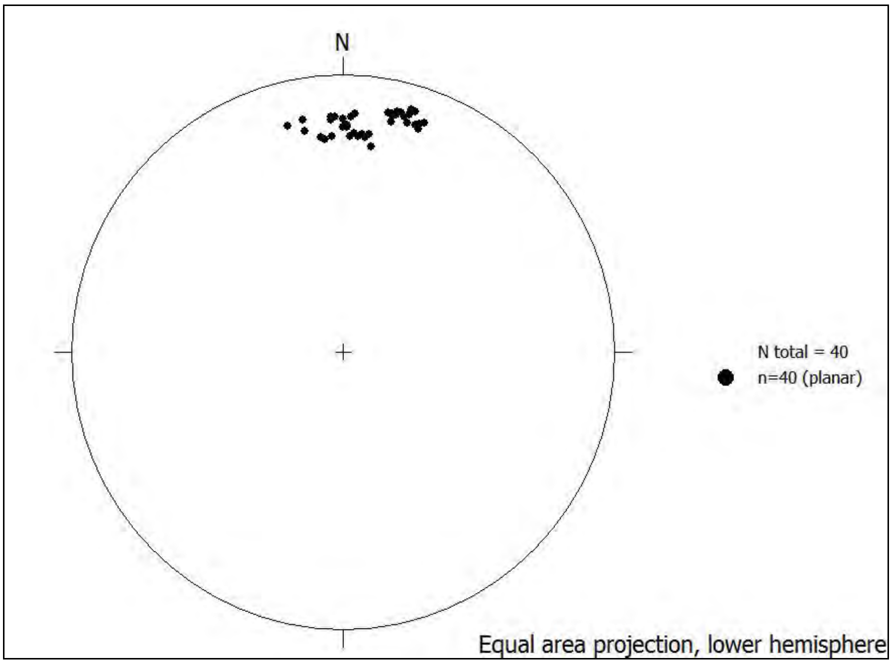

Fig 6-141: Stereogram showing poles to normal fault plane F1.

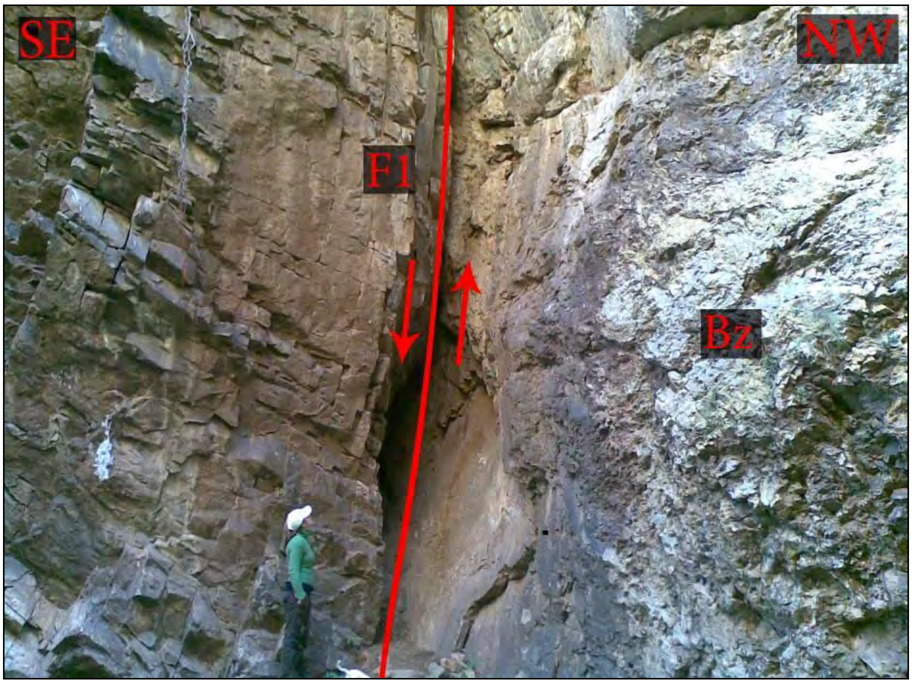

Fig 6-142: Normal fault F1 viewed from the east. Brecciated zone (Bz) is most prominent when viewed from the east, facing west; Josepha Zielke for scale.

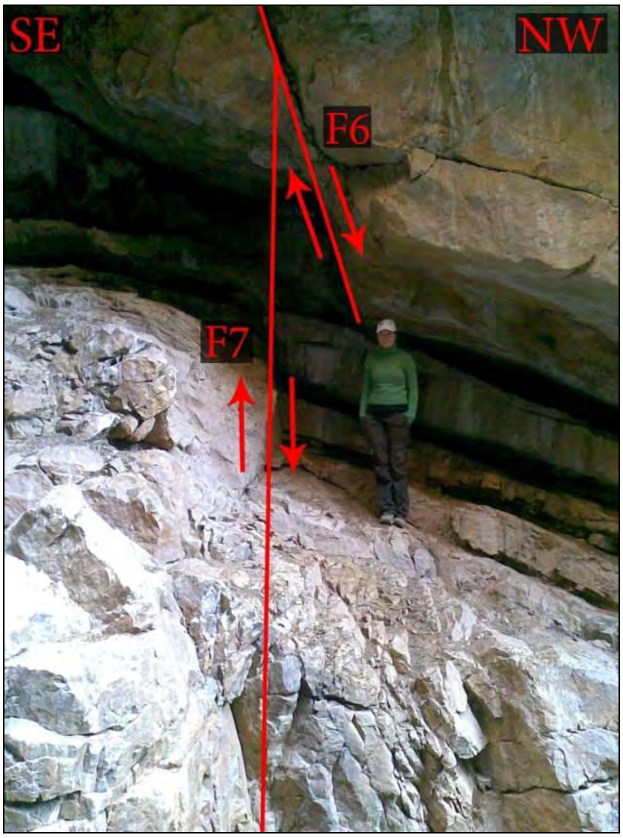

Fig 6-143: Normal faults F6 and F7 located in domain 2. Photo taken from the east, facing west; Josepha Zielke for scale.

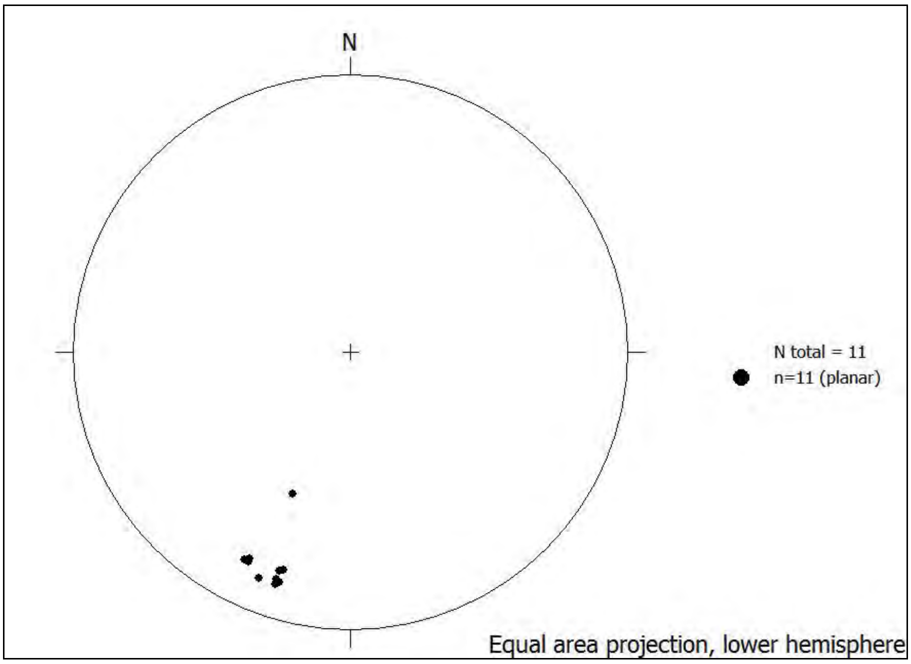

Fig 6-144: Stereogram showing poles to normal fault plane F6.

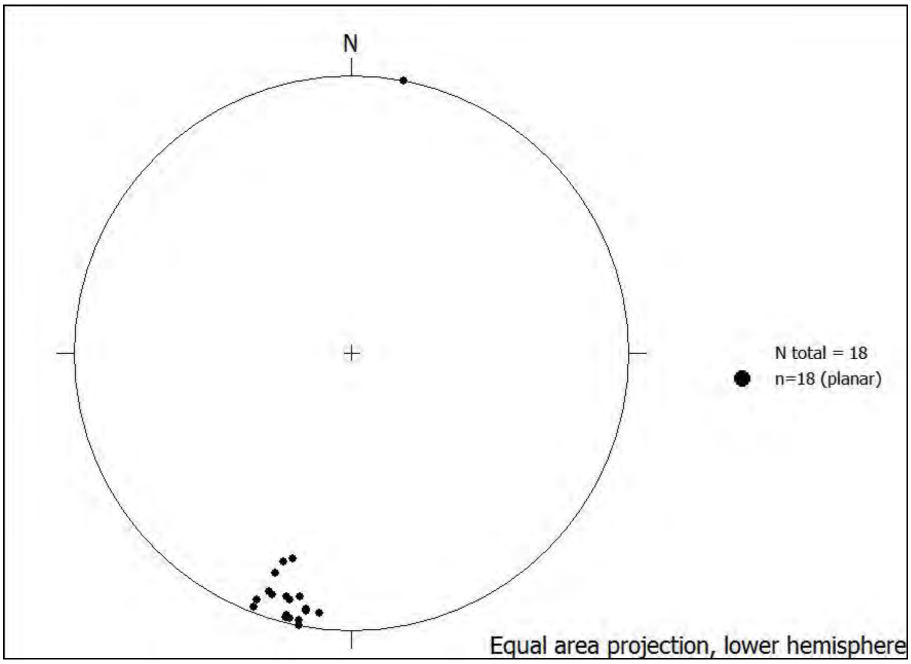

Fig 6-145: Stereogram showing poles to normal fault plane F7.

6.10.3.3 Strike – slip faults

No strike-slip faults were noted at station 7.

6.10.4 Folding

Folding is well developed in the study site (Fig 6-132). Domains 1 and 2 contain an anticline- syncline couplet, Fo1 and Fo2 (Fig 6-132 and Fig 6-146). Both folds verge towards the south-east. The interlimb angles of Fo1 and Fo2 were estimated by measuring in a cross sectional view. F1 can be described as tight and Fo2 as open. However, due to the near vertical limb shared by both Fo1 and Fo2 readings were ambigious and thus the constructed stereograms were not included in this results section.

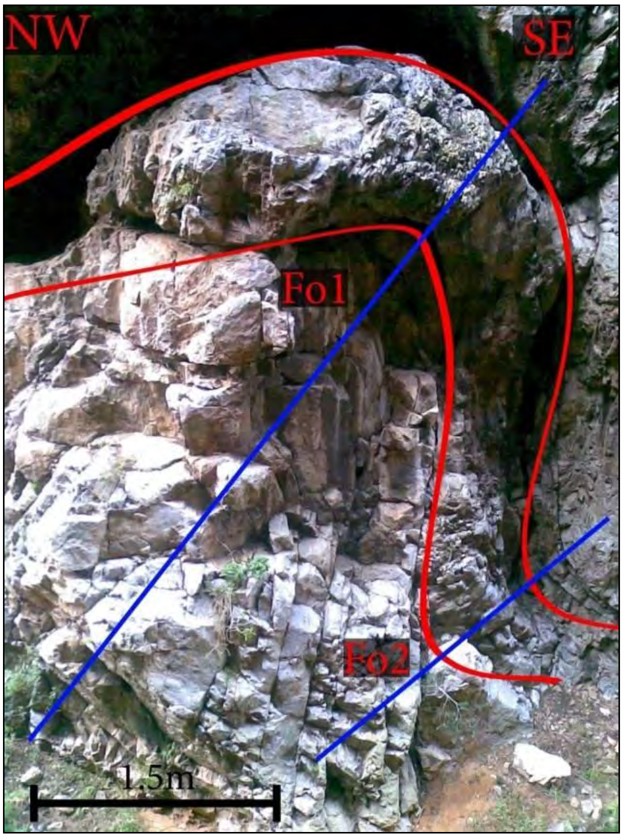

Fig 6-146: Anticline, syncline occurring together, fold Fo1 and Fo2 viewed from the west facing approximately east. Blue lines indicate axial planes.

6.10.5 Joints

The study section contains systematic jointing with two prominent (J1 and J2) and one less prominent joint set (J3) (Fig 6-147 and Fig 6-148). Joint sets cross-cut and are comparable to joints noted in at station2, 3 and 6. Fig 6-147 clearly shows the relationship between the two main joint sets, J1 and J2.

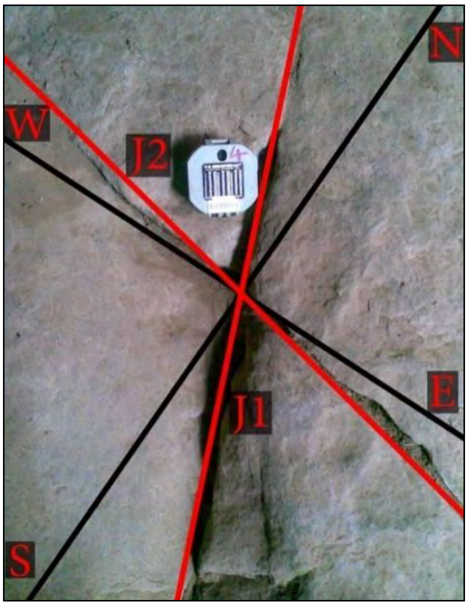

Fig 6-147: The main joint J1. Photo taken on top of bed. Geological compass for scale.

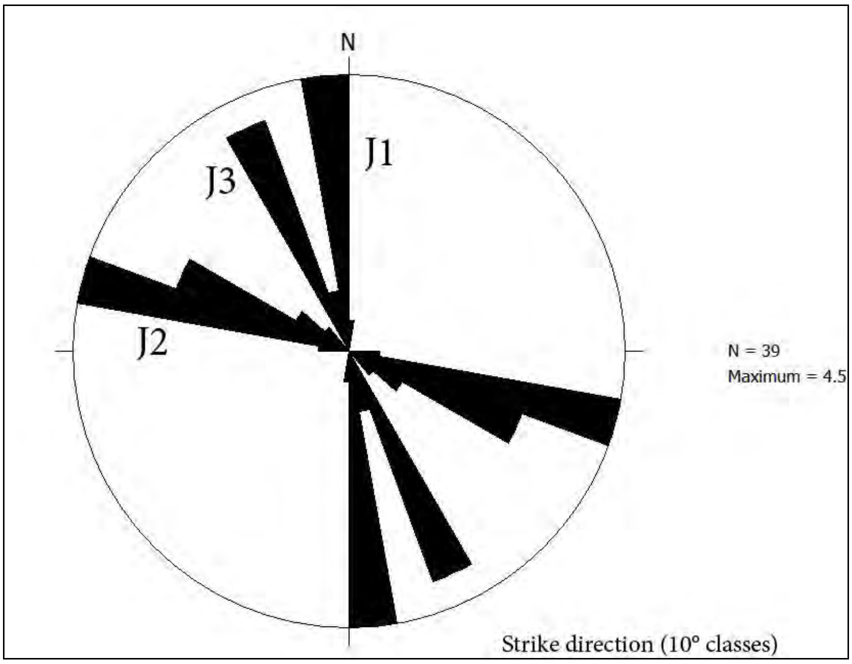

Fig 6-148: Rose diagram showing strike directions of main joint sets at station 7.

6.11 Station 8

6.11.1 Overview

Station 8 represents a cross section of Rooirand Member rocks located approximately 5km west of station 5, 6 and 7. The section was mapped from photographs in order to determine if structural features observed at station 5, 6 and 7 were laterally continuous. Seven major faults are present in this cross section (

Fig 6-149). Normal faults dip north and south. Normal faults F3 and F5 dip south and cut backthrusts F1 and F2 and fore-thrust F4 respectively. Normal fault F7 dips south and is cut by a north dipping normal fault F6. F5 cuts F6 which in turn cut F7 thus the relative ages of these normal faults are from eldest to youngest F7-F6-F5. Normal faults transect all previously formed structures and thus represent the latest component of tectonic evolution.

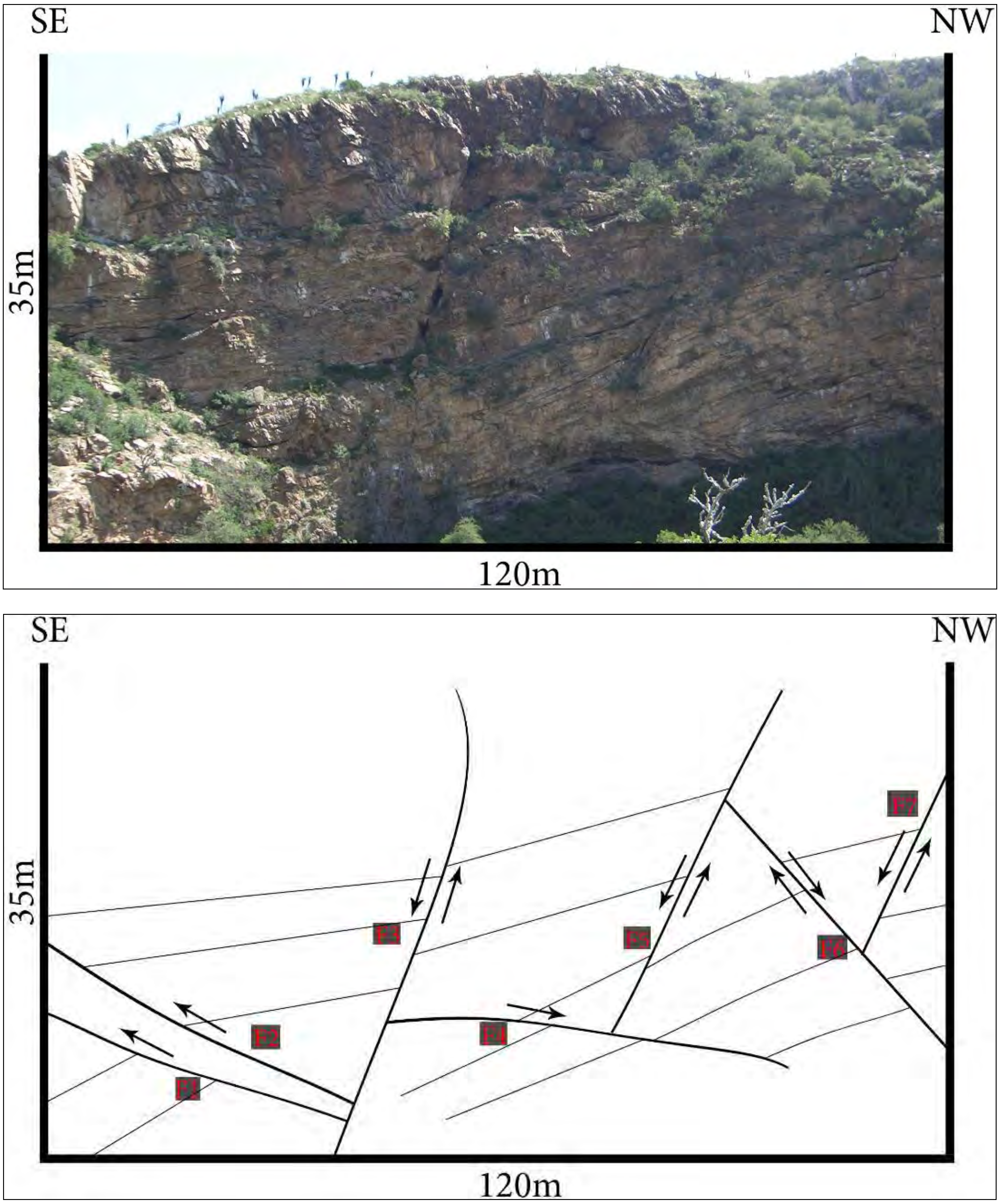

Fig 6-149: Top: Large exposure of Rooirand Member rocks located at station 8. Bottom: Overlay of structural features in the outcrop.

7. Discussion

7.1 Lithologies

7.1.1 Field observations

The Perdepoort Member at the study site can generally be described as a white massive quartzitic sandstone. The Rooirand Member in contrast displays a distinctive red-brown surface weathering. This leads one to believe that it should possess mineralogy, in geological terms, significantly different to that of the Perdepoort Member. This is however, not the case, see 7.1.2.

The Witpoort Formation is overlain by a dark-grey to dark-brown pyritic rich shale, the Kweekvlei Formation which represents a more argillaceous horizon in the study area. The later Formation was only described at mesoscale (station 1) in order to add to the structural unravelling of the study area. A mineralogical study of the Kweekvlei Formation was not conducted as it was immediately eliminated as a possible viable silica source.

7.1.2 Lab analysis and geochemistry

It can clearly be seen from Table 5-3 that all Perdepoort Member samples, designated as P, contain quartz (SiO_2) concentrations higher than 95%. Perdepoort Member samples have a mean SiO_2 weight percentage of 98.09% with a standard deviation of 1.34%. Samples from the Rooirand Member on the other hand have a mean SiO_2 weight percentage of 93.88% with a standard deviation of 2.25%. This is not significantly different in term of mineralogical classification. However, in terms of silica extraction these differences are immense.

It should be noted that only 16 samples from the Perdepoort- and 4 samples from the Rooirand Members were considered. This small sample size immediately lends itself to some uncertainty in mean values of both Members. This especially applies to the smaller sample population in the case of the Rooirand Member.

The main difference between samples from the Perdepoort- and Rooirand Members is the total iron content, which is nearly twice as high in samples from the Rooirand Member (Table 5-3). This is expected following the mesoscale observations of the Rooirand Member hand samples that showed significant iron staining. The second significant difference is higher levels of aluminium, magnesium, potassium and titanium for the Rooirand Member (Table 5-3).

The phosphorus data appears somewhat anomalous. The XRF analysis shows phosphate levels in the Perdepoort Member to be double that of in the Rooirand Member. In contrast, the SEM analysis shows that the Rooirand Member has higher concentrations of monazite, most likely the major phosphate mineral. The higher phosphate levels observed could possibly be due to apatite minerals, such as flouroapatite, which were observed in the Perdepoort Member (Section 5.1.2 and 5.1.1.1). The relatively high phosphorous levels in the Perderpoort are of concerns as phosphorous as an impurity is considered highly unfavouarable for silica extraction (Green, 1982, Green, 1987).

7.1.2.1 Mineralogy

(i) Petrology

The XRF data (Table 5-1 and Table 5-2) would appear to confirm the presence of micaceous minerals when one notes the percentages of Al_2O_3, K_2O and MgO. In addition the dominance of the mica minerals is confirmed by the strong positive correlation between these previously mentioned elements and SiO_2 and L.O.I (Table 5-5). The LOI is attributed to the water loss from the mica crystal structure during ignition.

Quartz grains show a relatively uniform size throughout both the Perdepoort- and Rooirand Members. Quartz always show undulose extinction, and is often crushed in-between areas where triple junctions are present. This along with the mineral assemblage that will partly still be discussed indicates the metamorphic grade of the local rocks to be greenschist facies, conforming to what is commonly observed in most of the Cape Supergroup rocks.

Heavy minerals identified in rocks of the Witpoort Formation are analogous to those found in modern beach deposits. The equigranular nature of grains indicates sediments to be well sorted, a feature also commonly encountered in modern beach deposits. These observations, together with the sedimentary structures observed in the field, are in keeping with the literature proposing beach and nearshore environment of deposition for the Witpoort Formation (see 3.2.1.1)

(ii) Correlation matrices of major and trace elements

Clear correlation between SiO_2, K_2O, Al_2O_3 and various trace elements are observed (Table 5-5). Elements such as Ba, Ga and Rb commonly substitute for K in interlayer sites in muscovite and biotite (Deer et al., 1992). The correlation of MgO to Ba and Rb can also be attributed to the same substitutions in micas.

A noticeable correlation observed between Zr and TiO_2 is not unexpected as minerals such as zircon and rutile commonly occur together (Table 5-6). The correlation between TiO_2 and Nb is common as Nb^{5+} regularly replaces the similar sized (ionic radius) Ti^{4+} ion in the crystal lattice of rutile and this Niobian variety is known as ilmenorutile (Deer et al., 1992).

Zirconium correlates extremely well with Hf and Th (Table 5-7). This is expected as zircon ($ZrSiO_4$) always contains some Hf and often a certain amount of Th (Deer et al., 1992). Yttrium (Y) correlates well with both Zr (zircon) and Ti (rutile) (Table 5-7). Phosphorus regularly replaces Si in zircon with the result that the electrostatic imbalances are neutralized by rare earth elements, especially from the yttrium group such as Y (Deer et al., 1992). Y is also known to substitute for the titanium ion in TiO_2 (Deer et al., 1992).

Monazite ($CePO_4$) is an accessory mineral frequently found in both Perdepoort and Rooirand samples. These commonly contain Th and also other rare earth elements which might explain the correlations between elements such as Ce, Nd, Th, Y and Zr in Table 5-7 (Deer *et al.*, 1992). The correlation is attributed to atomic substitution, common in minerals which contain rare earth elements such as monazite (Deer *et al.*, 1992). However, minerals such as monazite, zircon and rutile display a range in specific gravity, 4.6 to 6.5, thus all elements contained in these minerals may be indirectly correlated with one another due to sedimentary sorting in nearshore and beach environments.

In summary, most samples contain measurable phosphate levels, most likely mostly in apatite, with minor amounts present in monazite. Zircon is thought to contain virtually no phosphorus, as there was no correlation between P and Zr. Rare earth elements display relatively high concentrations, most likely forming part of minerals such as monazite, rutile and zircon. Phosphorus correlates best with Ca suggesting concentration in the form of fluorapatite, this is quite possible as some apatite was observed in the SEM analysis.

(iii) Trace element variability

Samples from the Rooirand Member fell within the upper range of concentration (all elements) (Fig 7-3). Despite this fact some samples considered to be Perdepoort Member showed increased concentration of certain trace elements. These include Ce, Ti and other elements found in in micas such as K as well as elements that commonly substitute for other elements in micas namely Rb and Ba. Samples showing increased Baryte and Rb were located near normal faults thus suggesting normal faults do alter samples, be it through a more plausible mechanism of hydrothermal enrichment or perhaps increased weathering of feldspars, which would explain increased mica concetrations (Fig 7-2). The latter appears to be more plausible as only K, Ba and Rb are enriched and not other elements such as Ti and Y. The relative concentration of elements in the Perdepoort Member appears totally haphazard at first but most relationships are thought to be attributed to original sedimentary sorting. For example, a sample that contains high levels of iron also displays high levels of rutile suggesting that at least some iron is detrital as was observed in Fig 5-6 (also see Table 5.1 PR1-PR4).

Increased phosphorus levels are associated with lower concentrations of elements commonly found in micas which include, Na, K and Mg. This suggests that minerals such as monazite do not occur in areas where micas are present but rather in areas where heavier reworking of sediments occurred during deposition. It thus appears that although faulting and other structures do play a role in enrichment and alteration of quartzites in the study area, the palaeodepositional environment appears to be a more important factor.

(iv) Study data compared to other data

Data obtained from the Council for Geoscience clearly indicates variability in chemical composition (Table 7-1). The data from this study and the Council data are presented in (Fig 7-1:).

Sediments may possess various provenances and their chemical compositions are a net result of a number of factors. These include among others, source rock composition, intensity of weathering, mineral sorting, and finally diagenesis (McLennan *et al.*, 1980). Provenance may play an important role in explaining the chemical viability of the Perdepoort Member. When compared to modern beach placer environments the mineralogy is expected to vary along strike.

Browning, (2005) found heavy mineral distributions varied markedly along parts of the Algoa Bay coast. The findings of Browning, (2005) suggests that although locally the Perdepoort Member may present a viable source of silica, local structural geology and analogies to modern beach deposits suggests that the mineralogy of the Perdepoort Member may vary greatly in terms of immediate location and structural imprints.

Although samples from the Perdepoort Member, in this study, do show great variability an overall trend can be observed (Fig 7-1). Data obtained from S.Frost-Killian from the Council of Geoscience shows great variability in for example Fe content. This variability in chemical composition thus suggests even greater variability in mineralogical composition if the area of study is increased as it was in the study by S.Frost-Killian. This clearly shows the variability in chemical composition could have been partly due to differing detrital composition during deposition and differing compositions of country rock present at the time of deposition. The previous statement may be supported by the fact that great variability can be observed in the concentrations of TiO_2 (rutile) and P_2O_5 (from monozite) between the two studies. The variations can thus be attributed to the availability of these detrital minerals during deposition. The variability in MgO, CaO, K_2O and Al_2O_3 may be due to more intense faulting in the areas sampled by S.Frost-Killian.

The data thus indicates that, although the Perdepoort Member may be deemed viable for extraction in one area it may not be considered viable in another area in relative close proximity to the former.

Table 7-1: *XRF analysis of nine samples from the Perdepoort Member, obtained from S. Frost-Killian from the Council for Geoscience.*

Sample	SiO_2	TiO_2	Al_2O_3	Fe_2O_3T	MnO	MgO	CaO	Na_2O	K_2O	P_2O_5	Cr_2O_3
1	90.4231	0.1927	1.2842	7.1500	bdl	0.15	0.161	bdl	0.2682	0.06564	bdl
2	98.797	0.2416	0.3181	0.0920	bdl	0.14	0.168	bdl	0.0356	0.0246	bdl
3	99.6115	0.0907	0.2963	0.1480	bdl	0.12	0.164	bdl	0.0289	bdl	bdl
4	98.9776	0.0929	0.7764	0.1318	bdl	0.11	0.174	bdl	0.1207	bdl	bdl
5	98.2804	0.3373	1.1296	0.0383	bdl	0.1	0.16	bdl	0.1277	bdl	bdl
6	92.5005	1.0757	4.5045	0.1256	bdl	0.25	0.169	bdl	0.8653	0.0265	bdl
7	99.0658	0.1226	0.2717	0.0340	bdl	0.11	0.2	bdl	0.0190	bdl	bdl
8	98.9842	0.0426	0.2482	0.0801	bdl	0.09	0.187	bdl	0.0051	bdl	bdl
9	98.5284	0.2293	0.8404	0.0437	bdl	0.11	0.176	0.04	0.1407	bdl	bdl

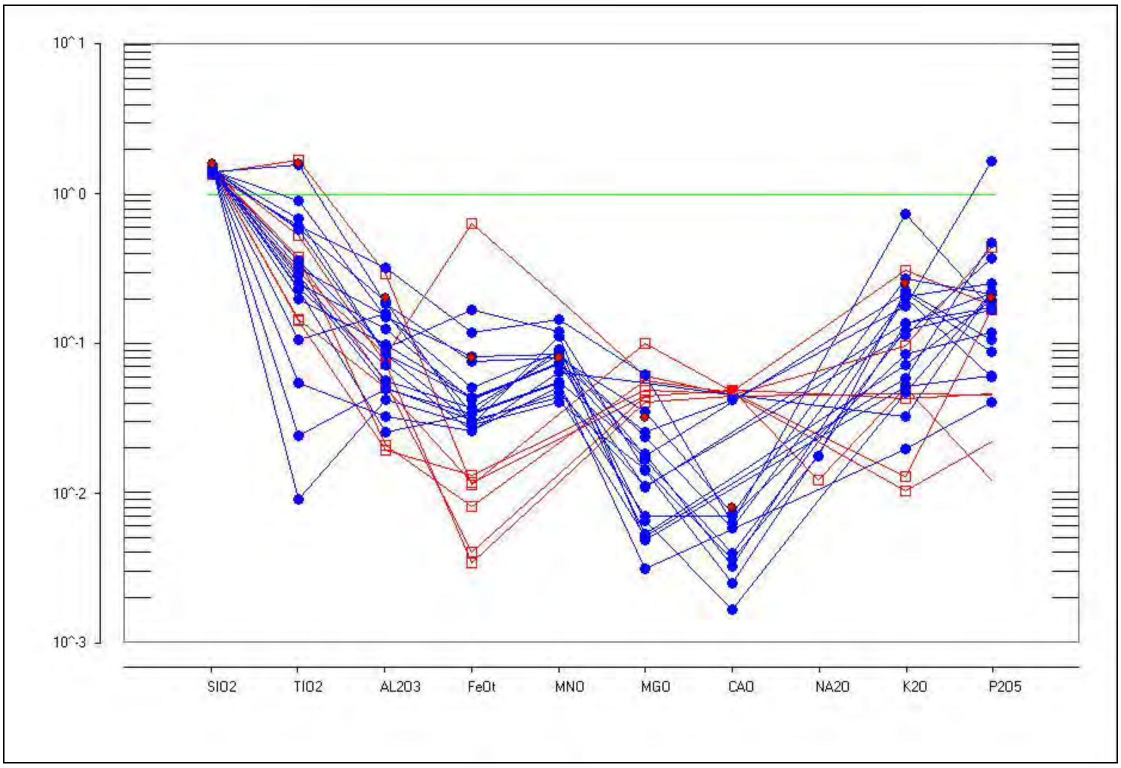

Fig 7-1: Major element Spider diagram of samples from the Perdepoort Member. Samples in red are the data obtained from S. Frost-Killian (Council for Geoscience) and those in blue are from this study. All concentration are normalized against material from upper continental crust (green line) (McLennan, 2001; as cited in Rudnick & Gao, 2003).

7.1.2.2 Structural control on geochemistry

In addition to the chemical variability induced by sedimentary processes, the geochemistry of the particular lithology may be impacted by structural controls. In the study area the main structures are thrusts faults and normal faults. These faults may either provide a conduit for fluid flow, connecting fractures to fluid sources, or act as a barriers to fluid flow (Evans & Forster, 1997, Hammond & Evans, 2003). The possibility of hypogene or supergene flow along these conduits can not be dismissed.

In this study lithologies sampled near normal fault zones contain elevated concentrations of Ba^{2+}. This is most likely derived from baryte, a mineral known to form in areas of hydrothermal enrichment (Fig 7-2) (Deer *et al.*, 1992). The samples near the faults also fell within the concentration upper ranges of elements such as Y, Ti, Sr, K and Rb. These elements easily replace Ba^{2+} thus also indicating possible enrichment.

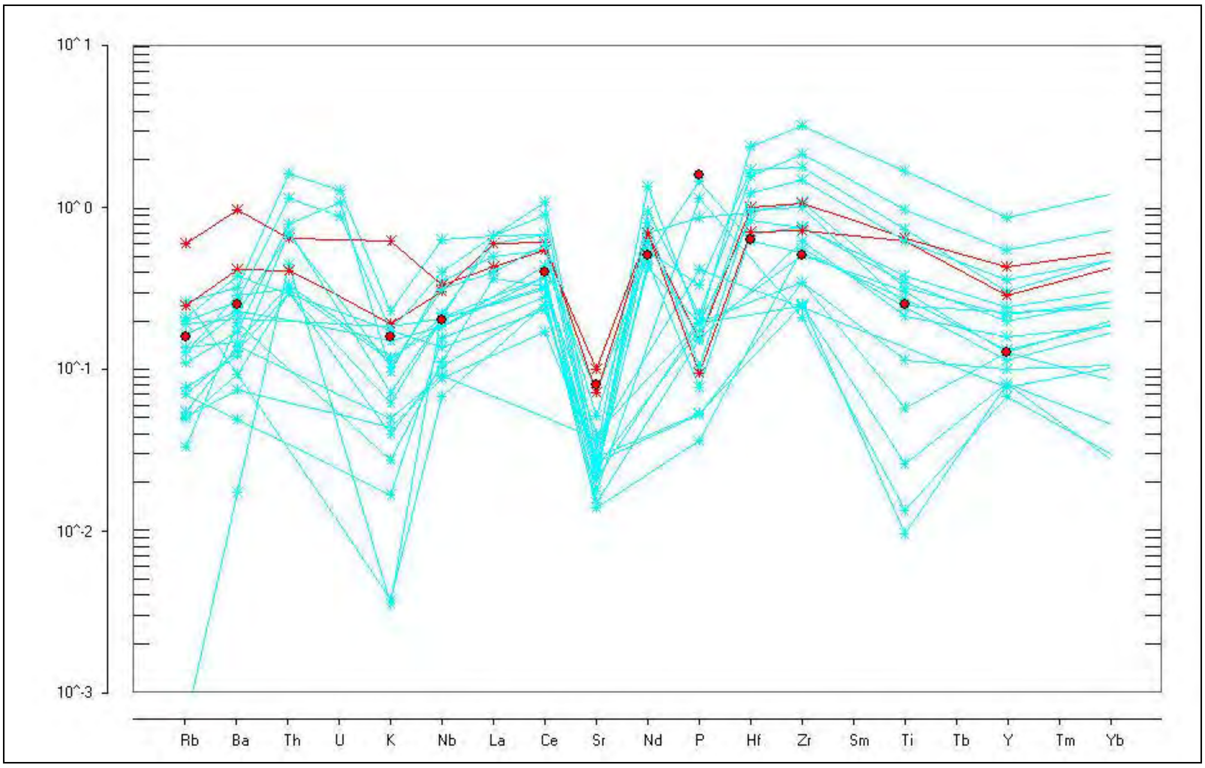

Fig 7-2: Spider diagram showing relative concentration of trace elements in the study. Samples located near normal fault zones are all indicated in red lines and dots, all other samples are indicated in blue, these include samples from both Perdepoort- and Rooirand Members. All concentration are normalized against material from upper continental crust from Taylor and McLennan (1982) as recommended by Rollinson, (1993).

7.1.3 Suitability pertaining to silica extraction

When the Perdepoort data in this study and that of the Council for Geoscience is compared to industry requirements the following conclusions can be made (Table 2-1 and Table 2-2). The Perdepoort Member is suitable for use in industries such as glass manufacturing and filler media, but insufficient for use in solar technologies. It would thus appear from the assay data as well as data from this study, that for use in solar cell production, the purity of the rock encountered in this study is not sufficient. The silica concentration is considerably less than the concentration recommended by for example Oosterhuis, (1998). However, when considering results in Table 5-1 and Table 5-2, individual quartz grains possess purities above the recommended levels, and thus could possibly be utilized if separated from accessory minerals. Quartz grains also contained no inclusions which further strengthens the possibility of utilization if separated from the bulk sample.

Elements from the Rooirand Member samples all possess high concentration ranges, indicating increased levels of impurities compared to most of the Perdepoort samples (Fig 7-3). This study thus eliminates the Rooirand Member as a potential silica source, despite the fact that the Perdepoort Member displays an increased phosphate concentration compared to the Rooirand Member (Table 5-3).

Shales provide an immediate source of possible mineralogical contamination of the quartzite of the Witpoort Formation. Although the Perdepoort – and Rooirand Members are known to possess thin shale beds these were scarce and may have been eliminated during deformation, as thought to have occurred in other areas of the Cape Fold Belt (Shone, pers comm). For this reason shales and the contact between the Perdepoort Member and Kweekvlei Formation should be avoided if silica extraction is deemed viable.

The significance of thrusting in term of geochemical variations could not be adequately established as nearly the entire study area is pervaded with thrust faults. A much more intense sampling scheme would be needed to make a comparison between zones nearly devoid of thrusting and those with pervasive thrusting.

The Perdepoort Member can be considered as the most viable lithology in the Witpoort Formation for silica extraction. The previous statement can however only be taken into account if the Perdepoort Member is mined in areas encapsulating minimal structural complexities such as, thrusts and normal faults.

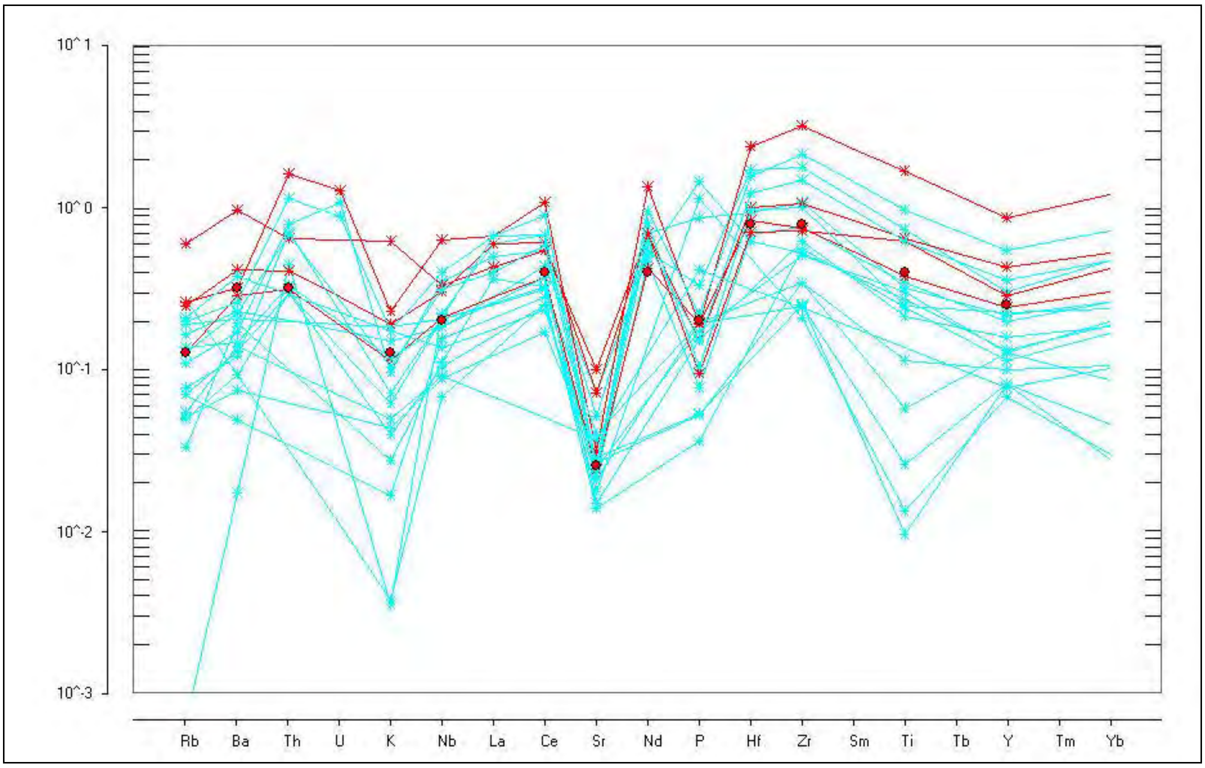

Fig 7-3 : Spider diagram showing relative concentration of trace elements in the study. Samples from the Perdepoort Member are indicated in blue and from the Rooirand Member in red. All concentration are normalized against material from upper continental crust from Taylor and McLennan (1982) as recommended by Rollinson, (1993).

7.2 Structural Geology

7.2.1 Bedding

Bedding generally dips at shallow to near vertical angles towards the south-west throughout the whole of the study area. Bedding towards the southern extent of zone 1 was confirmed as overturned as evident by associated cross-bedding (Fig 6-6). Towards the northern extent of zone 2 bedding is near vertical to slightly overturned (Fig 6-72).

Bedding in the more quartzitic rich units of the Witpoort Formation, is delineated by horizontal laminations and cross bedding. These sedimentary structures testify to depositional environment consistent with shallow marine to beach palaeo-environment.

Sedimentary structures proved difficult to indentify in the more argillaceous units of the Kweekvlei Formation. In cases where ambiguous bedding was observed facing direction was inferred by comparison with the stratigraphically lower Perdepoort Member cropping out strike.

7.2.2 Folds

The more resistant Perdepoort- and Rooirand Members generally display the best examples of folding. The Rooirand Member generally constitutes the cores of mega-anticlines while the less resistant Kweekvlei Shale Formation occurs in the cores of mega-synclines. No significant increase in bed thickness, resulting from volume compensation in folds, was observed.

Megascale and most mesoscale folds in the study area are asymmetrical, northward verging structures (Stations 1, 2). Despite this fact many mesofolds showing opposite, southward vergence were also noted (Stations 3, 5 and 7). These folds were however, always associated with some form of faulting. In the case of station 3 a large south verging anticline is associated with an inferred strike-slip fault (Fig 6-39 and Fig 6-62). This suggests that this fold was rotated during strike-slip faulting. Most opposite verging folds are however associated with, and often transected by fore- and backthrusts (Station 5, Fig 6-83 and Fig 6-98; Station 7, Fig 6-146). Opposite verging folds in the Witteberg Group have also been noted by Booth (2002), and according to the author they can be attributed to folds forming during or prior to thrusting. This process results in the rotation of the fold axes and the consequent southward verging folds.

Megascale folds progress from having a totally overturned northern fold limb (Zone 1, Fig 6-4) to a vertical or slightly overturned northern fold limb (Zone 2, Fig 6-72). Mega-folds appear to progress from tight in the south to gentle towards the northern extent of the study zone. Nearly all measured mesofolds are asymmetric, and display tight to close interlimb angles. Their fold axes plunge at low to moderate inclinations in an approximate westerly direction. The above-mentioned factors all indicate that these folds were formed by compressional forces directed from the south.

Well developed bedding-parallel lineations in the form of slickenfibres, on bedding planes, indicate a possible flexure-slip mechanism for initial folding (Stations 1, 2 and 5).

7.2.3 Axial planar Cleavage

South dipping axial planar cleavage is most prevalent in the argillaceous strata of the Kweekvlei Shale Formation (Station 1). No axial planar cleavage on a mesoscale was noted in any of the more arenaceous units of the Perdepoort- and Rooirand Members. Axial planar cleavage dips at moderate to steep angles to the south as a result of asymmetric northward verging open to tight mega-anticlines and synclines formed syn-Cape Folding. This south dipping cleavage can clearly be seen at station 1 which is located in the northern limb of an overturned syncline in zone 1.

7.2.4 Thrust faults

Thrust faults are numerous and most dip at moderate to steep angles in a south-westerly direction. Most movement, as indicated by lineations, is directed towards the north in fore-thrusts, and to the south in back-thrusts. This suggests that these are tectonically related and formed during the same northward directed stress as indicated by folding and axial planar cleavage.

Fore-thrusts, especially bedding parallel fore-thrusts, are often very closely spaced frequently less than a metre apart (Stations 1 and 2). Argillaceous Kweekvlei strata (Station 1) show closer spaced thrusting compared to the more arenaceous units of the Perdepoort- and Rooirand Members. This feature was also noted by Booth, (2002) in slightly higher stratigraphic argillaceous and arenaceous units.

Steeply dipping fore-thrusts are more prevalent than shallow dipping fore-thrusts especially towards the southern extent of the study zone (Stations 1 and 2). Steep dipping fore-thrusts dip approximately south, transect and are transected by shallower dipping fore-thrusts, and are often associated with subordinate backthrusts (Station 1). A triangle zone formed by the cut-off between a steep dipping backthrust and shallow dipping fore-thrust was also observed at Station 1 (Fig 6-16). Steep dipping fore-thrusts are also frequently transected by lower dipping bedding-parallel fore-thrusts (Station 1). Normal faults often appear to be reactivated steep thrust faults. This would imply that in many cases normal faults at station 6 can be envisaged as originally being steep thrust faults, as suggested in the work by Facenna *et al.*, (1995). If this is taken into account the cut-off relationships at station 6 clearly correlates with station 1, thus it can be deduced that shallow dipping thrust faults formed prior to steep dipping thrust faults. Shallow dipping thrust faults often form roof thrusts cutting through a whole imbricate stack resulting in a duplex forming (Stations 1 and 5).

Backthrusts dip towards the north and are identified as cutting through both shallow dipping and steep dipping fore-thrusts (Stations 1 and 2). Backthrusts were also observed to utilize preferential weaknesses such as axial planes of south verging folds (Station 5, Fo2 and Fig 6-83).

7.2.5 Normal faults

The east-west trending normal faults are ubiquitous structures in the study area, (Stations 1, 5, 6, 7 and 8). Normal faults together with some strike-slip faults are the youngest structures as they transect all previously formed structures (Stations 1, 2, 5, 6, 7 and 8).

The most important normal faults are located at stations 5 and 7, which occur along strike from each other. This normal fault zone dips steeply towards the south forming a half-graben structure comprising half of zone 1 and zone 2. This normal fault zone is laterally extensive and is comprised of three south dipping normal faults spaced only metres apart (Stations 5 and 7). These normal faults clearly displace marker beds juxtaposing near horizontal bedding and near vertical bedding (Station 7). The large normal fault zone located in zone 2 displays a large brecciated zone suggesting displacement along these normal faults to be significant. However, the fact that these normal faults do not juxtapose older stratigraphic units such as the Rooirand Member and units of the Perdepoort Member, suggests displacement was not in the magnitude of hundreds of metres.

North dipping normal faults such as F1 and F2 encountered at station 6 and north dipping normal faults at station 7 both immediately north of a large normal fault zone may be explained as reactivated backthrusts. This explanation may also be attached to certain south dipping normal faults at station 6. Previously mentioned steep dipping thrust faults all dip at steep angles greater than the 32° angles which allow thrust faults to be reactivated (Facenna *et al.*, 1995). All normal faults are believed to be associated with the Mesozoic break-up of Gondwana.

7.2.6 Strike-slip faults

Strike-slip faulting was noted at 4 stations and strikes predominantly east-west although some faults do strike northwest-southeast. Most strike-slip faults transect earlier formed thrust faults, except at station 1, where strike-slip movement has utilized two earlier formed thrust fault planes. At station 1 these strike-slip faults dip at moderate to shallow angles in an approximate northerly direction clearly displaying geometry similar to that of thrust faults at station 1. It can therefore be postulated that strike-slip faulting in the study area utilized preferential planes of weakness where possible (6.3.3.2).

Strike-slip faulting on a mesoscale was also prevalent at certain stations, for example station 2 where east-west and northwest-southeast striking strike-slip faults displayed complex cut-off relationships (Fig 6-42). The isolated evidence from station 2 indicates that northwest-southeast striking strike-slip faults developed contemporaneously with east-west striking strike-slip faults.

A large left-lateral strike-slip fault striking northwest-southeast at Station 3 (Fig 6-39) can be inferred from evidence such as lithological displacement, the presence of fault breccia and a localised ravine. This strike-slip fault appears to displace bedding by 10-20m, clearly indicating that strike-slip faulting both on a mesoscale and megascale is an important controlling factor on the local geology.

Strike-slip faulting may also be seen in local river morphology, for example the northwest strike-slip components recorded at station 6 lie approximately parallel to the 45° bend in the local riverbed (Fig 6-73).

Strike-slip faulting transects thrust faulting but was not observed to transect normal faults. Strike-slip faulting may thus be contemporaneous with normal faulting associated with the movement during the extensional tectonic phase at the time of the Mesozoic break-up of Gondwana.

7.2.7 Joints

Competent strata of the Perdepoort- and Rooirand Members showed the best developed joint planes. More poorly developed jointing was detected in the more argillaceous horizons of the

Kweekvlei Shale Formation. Joints often follow the morphology of rivers, approximately N-S to NW-SE, and in conjunction with strike-slip faults may be the cause of abrupt changes in river flow direction (Fig 6-73, Station 6).

Three joint sets can be observed in the study area showing strikes of approximately north-south (350°-10°), east-west (240°-275°) and a west-northwest to east-southeast (280°-285°) (Fig 7-5). Joints often form symmetrically to folding as a post-deformational expression of residual stresses in strata (Fisher & Wilkerson, 2000, Price & Cosgrove, 1990). When comparing Fig 7-4 and Fig 7-5 it is clearly evident that the main joint orientations in the study area strongly correlate with longitudinal and cross joints associated with residual stresses formed during folding. Joint sets may thus be classified as longitudinal and cross joint formed as an after-effect of folding (Price, 1966). Planes of weakness thus most probably formed as a result of more or less north-northeast to south-southwest directed rectilinear stresses a consequence of folding during the Cape orogeny. Subsequently joint planes formed along these residual stress planes.

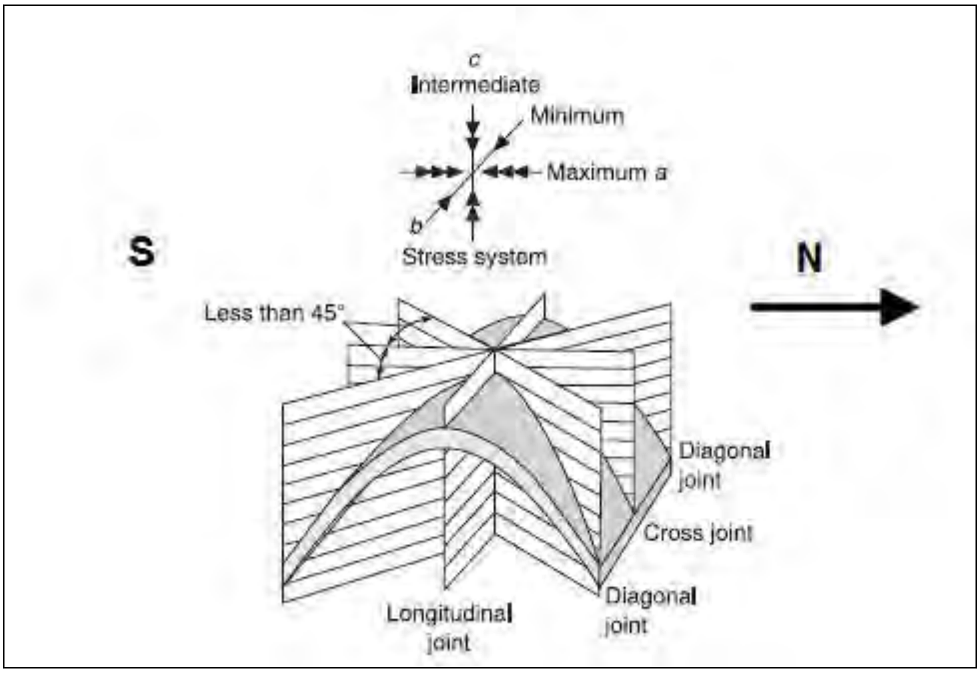

Fig 7-4: Diagram showing the main joint planes orientations associated with folding. The fold has been orientated according to the overall folding regime in the study area.(After Bell, (2007))

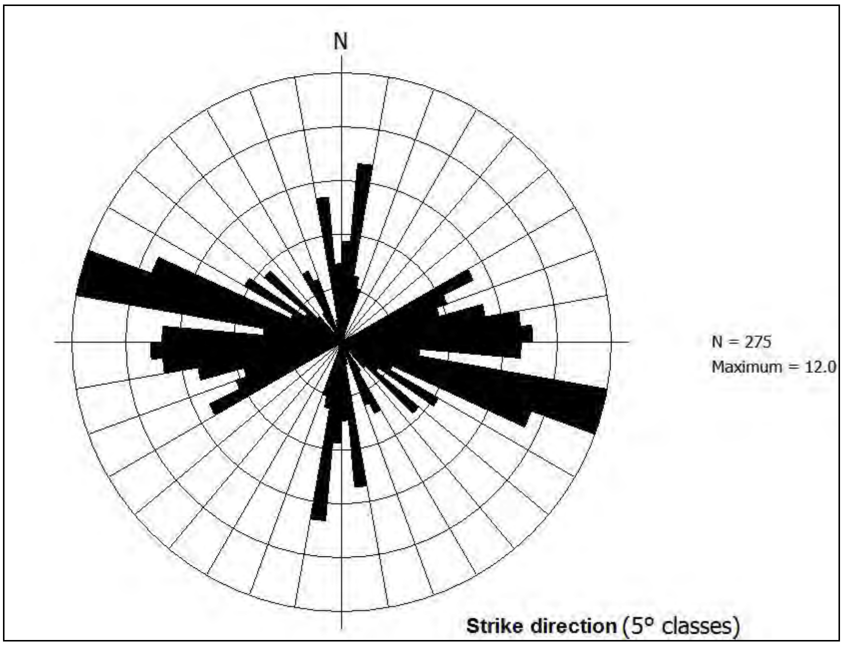

Fig 7-5: Rose diagram showing strike orientations of all joints in the structural study area.

7.2.8 Lineations

Lineations show varied orientations plunging towards the north in backthrusts, south and southwest in fore-thrusts and west in strike-slip fault planes. Slickensides along with mullions indicate a generally northwards directed movement associated with thrusting and flexure slip folding. Bedding surfaces in certain instances displayed multiple slickenside orientation indicating multiple deformational pulses acted on the area.

7.2.8.1 Slickensides

Slickensides were well developed particularly in thrust fault planes and in some instances on fold limb. A number of slickensided surfaces also exhibit two directions of movement on both fault planes and fold limbs, clearly indicating that reactivation has taken place along fault planes and fold limbs. This thus points to multiple deformational pulses acted on the area.

7.2.8.2 Boudinage

Boudinage at station 1 may be used to infer extensional strain. The clear difference in lithological competence has resulted in extensional fracturing. The extensional strain has thus exceeded the ductile rock strength causing brittle deformation resulting in pinch and swell structures (Fig 7-6). This may be a result of folding in which volume compensation could not be accommodated by the more brittle layer resulting in fracturing.

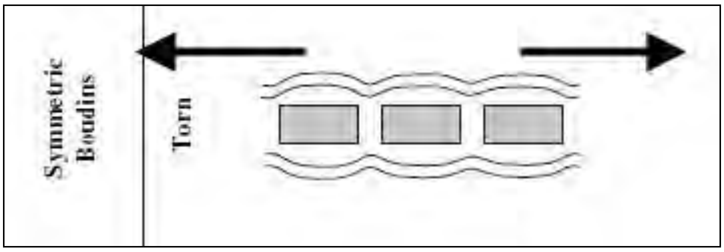

Fig 7-6: Diagram illustrating the shape of and the forces experience by boudins at station 1.

7.2.9 Deformation model and sequence

A northward directed stress field is confirmed in the study area by the presence of northward verging folds, showing approximate east-west fold axis orientations and east-west and north-south striking joint sets. Other structural features such as foreland (north) verging thrust system with lineations indicating northward transport are also consistent with an initial northward directed stress field.

Two main tectonic events resulted in the formation of structural features in the study area: firstly, the second first-order compression during the late Palaeozoic convergence of Gondwana, and secondly, extension during the mid to late Mesozoic break-up of Gondwana. A chronological description summarising the tectonic evolution of the study area is presented in Table 7-2.

Table 7-2: Chronological description of believed tectonic evolution of the study area.

System	Deformation event	Description
Compressional	Flexure-slip folding associated with mesoscale folding and bedding parallel to sub-parallel thrusting.	Northward verging folding and lineations on bedding planes are contemporaneous with and post-date low angle bedding parallel and sub-parallel thrusting. Tension gashes are formed on bedding surfaces indicating a north-south orientation for σ1. Volume compensation as a result of folding form pinch and swell structures including mullions and boudins.
	High angle thrusting.	High angle fore-and backthrust transect and in some cases reactivate previously formed low angle fore-thrusts. This forms triangle zones and pop-up structures. These also transect bedding and folding. Low angle thrusts also infrequently transect high angle thrusts to form duplex structures.
Extensional	Normal faulting and strike-slip faulting.	Strike-slip faults form contemporaneous with normal faulting. The Mesozoic break-up of Gondwana resulted in the formation of these structures.

8. Conclusion

The Perdepoort Member displays high concentrations (98.09%) of silicon in the form of SiO_2. This is however, of lower purity compared to various South African silicon sources. Silicon requirements needed for economically viable production of solar cells are extremely high purities. In this regards the Perdepoort Member appears to be insufficient. Sediments possessess various provenances and their chemical compositions are a net result of a number of factors. The presence of impurities are thought to be partly due to original depositional environment, namely nearshore and beach but certain impurities especially total Fe was most probably introduced largely due to tectonic influence on the study area. Contrasting depositional environments between the Perdepoort- and Rooirand Members may have facilitated later concentration of iron by oxidation of, for example, sulphide minerals. Data obtained from other studies such as S.Frost-Killian show great variability in certain chemicals and corroborates with the notion that greater chemical variations will be present if the area of study is increased by which ever degree.

SiO_2 concentrations in areas relatively far from areas of high degree of deformation are most probably the most viable for silica extraction. This study shows that normal fault zones should (according to what was found in the study) be avoided in order to maximize the silica concentrations of quartzites from the Perdepoort Member. Silica extraction from the Rooirand Member was ruled out as this Member contained higher levels of iron oxide and other impurities. Shales provide an immediate source of possible mineralogical contamination and for this reason shales and the contact between the Perdepoort Member and Kweekvlei Formation should be avoided if silica extraction is deemed viable.

The relatively pure Perdepoort Member was thus identified as the most favourable horizon for silica extraction in the study area. The sample population is however, small and thus may be erroneous, as one or two outliers may effect the data more drastically.

Deformation in the study area conforms to the general pattern of Cape Fold Belt deformation found in other studies in the vicinity. The local geology displays north-westward directed compression followed by strike-slip movement. Fore-thrusts are abundant and are often associated with subordinate backthrusts. Movement, as indicated by lineations, is directed towards the north in fore-thrusts, and to the south in back-thrusts. Thrust faults formed initial conduits for hypergene and supergene deposits to form. Overturned northward verging megafolds are the main controlling features in the study area and predominate over south verging folds. Fold axes plunge at low to moderate angles west-southwest. The study area displays a wide range of folding from tight to open. Normal faults and strike-slip faults formed later during the Mesozoic break-up of Gondwana, transecting all other structures in the study area. Strike-slip faulting has in places reactivated pre-existing thrust fault planes. Normal faults show increased amounts of accessory minerals and baryte indicating increased hydrothermal activity.

9. References

Agnello, V. N., 2004, The Silica Industry in the Republic of South Africa 2004, *Department of Minerals and Energy.* pp. 39.

Bell, F. G., 2007. Engineering Geology*. 2nd.* Elsevier, Oxford.

Booth, P. W. K., 1996. The relationship between folding and thrusting in the Floriskraal Formation (upper Witteberg Group), Steytlerville, Eastern Cape. *South African Journal of Geology* 3 (99): 235-243.

Booth, P. W. K., 1998. The effect of thrusting on fold style and orientation, Weltevrede Formation (Cape Supergroup), Steytlerville, Eastern Cape. *South African Journal of Geology* 101 (1): 27-37.

Booth, P. W. K., 2002. Thrust faults and fold vergence in the Paleozoic middle and upper Witteberg Group, Cape Supergroup (Cape Fold Belt), Steytlerville: an interpretation of their relationship. *South African Journal of Geology* 105: 25-38.

Booth, P. W. K., 2009. A review of structural geology of the Cape Fold Belt and challenges towards future research. *11th Saga Biennial Technical Meeting and Exhibition*, *Manzini, Swaziland.*

Booth, P. W. K., Brunsdon, G. & Shone, R. W., 2004. A Duplex Model for the Eastern Cape Fold Belt? Evidence from the Palaeozoic Witteberg and Bokkeveld Groups (Cape Supergroup), Near Steytlerville, South Africa *Gondwana Research* 7 (1): 211-222.

Booth, P. W. K., Munro, A. J. & Shone, R. W., 1999. Lithological and structural characteristics of Cape Supergroup rocks at Port Alfred, Eastern Cape, South Africa. *South African Journal of Geology* 4 (102): 391-404.

Booth, P. W. K. & Shone, R. W., 1992. Folding and thrusting of the Table Mountain Group at Port Elizabeth, eastern Cape, Republic of South Africa. A.A. Balkema/Rotterdam/Brookfield/1992, Cape Town. pp. 207-216.

Booth, P. W. K. & Shone, R. W., 1999. Complex thrusting at Uniondale, eastern sector of the Cape Fold Belt, Republic of South Africa: structural evidence for the need to revise the lithostratigraphy. *Journal of African Earth Sciences* 29 (1): 125-133.

Booth, P. W. K. & Shone, R. W., 2002. A review of thrust faulting in the Eastern Cape Fold Belt, South Africa, and the implications for the current lithostratigraphy interpretation of the Cape Supergroup. *Journal of African Earth Sciences* (34): 179-190.

Broad, D. S., Jungslager, E. H. A., McLachlan, I. R. & Roux, J., 2006. Offshore Mesozoic Basins. In: The Geology of South Africa. Eds. Johnson, M. R., Anhaeusser, C. R. and Thomas, R. J. *The Geological Society of South Africa and Council for Geoscience*, Pretoria. pp. 553-571.

Broquet, C. A. M., 1992. The sedimentary record of the Cape Supergroup: A review. In: Inversion Tectonics of the Cape Fold Belt, Karoo and Cretaceous Basins of Southern Africa. Eds. De Wit, M. J. and Ransome, I. G. D. Balkema, Rotterdam. pp. 269.

Browning, C., 2005. An investigation into the characteristics and distribution of heavy minerals along the northern margin of Algoa Bay, South Africa. Nelson Mandela Metropolitan University, pp. 51 (Unpublished).

Brunsdon, G., Booth, P.W.K., 2009. Faulting of the Witteberg Group rocks, Steytlerville, Eastern Cape. Nelson Mandela Metropolitan University, *11th Saga Biennial Technical Meeting and Exhibition*, *Mazini, Swaziland.*

Cole, D. I., 1992. Evolution and development of the Karoo Basin. In: Inversion Tectonics of the Cape Fold Belt, Karoo and Cretaceous Basins of Southern Africa. Eds. De Wit, M. J. and Ransome, I. G. D. Balkema, Rotterdam. pp. 269.

Cotter, E., 1999. Depositional setting and cyclic development of the lower part of the Witteberg Group (Mid-to Upper Devonian), Cape Supergroup, Western Cape, South Africa. *South African Journal of Geology* 103 (1): 1-14.

de Beer, C. H., 1995. Fold interference from simultaneous shortening in different directions: the Cape Fold Belt syntaxis. *Journal of African Earth Sciences* 21 (1): 157-169.

de Beer, C. H., Van Zijl, J. S. V. & Bahnemann, F. K., 1974. Plate Tectonic origin for the Cape Fold Belt? *Nature* (252): 675-676.

de Swardt, A. M. J. & Rowsell, D. M., 1974. Note on the Relationship between Diagenesis and Deformation in the Cape Fold Belt. *Transactions of the Geological Society of South Afirca* 77: 239-245.

De Villiers, J., 1944. A Review of the Cape Orogeny. *Ann. Univ. Stell.,* 22-A: 183-208.

De Wit, M. J. & Ransome, I. G. D., 1992 (a). Preliminary investigations into a microplate model of the South Western Cape. In: Inversion Tectonics of the Cape Fold Belt, Karoo and Cretaceous Basins of Southern Africa. Eds. De Wit, M. J. and Ransome, I. G. D. Balkema, Rotterdam. pp. 269.

De Wit, M. J. & Ransome, I. G. D., 1992 (b). Regional inversion tectonics along the southern margin of Gondwana. In: Inversion tectonics of the Cape Fold Belt, Karoo and Cretaceous Basins of Southern Africa. Eds. de Wit, M. J. and Ransome, I. G. D. A.A Balkema, Cape Town. pp. 269.

Deer, W. A., Howie, R. A. & Zussman, J., 1992. An introduction to the Rock-Forming Minerals. *2nd.* Longman Scientific and Technical, London.

Dingle, R. V., Seisser, W. G. & Newton, A. R., 1983. The configuration and Tertiary geology of southern Africa. Balkema, Rotterdam. pp. 300.

Evans, J. P. & Forster, C. B., 1997. Permeability of fault-related rocks, and implications for hydraulic structure of fault zones. *Journal of Structural Geology* 19 (11): 1393-1407.

Facenna, C., Nalpas, T., Brun, J. & Davy, P., 1995. The influence of pre-existing thrust faults on normal fault geometry in nature and experiments. *Journal of Structural Geology* 17 (8): 1139-1149.

Fisher, M. P. & Wilkerson, M. S., 2000. Predicting the orientation of joints from fold shape: Results of pseudo-three-dimensional modeling and curvature analysis. *Geology* 28 (1): 15-18.

Fleuty, M. J., 1964. The Description of Folds. *Proceedings of the Geologists' Association* 75: 461-492.

Fouché, J., Bate, K. J. & van der Merwe, R., 1992. Plate tectonic setting of the Mesozoic Basins, southern offshore, South Africa: A review. In: Inversion Tectonics of the Cape Fold Belt, Karoo and Cretaceous Basins of Southern Africa. Eds. De Wit, M. J. and Ransome, I. G. D. Balkema, Rotterdam. pp. 269.

Ghosh, S. K., 1993. Structural Geology Fundamentals and Modern Developments. *1ste.* Pergamon Press, Oxford. pp. 598.

Goossens, A. E. M., 2003. A study of the structural geology of the Witteberg Group and lowermost Karoo Supergroup, Darlington Dam, Jasenvillle District, Eastern Cape. University of Port Elizabeth, pp. 252 (Unpublished).

Green, M. A., 1982. Solar Cells Operating Principles, Technology, and System Applications. Prentice-Hall. pp 274.

Green, M. A., 1987. High Efficiency Silicon Solar Cells. Trans Tech Publications. pp 240.

Green, M. A., 2001. Ch 4. Crystalline silicon solar cells. pp 49.

Gresse, P. G., Theron, J. N. T., Fitch, F. J. & Miller, J. A., 1992. Tectonic inversion and radiometric resetting of the basement in the Cape Fold Belt. In: Inversion Tectonics of the Cape Fold Belt, Karoo and Cretaceous Basins of Southern Africa. Eds. De Wit, M. J. and Ransome, I. G. D. Balkema, Rotterdam. pp. 269.

Hashim, U., 2003. From Sand to Silicon Wafer. *My Kukkum. Ed. 3. pp. 16*

Hälbich, I. W., 1983. A Geodynamic model for the Cape Fold Belt. In: Geodynamics of the Cape Fold Belt. 1st Eds. Söhnge, A. P. G. and Hälbich, I. W. *The Geological Society of South Africa*, Johannesburg. pp. 184.

Hälbich, I. W., 1992. The Cape Fold Belt Orogeny: State of the art 1970's-1980's. In: Inversion tectonics of the Cape Fold Belt, Karoo and Cretaceous Basins of Southern Africa. Eds. de Wit, M. J. and Ransome, I. G. D. A.A Balkema, Cape Town. pp. 269.

Hälbich, I. W., Fitch, F. J. & Miller, J. A., 1983. Dating the Cape Orogeny. In: Geodynamics of the Cape Fold Belt. 1ste Eds. Söhnge, A. P. G. and Hälbich, I. W. *The Geological Society of South Africa*, Johannesburg. pp. 149-164.

Hammond, K. J. & Evans, J. P., 2003. Geochemistry, mineralization, structure, and permeability of a normal-fault zone, Casino mine, Alligator Ridge district, north central Nevada. *Journal of Structural Geology* 25: 717-736.

Jeffreys, D. G., 2003. Geological Structure of Witteberg Group Rocks, Northwest of Kirkwood, Eastern Cape. University of Port-Elizabeth, Port-Elizabeth. pp. 179 (Unpublished).

Johnson, M. R., 2003. Stratigraphy and sedimentology of the Cape and Karoo Sequences in the Eastern Cape Province.Rhodes University, Grahamstown. pp. 336, PhD Thesis.

Johnston, S. T., 2000. The Cape Fold Belt and Syntaxis and the rotated Falkland Islands: dextral transpressional tectonics along the southwest margin of Gondwana. *Journal of African Earth Sciences* 31 (1): 51-63.

Lock, B. E., 1980. Flat Plate Subduction and the Cape Fold Belt of South Africa. *Geology* 80: 35-39.

McLennan, S. M., Nance, W. B. & Taylor, S. R., 1980. Rare earth element–thorium correlation in sedimentary rocks, and the composition of the continental crust. *Geochimica et Cosmochimica Acta* 44: 1833-1839.

Newton, A. R., 1973. A gravity-folding model of the Cape Fold Belt. *Transactions of the geological Society of South Africa.* 76: 145-152.

Ontario 2000. A sunny future with silicon. *Ontario business report.*

Oosterhuis, W. R., 1998. Ch Silicon and Silica. In: The Mineral Resources of South Africa. Eds. Wilson, M. G. C. and Anhaeusser, C. R. Council for Geoscience, Cape Town. pp 740 .

Perry, M., 1998. Solar energy from sand: manufacturing a solar cell. *Union-Tribune news* paper. pp 1.

Price, N. J., 1966. Fault and Joint Development in Brittle and Semi-brittle Rock. *1st.* Pergamon Press Ltd., London. pp 176.

Price, N. J. & Cosgrove, J., 1990. Analysis of geological structures. Cambridge University Press, Cambridge.

Rhodes, R. C., 1974. A gravity model for the Cape Fold Belt: Discussion. *Transactions of the geological Society of South Africa.* (77): 207-209.

Rollinson, H., 1993. Using geochemical data: evaluation, presentation, interpretation. Pearson Prentice Hall, London. pp 352.

Rudnick, R. L. & Gao, S., 2003. Composition of the Continental Crust. *Treatise on Geochemistry* 3: 1-64.

SACS, 1980. Stratigraphy of South Africa. Part 1. (Comp. Kent, L.E.). Lithostratigraphy of the Republic of South Africa, South West Africa/Namibia, and the Republic of Bophuthatswana, Transkei and Venda. *Geological Survey of South Africa*

Shone, R. W., 2006. Onshore Post-Karoo Mesozoic Deposits. In: The Geology of South Africa. Eds. Johnson, M. R., Anhaeusser, C. R. and Thomas, R. J. *Geological Society of South Africa and Council for Geoscience*, Pretoria. pp. 541-552.

Shone, R. W. & Booth, P. W. K., 2005. The Cape Basin, South Africa: A review. *Journal of African Earth Sciences* (43): 196-210.

Söhnge, A. P. G., 1983. The Cape Fold Belt-Perspective. In: Geodynamics of the Cape Fold Belt. Eds. Söhnge, A. P. G. and Hälbich, I. W. The Geological Society of South Africa, Johannesburg. pp.

Tankard, A., Welsink, W., Aukes, P., Newton, R. & Stettler, E., 2009. Tectonic evolution of the Cape and Karoo basins of South Africa. *Marine and Petroleum Geology*: 1-34.

Thamm, A. G. & Johnson, M. R., 2006. 21: The Cape Supergroup. In: *The Geology of South Africa.* Eds. Johnson, M. R., Anhaeusser, C. R. and Thomas, R. J. Geological Society of South Africa and Council for Geoscience, Pretoria. pp. 691.

Toerien, D. K. & Hill, R. S., 1989, The Geology of the Port Elizabeth Area Explanation of Sheet 3324, *Council for Geoscience*, Pretoria.

Visser, J. N. J., 1992. Basin tectonics in southwestern Gondwana during the Carboniferous and Permian (from Rust 1973). In: *Inversion Tectonics of the Cape Fold Belt, Karoo and Cretaceous Basins of Southern Africa.* Eds. De Wit, M. J. and Ransome, I. G. D. Balkema, Rotterdam. pp. 269.

Watkeys, M. K., 2006. Gondwana Break-Up: A South African Perspective. In: The Geology of South Africa. Eds. Johnson, M. R., Anhaeusser, C. R. and Thomas, R. J. The Geological Society of South Africa and Council for Geoscience, Pretoria. pp. 531-539.

Whittingham, J. K., 1987, Palaeozoic Geology of Steytlerville-Klipplaat-Kirkwood-Paterson area, Eastern Cape, Cape Geological Survey of South Africa, Report No. 1987-0053, pp. 37.

Zhao, J., 2004. Recent advances of high-efficiency single crystalline silicon solar cells in processing technologies and substrate materials. *Solar Energy Materials and Solar Cells* (82): 53-64.

10. Appendix

10.1 Azimuth & Dip and Trend & Plunge Orientation Data

Station 1															
Bedding		Faults 1		Folds		Lineations		Joints		Cleavage		Faults 2		Cleavage 2	
azimuth	dip	azimuth	dip	azimuth	dip	trend	plunge	azimuth	dip	azimuth	dip	azimuth	dip	azimuth	dip
205	34	212	39	327	45	209	36	168	66	191	80	211	37	194	64
193	36	207	36	327	56	221	38	169	65	193	74	212	37	207	76
190	26	202	38	300	34	207	34	162	67	209	67	207	38	192	83
177	30	196	44	321	46	177	22	165	64	198	84	208	36	198	88
172	31	209	39	308	22	167	24	166	65	207	88	209	37	192	76
191	27	196	25	318	23	203	8	182	65	204	82	207	36	201	74
187	40	196	27	296	28	204	9	168	54	190	66	204	33	204	88
180	31	166	13	310	29	220	19	160	64	190	76	206	34	193	78
194	26	170	16	316	30	196	58	173	62	216	77	212	34	201	84
183	20	172	12	324	48	195	59	183	60	204	63	209	33	199	78
171	29	153	16	209	34	200	55	184	61	181	84	211	30	214	80
208	64	204	37	210	35	201	58	165	64	204	72	214	29	191	75
216	65	203	36	230	36	195	43	180	60	195	69	207	31	199	79
212	57	204	38	226	37	200	43	183	59	199	69	217	28	213	75
208	65	207	35	228	38	171	38	180	55	198	78	211	31	190	67
225	74	207	24	230	39	171	28	161	66	200	54	214	32	202	80
214	63	194	33	227	40	196	42	174	61	202	86	210	33	205	72
208	65	200	58	258	41	204	53	178	64	199	87	208	35	195	74
217	48	200	66	261	42	187	54	164	57	212	78	208	33	200	73
214	62	201	51	268	43	179	43	173	57	192	75	210	34	192	65
212	58	206	51	257	44	350	36	186	54	189	87	212	34	199	89
210	65	204	56			346	41			199	79	210	36	188	61
210	65	203	54			184	40			198	87	209	34	196	70
205	46	201	54			201	2			191	64	210	32	193	78
208	55	201	54			193	44			188	73	208	32	213	77
209	55	200	57			218	34			202	77	207	31	203	73
200	72	206	57			225	33			192	71	215	30	192	69
192	58	207	50			227	30			199	81	207	30	214	78
185	58	207	63			250	30			213	83	204	34	211	78
196	66	209	58			227	31			195	72	205	29	212	68
167	51	201	53			279	29			207	73	207	34	200	79
174	41	197	41			226	29			199	72	207	33	190	67
156	73	201	42			229	33			194	67	204	33	200	72
192	85	202	27			218	34			193	62	204	34	188	70
191	51	207	28			225	36					204	37	214	79
184	51	204	31			221	34					206	36	212	79
201	65	205	29			75	10					209	33	210	78
217	62	205	34			67	12					213	34		
210	57	201	37			68	2					209	36		
185	61	203	23			72	6					204	39		
202	54	205	29			75	12					206	57		
207	57	201	36			76	12					207	50		
201	46	197	33			76	15					207	63		

206	58	207	42			285	11					209	58		
201	53	210	41			286	16					201	53		
181	54	210	36			285	12					348	27		
187	60	211	36			288	19					345	30		
181	54	208	44			286	17					346	29		
201	66	209	40			296	3					344	29		
206	60					299	16					9	38		
201	65					300	16					360	39		
204	69					294	21					355	40		
202	69					298	5					190	32		
220	40					298	6					199	26		
216	48					298	8					206	32		
210	48					300	9					194	37		
217	48					306	11					195	24		
218	43					301	14					178	47		
215	44					300	13					172	45		
228	39					302	8					179	40		
217	48					302	9					173	44		
217	48					304	13					167	54		
220	45					305	12					176	44		
216	45											175	43		

Station 2									
Faults		Folds		Lineations		Joints		Faults	
azimuth	dip	azimuth	dip	trend	plunge	azimuth	dip	azimuth	dip
262	27	349	36	240	26	288	73	278	32
263	25	347	41	239	25	15	70	277	27
260	27	350	42	239	24	23	63	297	27
252	26	340	44	241	25	348	68	260	29
243	21	335	47	240	26	5	53	243	27
265	29	342	56	243	24	14	67	265	28
261	31	345	26	239	23	23	65	279	23
241	26	343	26	238	22	277	77	262	23
255	24	339	49	239	27	274	76	253	24
252	28	347	54	240	27	285	78	256	23
239	28	348	54	240	26	285	82	242	18
240	22	348	50	241	24	14	60	206	29
211	23	13	45	242	23	26	63	259	27
270	25	2	45	242	27	272	82	246	19
255	14	326	26	240	28	17	65	240	26
276	19	319	23	230	22	19	67	252	19
251	19	322	33	232	24	284	73	235	24
224	23	320	26	244	25	350	61	230	23
256	24	321	28	241	26	389	54	253	24
239	33	320	35	247	27	265	84	264	24
230	24	306	24	241	30	276	86	257	24
233	23	327	27	250	17	273	84	274	23
216	25	318	18	255	29	278	85	287	34
261	21	354	38	251	26	275	89	292	30
242	23	351	35	256	27	275	85	286	26
273	26	348	36	254	28	263	83	276	33
265	24	341	39	255	25	245	84	278	25
260	21	341	35	253	27			295	29
265	26	343	32	252	26			261	31
252	16	357	43	254	28			240	26
274	21	344	37	255	28			268	24
248	17	6	35	254	26			276	25
227	25	346	44	255	27			265	21
251	22	352	42	252	25			250	25
244	30	340	39	253	28			259	26
233	27	345	48	254	29			240	15
237	26	354	50	254	29			210	31
220	28	352	44	255	30			254	25
258	18	355	44	255	25			248	18
246	27	343	43	253	26			235	29
270	29	333	35	252	27			254	18
262	28	328	32	249	32			231	26
262	18	334	32	250	26			234	21
250	29	321	31	249	27			250	25

260	25	320	15	250	34			266	23
265	23	315	17	340	20			253	22
262	26	305	17	337	19			279	25
254	30	229	23	341	20			82	82
247	24	215	24	13	26			182	89
262	26	251	21	19	17			181	89
257	31	262	21	336	15			182	88
244	22	248	25	17	9			180	80
252	27	229	23	17	3			184	87
257	24	230	23	17	6			178	83
240	31	239	29	17	7			183	86
238	25	241	26	42	46			19	79
208	24	241	26	36	37			20	86
268	26	267	33	45	26			18	76
268	29	246	25	355	39			10	80
261	28	266	22	360	38			17	79
265	18	258	24	360	37			21	86
247	29	264	32	359	37			20	77
263	24	234	27	355	38			17	88
263	26	270	22	360	51			22	75
265	22	270	16	354	43			7	82
251	34	270	16	359	53			19	76
250	23	277	22	360	42			18	88
259	27	272	22	350	44			75	61
254	30	279	22	350	39			71	61
247	24	273	13	359	50			75	59
260	25	190	20	354	48			80	61
268	23	188	17	216	9			71	64
256	29	195	22	240	26			71	63
254	28	200	18	240	25			74	63
241	22	155	25	239	24			67	59
266	27	162	24	238	23			72	66
259	34	175	14	235	22			74	63
243	29	183	17	237	27			80	62
254	22	170	23	170	3			180	76
256	30	168	25	162	5			186	82
240	30	183	24	164	1			177	82
277	28	187	23	166	3			184	78
277	23	190	21	168	5			177	69
267	18	185	25	164	3			182	82
265	21	176	14	253	19			176	83
267	21	172	11	253	23			184	86
282	24	165	15	256	23			20	75
251	17	167	13	255	26			22	82
205	24	166	15	252	17			16	78
238	23	160	14	290	21			13	76
270	22	349	36	289	23			18	84
289	22	347	41	281	26			18	83

290	21	350	42	282	24			23	78
232	24	340	44	291	22			15	81
280	29	335	47	294	21			25	78
284	21	342	56	283	27			9	76
297	21	345	26	25	44			17	80
226	23	343	26	23	47			20	81
273	15	339	49	26	49				
286	20	347	54	23	43				
281	13	348	54	22	41				
278	26	348	50	20	43				
275	24	13	45						
269	19	2	45						
263	23	326	26						
268	18	319	23						
280	26	322	33						
254	14	320	26						
251	25	321	28						
239	20	320	35						
266	23	306	24						
291	20	327	27						
287	23	318	18						
234	22	354	38						
278	31	351	35						
286	19	348	36						
294	24	341	39						
228	20	341	35						
274	16	343	32						
285	17	357	43						
281	14	344	37						
288	21	6	35						
290	22	346	44						
231	24	352	42						
276	34	340	39						
288	17	345	48						
292	25	354	50						
230	19	352	44						
270	17	355	44						
291	16	343	43						
278	16	333	35						
286	32	328	32						
294	28	334	32						
284	28	321	31						
		320	15						
		315	17						
		305	17						
		300	22						
		316	22						
		345	55						

		243	50						
		10	43						
		6	43						
		342	35						
		255	45						
		354	46						
		330	34						
		324	16						
		338	28						
		335	33						
		340	38						
		324	24						
		345	48						
		345	55						
		329	26						
		190	20						
		188	17						
		195	22						
		200	18						
		155	25						
		162	24						
		175	14						
		183	17						
		170	23						
		168	25						
		183	24						
		187	23						
		190	21						
		185	25						
		176	14						
		172	11						
		165	15						
		167	13						
		166	15						
		160	14						

Station 3					
Bedding		Joints		Bedding 2	
azimuth	dip	azimuth	dip	azimuth	dip
219	32	285	82	213	63
217	33	14	60	211	48
220	40	26	63	218	46
197	42	272	82	211	42
202	52	17	65	200	53

201	48	19	67	198	50
211	59	284	73	214	35
211	45	350	61	222	42
212	62	389	54	203	41
207	65	265	84	211	55
213	39	276	86	209	35
199	39	273	84	219	41
208	34	278	85	211	40
225	30	275	89	201	53
250	18	275	85	197	50
244	22	263	83	218	41
209	44	245	84	210	60
211	38	285	73	206	35
210	35	17	62	200	50
204	51	25	61	209	61
215	40	351	57	206	46
222	42	3	55	198	54
213	60	12	59	197	50
207	36	22	64	207	61
216	41	353	63	214	44
214	37	279	85	217	62
198	54	276	83	210	50
200	52	265	80	196	50
211	57	267	86	216	34
212	40	15	65	218	41
200	37	24	63	196	43
210	25	353	63	218	56
222	31	6	55	209	37
220	33	17	63	224	41
218	44	16	68	213	54
202	44	354	63	210	33
215	35			211	37
200	50			197	37
199	49			206	35
242	23			214	41
213	44			213	37
212	40			198	56
219	46			197	45
209	61			216	41
205	32			212	52
193	50			206	33
215	61			197	51
217	43			219	41
198	49			221	41
236	24			211	55
208	47			208	36
210	40			197	46
215	41			218	41

218	42			196	44
212	61			210	56
210	35			206	36
203	50			211	41
222	41			200	50
215	38			198	47
204	50			246	23
203	47			214	47
213	34			215	40
211	38			221	41
218	41			210	59
207	64			209	34
206	37			200	49
200	50			210	57
				210	47
				200	49
				245	23
				203	50
				200	47
				218	41
				213	57
				210	35
				197	47
				208	57
				207	46

Station 4			
Faults (Backthrusts)		Lineations	
azimuth	dip	azimuth	dip
20	63	21	59
19	60	19	58
19	61	25	64
12	60	21	59
28	53	25	62
20	49	8	64
15	59	30	56
27	59	8	41
15	66	46	46
355	53	18	29

352	49	13	34
357	46	27	66
5	53	21	81
3	53	356	61
5	51	0	58
357	47	41	48
356	48	36	42
359	41	23	34
350	51	20	30
11	76	22	41
15	49	21	38
351	32	22	42
354	32	354	39
353	30	8	39
354	36	17	40
354	36	13	36
8	79	17	47
7	84	17	48
359	65	12	54
0	66	40	47
358	61	36	46
2	59	21	55
23	62	10	50
358	51		
353	43		
0	59		
2	42		
14	49		
15	42		
19	43		
28	37		
31	34		
4	37		
16	38		
18	44		
15	40		
12	41		
22	38		
21	39		
19	29		
13	32		
11	48		
350	50		
354	48		
1	47		
351	42		
350	50		
15	54		

356	53		
0	48		
20	37		
12	48		
11	56		
46	16		
41	15		
9	45		
33	33		
359	38		
18	34		
19	43		
21	38		
17	39		
12	27		
0	60		
21	61		
359	54		
22	37		
24	41		
20	30		
359	57		
1	53		
22	65		
22	65		
12	64		
0	52		
22	63		
10	66		
32	54		
22	26		
15	34		
9	47		
352	51		
18	52		
0	51		
2	49		
356	52		
3	46		
350	40		
349	53		
13	51		
359	57		
19	52		
12	60		
30	64		
12	62		
359	49		

Station 5											
Bedding		Faults		Folds		Lineations		Joints		Bedding 2	
azimuth	dip	azimuth	dip	azimuth	dip	trend	plunge	azimuth	dip	azimuth	dip
192	48	24	41	318	35	186	41	170	32	214	45
193	43	19	49	313	34	181	11	177	33	211	40
205	45	21	38	315	36	179	9	178	32	206	49
199	43	19	59	310	34	181	10	158	22	206	50
204	42	18	39	316	33	190	41	157	17	208	41
195	39	15	44	311	33	183	39	167	16	206	35
186	57	33	57	314	31	183	37	182	17	202	40
192	30	6	36	323	28	186	46	240	13	187	41
190	43	19	39	314	35	179	32	260	8	190	44
195	35	11	17	309	33	190	70	219	13	171	54
190	53	29	24	317	37	200	71	225	14	187	49
197	46	22	20	313	37	175	26	236	18	178	47
193	43	19	12	262	23	173	36	224	19	178	46
194	38	14	23	256	29	161	46	202	23	178	48
210	47	23	24	235	34	171	34	214	18	271	53

195	43	19	19	234	36	178	31	223	18	183	54
197	55	31	20	259	24	174	46	225	14	191	50
221	57	33	27	234	35	173	31	222	17	197	55
207	46	22	82	255	29	180	46	201	20	180	49
204	46	22	84	256	29			194	23	196	49
210	37	13	83	261	22			231	17	195	51
190	38	14	83	235	34			183	20	201	45
198	33	9	82	170	54			224	15	190	50
194	38	14	87	170	56			214	26	198	45
193	34	10	81	175	56			213	26	193	54
190	37	13	82	169	57			183	16	192	47
194	34	10	82	172	59			199	26	190	53
187	37	13	84	170	62			200	25	192	54
199	30	6	84	178	60			183	15	200	54
196	38	14	83	185	62			189	26	186	60
193	35	11	54	180	58			190	17	182	50
194	34	10	44	170	48			189	24	185	49
190	38	14	49	172	59			196	19	192	48
194	46	22	52	169	56			202	22	190	44
198	36	12	49	169	57			192	20	202	46
202	51	27	53	165	59			200	24	190	36
210	44	20	54	169	42			184	17	190	49
204	39	15	55	176	46			190	18	188	51
191	46	22	52	185	31			190	18	188	49
186	38	14	49	185	32			195	18	184	49
214	47	23	36	183	30			201	21	210	44
179	50	26	54	169	48			190	16	190	38
189	45	21	62	176	55			198	24	193	34
186	40	16	42	168	54			190	23	215	39
202	40	16	39	170	47			196	18	186	41
180	47	23	41	192	35			240	12	198	40
178	41	17	38	182	33			226	15	206	36
180	48	24	39	178	28			156	17	190	55
173	57	33	37	183	30			176	32	219	21
190	45	21	37	191	30			157	22	212	20
213	37	13	40	180	22			211	17	229	19
210	44	20	44	192	30			150	27	231	16
212	35	11	46	191	37			153	17	211	21
206	40	16	43	180	32			153	17	206	30
215	39	15	48	181	21			177	24	238	19
197	53	29	47	184	35			155	23	236	25
205	36	12	47	176	43			210	18	199	34
194	42	18	33	185	43			179	31	245	23
190	54	30	35	182	51			176	31	228	19
197	50	26	33	189	56			179	13	205	28

192	50	26	32	180	79			213	15	219	21
198	43	19	27	184	66			223	15	231	20
217	50	26	66	191	57			235	17	211	21
195	52	28	74	182	57			153	17	216	57
215	48	24	51	184	54			154	15	220	60
202	47	23	88	190	38			235	19	197	56
198	41	17	84	181	50			218	13	198	54
181	56	32	81	181	77			189	24	203	56
203	47	23	74	184	35			210	18	192	54
198	42	18	70	353	64			222	18	210	39
206	36	12	72	358	61			166	17	192	40
203	42	18	79	353	61			168	31	200	44
205	41	17	77	350	57			177	31	202	44
208	42	18	28	347	61			213	25	199	46
206	51	27	37	352	64			219	13	210	37
217	37	13	28	352	62			176	31	191	54
213	35	11	28	354	62			170	32	201	44
215	40	16	30	358	66			200	22	201	44
		21	42	351	62			224	13		
		16	30	352	61			213	19		
		25	36					224	16		
		26	31					151	17		
		17	42					149	27		
		11	42					154	17		
		16	42					176	23		
		17	33					198	26		
		20	39					155	24		
		30	42					153	25		
		25	32					154	24		
		23	48					176	32		
		22	49					156	21		
		24	43					166	17		
		29	44					195	18		
		30	45					190	18		
		26	48					195	12		
		31	44					194	12		
		25	46					194	11		
		25	46					198	16		
		27	44					197	16		
		21	48					179	24		
		26	44					176	23		
		21	46					180	12		
		30	44					162	24		
		23	44					168	23		
		29	42					163	21		

		30	41					162	20		
		30	43					150	23		
		36	32					160	26		
		26	32					162	24		
		25	42					158	21		
		24	43					150	34		
		20	44					152	22		
		22	31					183	29		
		12	44					159	20		
		25	38					159	25		
		27	30					151	33		
		25	49					180	12		
		25	51					176	24		
		20	62								
		14	61								
		10	55								
		15	59								
		17	50								
		16	64								
		12	57								

Station 6							
Bedding		Faults		Lineations		Joints	
azimuth	dip	azimuth	dip	trend	plunge	azimuth	dip
170	32	52	29	38	36	260	85
177	33	32	46	36	36	276	89
178	32	39	42	24	64	272	88
158	22	50	29	22	64	277	87
157	17	35	43	23	64	274	87
167	16	37	46	19	48	271	87
182	17	36	43	284	89	259	86
240	13	39	42	276	87	240	89
260	8	50	30	37	50	80	86
219	13	31	47	37	51	281	81
225	14	31	48	36	50	277	81
236	18	207	63	37	52	281	73
224	19	192	66	38	53	283	78
202	23	200	67	176	50	15	66
214	18	206	65	356	38	21	65
223	18	203	62	179	36	350	62
225	14	185	86	161	78	1	58

222	17	195	87	171	76	14	65
201	20	181	88	157	89	20	65
194	23	200	62	176	83	351	61
231	17	190	74	166	83	13	66
183	20	195	69	171	88	20	65
224	15	190	73	166	82	349	61
214	26	197	72	173	84	359	57
213	26	39	64			13	65
183	16	35	66			277	88
199	26	43	67			278	86
200	25	24	62			262	82
183	15	38	63			269	86
189	26	15	43			13	61
190	17	360	47			16	63
189	24	38	64			282	77
196	19	42	67			353	65
202	22	26	59			358	51
192	20	18	40				
200	24	37	62				
184	17	198	85				
190	18	207	86				
190	18	201	84				
195	18	206	83				
201	21	202	79				
190	16	200	77				
198	24	196	82				
190	23	203	83				
196	18	210	78				
240	12	200	77				
226	15	204	82				
156	17	39	55				
176	32	40	54				
157	22	37	49				
211	17	37	54				
150	27	39	53				
153	17	50	54				
153	17	40	53				
177	24	39	53				
155	23	39	54				
210	18	39	54				
179	31	48	52				
176	31	46	55				
179	13	39	54				
213	15	30	50				
223	15	20	38				
235	17	29	36				
153	17	195	78				
154	15	187	76				

235	19	209	89				
218	13	205	83				
189	24	308	83				
210	18	308	88				
222	18	302	82				
166	17	307	84				
168	31						
177	31						
213	25						
219	13						
176	31						
170	32						
200	22						
224	13						
213	19						
224	16						
151	17						
149	27						
154	17						
176	23						
198	26						
155	24						
153	25						
154	24						
176	32						
156	21						
166	17						
195	18						
190	18						
195	12						
194	12						
194	11						
198	16						
197	16						
179	24						
176	23						
180	12						
162	24						
168	23						
163	21						
162	20						
150	23						
160	26						
162	24						
158	21						
150	34						
152	22						
183	29						

159	20						
159	25						
151	33						
180	12						
176	24						

Station 7									
Bedding		Faults		Folds		Joints		Bedding 2	
azimuth	dip	azimuth	dip	azimuth	dip	azimuth	dip	azimuth	dip
207	39	175	66	30	29	91	80	35	17
198	27	177	67	25	35	84	49	4	24
192	39	174	67	34	46	82	57	28	24
190	40	186	67	16	55	75	59	26	28
198	34	166	73	9	66	69	67	30	24
192	39	170	74	72	19	30	59	24	19
191	45	183	75	30	42	29	48	21	24
195	36	188	64	24	37	21	48	31	24
190	34	184	67	19	33	18	69	15	18
186	35	170	70	39	43	63	69	16	17
191	35	181	71	5	64	62	72	30	24
191	36	181	70	14	54	69	76	15	32
193	34	196	80	40	41	82	67	25	31
200	38	193	77	21	38	22	57	29	27
191	34	180	73	22	35	21	44	23	24
199	41	192	77	24	34	18	82	10	27
190	39	191	77	19	33	39	63	32	23
186	35	178	74	30	87	28	43	28	28
191	37	182	74	24	88	23	74	32	27
191	39	182	67	206	88	10	68	15	30
193	34	177	73	18	77	11	75	4	25
200	41	197	80	26	82	17	67	4	24
191	43	196	75	26	70	7	59	29	27
199	34	199	74	30	77	10	74	25	22

190	35	200	77	33	72	66	68	0	21
192	37	195	77	24	68	62	74	359	21
195	38	192	76	14	65	68	76	346	23
205	41	192	74	216	23	71	76	21	29
192	39	180	70	186	28	82	73	22	30
201	39	183	68	187	28	81	73	3	24
192	37	199	76	184	13	85	62	14	24
196	33	187	68	192	18	80	51	4	26
202	32	198	75	199	34	81	69	15	30
193	43	193	78	189	28	85	61	16	31
197	33	185	68	188	24	10	64	2	20
196	42	193	78	182	25	10	60	14	25
198	42	177	74	188	29	11	64	27	27
198	31	196	79	187	27	41	63	15	29
199	37	194	78	183	12	62	73	26	22
199	39	196	78	189	25			15	26
200	36	204	86	215	25			11	28
190	33	213	87	189	30			26	28
194	38	201	87					21	30
196	36	196	73					26	28
197	33	197	67					10	27
200	40	200	70					29	25
197	41	199	86					3	21
193	43	196	70					15	28
197	33	199	87					4	25
200	37	195	72					21	31
195	38	203	86					200	84
206	40	10	72					202	82
203	33	10	76					195	82
204	33	7	77					182	85
195	43	4	83					202	77
196	37	10	82					195	76
198	40	9	71					180	77
191	37	9	75					181	84
198	37	8	80					200	85
203	35	6	76					201	82
197	35	176	89					199	83
206	38	173	86					212	86
202	35	196	77					192	78
207	37	183	87					195	75
205	36	27	73					197	76
206	38	22	77					194	80
200	32	18	77					192	77
197	30	17	76					196	83
200	36	26	73					176	76
206	39	18	72					186	70
189	34	17	71					183	75
190	35	26	72					183	71

200	33	18	75					186	74
197	31	22	46					170	76
191	36	27	73					169	56
190	33	21	74					171	62
194	39	14	81					177	69
191	36	18	81					181	65
200	37	21	85					182	68
198	39	10	84					189	67
190	36	12	79					201	80
186	39	7	84					195	75
197	41	14	88					182	73
196	35	10	83					176	76
190	43	11	90					180	77
193	40	18	68						
200	39	19	73						
195	32	16	66						
200	40	13	88						
188	28	11	88						
195	29	21	88						
25	20	15	80						
21	17	19	80						
		14	87						

11. Appendix 2: Geochemical data

Major element weight percentages using XRF																				
Sample	DFE1	DFE2A	WP2	WP6	WP8	FP7	GPT1	GPT4	GPT11	CT2	CT9	GPW5	SP2	RF2	MFE1	FP3	GPE3	MFW2	DFE-2B	GPW-11
SiO_2	99.48	97.33	99.49	99.34	98.84	99.28	96.12	94.41	90.57	99.63	98.99	96.46	95.46	95.09	97.45	98.61	96.90	95.43	98.33	97.76
TiO_2	0.15	0.44	0.19	0.01	0.02	0.01	0.16	1.01	0.39	0.03	0.18	0.21	0.23	0.37	0.37	<0.01	0.07	0.58	0.15	0.13
Al_2O_3	0.39	1.29	0.19	0.15	0.76	0.64	1.91	2.81	4.93	0.50	0.87	2.34	1.43	2.94	1.31	0.77	2.44	2.30	1.11	1.51
Fe_2O_3(t)	0.38	0.33	0.40	0.52	0.38	0.32	0.47	0.85	1.33	0.29	0.41	0.56	1.87	0.32	0.48	0.34	0.38	0.91	0.29	0.48
MnO	0.005	0.005	0.012	0.009	0.009	0.011	0.007	0.008	0.014	0.006	0.008	0.009	0.012	0.004	0.007	0.004	0.006	0.008	0.005	0.007
MgO	0.01	0.03	0.01	0.01	0.02	0.01	0.06	0.09	0.15	<0.01	0.01	0.04	0.03	0.04	0.04	0.01	0.05	0.06	0.02	0.03
CaO	<0.01	<0.01	0.02	0.01	0.01	<0.01	0.15	0.03	0.02	<0.01	<0.01	<0.01	0.01	0.01	0.01	<0.01	0.01	0.02	0.03	<0.01
Na_2O	<0.05	<0.05	<0.05	<0.05	<0.05	<0.05	<0.05	<0.05	<0.05	<0.05	<0.05	<0.05	<0.05	0.06	<0.05	<0.05	<0.05	<0.05	<0.05	<0.05
K_2O	0.05	0.32	0.01	0.01	0.13	0.14	0.50	0.76	2.05	0.09	0.20	0.61	0.38	0.63	0.34	0.16	0.57	0.57	0.24	0.39
P_2O_5	0.006	0.056	0.149	0.194	0.033	0.009	0.251	0.032	0.026	0.033	0.029	0.013	0.033	0.016	0.025	0.071	0.009	0.038	0.018	0.026
Cr_2O_3	0.001	0.001	0.002	<0.001	0.001	0.001	<0.001	0.003	0.002	0.001	0.001	0.002	<0.001	<0.001	0.002	<0.001	<0.001	0.001	0.001	0.001
L.O.I.	0.12	0.38	0.14	0.26	0.27	0.15	0.62	0.57	0.88	0.22	0.29	0.45	0.43	0.59	0.34	0.15	0.44	0.60	0.38	0.38

Trace element concentrations in parts per million using XRF																				
Sample	DFE1	DFE2A	WP2	WP6	WP8	FP7	GPT1	GPT4	GPT11	CT2	CT9	GPW5	SP2	RF2	MFE1	FP3	GPE3	MFW2	DFE-2B	GPW-11
As	<4	<4	<4	<4	<4	<4	<4	<4	<4	<4	<4	<4	<4	<4	<4	<4	<4	<4	<4	<4
Ba	34	120	12	65	65	52	162	225	678	135	91	143	200	289	157	97	265	183	85	103
Bi	<3	<3	<3	<3	<3	<3	<3	<3	<3	<3	<3	<3	<3	<3	<3	<3	<3	<3	<3	<3
Br	<2	<2	<2	<2	<2	<2	<2	<2	<2	<2	<2	<2	<2	<2	<2	<2	<2	<2	<2	<2
Ce	18	35	44	16	16	11	28	70	35	21	20	21	24	39	38	<10	15	58	44	24
Co	<1	<1	<1	<1	<1	<1	<1	1.6	2.7	<1	<1	<1	1.6	<1	<1	<1	<1	1.4	<1	<1
Cr	39	68	72	37	52	57	50	60	66	100	47	44	44	55	82	43	43	45	61	56
Cs	<5	<5	<5	<5	<5	<5	<5	<5	<5	<5	<5	<5	<5	<5	<5	<5	<5	<5	<5	<5
Cu	<2	3.1	3.5	2.8	3.6	3	5.4	3.4	4.0	4.2	3.2	4.0	4.7	3.6	3.4	3.8	3.5	5.5	3.4	3.5
Ga	<1	1.7	<1	<1	1.6	<1	2.9	4.0	5.8	<1	1.5	3.0	2.0	4.2	1.6	1.6	2.8	3.1	1.6	1.9
Ge	<1	<1	<1	<1	<1	<1	<1	<1	<1	<1	<1	<1	1.0	<1	<1	<1	<1	1.6	<1	<1
Hf	<3	10	5.4	<3	<3	<3	3.6	14	5.9	<3	<3	4.0	4.9	4.1	7.2	<3	<3	9.2	5.6	<3
La	<10	15	18	<10	<10	<10	<10	20	13	11	<10	<10	<10	18	12	<10	<10	20	20	<10
Mo	<2	<2	<2	<2	<2	<2	<2	<2	<2	<2	<2	<2	<2	<2	<2	<2	<2	<2	<2	<2
Nb	3.9	8.8	5.5	1.7	2.6	2.2	4.6	16	8.3	2.8	5.1	5.1	5.2	7.6	7.9	2.3	3.4	10	5.2	4.6
Nd	<10	14	18	<10	<10	<10	13	35	18	<10	<10	12	11	18	16	<10	<10	25	21	<10
Ni	<2	<2	<2	<2	<2	<2	<2	2.8	5.7	<2	<2	<2	<2	<2	<2	<2	<2	2.0	<2	<2
Pb	3.9	8.9	5.0	3.2	2.5	3.3	6.4	14	15	4.4	5.7	12	7.3	6.7	6.5	4.4	4.5	11	4.9	6.4
Rb	<2	12	<2	<2	5.4	5.6	18	29	66	3.6	7.7	21	14	27	14	6.0	23	22	8.5	15
Sc	<3	<3	<3	<3	<3	<3	<3	<3	<3	<3	<3	<3	<3	<3	<3	<3	<3	<3	<3	<3
Se	<1	<1	<1	<1	<1	<1	<1	<1	<1	<1	<1	<1	<1	<1	<1	<1	<1	<1	<1	<1
Sm	<10	<10	<10	<10	<10	<10	<10	<10	<10	<10	<10	<10	<10	<10	<10	<10	<10	<10	<10	<10
Sr	4.8	18	9.0	6.1	7.3	10	25	11	35	14	8.6	7.7	8.5	25	8.3	13	9.3	8.9	9.3	5.2
Ta	<2	<2	<2	<2	<2	<2	<2	<2	<2	<2	<2	<2	<2	<2	<2	<2	<2	<2	<2	<2
Th	<3	8.3	4.7	<3	3.1	<3	<3	17	6.8	<3	3.1	<3	3.3	4.3	7.2	<3	<3	12	7.4	3.5
Tl	<3	<3	<3	<3	<3	<3	<3	<3	<3	<3	<3	<3	<3	<3	<3	<3	<3	<3	<3	<3

U	<2	2.7	<2	<2	<2	<2	<2	3.2	<2	<2	<2	<2	<2	<2	<2	<2	<2	2.2	<2	<2
V	6.2	15	8.9	4.4	8	7.9	12	27	27	12	9.8	13	14	22	16	5.4	10	21	12	12
W	<3	<3	<3	<3	<3	<3	<3	<3	<3	<3	<3	<3	<3	<3	<3	<3	<3	<3	<3	<3
Y	2.5	6.7	4.8	1.5	1.8	1.8	2.9	19	9.4	2.8	2.8	4.4	5.3	6.3	7.9	1.7	2.2	12	5.0	3.5
Yb	<3	<3	<3	<3	<3	<3	<3	<3	<3	<3	<3	<3	<3	<3	<3	<3	<3	<3	<3	<3
Zn	<3	<3	<3	<3	3.1	<3	<3	13	14	<3	<3	3.1	5.1	<3	6.1	<3	<3	7.3	17	<3
Zr	134	427	262	50	59	61	126	771	257	83	122	182	180	173	358	58	83	519	242	150